Collective Behaviour of Polar Active Matter in Two Dimensions

Inaugural-Dissertation

zur
Erlangung des Doktorgrades
der Mathematisch-Naturwissenschaftlichen Fakultät
der Universität zu Köln
vorgelegt von

Özer Duman
aus Bismil, Türkei

Berichterstatter:	**Prof. Dr. Gerhard Gompper**
(Gutachter)	**Prof. Dr. Stefan Klumpp**

Tag der mündlichen Prüfung: 19.01.2018

Abstract

Self-organization is a common way of forming functional structures in biology. It involves biochemical signalling pathways, triggered by a host of external conditions, that alter the mechnical properties of the individual constituents. These changes then propagate up in scale and, via changes in the self-organization, alter the biological function. In this work, we investigate self-organization and pattern formation due to self-propulsion in biological systems. The aim is to understand and map the collective dynamics in terms of mechanical properties of single constituents. We study dense ensembles of self-propelled vesicles that act as models for motile cells and ensembles of self-propelled semiflexible filaments that mimic actin filaments and microtubules in motility assays. Both systems are made of polar and active objects that possess extended shapes with an associated flexibility. We explore the collective dynamics in both systems as a function of activity, flexibility, and interactions between objects.

Epithelial tissue serves as barrier for tissues and organs. To achieve this function, epithelial cells are typically tightly-packed, spatially well-ordered, and non-motile. However, a set of conditions can turn epithelial cells motile. During vertabrate embryonic development, wound healing, and cancer metastasis, cells become motile to rearrange the tissue, heal the wound, or travel away from the primary tumor, respectively. In vitro experiments on motile cell monolayers furthermore revealed a jamming transition in which an initially motile, fluid-like tissue undergoes a dynamic arrest. We study such motility transitions of dense cell monolayers in a minimal model approach. We go beyond existing models by including finite extension and flexibility of cells. To this end, we develop a novel computational model of cells as active vesicles that incorporates cell motility, cell-cell adhesions, compressibility, and flexibility. Increasing motility strength and decreasing cell-cell adhesions, area compression modulus, and bending rigidity lead to fluidization of the monolayer. In between the jammed and completely fluid-like states, we identify an active turbulence regime where cell motion is dominated by the formation of vortices. We thus uncover deformability-driven motility transitions and predict an active turbulent state for motile cell monolayers.

In a second part, we study the collective behaviour of self-propelled semiflexible filaments by introducing self-propulsion as a constant magnitude force acting tangentially along the bonds of each filament. The combination of polymer properties, excluded-volume interactions, and self-propulsion leads to distinct phases as a function of rigidity, activity, and aspect ratio of individual filaments. We identify a transition from a free-swimming phase to a frozen steady state wherein strongly propelled filaments form spirals at a regime of low rigidity and high aspect ratio. Filaments form clusters of various sizes depending on rigidity and activity. In

particular, we observe that filaments form small and transient clusters at low rigidities while stiffer filaments organize into giant clusters. However, as activity increases further, the clustering of filaments displays a reentrant phase behaviour where giant clusters melt, due to the strong propulsion forces bending the filaments.

Our results highlight the role of mechanical properties and the finite extent of the constituents on the collective motion patterns. Cells and filaments display different symmetry properties at high densities due to structural differences. Filaments show an effective nematic symmetry, which results in an active turbulence regime characterized by half-integer topological defects. Cells, with polar symmetry, exhibit an active turbulence phase dominated by vortices.

Kurzzusammenfassung

Funktionale Strukturen in der Biologie werden häufig durch Selbstorganisation gebildet.Teil der Selbstorganisation sind biochemische Signalwege, die durch eine Vielzahl von äußeren Bedingungen ausgelöst werden und die mechanischen Eigenschaften der einzelnen Bestandteile verändern. Diese Veränderungen wirken sich dann auf die größeren Skalen aus und verändern so die biologische Funktion. In dieser Arbeit untersuchen wir Selbstorganisation und Musterbildung durch Selbstantrieb in biologischen Systemen. Ziel ist es, die kollektive Dynamik ausgehend von den mechanischen Eigenschaften einzelner Bestandteile zu verstehen und abzubilden. Wir untersuchen dichte Verbände von selbstangetriebenen Vesikeln, die als Modelle für bewegliche Zellen dienen, sowie dichte Systeme selbstangetriebener, semiflexibler Filamente, die Aktinfilamente und Mikrotubuli in *motility assays* nachahmen. Beide Systeme bestehen aus polaren und aktiven Objekten, die ausgedehnte Formen mit entsprechender Flexibilität besitzen. Wir untersuchen die kollektive Dynamik in beiden Systemen als Funktion von Aktivität, Flexibilität und Interaktionen zwischen Objekten.

Epithelgewebe dienen als Begrenzung für Gewebe und Organe. Um diese Funktion zu erfüllen, sind Epithelzellen typischerweise dicht gepackt, geordnet und nicht-beweglich. Unter bestimmten Bedingungen können Epithelzellen jedoch mobiel werden. Während der embryonalen Entwicklung, Wundheilung und Krebsmetastase werden die Zellen motiel, um das Gewebe neu zu ordnen, die Wunde zu heilen oder sich vom Primärtumor fort zu bewegen. In-vitro-Experimente an Monoschichten beweglicher Zellen zeigten darüber hinaus einen *jamming* Übergang, bei dem ein zunächst bewegliches, flüssiges Gewebe eine dynamische Blockade erfährt. Wir untersuchen solche Motilitätsübergänge von dichten Zellmonoschichten mit einem Minimalmodell Ansatz. Dabei gehen wir über bestehende Modelle hinaus, indem wir die endliche Ausdehnung und Flexibilität von Zellen mit in die Betrachtung einbeziehen. Zu diesem Zweck entwickeln wir ein neues Computermodell von Zellen in Form von aktiven Vesikeln, das Zellmotilität, Zell-Zell-Adhäsionen, Kompressibilität und Flexibilität umfasst. Zunehmende Motilitätsstärke und abnehmende Zell-Zell-Adhäsionen, Flächenkompressionsmodul und Biegesteifigkeit führen zu einer verflüssigung der Monoschicht. Zwischen den flüssigkeitsähnlichen, und den dynamisch blokierten Zuständen finden wir ein Regime aktiver Turbulenz, in dem die Zellbewegung durch die Bildung von Wirbeln dominiert wird. Wir entdecken so einen aktiver Turbulenz deformierbarkeitsgesteuerten Motilitätsübergang und sagen einen Zustand für Monoschichten motiller Zellen voraus.

In zweiten Teil dieser Arbeit untersuchen wir das kollektive Verhalten von selbstangetriebenen, semiflexiblen Filamenten. Wir modelieren den Antrieb als eine Kraft konstanter Größe

tangential entlang der Bindungen des Filaments. Die Kombination von Polymereigenschaften, Volumenausschluss-Wechselwirkungen und Selbstantrieb führt zu unterschiedlichen Phasen als Funktion von Steifigkeit, Aktivität und Länge einzelner Filamente. Wir identifizieren einen Übergang von einer frei schwimmenden Phase zu einem eingefrorenen stationären Zustand, wo lange stark angetriebene Filamente mit geringer Steifigkeit Spiralen ausbilden. Abhängig von Steifigkeit und Aktivität bilden Filamente Cluster verschiedener Größe. Insbesondere beobachten wir, dass Filamente kleine und transiente Cluster bei niedrigen Steifigkeiten bilden, während steifere Filamente sich zu sehr grossen, systhem spannenden Clustern zusammenfinden. Wenn jedoch die Aktivität weiter zunimmt, sinkt die Clustergrösse wieder aufgrund der starken Antriebskräfte, die die Filamente verbiegen und so die Cluster schmelzen.

Unsere Ergebnisse unterstreichen die Rolle der mechanischen Eigenschaften und der endlichen Ausdehnung der einzelnen Bestandteile auf die kollektive Bewegung. Zellen und Filamente zeigen aufgrund struktureller Unterschiede unterschiedliche Symmetrieeigenschaften bei hohen Dichten. Filamente zeigen eine effektive nematische Symmetrie, die zu einem regime aktiver Turbulenz führen, das durch halbzahlige topologische Defekte gekennzeichnet ist. Zellen mit polarer Symmetrie weisen dagegen eine Phase aktiver Turbulenz auf, die von Wirbeln dominiert wird.

Contents

1. Introduction 1

1.1. Active Matter and Collective Behaviour 1
1.2. Cytoskeletal Filaments 3
1.3. Molecular Motors 6
1.4. Motility Assays 8
1.5. Cell Motility 9
1.6. Modelling Collective Cell Motility 11
1.7. Confluent Cell Monolayers 14
1.8. Structure of the Thesis 16

2. Theoretical Background and Computational Models 17

2.1. Brownian Motion 17
2.2. Molecular Dynamics 22
2.3. Simulation Model of a Cell 24
2.4. Simulation Model of a Filament 29
2.5. Liquid Crystals 31
2.6. Turbulence 34

3. Collective Dynamics of Dense Cell Monolayers 41

3.1. Introduction 41
3.2. Structure of the Monolayer 42
3.3. Dynamics of the Monolayer 48
3.4. Jamming Transition 49
3.5. Active Turbulence 57
3.6. Phase Space 65
3.7. Discussion 67
3.8. Summary 69

4. Collective Dynamics of Self-propelled Semiflexible Filaments 70

4.1. Introduction 70
4.2. Single Filament Dynamics 71
4.3. Collective Dynamics at Finite Densities 75
  4.3.1. Spiral Formation 77
  4.3.2. Cluster Formation and Disintegration 84

4.3.3. Melting of Giant Clusters . . . 91
4.3.4. Dynamics of Giant Clusters . . . 94
4.3.5. Isotropic-Nematic Transition . . . 98
4.4. Collective Dynamics at High Densities . . . 100
4.5. Discussion . . . 106
4.6. Summary . . . 109

5. Concluding Summary **110**

Bibliography **113**

A. Biological Background **A 129**
A.1. Microtubules . . . A 129
A.2. Intermediate Filaments . . . A 131
A.3. Organisation of Cells into Tissues . . . A 131
A.4. Epithelial Cells . . . A 132

B. Mathematical Background **B 135**
B.1. Probability Density . . . B 135
B.2. Characteristic Function . . . B 135
B.3. Conditional Probability Density . . . B 136
B.4. Generalized Langevin Equation . . . B 137
B.5. Fokker-Planck Equation . . . B 143
B.6. Numerical Accuracy of the Velocity Verlet Algorithm . . . B 145

C. Polymers **C 147**
C.1. Freely Jointed Chain . . . C 147
C.2. Freely Rotating Chain . . . C 148
C.3. Rouse Chain . . . C 148
C.4. Kratky-Porod Worm-Like Chain . . . C 151
C.5. Circular Chain . . . C 152
C.6. Helfrich Hamiltonian . . . C 153

D. Additional Remarks on Turbulence **D 157**
D.1. Onsager Phenomenology of Vortex Formation . . . D 157
D.2. Fjortoft's Theorem . . . D 157
D.3. Active Turbulence . . . D 159

E. Dynamics of a Single Cell **E 181**

Eigenhändigkeitserklärung **E 184**

F. Curriculum Vitae **F 185**

Curriculum Vitae **F 186**

1. Introduction

1.1. Active Matter and Collective Behaviour

Active matter is a paradigm for a large class of systems that can convert internal or ambient energy into sustained motion, internal stresses or growth. This paradigm is applied to phenomena across many length scales from bird flocks and fish schools at macroscales [164, 24], to microswimmers like bacteria and sperm cells at mesoscopic scales [165, 33, 118], all the way down to Janus particles and enzymes at nanoscales [115]. In all of these examples, internally generated (e.g., ATP consumption) or externally produced (e.g., thermal gradients) energy is used for activity. The defining property of active matter is that this energy conversion happens on the local scale of the constituents. A Janus colloid, turning energy from light into a local thermal gradient driving the particle, is an active particle, whereas a charged DNA undergoing electrophoresis in an external field is not.

Phenomena known from statistical mechanics can often be used as analogs to describe active matter systems. Velocities of individual units in bird flocks are similar to the local spins in the XY model. Extending the XY model by adding convection and alignment of local spins captures a regime of long-range order similar to the flocking behaviour of birds, slime molds, or bacteria [195]. Collections of shaken granular particles display chaotic regimes with anomalous number fluctuations [138]. Monolayers of gliding bacteria like *Mixococcus xanthus* and *Bacillus subtilis* exhibit cluster formation above a critical density threshold [153, 30]. At even higher densities, *B. subtilis* suspensions form vortices showing turbulent behaviour, while *M. xanthus* suspensions show liquid crystalline ordering (Fig. 1.1-a) [204, 205, 129]. When momentum is dissipated with the background, the ordered phases of incompressible polar active fluids in two dimensions can be mapped to the same universality class as growing one-dimensional interfaces, two-dimensional smectic liquid crystals, and divergence-free XY model (Fig. 1.1-b) [27]. Self-propelled particles with purely repulsive interactions can undergo liquid-gas phase separation (Fig. 1.1-c) [57, 23]. At high densities, soft self-propelled particles undergo dynamic arrest, resulting in a phase similar to equilibrium glass transition, or jamming transition of epithelial cell monolayers (Fig. 1.1-d) [79, 4]. Non-equilibrium collective phenomena (often of biological origin) are linked to active matter in all of these examples.

Many different factors combine in many different ways, due to many different reasons, to generate many different varieties of collective motion. A bird flock may form to protect the birds from predators, whereas a bacterial swarm may form to elevate the antibiotic resistance of bacteria [103]. Birds may move in such a way to maintain a large view of the surrounding area, whereas bacteria may move in response to a chemical gradient. Bird flocks may make almost instantaneous hairpin turns, while bacterial swarms may move in vortices [204]. How does the simple paradigm of active matter help with explanation of such complex collective behaviour? Active matter connects these systems across length scales in a simple unifying framework, in which the collective motion emerges from the motion of individual units. By reducing the collective dynamics of birds, sperm cells, or self-propelled rods to the movement of individual units, we can find general principles that govern collective motion. We can identify patterns that apply to different systems and find the minimal reasons underlying these patterns.

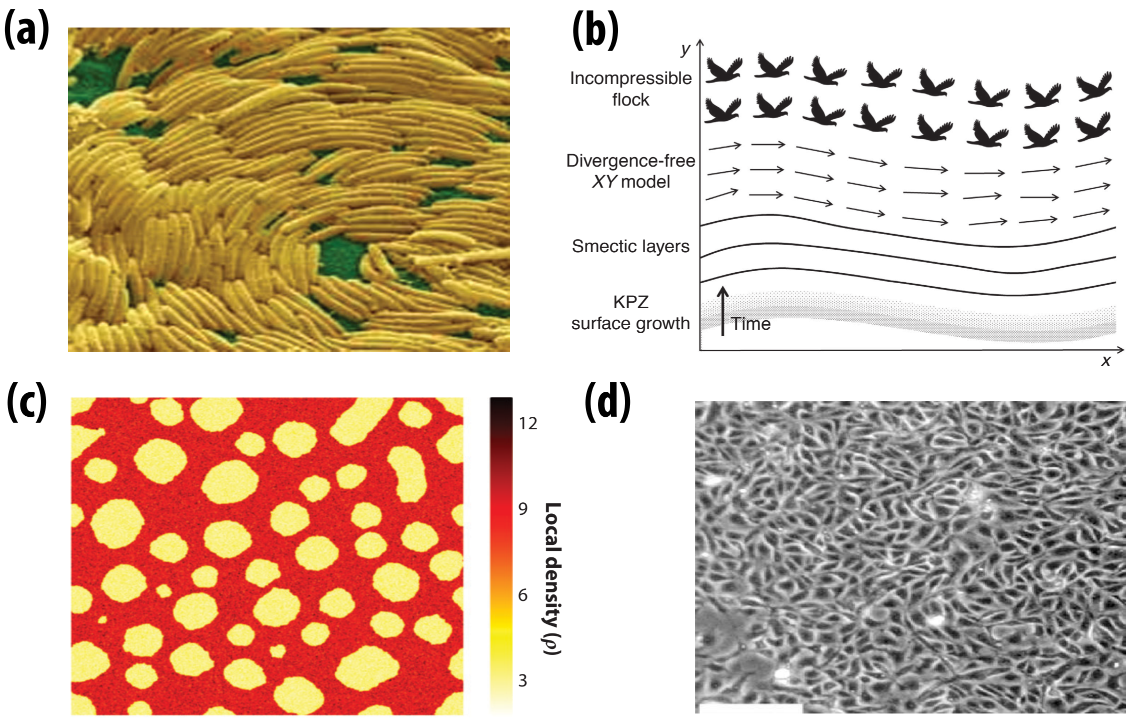

Figure 1.1.: Examples of collective behaviour in active systems: (a) A high density suspension of *Mixococcus xanthus* with liquid crystalline ordering. Image is taken from ref. [129]. (b) Incompressible polar active fluids in 2D can be mapped to the same universality class as divergence-free XY model, smectic liquid crystals in 2D, and growing one-dimensional interfaces. Image is taken from ref. [27]. (c) A two-dimensional run-and-tumble system showing motility-induced phase separation. Image is taken from ref. [23]. (d) A confluent MDCK monolayer undergoing dynamical arrest. The scale bar marks 100 μm. Image is taken from ref. [4].

In this thesis, our aim is to study the collective motion in motile cell monolayers and motility assays of cytoskeletal filaments with a minimal computational modelling approach based on polar active matter. In particular, we analyse the role of mechanical properties, shape and finite extent of individual constituents in collective motion. To this end, we start by an exploration of the properties of cytoskeleton and motile cells, which make up the biological background of this thesis.

1.2. Cytoskeletal Filaments

The cytoskeleton is mainly made up of three classes of filamentous polymers: Actin filaments, microtubules and intermediate filaments. Actin filaments demonstrate the most essential properties shared among these polymers. Therefore, we discuss actin filaments to introduce these properties [1].

Actin filaments (F-actin) are made up of small actin proteins that have a globular shape. Globular actin (G-actin) is a protein that can bind to an ATP molecule and other actin proteins. As a result, actin proteins have the ability to reversibly assemble, generating a helix-shaped filamentous polymer (Fig. 1.2).

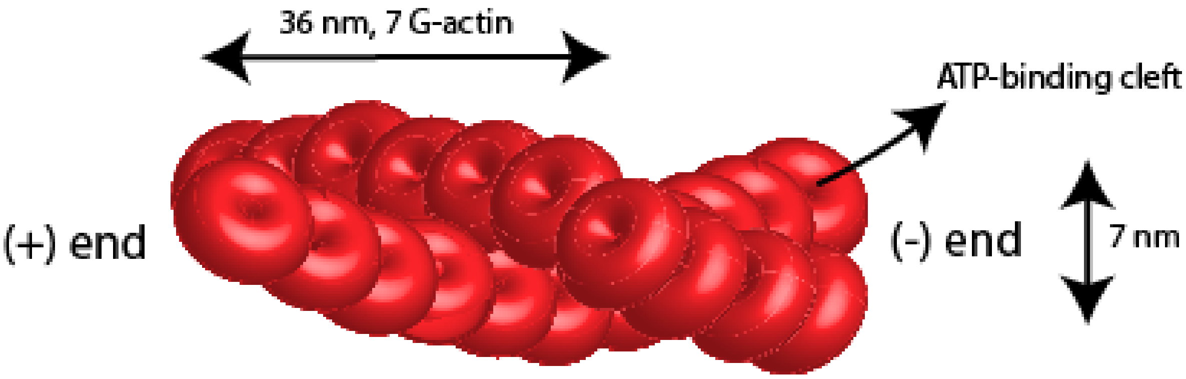

Figure 1.2.: Sketch of an actin filament as two helical strands: One repeating unit is 72 nm long with 14 G-actin on each strand (28 G-actin in total). The filament has a diameter of ~ 7 nm. ATP-binding cleft of G-actin contacts neighbouring G-actin at the (+) end. The cleft is exposed outside at the (−) end.

Actin assembly occurs in three stages. At the first (and the hardest) stage, actin proteins assemble spontaneously into small structures. Actins need to make contact in a specific configuration in order to assemble. Namely, an actin can attach to the ATP-binding side of another actin. Therefore, the resultant structure has a polarity with the ATP-binding site of actins facing the (−) direction. After the assembly of a few actins in this way, the formed structure becomes stable (Fig. 1.3-a). This stable structure serves as a nucleus for more actins to assemble (Fig. 1.3-b). Therefore, from a physical point of view, formation of an actin nucleus is a function of the free actin concentration inside the cell. If the actin concentration is high enough, stable nuclei will start to form. In the next stage, free actins in the cell attach to these nuclei and elongate them, generating growing actin filaments (Fig. 1.3-c). Filament growth comes to a halt for two reasons: Firstly, concentration of free actins decreases as filaments grow. Secondly, actins at the ends of a filament can detach from the filament. At the final stage of actin assembly, these two factors balance each other in a steady state, as actins attach to and detach from the ends of filaments.

---

[1] For an extended discussion on other cytoskeletal filaments, see Appendix A.

Within this simplified model, actin filament formation is a spontaneous self-assembly event without even the need for ATP hydrolysis. Therefore, filament dynamics can be analysed in terms of simple kinetic arguments. By assuming that filaments have similar lengths and the number of filaments is fixed, we can describe the number of monomers associated with the average filament length by the rate equation

$$\frac{\mathrm{d}n}{\mathrm{d}t} = k_{\mathrm{on}}\left(c - \frac{Mn(t)}{V}\right) - k_{\mathrm{off}}, \tag{1.1}$$

where n is the number of monomers making up a filament, c is the actin monomer concentration within a volume V, and M is the number of filaments [156]. k_{on} and k_{off} are rate constants determining the rates of monomer attachment and detachment, respectively. The first term on the right-hand side describes the growth of filaments, which is proportional with the free monomer concentration. As filaments grow, the number of free monomers decreases. The second term describes the shrinkage of filaments through monomer detachments. This simple dynamical model captures the polymerization dynamics with the solution

$$n(t) = \frac{V}{Mk_{\mathrm{on}}}(k_{\mathrm{on}}c - k_{\mathrm{off}})(1 - \mathrm{e}^{-k_{\mathrm{on}}Mt/V}), \tag{1.2}$$

At the short time limit, expanding the exponential in a Taylor series shows that filaments grow linearly in time. At the long time limit, the growth saturates towards an average filament length of $V(k_{\mathrm{on}}c - k_{\mathrm{off}})/k_{\mathrm{on}}M$ [156].

So far, we assumed that monomers can assemble and disassemble from either end of a filament with equal probability. However, monomers with bound ATP have a higher probability of assembly than free monomers [122]. Monomers with bound ADP, on the other hand, have a higher probability of disassembly. These properties alter the filament dynamics dramatically. Due to their high affinity, monomers with ATP attach to the growing end of a filament, creating a cap of ATP-monomer subunits there. As filament length grows, ATP in the earlier added subunits start to hydrolize into ADP and $\mathrm{P_i}$. $\mathrm{P_i}$ dissociates from the subunit later. Therefore, due to ATP hydrolysis, filaments end up having a cap of ATP-monomers at the (+) end, ADP-$\mathrm{P_i}$-monomers in the middle, and ADP-monomers at the (−) end. As ATP-monomers continue to assemble at the (+) end and ADP-monomers disassemble from the (−) end, filaments appear to be *treadmilling* (Fig. 1.3-d).

Cells cannot use preassembled structures to respond to ever-changing internal conditions or external cues. The dynamic nature of actin polymerization is helpful for cell response in this regard. For example, actin polymerization can be used to apply forces. Such forces are measured in experiments with optical tweezers. It is found that a growing actin filament exerts a force on the order of 5 pN on an optically trapped microscopic bead [59]. This value is actually close to the force exerted by gravity on a single bacterium, or by molecular

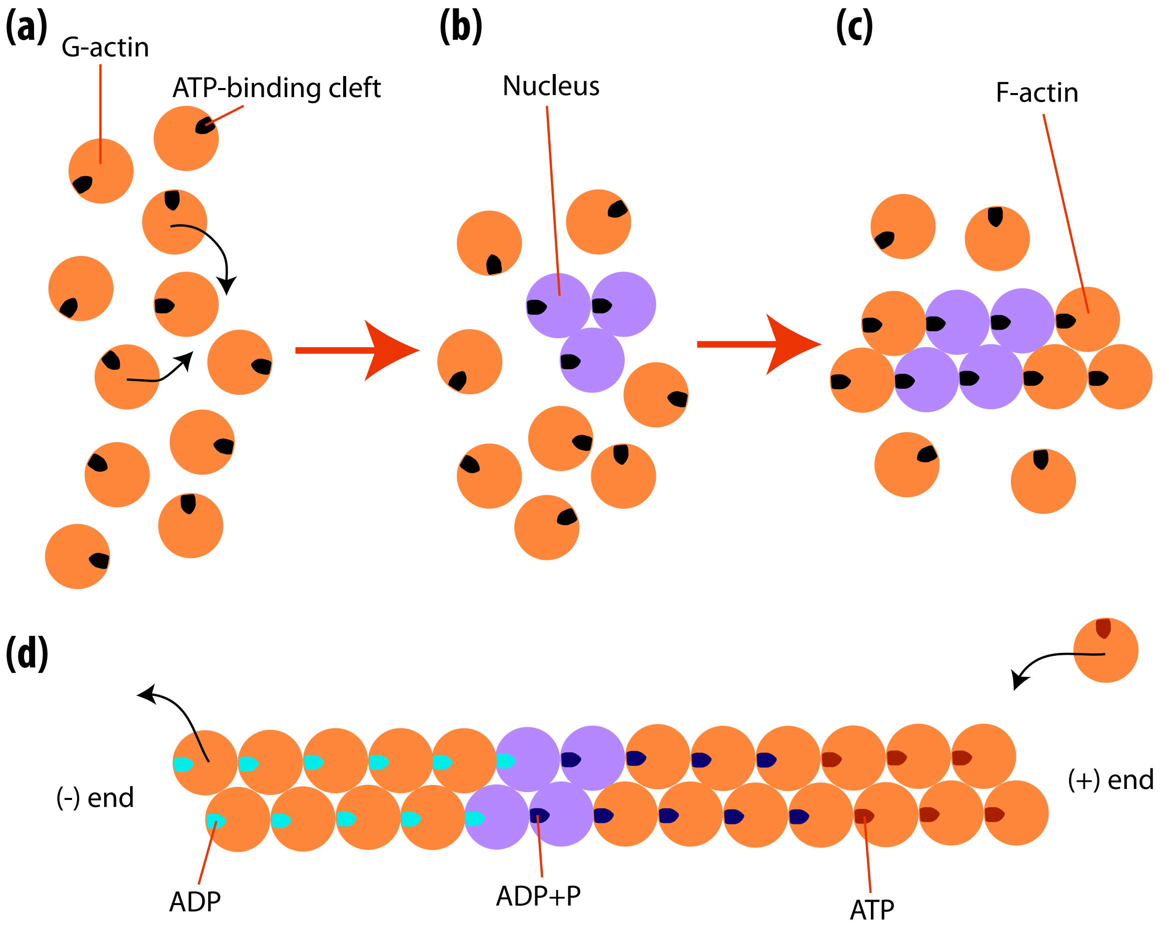

Figure 1.3.: Sketch of actin assembly: (a) Monomers assemble spontaneously into a small structure. (b) After the assembly of a few monomers, small structures stabilize and serve as nuclei for assembly of further monomers. (c) Free monomers attach to nuclei and elongate them into actin filaments. (d) ATP-monomer units are more likely to attach and ADP-monomer units are more likely to detach. Due to these affinities and ATP hydrolysis, filament has a structure with ATP-monomers at the (+) end, ADP-P_i-monomers in the middle and ADP-monomers in the (−) end. As ATP-monomers assemble at the (+) end, and ADP-monomers disassemble from the (−) end, filaments treadmill.

motors such as myosin or kynesin that utilise ATP or GTP hydrolysis [122]. These hydrolysis reactions provide $\sim 20 k_\mathrm{B}T$ per nucleotide [156]. A force of 5 pN exerted by the actin filament over the monomer extension length of 4 nm has an energy of 20 pN$x$nm. Considering that $k_\mathrm{B}T \sim 4$ pN$x$nm, the filament force has an associated energy of $5 k_\mathrm{B}T$ over a distance of 4 nm. Therefore, the energy associated with a polymerizing actin filament is in the same order of magnitude as the energy available from nucleotide hydrolysis.

To utilise actin polymerization to do work, cells use actin-binding proteins. We will introduce some of the most important ones here. *Profilin* facilitates the exchange of ADP to ATP in a monomer, thereby promoting polymerization. *Cofilin* acts the opposite by facilitating the exchange of ATP to ADP in a monomer, thereby promoting depolymerization. *Capping proteins* bind to filament ends and block both assembly and disassembly [122]. These proteins that control the actin dynamics play a critical role in the function of actin filaments inside the cell. For example, cancer cells often have actin filaments of higher motility, which is facilitated by these actin-regulating proteins [126].

Actin filaments can be assembled long or short depending on their function. In stress fibers, and in contractile rings, actin filaments are long. Formation of such long filaments is facilitated by the protein class of *formins*. Formins form a donut-shaped ring around the (+) end of filaments, removing capping proteins and blocking the attachment of further capping proteins [122]. Without capping proteins at the (+) end, actin filaments can grow longer. On the other hand, actin filaments that attach to the plasma membrane, or the leading edge of motile cells, are relatively short. Such short actin filaments assemble in a complex network by the protein family *Arp2/3*. These proteins are structurally similar to the (+) end of actin filaments. Therefore, they can bind to the side of actin filaments and serve as hubs for formation of new actin filaments as branches from the binding site. These branches are then connected via cross-linking proteins to form a network. Arp2/3 proteins are essential in the formation of leading edge of motile cells [122].

1.3. Molecular Motors

Molecular motor proteins are a class of proteins that are extremely important for the function of cytoskeletal filaments inside cells. Motor proteins use cytoskeletal filaments as tracks to perform mechanical work by utilising ATP hydrolysis. Myosins are motor proteins associated with actin filaments. They consist of a head, a neck, and a cargo-binding tail domain [122].

A myosin performs work, by using ATP hydrolysis to change the position of its head domain with respect to its neck domain while it is bound to an actin filament. ATP can bind to a myosin head attached to a filament (Fig. 1.4-a). ATP-bound head cannot stay attached to the filament and dissociates (Fig. 1.4-b). ATP then hydrolizes into ADP and $\mathrm{P_i}$ in the dissociated head. The energy released from ATP hydrolysis rotates the head with respect to the neck. The head, freed from ATP, can then bind again to the filament at its new rotated position (Fig. 1.4-c). At this point, myosin head with ADP and $\mathrm{P_i}$ is bound to the filament at the rotated position. In the next step, $\mathrm{P_i}$ cannot stay bound to the head and detaches. The elastic energy associated with the release of $\mathrm{P_i}$ straightens the head with respect to the neck (Fig. 1.4-a). This straightening motion acts like a power stroke on the filament. The filament slides with the straightening myosin head. After this, ADP dissociates and frees the filament-bound head once again. Thereafter, the cycle can start again with the binding of ATP to a filament-bound head [122]. Through this cycle, myosins can take discrete steps along the actin filament. During each step, myosins generate a force of ~ 3 – 5 pN on the filament [156].

Many eukaryotes have three myosin classes with each class having a distinctive number of

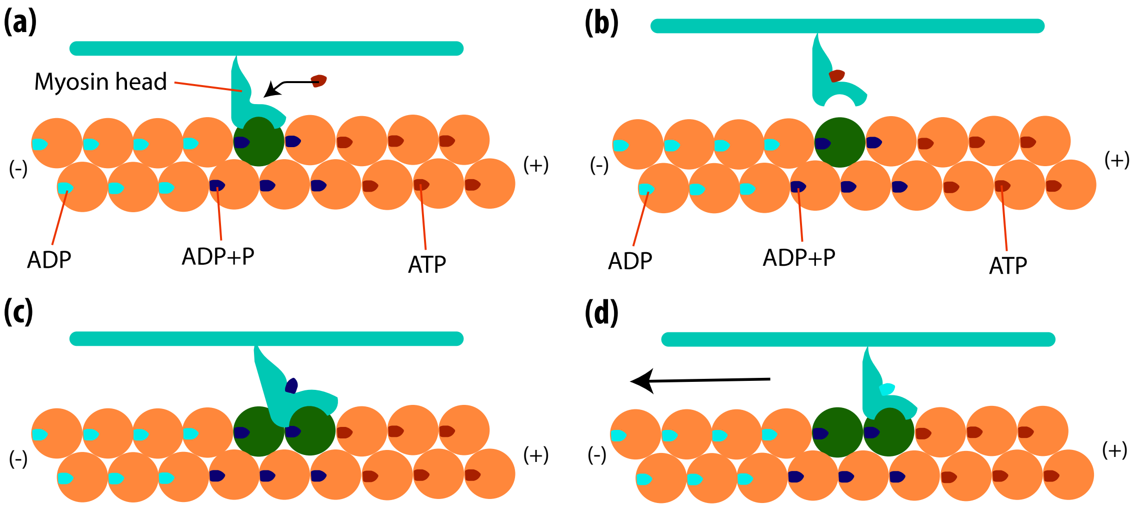

Figure 1.4.: Sketch of a myosin head walking along an actin filament: (a) ATP binds to a myosin head that is attached to the filament. (b) ATP-bound head dissociates from the filament. (c) ATP hydrolyzes into ADP and P_i. The energy generated from hydrolysis rotates the head with respect to the neck. The head, freed from ATP, can then bind again to the filament at the rotated position. (d) P_i dissociates and the energy gained from the release of P_i straightens the myosin head. This straightening motion acts like a power stroke sliding the filament along.

elements in myosin domains. Myosin I has a single head domain. Myosin II has two head domains, which help in assembling bipolar filaments. The step sizes of myosin II are small (~ 5 – 15 nm) and nonprocessive (that is, the steps do not follow one another successively, as the motor detaches frequently). Myosin II plays an important role in the contraction of skeletal muscle cells. Muscle cells are large cylindrical cells (1 – 40 mm in length, 10 – 50 μm in width) with around 100 nuclei. Each cell contains myofibrils made of repeating sarcomeres. A sarcomere consists of interlocking myosin thick filaments and actin thin filaments. Muscle contraction is facilitated by the sliding of myosin thick filmanets along actin thin filaments, which shortens the sarcomere. The small and nonprocessive steps of myosin II motors are helpful to perform this function [122].

Myosin V has two head domains. It carries cargo like organelles or endocytosis products by using actin filaments as tracks. The steps of myosin V are large (~ 36 nm) and processive, which help in carrying cargo. Myosin V also plays a role in cytoplasmic streaming of large cells, such as plant cells and amoebas. During cytoplasmic streaming, cytosol flows rapidly around the cell distributing metabolites with the help of myosin V and microtubules [122].

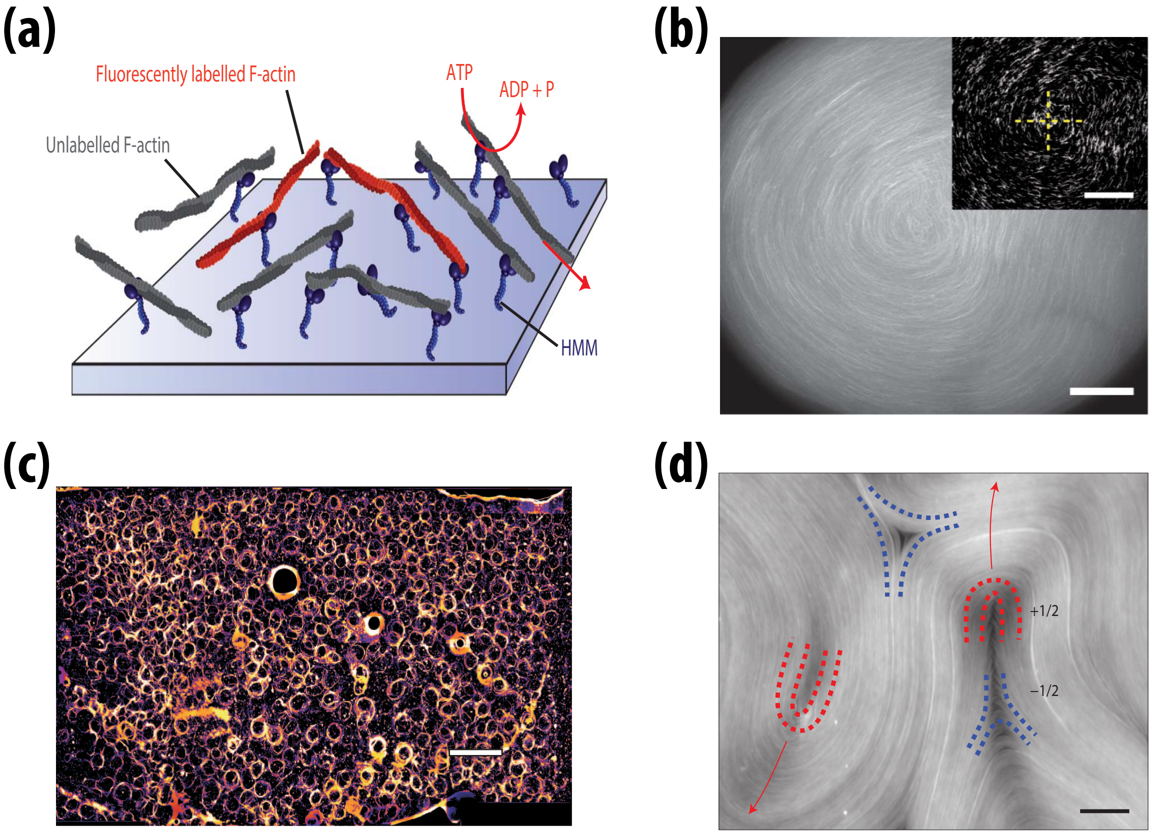

Figure 1.5.: Examples of *in-vitro* experiments on gliding motility assays: (a) Molecular motor proteins heavy meromyosin (HMM), immobilized on the coverslip, slide actin filaments in the presence of ATP. Fluorescence labelling of filaments (with a ratio of $\sim 1:200$) allows visualization of filament motion. Image is taken from ref. [174]. (b) At high filament concentrations, actin filaments exhibit swirling motion. The depicted image is a time overlay of 10 consecutive images over 1.17 s, starting from the image in the inset. Scale bars show 50 μm. Image is taken from ref. [174]. (c) Microtubules self-organize into a large-scale hexagonal vortex lattice. Scale bar is 2 mm. Image is taken from ref. [182]. (d) Fluorescence microscopy image shows half-integer topological defects in microtubule assays grafted with kinesins. Due to the intrinsic non-equilibrium nature of microtubule dynamics, +1/2 defects are motile. Scale bar is 50 μm. Image is taken from ref. [37].

1.4. Motility Assays

From a structural perspective, the networks of cytoskeletal filaments inside the cell resemble physical gels. However, unlike gels, the cytoskeleton is driven out of thermodynamic equilibrium through the action of molecular motors and treadmilling. Non-equilibrium conditions can lead to *in vitro* self-organization and complex collective motion of purified cytoskeletal elements on motility assays. In motility assays, filaments glide over a surface decorated with molecular motors. By controlling a few adjustable parameters such as the filament density, or motor density, coherently moving patterns with sizes much larger than individual constituents can appear.

For actin assays, in which actin filaments and fluorescently labelled reporter filaments are driven by immobilized non-processive molecular motors (the protein heavy meromyosin), large-scale structures form as a function of filament density (Fig. 1.5-a) [174]. As filament density increases, clusters of filaments start to form from an initial disordered state. A further increase of density generates density waves in which high-density bands of filaments move coordinated in wave-like patterns. At high densities, filaments form spontaneously swirls and spiralling patterns due to steric and hydrodynamic interactions (Fig. 1.5-b). In experiments on microtubule assays with grafted dynein motors, microtubules are found to align upon binary collisions [182]. At high densities, microtubules self-organize into vortices due to the effective alignment of collisions. Such vortices have diameters of 400 μm (in comparison to the average microtubule length of 15 μm) and on longer time scales, vortices further self-organize into a hexagonal lattice structure (Fig. 1.5-c). This vortex lattice formation is pinned down numerically to the short-range steric interactions of microtubules [182]. In gliding microtubule assays with kinesin-coated carpets, microtubules are observed to form half-integer topological defects similar to the nematic phase of equilibrium liquid crystals (Fig. 1.5-d) [37]. However, in active nematics, a higher-order emerges in which defects self-organize into an orientationally ordered structure. Therefore, stable complex patterns, with lengths much larger than filament lengths, can form in motility assays by varying only minimal control parameters, such as density.

1.5. Cell Motility

One of the most important functions of actomyosin system *in vivo* is in cell motility. Cells become motile under a variety of circumstances. Cells move to generate structural rearrangements during vertrebrate embryogenesis. Epithelial cells in an animal move to heal a wound. White blood cells migrate to infection sites. Intestinal epithelial cells along the villi of the intestine migrate slowly and continuously. Besides these, cell motility also arises in pathogenic conditions. Cancer cells migrate away from the primary tumor, which causes metastasis [122].

Cell motility occurs through coordinated organization of the cytoskeleton in various steps. Cells have a polarity, that is, they have a preferred direction to move. The first step in motility is the formation of a large membrane protrusion in the preferred movement direction. This membrane protrusion at the leading edge of the cell is known as a *lamellipodium.* Actin filaments form a cross-linked network at lamellipodia. They can also form fingerlike protrusions that are known as *filopodia.* In these structures, actin is nucleated by Arp2/3 proteins to form branched networks with (+) ends of the actin filaments growing towards the membrane. As actins polymerize, the membrane is pushed to the front in the direction of the leading edge. Actin polymerization is supplied by profilin and cofilin [122].

Actins do work on the cell membrane by polymerization. When the polymerizing actin arrives at the membrane, polymerization halts until the membrane diffuses forward by thermal motion. Upon forward motion of the membrane, space opens up for the addition of a new monomer in front of the filament. The newly added monomer then prevents the membrane from retracting back. Thus, polymerization of actin filaments coupled with the thermal motion of the membrane leads to an effective displacement of the membrane, which generates the leading edge of the motile cell [156]. As actin filaments at the leading edge are short, they have higher stiffness. The networks they form further increases their stiffness. This prevents actin from buckling upon the stress generated by the membrane pushing backward through thermal motion.

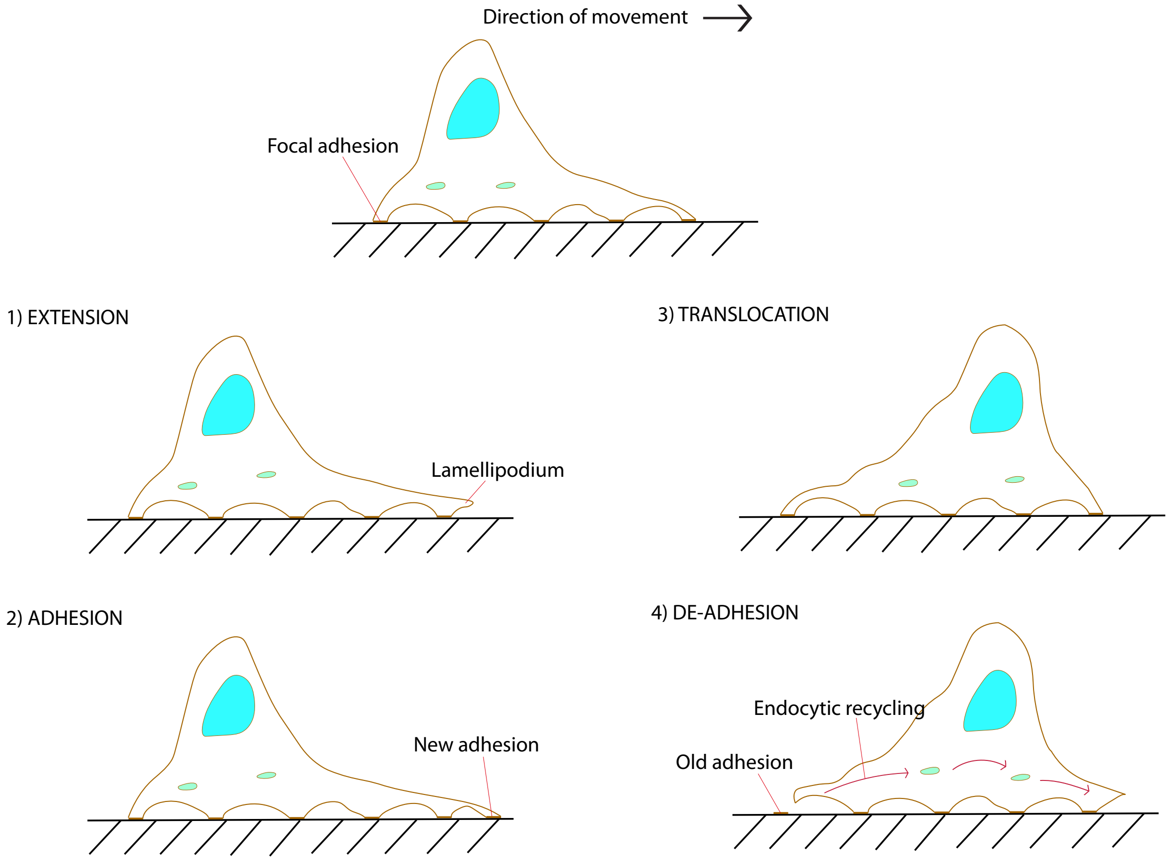

Figure 1.6.: Motility of fish keratinocyte: Cell starts moving by extending the membrane in the direction of movement. Extended membrane (lamellipodium) adheres to the substrate through focal adhesions. Then cytoplasm is pushed forward in the direction of movement by contracting actomyosin skeleton at the rear end of the cell. The rearmost adhesion point rips from the substate. Membrane and integrins at the rear end are internalized via endocytosis and they are moved to the front of the cell to be used as lamellipodium in the newer extensions of the membrane. Redrawn from ref. [122].

After extension of membrane at the leading edge and the assembly of actin filaments at the lamellipodium and filopodia, the membrane makes stable contacts with the substrate through actin filaments, so that the membrane is prevented from retracting. Bundles of actin filaments are anchored to the substrate by structures called *focal adhesions*. The membrane proteins *integrins* have a domain that is external, which binds to the extracellular matrix elements like collagen and fibronectin, and an internal domain binding to the actin filaments inside the cell. As cells move forward, integrins that are at the rear part of the cell are transported to the front so that they are recycled [122]. After the substrate attachments are made, the contents of the cell are pushed forward by contraction of myosin II at the rear part of the cell, a mechanism similar to squeezing toothpaste tube from the bottom. The focal adhesions at the rear part are subsequently broken. Cell motility is thus facilitated by the balance of mechanical forces generated by the actin cytoskeleton and the resistive forces generated by the cell adhesions to the substrate (Fig. 1.6) [122].

Cell polarity is an essential part of cell motility. Cells can choose directions through growth factors, such as epidermal growth factor (EGF) or platelet-derived growth factor (PDGF). Growth factors bind to receptors at the cell surface and through signal transduction pathways, stimulate cells to grow and divide. Blood platelets become activated upon exposure to collagen in the extracellular matrix when a wound opens up. These platelets secrete PDGF to attract fibroblats and epithelial cells to close and heal the wound [122].

Signalling pathways determine the assembly of actin filaments for cell motility. *Cdc42* determines the cell polarity and filopodia formation. *Rac* regulates the actin meshwork at the leading edge of the cell via the Arp2/3 proteins. *Rho* controls actin filament formation via formins and filament contraction via myosin II. Therefore, Rac and Cdc42 are active at the cell front, while Rho is active at the rear part of the cell. Chemotaxis, that is the ability of cells to sense and move down chemical concentration gradients, occurs through signalling pathways that generate a difference of phosphoinositides between the front and rear parts of the cell. This difference generates cell polarity through the regulation of actin cytoskeleton [122].

1.6. Modelling Collective Cell Motility

Some properties of cell motility such as polarity, formation of membrane extensions at the cell front, and membrane retractions at the cell back are common accross different cell types. However, other properties such as persistence of polarity, or cell shapes during individual locomotion can change significantly due to cell type, or environment. Cells such as keratinocytes (fish skin cells) and neutrophils (a type of white blood cell) move with stable lamellipodia, whereas other cells such as *Dictyostelium discoideum* (a soil-living amoeba species) or macrophages (another type of white blood cell) crawl by extending temporary protrusions, that are called pseudopodia, in multiple directions at the cell front [76]. Therefore, physical modelling of cell motility depends on the context of the particular study. We will introduce some of the most important models that are utilized to study collective cell migration.

One of the standard ways of describing cells is to model them as interacting ideal point particles that perform overdamped active Brownian motion. A minimal model of cell-cell interactions is a Lennard-Jones potential with short-range repulsion representing impenetrability of cells and longer-range attraction representing adhesion between cells. Additional complexity can be added on top of these minimal ingredients to capture various specific phenomena. Vicsek model describes self-propelled particles that align their orientations according to the average orientation of their neighbours [201]. In this model, increasing density and decreasing noise strengths drive a first-order phase transition towards a large-scale correlated motion with polar alignment of particles. Variations on Vicsek model are frequently used to describe flocking transitions in collective motion [26]. In one such variation, separating the velocity of cells from their motility, and adding a tendency for the motility direction to align with the velocity direction in time, is shown to result in a flocking transition as a function of increasing density [183]. More complicated interaction schemes include boundary-dependent forces such as forces that pull cells at the borders of cell clusters inward, or curvature-dependent forces at the cell cluster boundaries [46, 187].

A common choice of friction force is to assume a linear dependence on the velocity of cells relative to a fixed background. However, it can also be modelled based on dissipative particle dynamics, or with respect to relative velocities of neighbouring cells [81, 8].

Cell shape is often coupled to the motility of cells. For example, the collision of lamellipodia of two cells causes the lamellipodia to retract, which hinders the cell motion. This is known as *contact inhibition of locomotion* [215]. Particle-based models can be extended to include more realistic cell shapes. *Dictyostelium* cells are represented as ellipsoids that are deformable along three axes upon contact with other cells [150, 149]. Ellipsoidal shapes can also be introduced by invoking deformations from an initial isotropic cell shape via a shape tensor $S_{\alpha\beta} = s(\hat{n}_\alpha \hat{n}_\beta - 1/2)$, where $\hat{\mathbf{n}}$ describes the deformation axis and s describes the strength of deformations [142, 131, 186]. Cell velocity is then coupled to the shape tensor. Cell can move in circular or straight trajectories depending on the parameter of deformation strength. These extended-shape models are particularly useful in predicting the effect of shape on collisional dynamics at finite density suspensions of cells. However, capturing some of the experimental results on confluent cell monolayers, in particular the jamming transition, with these extended-shape models, remains an open question.

For confluent monolayers, it is very common to use computational models that describe cells through their geometric boundaries. In cellular Potts model, the monolayer is represented with a two-dimensional lattice with spins σ_i. This model is an extension of the Potts model (which is itself an extension of the classical Ising model). In the Ising model, spins take on two values, usually $+1$ and -1. Potts model generalizes this, so that spins can take on multiple values. Lattice sites with the same spin depicts a distinct cell (Fig. 1.7-a) [70, 73]. The energy of the cell is described in terms of spin-spin interactions

$$H = \sum_{i,j} J_{ij}(1 - \delta_{\sigma_i,\sigma_j}) + \sum_i \lambda (A_i - A_{i,0})^2, \tag{1.3}$$

where J_{ij} describes the interaction between neighbouring spins i and j. The Kronecker delta makes sure that spins of the same cell do not have an energetic cost for being near each other. The second term describes the generalization of Potts model to the cellular Potts model by prescribing a target area for the cells. The target area is the preferred number of sites of a cell and λ is a term that penalizes deviations from this number. The model is propagated in time by Monte Carlo steps in which attempts are made to copy the spin from one site to a neighbouring site with an outcome dictated by the energetic cost of the move. In this way, adhesion between cells is implemented without tracking an interface explicitly. Incidentally, this model is developed originally to study the *differential adhesion hypothesis*, which explains cell sorting during morphogenesis in terms of simple thermodynamic arguments [70]. According to differential adhesion hypothesis, the same cells interact with each other the same way, but differently with other cells [181]. This adhesion difference can lead to a cell sorting behaviour that is similar to the coalescence of the same phase droplets in emulsions to reduce the interface surface area (as can be observed, for example, in mixing vinegar with oil). Introducing two cell types in the cellular Potts model shows that cells are sorted into distinct regions [70]. The way adhesion is implemented indirectly renders the cellular Potts model very efficient from a computational perspective. However, one problem is that cell motion can only occur through fluctuations in the cell boundary, which is not always realistic.

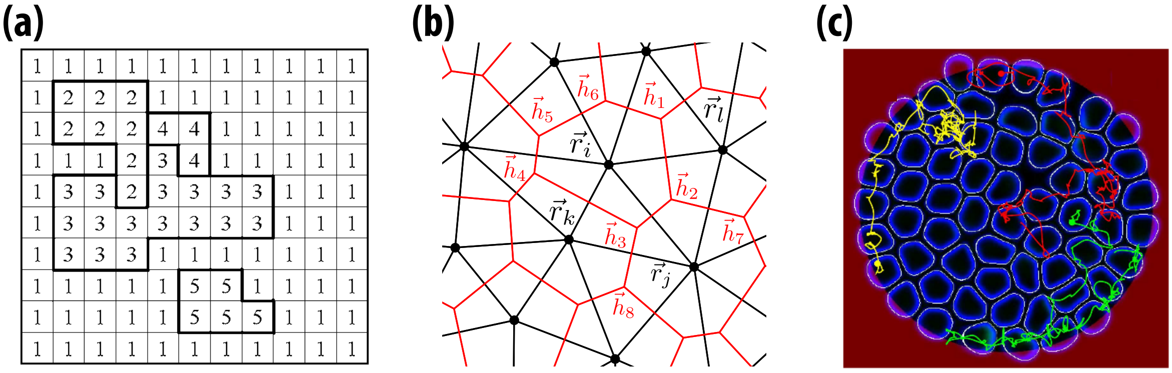

1	1	1	1	1	1	1	1	1	1	1
1	2	2	2	1	1	1	1	1	1	1
1	2	2	2	4	4	1	1	1	1	1
1	1	1	2	3	4	1	1	1	1	1
1	3	3	2	3	3	3	3	1	1	1
1	3	3	3	3	3	3	3	1	1	1
1	3	3	3	1	1	1	1	1	1	1
1	1	1	1	1	5	5	1	1	1	1
1	1	1	1	1	5	5	5	1	1	1
1	1	1	1	1	1	1	1	1	1	1

Figure 1.7.: Examples of modelling collective cell motility: (a) Cellular Potts model describes cells as lattice sites with the same spin. Image is taken from ref. [35]. (b) Voronoi model describes cells through a Voronoi tessellation of two-dimensional space. Image is taken from ref. [14]. (c) Phase-field models describe cells as moving interfaces. Image is taken from ref. [121].

Vertex and Voronoi models are off-lattice models, which offer more control over cell-cell adhesion and contractility in comparison to the fixed-lattice structure of the cellular Potts model. In the vertex model, cells are represented as polygons [58, 76]. Vertices are points where three cells meet and edges, that connect vertices, are shared between neighbouring cells. Equations of motion move vertices and in addition, a couple of topological transition rules can be incorporated to achieve cell-like behaviour. For example, cells can be extruded if their area drops down below a certain threshold. Cells can be allowed to make neighbour exchanges, when the distance between two vertices goes down below a certain threshold [58, 47, 2]. In the Voronoi model, cells are also represented as polygons through a Voronoi tessellation of a two-dimensional surface (Fig. 1.7-b). The shape of the cell is then described by the set of points that are closer to the given cell center than to any other cell center. The main difference between the vertex and the Voronoi models is that equations of motion are applied to the cell centers directly in the Voronoi model [13]. In both models, there are coarse-grained energy descriptions similar to

$$H = \sum_i K_\mathrm{a}(A_i - A_0)^2 + K_\mathrm{p}(P_i - P_0)^2, \tag{1.4}$$

where A_i is the area and P_i is the perimeter of cell i. These energy terms describe the preference of a cell to have a certain target area A_0 and a target perimeter P_0. Activity can also be incorporated by adding a self-propulsion term to the Hamiltonian with desired noise characteristics. Vertex and Voronoi models capture cell-shape driven collective motion in confluent tissues [13, 14, 151]. The main problem with these models lies on the description of free boundaries. As cells are defined with respect to other cells, vertex and Voronoi models are mainly useful for confluent tissues.

A rather recent approach that is particularly useful in simulations of finite density monolayers is based on phase-field models. Phase fields define a given region of space $\phi(\mathbf{r})$ as a cell through a smooth transition of $\phi(\mathbf{r})$ to nonzero values inside the region defined as the cell (Fig. 1.7-c). The equations of motion are derived from the minimization of an Hamiltonian that has the general form

$$\partial_t \phi + \mathbf{v}_\mathrm{m} \cdot \nabla \phi = -\frac{1}{\gamma \epsilon} \frac{\delta H}{\delta \phi}, \tag{1.5}$$

where γ is the friction coefficient, ϵ the interface width, and $\mathbf{v}_\mathrm{m}$ is the motility force [22, 112, 29, 121]. Hamiltonian can then be modified with properties that encode cell shape and motility. Even though phase field approaches are very useful for describing single cell motility and collisions between multiple cells at finite densities, they suffer from high computational costs. As a result, they are not used as much in simulating dense monolayers or confluent tissues.

1.7. Confluent Cell Monolayers

During locomotion, a single cell extends its membrane forwards, makes adhesive contacts with the substrate, and retracts its membrane from the back. In cell monolayers, the coupling of these cyclic shape changes to the behaviour of neighbouring cells could lead to complex collective migration patterns. *In-vitro* characterization of such migration patterns usually involves mapping the displacement fields of cells, the traction forces cells exert on the substrate, and the forces cells exert on each other. A common experimental model is a confluent layer of Madin-Darby canine kidney (MDCK) cells grown on soft polyacrylamide gels functionalized with extracellular matrix proteins such as collagen, or fibronectin [4, 76]. MDCK cells develop strong cell-cell adhesions, and consequently exhibit long correlations (~ 150 μm, on the order of 10 cells length) [38].

The average velocity of MDCK cells on polyacrylamide gels is observed to slow down after the monolayer reaches confluency due to proliferation of cells [4]. This slowing down is accompanied by correlations in the cell displacements. The dual picture of slowing down dynamics and growing displacement correlations is analogous to the jamming transition of granular systems driven mainly by increasing density, or the glass transition of molecular systems driven mainly by decreasing temperature. This analogy suggests a jamming phase diagram of cell monolayers that is similar to that of colloidal suspensions. For colloids, decreasing temperature, increasing density, or decreasing shear stress drives a jamming transition [198]. Active forces can be incorporated into this jamming diagram as effective temperature [180].

For MDCK cells grown on glass substrates (instead of soft polyacrylamide substrates), the displacement correlation length decreases with increasing density [3]. For human bronchial epithelial cells (HBEC), the correlation length is not correlated with density after the monolayer reaches confluency. Instead, the correlation length increases with increasing cell-cell adhesion, or cell-substrate adhesion [62]. These experiments challenge the role of density in driving the jamming transition of cell monolayers. As there are no gaps between cells after the monolayer reaches confluency, the role of density remains somewhat limited in favour of other parameters such as adhesion, or friction with the substrate.

Cell shape plays an important role in transmitting intercellular forces across the monolayer. Similar to the jamming of soft colloids [130], the notion of jamming can also apply to softer cell lines, for which the deformability is important, such as MCF-10A human breast cancer cells [141], or HBEC human bronchial epithelial cells [151]. For HBECs derived from asthmatic donors, the jamming transition is observed to be delayed in comparison to that of non-asthmatic donors [151]. In light of earlier experiments, this can, in principle, be attributed to higher cell-cell adhesions in cells of non-asthmatic donors. However, intercellular tension, which can be regarded as correlated to intercell adhesions, is observed to be lower in cells of non-asthmatic donors [151]. Therefore, it appears as unjamming is correlated with high cell-cell adhesions. The Voronoi model is employed to explain this paradox. A general shape parameter can be deduced from eq. 1.4 in terms of the preferred cell perimeter and the preferred cell area by $p = P_0/\sqrt{A_0}$. Lower values of p, corresponding to cells that prefer to change their area instead of perimeter, result in a jamming phase. Higher values of p, on the other hand, where cells prefer to change their perimeter over their area, lead to fluidization of the monolayer [151]. This model intrinsically combines the effects of cell-cell adhesion and cortical tension via the shape parameter. The preference of cells to change their area over perimeter (low p values) is regarded as a state where cortical tension dominates over cell-cell adhesion. The preference to change the cell perimeter over area (high p values) is a state where cell-cell adhesion dominates over cortical tension, as changing the perimeter corresponds to making new contacts between cells, and thereby implies lower cell-cell adhesion. As a result, the Voronoi model proposes a solution to the adhesion paradox by suggesting that increasing cell-cell adhesion (high p), or decreasing cortical tension (low p) fluidizes the tissue [13].

Other computational and theoretical models also capture jamming phase diagrams. Soft self-propelled particle models suggest that increasing density, and decreasing activity drive the particles towards jamming [79]. Cellular Potts model indicates the existence of a jamming transition as a function of decreasing activity, and increasing cell-cell adhesions [28]. Extending the Voronoi model with self-propulsion, by adding an activity term to eq. 1.4, shows a jamming transition as a function of decreasing cell-cell adhesions, and increasing activity [14]. However, a complete jamming phase diagram of cell monolayers remains an active area of research due to the involved biological and mechanical complexities.

Cells can express a broad spectrum of activities. Correspondingly, different levels of activity lead to different types of dynamical behaviour of the cell monolayer. Jamming monolayers exhibit swirling patterns, whereas highly active monolayers include mostly erratically displacing cells. In between these two phases, recent experiments indicate the existence of a turbulent regime in cell monolayers. In HBEC monolayers, cells are observed to form large-scale vortices at intermediate time scales ($\sim 20\ h$) [16]. This time scale corresponds to intermediate levels of propulsion speeds for cells. In endothelial cell monolayers, similar large-scale vortex patterns develop due to cell divisions stirring the monolayer [167]. Cell divisions can be regarded as local energy injections, which then propagate to nearby cells through cell-cell adhesion, causing a long-range stirring of the monolayer. In addition to vortex-dominated turbulence regimes, cells are also observed to form half-integer topological defects that are similar to the nematic phase of liquid crystals [48, 171, 101].

1.8. Structure of the Thesis

Our aim is to understand the complex collective motion of active cell monolayers and cytoskeletal filaments in terms of simple mechanical rules. We computationally model cells and filaments as coarse-grained self-propelled objects with structures inspired from their biological counterparts. We identify patterns of collective behaviour and map the observed phases to mechanical properties of individual cells and filaments.

This thesis is organized as follows. In Chapter 2, we review the key physical and computational concepts such as Brownian motion, liquid crystals, turbulence, and molecular dynamics simulations which are invoked throughout the thesis. The results are presented in separate chapters in a self-contained format. Results on dense motile cell monolayers are presented in Chapter 3 and results on self-propelled semiflexible filaments at finite and high densities are presented in Chapter 4. The final chapter contains conclusive remarks highlighting the main results of the thesis as well as providing an outlook for the next steps.

2. Theoretical Background and Computational Models

2.1. Brownian Motion

Mesoscale refers to length scales (≈ 10s of μm) that fall between molecular (≈ 10s of Å) and macroscopic length scales (≈ 10s of mm and larger). A large class of inert and living matter, from colloids, emulsions, and foams to bacteria, epithelial cells, and cytoskeletal filaments live within the meso-length scales. They share certain properties of molecular and macroscopic systems, especially within a statistical mechanics description. One key peculiarity of mesoscale systems is the distinct separation of length scale in dynamics. They are large enough to be treated separately with respect to molecules, while being at the same time small enough to be affected by the surrounding molecular system in contrast to macroscopic systems. As such, their description requires taking into account the effect of the surrounding molecules.

The quintessential example depicting the effect of smaller length scales on mesoscale dynamics is Brownian motion. It describes the dynamics of a mesoscopic object immersed in a fluid. It is first observed by Robert Brown who noticed in early 19th century the random motion of pollen grains inside a fluid. Pioneers like Albert Einstein and Jean Perrin attributed this random motion to the constant bombardment of the mesoscale object by the fluid molecules [51]. It is mathematically expressed as a random, fluctuating force field $\eta(t)$ acting on the Brownian particle.

The equation of motion of a Brownian particle can be written via Newton's second law,

$$\frac{\mathrm{d}v(t)}{\mathrm{d}t} = -\frac{\gamma}{m}v(t) + \frac{1}{m}\eta(t), \tag{2.1}$$

where $v(t)$ denotes the velocity of the Brownian particle, γ is the friction coefficient and $\eta(t)$ is the fluctuating force field exerted by the solvent molecules. This equation is known as the Langevin equation [1]. If we neglect the stochastic term, the Langevin equation becomes a homogenous differential equation with a linear scaling in the form of

$$\frac{\mathrm{d}v(t)}{\mathrm{d}t} = -\frac{\gamma}{m}v(t) \tag{2.2}$$

---

[1] The general name for this type of stochastic differential equations with a damping term linearly depending on velocity is referred as *Ornstein-Uhlenbeck process.* Without the damping term, the equation is called as *Wiener process.*

which has a simple exponential solution

$$v(t) = v(0)e^{-t/\tau_v}, \tag{2.3}$$

with the exponential solution relaxation time for the velocity of the particle $\tau_v = m/\gamma$. Typically, for a Brownian particle, the velocity relaxation time is on the order of $\approx 10^{-9}$ s. This falls between the solvent relaxation time τ_s, typically on the order of $\approx 10^{-14}$ s, and the self diffusion time of the Brownian particle τ_B, that is the time the particle has diffused its own radius, which is typically around $\approx 10^{-3}$ s [40]. Thus, in general, we have the relation, $\tau_s \ll \tau_v \ll \tau_B$, which clearly indicates a separation of time scales. As the dynamics of solvents is orders of magnitude faster than the dynamics of the Brownian particle, solvent molecules collide very frequently with the Brownian particle.

Without the random force term, the solution of the Langevin equation in eq. 2.3 predicts that the velocity of the Brownian particle decays to zero with time. However, we must have $\langle v^2(t) \rangle = \mathrm{k_B}T/m$ at thermodynamic equilibrium, by the equipartition theorem. Thus, the random force must be included to get the correct equilibrium solution.

The random force can be modelled with a Gaussian distribution with specified first and second moments, indicating its average and its variance, respectively. Conceptually, its average should be zero, and it should be delta correlated in time, which gives $\langle \eta(t) \rangle = 0$, and $\langle \eta(t_1)\eta(t_2) \rangle = g\delta(t_1 - t_2)$. g here describes the strength of the random force. Delta correlation in time follows simply from the separation of time scales that is mentioned earlier. Imagine a small time scale of $\mathit{\Delta} t = 10^{-6}$ s with respect to the velocity relaxation time scale of $\tau_v = 10^{-3}$ s. During this small time scale $\mathit{\Delta} t$, approximately $\mathit{\Delta} t/\tau_s \approx 10^8$ collisions between the Brownian particle and the solvent molecules occur. As a result of these very frequent collisions, any kind of memory between the forces imparted by the solvent molecules at different times will be lost.

Going back to the solution of the Langevin equation in eq. 2.1, but this time including the random force, to acquire a solution for the velocity, we multiply both sides of the Eqn. 2.1 with $e^{\gamma t/m}$. Rearranging the terms, we have

$$\frac{\mathrm{d}}{\mathrm{d}t}(ve^{\gamma t/m}) = \frac{\eta(t)}{m}e^{\gamma t/m} \tag{2.4}$$

From this equation, the analytic solution for the velocity of the Brownian particle can be expressed as,

$$v(t) = v(0)e^{-t/\tau_v} + \frac{1}{m}\int\limits_0^t \mathrm{d}t' e^{-(t-t')/\tau_v}\eta(t') \tag{2.5}$$

Note that, the homogenous solution is superposed with the inhomogenous solution to arrive at this expression. Equivalently we could have made a change of variables with $v(t) = u(t)\mathrm{e}^{-\gamma t/m}$ to arrive at the same solution. This relation in eq. 2.5 allows the calculation the dynamics of a Brownian particle.

Integrating for particle positions from the velocity expression yields,

$$x(t) = x(0) + v(0)\tau_v(1 - e^{-t/\tau_v}) + \frac{\tau_v}{m}\int_0^t \mathrm{d}t'(1 - e^{-(t-t')/\tau_v})\eta(t') \tag{2.6}$$

Velocity autocorrelation function for Brownian motion can be calculated from the analytical expression of velocity,

$$\begin{aligned}
\langle v(t_1)v(t_2)\rangle = v_0^2 e^{-(t_1+t_2)/\tau_v} & \\
& + \frac{v_0}{m} e^{-t_1/\tau_v} \int_0^{t_2} \mathrm{d}t' e^{-(t_2-t')/\tau_v} \underbrace{\langle \eta(t')\rangle}_{=0} \\
& + \frac{v_0}{m} e^{-t_2/\tau_v} \int_0^{t_1} \mathrm{d}t' e^{-(t_1-t')/\tau_v} \underbrace{\langle \eta(t')\rangle}_{=0} \\
& + \frac{1}{m^2} \int_0^{t_1}\int_0^{t_2} \mathrm{d}t'_1 \mathrm{d}t'_2 e^{-(t_1+t_2-t'_1-t'_2)/\tau_v} \underbrace{\langle \eta(t'_1)\eta(t'_2)\rangle}_{g\delta(t'_1-t'_2)} \\
& = v_0^2 e^{-(t_1+t_2)/\tau_v} + \frac{g\tau_v}{2m^2}(e^{-|t_1-t_2|/\tau_v} - e^{-(t_1+t_2)/\tau_v})
\end{aligned} \tag{2.7}$$

where the double integral is solved by a change of variables with $t'_1 = t'_2 - t$.

In the limit of small relaxation time, asymptotic behaviour, determined by $t_1/\tau_v, t_2/\tau_v \gg 1$, gives,

$$\langle v(t_1)v(t_2)\rangle = \frac{g\tau_v}{2m^2} e^{-|t_1-t_2|/\tau_v} \tag{2.8}$$

indicating an exponential decay for the autocorrelation function. Accordingly, the stationary state is given by,

$$\langle v(t)v(t)\rangle = \langle v(t)^2\rangle = v_0^2 e^{-2t/\tau_v} + \frac{g\tau_v}{2m^2}(1 - e^{-2t/\tau_v}) \overbrace{=}^{t\to\infty} \frac{g\tau_v}{2m^2} \tag{2.9}$$

Applying equipartition theorem to the stationary state solution,

$$\langle E_k\rangle = \frac{1}{2}m\langle v^2\rangle = \frac{1}{2}m\frac{g\tau_v}{2m^2} = \frac{1}{2}\mathrm{k_B}T \tag{2.10}$$

we find that the noise strength has to obey $g = 2\gamma \mathrm{k_B}T$. This important relation between the fluctuating force strength and the dissipation via friction is known as the fluctuation-dissipation theorem. It relates an increase in the magnitude of fluctuations to increasing temperature and friction. It is a crucial relationship to ensure thermal equilibrium. Note that both friction and fluctuations are coming from the environment. We rewrite the time correlation of the noise, in light of this relation, as

$$\langle \eta(t_1)\eta(t_2)\rangle = 2\gamma \mathrm{k_B}T\delta(t_1 - t_2) \tag{2.11}$$

The dynamics of the particle is then obtained by taking the average of eq. 2.6,

$$\langle x \rangle = x_0 + v_0 \tau_v (1 - e^{-t/\tau_v}) \tag{2.12}$$

with the third term on the right-hand side of eq. 2.6 dropping out as $\langle \eta(t) \rangle = 0$. In other words, the average position of the Brownian particle is determined by its initial position and its initial velocity multiplied with its velocity relaxation time. For $x_0 = 0$ and $v_0 = 0$, we obtain $\langle x \rangle = 0$. This is due to the symmetry that displacements to the left are as likely as displacements to the right. We thus turn to the mean square displacement via the second moment of eq. 2.6.

We can calculate the second moment directly from eq. 2.6, by averaging over the square of this expression,

$$\begin{aligned}
\langle (x(t) - x(0))^2 \rangle &= v_0^2 \tau_v^2 (1 - e^{-t/\tau_v})^2 \\
&+ \frac{\tau_v^2}{m^2} \int_0^t \int_0^{t'''} \mathrm{d}t' \mathrm{d}t'' (1 - e^{-(t-t')/\tau_v})(1 - e^{-(t'''-t'')/\tau_v}) \overbrace{\langle \eta(t') \eta(t'') \rangle}^{g\delta(t'-t'')} \\
&= v_0^2 \tau_v^2 (1 - e^{-t/\tau_v})^2 + \frac{g\tau_v^2}{m^2} \int_0^t \mathrm{d}t'' (1 - e^{-(t-t'')/\tau_v})^2 \\
&= \tau_v^2 (1 - e^{-t/\tau_v})^2 \left(v_0^2 - \frac{g}{2m\gamma} \right) + \frac{g}{\gamma^2} \left[t - \tau_v (1 - e^{-t/\tau_v}) \right]
\end{aligned} \tag{2.13}$$

where the double integral is solved with a change of variables with $t' - t'' = u$.

Note that, at equilibrium, we found in eq. 2.9 that $\langle v_0^2 \rangle = \frac{g\tau_v}{2m^2} = \frac{g}{2m\gamma}$. Thus, in equilibrium, the first term on the right-hand side of 2.13 vanishes. Therefore only the second term remains as,

$$\langle (x(t) - x(0))^2 \rangle = \frac{g}{\gamma^2} t - \frac{gm}{\gamma^3} (1 - e^{-t/\tau_v}) \tag{2.14}$$

- As $t \to 0$, Taylor expanding the exponential gives,

$$\langle (x(t) - x(0))^2 \rangle = \frac{g}{\gamma^2} t - \frac{gm}{\gamma^3} \left(1 - 1 + \frac{\gamma}{m} t - \frac{1}{2} \frac{\gamma^2}{m^2} t^2 + \dots \right) = \frac{g}{2\gamma m} t^2 \tag{2.15}$$

Noting that $\langle v_0^2 \rangle = \frac{g}{2\gamma m}$, we end up with,

$$\langle (x(t) - x(0))^2 \rangle = \langle v_0^2 \rangle t^2 \tag{2.16}$$

The result indicates that at short times the Brownian particle performs ballistic motion with $x(t) - x(0) = v_0 t$, in line with the observation that the Brownian particle did not collide enough with the solvent molecules to change its velocity too much at short times.

- As $t \to \infty$, the second term drops out, leaving us with,

$$\langle (x(t) - x(0))^2 \rangle = \frac{g}{\gamma^2} t = \frac{2 \mathrm{k_B} T}{\gamma} t \tag{2.17}$$

where we used the earlier derived relation $g = 2\gamma \mathrm{k_B} T$.

A very simple and elegant derivation of mean squared displacement is given in [216]. Starting from the one-dimensional diffusion equation of concentration $C(x,t)$ for a tagged Brownian particle,

$$\frac{\partial}{\partial t} C(x,t) = D \frac{\partial^2}{\partial x^2} C(x,t) \tag{2.18}$$

For a particle with initial position at $x = 0$, the concentration $C(x,t)$ spreads out from an initial delta function at $x = 0$ to a Gaussian. By symmetry, the mean displacement will be zero, while the second moment of displacement can be calculated by noting that $\langle x^2 \rangle = \int \mathrm{d}x x^2 C(x,t)$. Thus multiplying the diffusion equation by x^2 and integrating over x, we get,

$$\begin{aligned} \frac{\partial}{\partial t} \langle x^2 \rangle = \int \mathrm{d}x x^2 \frac{\partial}{\partial t} C(x,t) &= D \int \mathrm{d}x x^2 \frac{\partial^2}{\partial x^2} C(x,t) \\ &= 2D \int \mathrm{d}x C(x,t) = 2D \end{aligned} \tag{2.19}$$

where the integration of the second derivative of $C(x,t)$ is carried out with integration by parts. Upon integrating over t, we get the relation $\langle x^2 \rangle = 2Dt$.

Combining eq. 2.19 with eq. 2.17, we identify $D = \frac{\mathrm{k_B} T}{\gamma}$ for the diffusion coefficient. This definition is known as the Stokes-Einstein relation. Therefore, at long times the Brownian particle performs diffusive motion with $\langle (x(t) - x(0))^2 \rangle = 2Dt$, as the Brownian particle collides with the solvent molecules too much which reduces its displacement in comparison to ballistic motion.

All of the derivations so far are performed for one dimension. We can argue by symmetry that at thermal equilibrium, each dimension will statistically contribute the same amount for the first and second moments of the position, resulting in,

$$\langle x^2 \rangle = 2dDt, \tag{2.20}$$

for d dimensions.

The diffusion coefficient is also related to the correlations in velocity. To observe this, we relate the second moment of displacement to the velocities,

$$\langle x^2 \rangle = \left\langle \int_0^t \mathrm{d}t' v(t') \int_0^{t'''} \mathrm{d}t'' v(t'') \right\rangle = \int_0^t \mathrm{d}t' \int_0^{t'''} \mathrm{d}t'' \langle v(t') v(t'') \rangle \tag{2.21}$$

assuming that the average commutes with the integral. At equilibrium, the time axis can be shifted from $\langle v(t')v(t'')\rangle$ to $\langle v(s)v(0)\rangle$, as long as $t' - t'' = s$. Taking the time derivative of this shifted expression,

$$\langle x^2 \rangle = 2 \int_0^t \mathrm{d}s \langle v(s) v(0) \rangle \tag{2.22}$$

As $t \to \infty$, we compare this expression with the long-time behaviour of the mean square displacement as expressed in eq. 2.20, which gives the self-diffusion coefficient as,

$$D = \frac{1}{d} \int_0^\infty \mathrm{d}t \langle \boldsymbol{v}(t) \cdot \boldsymbol{v}(0) \rangle \tag{2.23}$$

This general type of relation where a transport coefficient like D is calculated from the time correlations of observables is known as a *Green-Kubo relation.*

In light of the derived relations so far, we highlight the relevant time scales of Brownian motion. The time scale for the of solvent molecule relaxation τ_s surrounding the Brownian particle is on the order of 10^{-14} to 10^{-12} s [40]. At this time scale, Brownian particle performs ballistic motion with mean squared displacement scaled with t^2, and a statistical description of the Brownian particle requires both its position and its velocity, or equivalently its momentum. This ballistic motion at extremely small timescales is observed experimentally rather recently [84].

The velocity of the Brownian particle relaxes with $\tau_v = m/\gamma$, for which the typical values are around $\approx 10^{-9}$ s. For time scales larger than τ_v, the velocity of the Brownian particle is in thermal equilibrium, so a statistical description of the particle requires only the consideration of its position. The mean squared displacement of the particle scales with t in this regime.

To calculate statistically significant observables from particle displacements, a longer time scale is needed. This is set by the so-called *diffusive* or *Brownian* time scale, τ_B. It is typically defined as the time it takes for a Brownian particle to diffuse its own radius or diameter, $\tau_B = d/\sqrt{\langle v^2 \rangle}$, with d denoting the particle diameter, and $\langle v^2 \rangle$ is known from eq. 2.9. Typical value of τ_B is around 10^{-4} to 10^{-3} s.

For Brownian particles that are interacting with each other, there are two more relevant time scales. An *interaction time scale*, related to the direct interactions between the particles, has a value that depends on the nature of interactions between the particles. A *hydrodynamic time scale* is related to the solvent-mediated interactions between the Brownian particles. This is typically on the order of the diffusive time scale [40].

2.2. Molecular Dynamics

Molecular dynamics is a computer simulation technique to simulate a broad variety of systems across different length scales. It can be employed to describe the motion of atoms and molecules as well as that of planets and stars. It is also the tool we use to simulate dynamics at the meso-length scale. The main idea behind molecular dynamics is to reduce the properties of the investigated system to an effective Hamiltonian which is then integrated in time to propagate the system. We start by outlining such time-integration schemes.

The core of all of time integration algorithms is the combination of Taylor expansion of position in small times with Newton's second equation of motion. Truncation point determines different algorithms with varying accuracies. The simplest algorithm is truncating the expansion after the linear term, which gives,

$$r(t + \Delta t) = r(t) + v(t)\Delta t + O(\Delta t^2) \tag{2.24}$$

which is known as the *Euler algorithm.*

As the numerical accuracy of Euler scheme goes with $O(\Delta t^2)$, we have to choose very small time steps to get reasonable results. Another problem comes from energy conservation. To illustrate, we consider a particle under a harmonic trap which has an energy of $E(t) = kx^2/2 + mv^2/2$ at time t, which should be a constant of the motion at thermodynamic equilibrium. If we propagate the particle in time with Euler algorithm, the energy expression at the next time instant becomes,

$$E(t+\Delta t) = \frac{1}{2}k[x(t)+v(t)\Delta t]^2 + \frac{1}{2}m[v(t)+a(t)\Delta t]^2 = E(t) + C(t) \tag{2.25}$$

We can see from this expression that energy drifts away from $E(t)$ by an amount that goes with Δt^2 at every time step. Thus, at long times, we may end up with a significant energy drift.

Verlet algorithm provides a more accurate integration scheme. It is derived from truncating the Taylor expansion of position at $O(\Delta t^4)$. The forward and backward Taylor expansions yield,

$$\begin{aligned} r(t+\Delta t) &= r(t) + v(t)\Delta t + \frac{f(t)}{2m}\Delta t^2 + \frac{1}{6}r'''(t) + O(\Delta t^4) \\ r(t-\Delta t) &= r(t) - v(t)\Delta t + \frac{f(t)}{2m}\Delta t^2 - \frac{1}{6}r'''(t) + O(\Delta t^4) \end{aligned} \tag{2.26}$$

If we add these two expressions up, we end up with,

$$r(t+\Delta t) = 2r(t) - r(t-\Delta t) + \frac{f(t)}{m}\Delta t^2 + O(\Delta t^4) \tag{2.27}$$

This expression is numerically much more accurate as it scales with $O(\Delta t^4)$, but note that is harder to evaluate as we have to keep track of positions from the previous time step $r(t-\Delta t)$ too. One other problem is that we did not integrate the velocity explicitly. Therefore, we can only calculate it from positions.

We arrive at the leap frog scheme by integrating the velocities explicitly while leaving the position integration intact. If we integrate the velocities at half-steps as,

$$\begin{aligned} v\Big(t - \frac{\Delta t}{2}\Big) &= \frac{r(t) - r(t-\Delta t)}{\Delta t} \\ v\Big(t + \frac{\Delta t}{2}\Big) &= \frac{r(t+\Delta t) - r(t)}{\Delta t} \end{aligned} \tag{2.28}$$

Now if add these two up and combine the resulting expression with eq. 2.27, we arrive at,

$$v\Big(t + \frac{\Delta t}{2}\Big) = v\Big(t - \frac{\Delta t}{2}\Big) + \frac{f(t)}{m}\Delta t \tag{2.29}$$

The caveat is that position and velocity is integrated at different time steps, consequently potential and kinetic energies are not defined for the same time steps. Hence it is not possible to compute the total energy with leap frog algorithm. This brings us to the next algorithm.

Integrating positions and velocities at the same time step explicitly gives the velocity Verlet algorithm with the set of equations,

$$\begin{aligned} r(t+\mathit{\Delta} t) &= r(t) + v(t)\mathit{\Delta} t + \frac{f(t)}{2m}\mathit{\Delta} t^2 \\ v(t+\mathit{\Delta} t) &= v(t) + \frac{f(t)+f(t+\mathit{\Delta} t)}{2m}\mathit{\Delta} t \end{aligned} \tag{2.30}$$

With this algorithm, it is now possible to compute the total energy. Note also the symmetry of equations in time: We can back propagate the equations in time. Therefore, this scheme is fully time-reversal just like Newton's equation of motion. One thing to be careful, however, is that velocity integration requires the calculation of forces, which then requires the calculation of positions. Thus, calculation of velocity dependent forces usually requires modification to this general numerical scheme. We discuss the numerical accuracy of velocity Verlet algorithm further in Appendix B.

The time integration schemes discussed so far pertain to deterministic equations. However, as we have seen, description of mesoscopic dynamics requires the involvement of a stochastic forcing term. The idea behind Langevin dynamics is to describe the motion of meso length scale objects immersed in a fluid by mimicking the effect of explicit solvent molecules with a stochastic force term a la Langevin equation. In light of our findings in the previous chapter, we can write down the Langevin equation with,

$$m\ddot{r}(t) = F(r(t)) - m\gamma\dot{r}(t) + \sqrt{2m\gamma \mathrm{k_B} T}\eta(t) \tag{2.31}$$

where $\langle\eta(t)\rangle = 0$ and $\langle\eta(t)\eta(t')\rangle = \delta(t-t')$.

In the overdamped limit, we can neglect the inertia term of $m\ddot{r}$, as viscosity of the fluid dominates over inertia. In other words, the total force acting on the particle vanishes as $F = F_c + F_d + F_r = 0$, where F_c denote the conservative forces via inter-particle interactions, F_d is the frictional drag or viscous damping that is proportional to the velocity of the particle, and F_r is the stochastic force term to implement an implicit solvent. In this case, we can integrate the Langevin equation to first order through,

$$r(t+\mathit{\Delta} t) = r(t) + \frac{F(r(t))}{m\gamma}\mathit{\Delta} t + \sqrt{\frac{2\mathrm{k_B}T}{m\gamma}}\eta\sqrt{\mathit{\Delta} t} \tag{2.32}$$

where the noise term is scaled with $\sqrt{\mathit{\Delta} t}$ to preverse the linear scaling of mean square displacement with time for Wiener process (or random walk). This overdamped limit is also known as *Brownian dynamics*.

2.3. Simulation Model of a Cell

We simulate a single cell as a 2D vesicle made of N beads connected by N bonds over a circle. Dynamics of each bead is determined with the Langevin equation

$$m\ddot{\boldsymbol{r}}_i = -\nabla_i U - \gamma\dot{\boldsymbol{r}}_i + \boldsymbol{F}^{(i)}_{\mathrm{k_B}T} + \boldsymbol{F}^{(i)}_m, \tag{2.33}$$

where $i = 0, 1, \ldots, N$ denote individual beads and dots derivatives with respect to time. The first term on the right-hand side describes the conservative forces deriving from a potential, while the other forces are dissipative and active forces. We next describe these forces in detail.

• **Bond forces:** Beads of each cell are connected by stiff bonds that derive from a finite-length spring potential of the form

$$U_{\text{bond}} = \begin{cases} \frac{k_S}{2} \sum_j \sum_{i=0}^{N-1} \left(|\boldsymbol{r}_{i+1}^{(j)} - \boldsymbol{r}_i^{(j)}| - r_0 \right)^2 \\ k_S \sum_j \left(|\boldsymbol{r}_0^{(j)} - \boldsymbol{r}_{N-1}^{(j)}| - r_0 \right)^2 \end{cases} \tag{2.34}$$

where i denotes beads of a cell and j denote individual cells. k_S is the strength of the spring potential (A typical value is $\approx 3000 \mathrm{k_B} T$). It is chosen extremely high to render the bond length r_0 constant. Therefore, the perimeter of a cell is rendered constant. The radius of the cell is thus given by $R = N r_0 / 2\pi$. The average number of beads for a cell is $N = 40$, therefore $R \approx 3.18$.

• **Bending forces:** Bonds of a cell are connected by harmonic bending potentials to induce an energetic penalty for bending of the membrane. This potential acts as a constraint on the angle between successive bonds

$$U_{\text{bend}} = \begin{cases} \frac{\kappa_B}{4 r_0^3} \sum_j \sum_{i=0}^{N-1} \left(\boldsymbol{R}_{i+1}^{(j)} - \boldsymbol{R}_i^{(j)} \right)^2 \\ \frac{\kappa_B}{2 r_0^3} \sum_j \left(\boldsymbol{R}_0^{(j)} - \boldsymbol{R}_{N-1}^{(j)} \right)^2 \end{cases} \tag{2.35}$$

where κ_B is the bending rigidity and $\boldsymbol{R}_i$ is given by $\boldsymbol{R}_i = \boldsymbol{r}_{i+1} - \boldsymbol{r}_i$. The bending rigidity is a measure of the stiffness of the cell. We vary the bending rigidity, but a typical value is $\approx 100 \mathrm{k_B} T$. We non-dimensionalize the bending rigidity via the dimensionless thermal persistence length ξ_p / R by

$$\frac{\xi_p}{R} = \frac{\kappa_B}{k_{\mathrm{B}} T R} \tag{2.36}$$

where R is the radius of the cell.

• **Area forces:** Cells have a preferred target area A_0 set by a harmonic area constraint potential

$$U_{\text{area}} = \frac{\kappa_A}{2} \sum_j (A_j - A_0)^2, \tag{2.37}$$

with A_j denoting the area of a cell at a given time, which can be calculated by taking the cross product of consecutive beads in a cell. κ_A represents the area compression modulus. It is a measure of compressibility of the cell. We use it as a changing parameter, but a typical value is $\kappa_A \approx 100 \mathrm{k_B} T$. Since the perimeter of the cell is kept constant, the target area determines the shape of the cell. If A_0 is equal to the area of a circle defined by the cell perimeter, then the cell remains as a circle. If it is smaller than this circular area, then the cell relaxes into an ellipse, so that the area decreases while the perimeter remains constant. These shapes as a function of A_0 is depicted in Fig. 2.1. We fix A_0 at $0.9 A_c$ to generate a slightly ellipse-like cell shape. As κ_A has the units of energy per area square, we non-dimensionalize it by multiplying with σ^4. However, we keep the notation as κ_A throughout the text, for convenience.

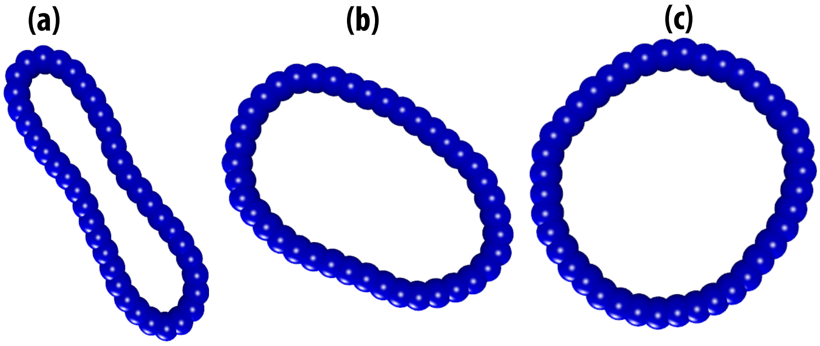

Figure 2.1.: Rendering of cell shapes from simulation snapshots as a function of target area parameter A_0: (a) $A_0 = 0.5A_c$, (b) $A_0 = 0.9A_c$, and (c) $A_0 = A_c$, where A_c denotes the circular area of the cell as defined from the cell perimeter.

• **Motility forces:** Cell motility is modelled as a constant magnitude force. Its direction $\hat{n}$ is the same for beads of the same cell. Therefore, beads of a cell are propelled the same way with

$$\boldsymbol{F}_j = \sum_{i=0}^{N-1} f_m \hat{n}_j, \tag{2.38}$$

where f_m is the magnitude of the force per bead. The direction of the motility force changes randomly with rotational Langevin dynamics

$$\dot{\hat{n}} = \sqrt{2D_r}\eta_r \times \hat{n}, \tag{2.39}$$

where D_r defines a rotational diffusion coefficient. We consider the rotational diffusion as independent from translational diffusion, as its origin is not thermal in the context of cell motion. The rotational diffusion coefficient is fixed at $D_r = 0.1/\tau_D$, where τ_D is the diffusive time scale. η_r is a delta-correlated Gaussian noise term with zero mean. We characterize the motility force by *Peclet number*

$$\mathrm{Pe} = \frac{v_0 P_c}{D_t} = \frac{2\pi N f_m R}{\mathrm{k_B}T}, \tag{2.40}$$

where $v_0 = f_m/\gamma_0$ is the cell velocity, $P_c = 2\pi R$ is the cell perimeter, and R is the average cell radius.

The bond, bending, area and motility forces set the internal dynamics of the cell.

• **Interaction Forces:** Interactions between cells is modelled as a 12-6 Lennard-Jones potential in which cells are attracted to each other while remaining impenetrable. The potential is defined with

$$U_{\mathrm{LJ}}(r_{ij}) = 4\epsilon\left[\left(\frac{\sigma}{r_{ij}}\right)^{12} - \left(\frac{\sigma}{r_{ij}}\right)^{6}\right], \tag{2.41}$$

where r_{ij} is the distance between beads of different cells. σ acts as an effective diameter for the beads, which is fixed at $\sigma = 1$. ϵ defines the strength of interaction potential, which is a varying parameter with a typical value on the order of a few $\mathrm{k_B}T$s. Due to stiff bonds, the bond length is kept constant at a value of $r_0 = 0.5\sigma$. This leads to overlaps between successive beads of a cell, creating a smoother potential preventing artificial interlocking of surrounding beads at the bonds.

• **Dissipative forces:** The dissipative force of the monolayer is the friction force chosen to be linearly proportional with bead velocity

$$\boldsymbol{F}_j = -\sum_{i=0}^{N-1} \gamma_0 \boldsymbol{v}_i \tag{2.42}$$

where γ_0 is the friction coefficient per bead. Its value is $\gamma_0 = 1$, which together with the convention of unit mass for beads, gives the viscous time scale as $m/\gamma_0 = 1$.

• **Stochastic forces:** A random force is applied to each bead to mimic the effect of an implicit background solvent. This force has Gaussian noise properties with zero mean and a variance of $2\mathrm{k_B}T\gamma/\Delta t$. The translational diffusion coefficient for the cell can be defined as $D_t = \mathrm{k_B}T/\gamma_c$, where $\gamma_c = N\gamma_0$ denote the total friction coefficient of the cell. Therefore, the translational diffusion coefficient of the cell is given by $D_t = \mathrm{k_B}T/\gamma_0 N$.

The equations of motion are integrated with Langevin dynamics simulations, that is, the mass of beads are kept within a second-order Verlet numerical integration scheme (see Chapter 2).

For the collective system, we introduce polydispersity in cell radii to prevent crystallization. We change the number of beads to change the radii of cells, while keeping the bond lengths constant throughout the system. The scale of polydispersity is set by a Gaussian distribution for the cell radii with a standard deviation of 5% around a mean radius of R. This leads to an area distribution with a standard deviation of 7.4% around the mean area of $59\sigma^2 = 5.8R^2$.

It is important to highlight that area of the cell does not just scale with πR^2, but also includes a contribution from the effective diameter of the beads. This is accounted for in the cell area calculations by adding the area a factor of $\pi\sigma^2/4$ for each bead of the cell. It is divided by 4 instead of 2 due to the overlapping of successive bonds. The area distribution is visualized in Fig. 2.2-d.

We choose a mass of $m = 1$ and a friction coefficient of $\gamma_0 = 1$ for each bead, with the cell mass $m_c = Nm$, and the friction coefficient $\gamma_c = N\gamma_0$. Therefore, the velocity relaxation time of the cell is given by $\tau_v = m_c/\gamma_c = 1$.

The energy unit is fixed by $\mathrm{k_B}T = 1$.

The value of translational diffusion coefficient is given with $D_t = \mathrm{k_B}T/\gamma N = 0.025$ in units of $1/\tau_v$.

As discussed in Chapter 2, the diffusive time scale is an important for mesoscopic dynamics. It is defined as the time it takes for a cell to diffuse its own radius (the average cell radius, in this case). From the scaling of mean square displacement with time, the diffusive time scale can be derived as $\tau_D = R^2/4D_t \approx 101\tau_v$.

The total motility force magnitude on the cell is given by $F_m = Nf_m$. Therefore, the propulsion velocity of the cell is $v_0 = F_m/\gamma_c = f_m$. From the propulsion velocity, we can define

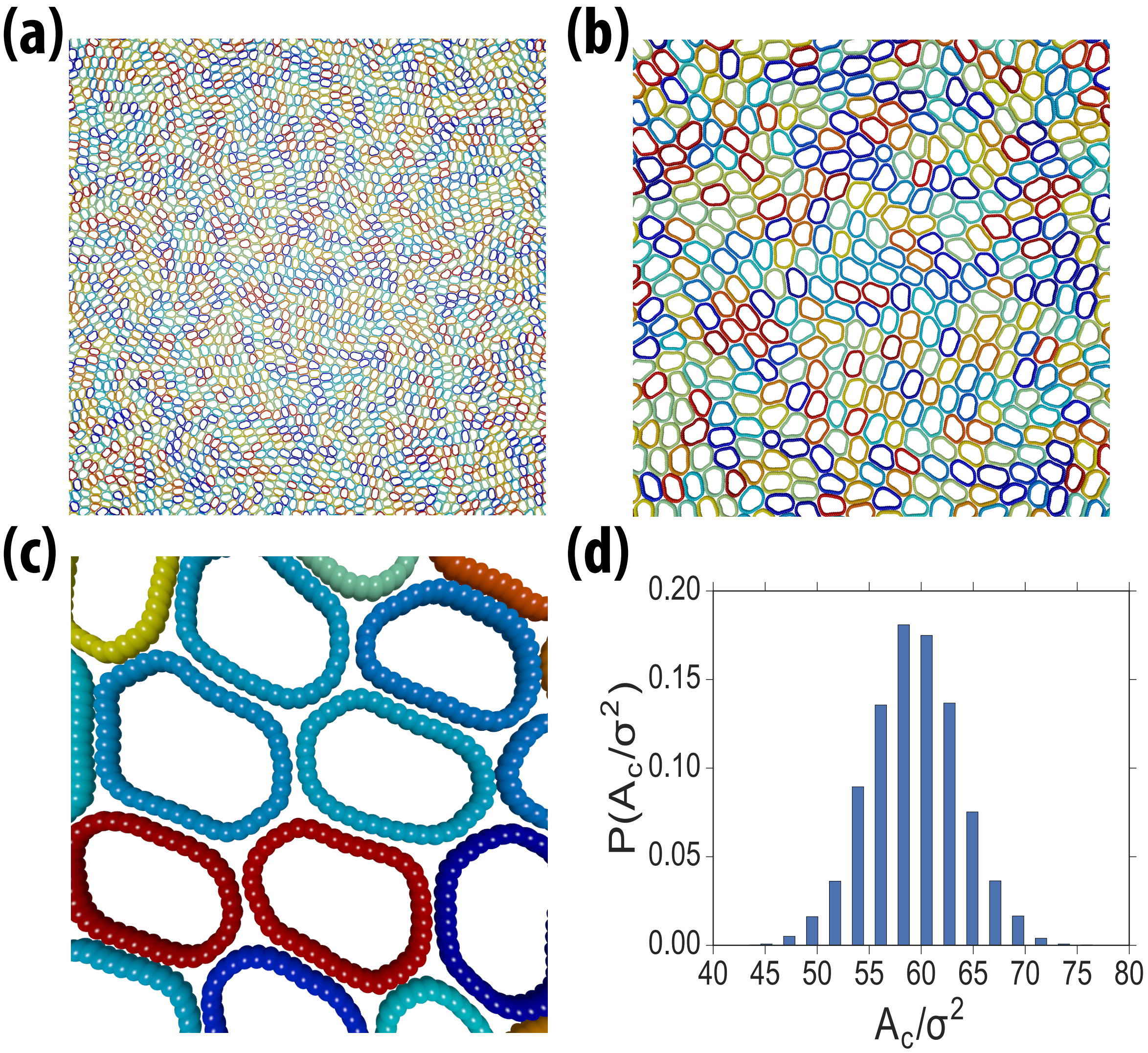

Figure 2.2.: (a) Shape of the entire monolayer depicting the initial conditions for each simulation, (b) the monolayer with 4 times zooming in, (c) with 750 times zooming in, (d) histogram of the cell areas.

an advective time scale as the time it takes for an active cell to displace the averagex cell radius, which is given by $\tau_A = R/v_0 = R/f_m$.

We use a periodic simulation box with a packing fraction of

$$\phi = \frac{N_c \pi R^2 + N\pi\sigma^2/4}{L_x L_y} \tag{2.43}$$

where N_c is the number of cells, N is the number of beads with L_x and L_y defining the box lengths in x and y dimensions, respectively. The packing fraction is fixed at $\phi = 1.5$ and $N_c = 5000$. The number density of the system is given by $\rho = N_c/L_xL_y$, and it is fixed at $\rho = 1.015$.

The initial conditions with these density values is shown in Fig. 2.2-a to c.

We refer the reader to Appendix E on single cell dynamics to see a validation of the model in terms of the theoretical results we derived in this Chapter.

2.4. Simulation Model of a Filament

We combine Kratky-Porod worm-like chain model with self-propulsion to simulate a single filament (See Appendix E for a discussion on Kratky-Porod worm-like chain model). The model is developed by Holder, *et.al.* to study the dynamics of a single filament [87, 89]. A single such filament is represented by $N_b + 1$ beads with N_b bonds. The equation of motion is given by Langevin equation as in eq. 2.33 of the cell model and as such, it is integrated with the same Langevin dynamics scheme. In fact, the filament model is overall very similar to the cell model. Similar to the cell model, beads of a filament are held together by finite bond length springs and bonds are further connected by bond bending potentials. Therefore, here we will suffice with highlighting the different properties to avoid unnecessary repetition.

The main difference between the cell and filament models is the different boundary conditions. The first and the last beads are not bonded in the filament model. As such, there is no area constraint potential. Furthermore, the interaction energy in the filament model does not contain an attractive part. It is modeled as a Weeks-Chandler-Anderson potential with

$$U_{\text{WCA}} = \sum_i \sum_{j>i} u_{VE}(\mathbf{r}_{i,j}) \tag{2.44}$$

$$u_{\text{VE}}(r) = \begin{cases} 4\epsilon\left[\left(\frac{\sigma}{r}\right)^{12} - \left(\frac{\sigma}{r}\right)^{6} \right], & r < 2^{1/6}\sigma \\ 0, & r \geq 2^{1/6}\sigma \end{cases} \tag{2.45}$$

where $\mathbf{r}_{i,j} = \mathbf{r}_i - \mathbf{r}_j$ is the vector between the positions of the beads i and j (which may belong to the same or another filament). ϵ and σ are the characteristic volume-exclusion energy and effective filament diameter, respectively.

Self-propulsion is introduced as a constant magnitude force f_p acting along each bond of a filament tangentially, i.e., $f_p \hat{r}_{i,i+1}$ (See Fig. 2.3). This force is distributed equally onto both adjacent beads making up the bond.

The drag force $\gamma \dot{\mathbf{r}}_i$ is the velocity of each bead times the friction coefficient per bead γ. In relation to the friction coefficient, the thermal force $\mathbf{F}^{(i)}_{k_B T}$ is modeled as white noise with zero mean and a variance of $2k_B T\gamma/\Delta t$.

The parameter choice is done such that (i) k_S is sufficiently large to render the bond length constant at r_0, and (ii) the local filament curvature is low such that the bead discretization does not violate the worm-like chain description. When the aforementioned conditions are met, the dynamics of a single filament is described by two dimensionless numbers,

$$\xi_P/L = \frac{\kappa}{k_B T L}, \tag{2.46}$$

$$Pe = \frac{f_p L^2}{k_B T}, \tag{2.47}$$

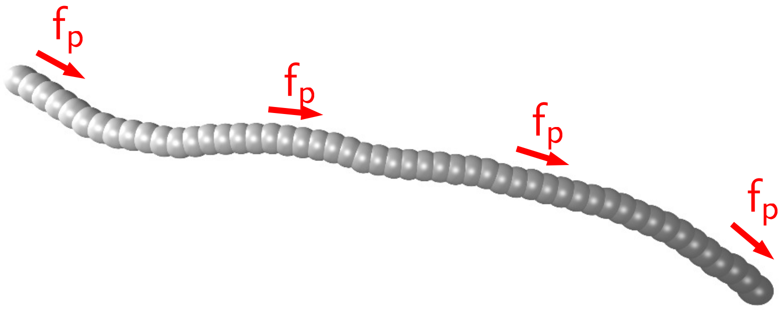

Figure 2.3.: Rendering of a filament from a simulation snapshot. Adapted from [87].

where $L = N_b r_0$ is the filament length (with N_b denoting the number of bonds of a filament) and ξ_p is the persistence length of the chain. The thermal persistence length ξ_P/L is a measure of the bending rigidity over noise of a single filament, whereas Peclet number Pe is the ratio between convective and diffusive transport, thereby, providing a measure for the degree of self-propulsion.

The aspect ratio $a = L/\sigma$ is the ratio of the length of the filament to the effective diameter of a bead.

The contour velocity of a filament is given by $v_c = f_p/\gamma_l$, and the translational diffusion coefficient is $D_t = k_B T/\gamma_l L$. The friction coefficient per unit length is given with $\gamma_l = \gamma(N_b + 1)/L$. Flexure number, defined with,

$$\mathfrak{F} = PeL/\xi_p = \frac{f_p L^3}{\kappa} \tag{2.48}$$

is the ratio between activity and bending rigidity.

The results are normalized for length with the bond length r_0 and filament body length L, for energies with the thermal energy $k_B T$, and for time in units of the characteristic time for the filament to diffuse its own body length (diffusive time) as well as the characteristic time for the filament to propel itself along its own body length (advective time), unless otherwise stated. These time scales are set, respectively, by,

$$\tau_D = L^3 \gamma_l / 4 k_B T, \tag{2.49}$$

$$\tau_A = L\gamma_l/f_p \tag{2.50}$$

In our simulations we used $k_S = 5000 k_B T/r_0^2$, $r_0 = \sigma/2 = L/N_b$, and $\epsilon = k_B T$, unless stated otherwise. We defined the packing fraction with $\phi = N_b N_f \sigma r_0 / L_x L_y$, with L_x and L_y describing the length of the box in the x and y directions, respectively. N_b denotes the number of bonds making up a single filament. N_f is the number of filaments. We used $N_f = 6000$ filaments for low aspect ratio filaments ($a = 25$) and $N_f = 2000$ filaments for high aspect ratio filaments ($a = 100$) in a periodic square box with $\phi = 0.2$ in simulations of finite densities and $\phi = 0.8$ in simulations of high densities. The parameter space was explored via changing N_b, f_p and κ to vary a, Pe and ξ_P/L, respectively.

2.5. Liquid Crystals

Many active systems in biology, from cytoskeletal filaments to bacteria, have elongated constituents. Such systems display ordered phases that are similar to liquid crystalline ordering. In this section, we describe liquid crystalline phases, in particular, focusing on the nematic phase and the topological defects associated with the discontinuties in the nematic field.

A liquid crystal phase is a phase somewhere between a solid and a liquid. One way of distinguishing a solid from a liquid is to look at the molecular structure. A solid has a well-defined spatial molecular arrangement whereas a liquid is spatially disordered. Density-density correlations underline this difference. For a solid, it is $\lim_{|x-x'|\to\infty}\langle\rho(x)\rho(x')\rangle = P(x-x')$ where x and x' denote particle positions, ρ is density, and $P(x-x')$ is a periodic function. The density-density correlations remain large as periodic spatial ordering persists even at very large distances. A liquid, on the other hand, is inherently disordered with correlations of $\lim_{|x-x'|\to\infty}\langle\rho(x)\rho(x')\rangle = \rho^2$, assuming isotropy. Oscillations in the density-density correlations decay over a certain characteristic length scale.

In a liquid crystal, liquid-like order presides over at least one spatial dimension, but with some anisotropy, over which there could be order. More formally, the density-density correlation function could depend on the orientation of the separation vector between two particles instead of depending on the distance $x-x'$ [159]. A liquid crystal is characeterized by the type of ordering it exhibits.

- Orientational-order in a liquid, corresponding to a liquid with anisotropic correlations, is referred as *nematic* ordering,
- One-dimensional order in $3D$, corresponding to $2D$ liquid layers stacked on each other with a well-defined spacing in-between, is referred as *smectic* ordering,
- Two-dimensional order in $3D$, corresponding to $2D$ arrays of liquid tubes, is referred as *columnar* ordering.

Anisotropic materials such as rods in a liquid suspension, polymers, rod- or disk-like small organic molecules can exhibit liquid crystalline ordering [159]. In the case of nematic liquid crystals, order is characterized by considering the distribution of alignment of molecules $\hat{a}$ with respect to the nematic director field $\hat{n}$,

$$\langle\hat{a}\cdot\hat{n}\rangle = \langle\cos(\theta)\rangle = \int f(\theta)\cos(\theta)\mathrm{d}\Omega = 0 \tag{2.51}$$

where $f(\theta)$ denote the distribution function of alignment angle θ. As the direction $\hat{n}$ and $-\hat{n}$ are equally likely, this term corresponding to the first term of the multipole expansion vanishes. The first non-vanishing term is the quadropole term, which gives the scalar nematic order parameter S,

$$S = \frac{1}{2}\langle(3\cos^2(\theta)-1)\rangle = \int f(\theta)\frac{1}{2}(3\cos^2(\theta)-1)\mathrm{d}\Omega \tag{2.52}$$

When the distribution $f(\theta)$ is peaked around $\theta = 0$ or $\theta = \pi$, which corresponds to molecules oriented parallel to the nematic director on average, $\cos(\theta) = \pm 1$ and $S = 1$. When $f(\theta)$ is peaked around $\theta = \pi/2$, corresponding to perpendicular alignment, $\cos(\theta) = 0$ and $S = -1/2$. When the distribution is random, $\langle \cos^2\theta \rangle = 1/3$ and $S = 0$. Therefore, the scalar nematic order parameter S characterizes the degree of nematic ordering of liquid crystalline molecules.

The order parameter to characterize nematic order is a concept that we will use throughout the thesis. Therefore, it is useful to generalize it across space dimensions. In general, we are interested in calculating an order tensor $Q_{\alpha\beta} \sim \langle \mathbf{i}_{\mathbf{ff}}\mathbf{j}_{\mathbf{fi}} \rangle$, where $\mathbf{i}$ and $\mathbf{j}$ are vectors representing the molecular orientation and α and β represent the laboratory frame. The order tensor Q can be rendered traceless by subtracting $\mathbf{I}/3$ in three dimesions, $\mathbf{I}/2$ in two dimensions, or in general, $\mathbf{I}/d$ in d dimensions. If the system is isotropic, that is $\langle x^2 \rangle = \langle y^2 \rangle = \langle z^2 \rangle = 1/3$ in three dimensions, the order parameter tensor becomes $Q_{xx} = -1/3$, $Q_{yy} = -1/3$, and $Q_{zz} = 2/3$. For convenience, we embed two more properties. The scalar nematic order parameter S should be the largest eigenvalue of the order tensor with an eigenvector corresponding to the director $\hat{n}$. We also want S to take on values between 0 and 1. To do so, we multiply the tensor with $Sd/d - 1$, which gives the general form of,

$$Q_{ij}^{\alpha\beta} = \frac{S}{d} \langle d i_\alpha j_\beta - \delta_{\alpha\beta}\delta_{ij} \rangle \tag{2.53}$$

where $\alpha, \beta = x, y, z$ describe the laboratory frame, and $i, j = \hat{a}, \hat{b}, \hat{c}$ describe the molecule orientation [159]. This is a symmetric and traceless tensor with the largest eigenvalue giving the degree of nematic order S with the corresponding eigenvector giving the director $\hat{n}$. The other two eigenvalues are $-S/2$ with eigenvectors perpendicular to $\hat{n}$.

Distortions of the nematic director has an energetic penalty. The elastic energy associated with such distortions has three contributions. A splay distortion corresponds to a non-vanishing divergence in the director field ($\nabla \cdot \hat{n} \neq 0$). A bend distortion corresponds to in-plane rotations of the director ($\nabla \times \hat{n} \perp \hat{n}$). A twist distortion corresponds to out-of-plane rotations of the director ($\nabla \times \hat{n} \parallel \hat{n}$). The distortion free energy per unit volume is then given by,

$$F_d = \frac{1}{2} K_s (\nabla \cdot \hat{n})^2 + \frac{1}{2} K_t (\hat{n} \cdot \nabla \times \hat{n})^2 + K_b (\hat{n} \times \nabla \times \hat{n})^2 \tag{2.54}$$

which is known as *Frank free energy* [159]. Assuming that the splay, bend, and twist constants (K_s, K_b, and K_t, respectively) are equal simplifies the expression to,

$$F_d = \frac{1}{2} K \big((\nabla \cdot \hat{n})^2 + (\nabla \times \hat{n})^2 \big) = \frac{1}{2} K \partial_\alpha n_\beta \partial_\alpha n_\beta \tag{2.55}$$

where K is an elastic constant under one-constant approximation ($K = K_b = K_s = K_t$) [159].

For two dimensions, we can simplify the energetic cost of distortions of nematic director greatly,

$$F_N = K \int \mathrm{d}x (\nabla\theta)^2 \tag{2.56}$$

where θ is the rotation angle of the director $\hat{n}$. Fourier transforming eq. 2.56, we get $F_N = K \int \mathrm{d}q q^2 \theta(q)^2/(2\pi)^2$. By the equipartiation theorem $K q^2 \langle \theta(q)^2 \rangle = \mathrm{k_B} T/2$, the mean square rotations of the nematic director are,

$$\langle \theta(q)^2 \rangle = \frac{\mathrm{k_B} T}{2Kq^2} \tag{2.57}$$

Frank free energy that describes the nematic director distortion cost assumes smooth distortions. However, there could be regions in the director field $\hat{n}(\mathbf{r})$ that are not smooth as a function of $\mathbf{r}$. Topological defects are these regions of heterogeneity in the director field that cannot be transformed continuously into a uniform state [159]. Given that $\mathbf{r}$ is the distance between the singularity in the director field associated with the defect and the observation point in the system, $\phi(\mathbf{r})$ is the angle between $\mathbf{r}$ and the arbitrarily chosen x axis, and $\theta(\mathbf{r})$ is the angle between $\mathbf{n}$ and x axis, the defect is characterized by the rotation of the director around the singularity, that is, $\theta(\mathbf{r}) = m\phi(\mathbf{r})$ where m is the strength of the defect. The director can rotate $\pm\pi$ or $\pm 2\pi$, thus the defect strength m can take on integer or half integer values (see Fig. 2.4). Such conformations will be continuous around the defect everywhere, except for the singularity associated with the defect.

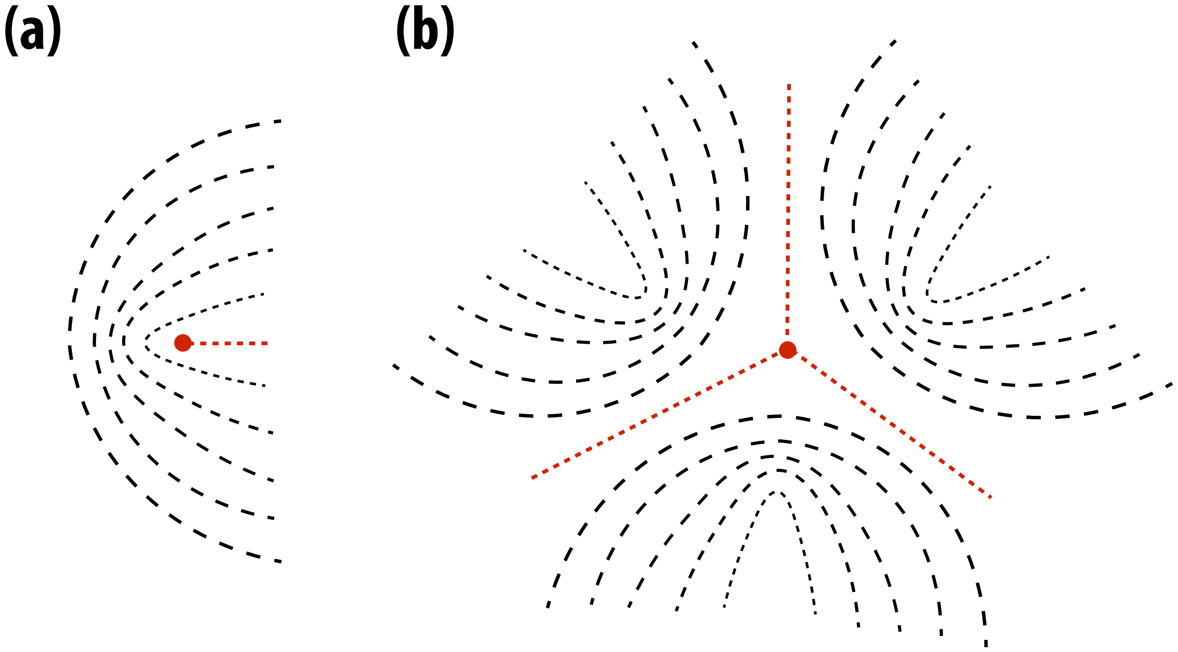

Figure 2.4.: Defect configurations with a sketch of the director field $\hat{n}$: (a) +1/2 defect, (b) −1/2 defect.

Minimizing the free energy given in eq. 2.56 yields the equilibrium condition $\nabla^2\theta = 0$. We can test this equilibrium condition for the defects. The gradient of defect angle $\theta = m\phi = m\tan^{-1}(y/x)$ is $\nabla\theta = m/r$ where $r = \sqrt{x^2 + y^2}$ is the distance between defect and observation point. Taking the divergence of this equation to get the Laplacian of defect angle, $\nabla\cdot\nabla\theta = \nabla^2\theta = 0$, thus the defect conformation obeys the equilibrium condition. Defects can be generated under equilibrium by external perturbations such as applying an electric or magnetic field, or inducing a certain geometry upon the system.

The free energy per unit volume associated with defects is,

$$F = \int_a^{r_{\max}} \mathrm{d}r 2\pi r \frac{1}{2} K \frac{m^2}{r^2} = \pi K m^2 \ln\Big(\frac{r_{\max}}{a}\Big) \tag{2.58}$$

where a is on the order of molecules and $r_{\max}$ is the distance between defect and the walls of the container [159].

We can also calculate the interaction energy between two defects. We assume two opposite-signed defects at a distance $\varDelta$ with $\theta = m(\phi_1 - \phi_2)$. If we consider a circle around the observation point that crosses the separation vector of the two defect points, the director will change by π each time it crosses the separation vector. Therefore, the defect angle is still given by $\theta = 2\pi m$. Integrating eq. 2.56 by parts,

$$\frac{1}{2} K \int (\nabla\theta)^2 \mathrm{d}r = -\frac{1}{2} \int \theta \nabla^2 \theta \mathrm{d}r + \frac{1}{2} K \int \theta \nabla \theta \mathrm{d}r \tag{2.59}$$

where the first term on the right-hand side vanishes as $\nabla^2\theta = 0$ at equilibrium. Evaluating the integral in the second term gives the interaction free energy per unit line,

$$F_{\mathrm{int}} = \frac{K}{2} \int_a^{\varDelta - a} \theta m \left(\frac{1}{r_1} + \frac{1}{\varDelta - r_1} \right) \mathrm{d}r_1 = 2\pi K m^2 \ln\Big(\frac{\varDelta}{a}\Big) \tag{2.60}$$

Therefore, the interaction energy increases with the separation distance $\varDelta$ between the defects logarithmically. It is attractive for opposite-signed defects and repulsive for same-signed defects.

For a pair of opposite-signed defects (which attract each other), we can calculate the annihilation dynamics. The forces on each defect is given by the spatial derivative of eq. 2.60. Assuming overdamped dynamics, force balance gives the equation of motion,

$$\begin{aligned} \frac{\mathrm{d}r_1}{\mathrm{d}t} &= -\frac{M}{\varDelta} \\ \frac{\mathrm{d}r_2}{\mathrm{d}t} &= \frac{M}{\varDelta} \end{aligned} \tag{2.61}$$

where $M = 2\pi m^2 K/\xi$ with ξ the friction coefficient. Therefore, $\frac{\mathrm{d}\varDelta}{\mathrm{d}t} = -2M/\varDelta$, which shows that the distance $\varDelta$ between opposite-signed defects decreases as a square root in time $\varDelta(t) \sim \sqrt{t_a - t}$ with $t_a = \varDelta^2(0)/4M$ indicating the defect annihilation time. Defects move towards each other in symmetric trajectories and annihilate at $\varDelta(0)/2$ within a time t_a. More precise calculations lifting the overdamped dynamics assumption showed that the effective friction itself depends logarithmically on the distance between defects, $\xi = \xi_0 \ln(\varDelta/a)$ [67].

2.6. Turbulence

Turbulence is a phenomenon that describes the seemingly universal features of disordered flows with vortices and swirls at very high flow velocities and driving. This very general and simplistic definition led to a broad colloquial usage of the word turbulence. The word turbulence colloquially describes phenomena that are deeply engrained in our daily lives from the smoke of a cigarette to the mixing of coffee and milk. Indeed, there appears to be a resemblance between the flow patterns of the interface between coffee and milk and the atmospheric motion around Jupiter or Saturn. They are disordered flows characterised with patterns of vortices and swirls. This ostensibly general character of turbulent flow intrigued many scientists like Kelvin, Onsager, Kolmogorov, and Landau to try to come up with theoretical frameworks that capture the universal features of turbulent flow across length scales.

In line with the empirical definition, first attempts to understand turbulence were phenomenological with a focus on the vortex-filled nature of the turbulent flow field. Lord Kelvin discovered that in the limit of vanishing viscosity, vorticity is a constant of the motion along the fluid path [60]. To see it mathematically, we write down the Navier-Stokes equation without the viscosity term (which is known as the Euler equation),

$$\frac{\partial \mathbf{v}}{\partial t} + \mathbf{v} \cdot \nabla \mathbf{v} = -\nabla p \tag{2.62}$$

where $\mathbf{v}$ is the velocity field and p is pressure. If we now write the Euler equation in terms of vorticity by taking the curl of velocity, then

$$\frac{\partial \mathbf{w}}{\partial t} + \mathbf{w} \cdot \nabla \mathbf{v} + \mathbf{v} \cdot \nabla \mathbf{w} = 0 \tag{2.63}$$

In two dimensions, the vorticity $\mathbf{w}$ is a pseudoscalar in the z direction while $\mathbf{v}$ is in the $x - y$ plane. Therefore, due to orthogonality, $\mathbf{w} \cdot \nabla \mathbf{v}$ term drops out leaving only $\mathrm{D}w/\mathrm{D}t = 0$, where D denotes the material or Lagrangian derivative. In other words, vorticity does not change in time, and is conserved along the fluid path for an inviscid fluid ($\nu = 0$) in two dimensions. In 3D, eq. 2.63 yields an exponential solution with the exponent $\mathbf{w} \cdot \nabla \mathbf{v}$ for vorticity. As a result, $\mathbf{w} \cdot \nabla \mathbf{v}$ term is known as vortex stretching in 3D. Physically, it corresponds to the stretching of vortices in the perpendicular direction to the flow, which will increase the enstrophy (which is the vortical energy defined as $\boldsymbol{w}^2/2$). However, as there is no such perpendicular axis in 2D, enstrophy is conserved. Lars Onsager used this idea to explain vortex formation in turbulence in terms of equilibrium statistical mechanics, which is presented in Appendix D [145].

We next turn to conservation laws to explore the phenomonelogy of turbulence in dissipative systems. We first write down the incompressible Navier-Stokes equation with index (Eulerian) notation as $\partial_t v_i + v_j(\partial_j v_i) = -\partial_i p + \nu \partial_{jj} v_i$ where ∂_i represents the derivative with respect to the subscripted index. The incompressibility condition translates into $\partial_i v_i = 0$ in this notation. Due to this condition, $v_j(\partial_j v_i)$ can be written as $\partial_j(v_j v_i)$. The Navier-Stokes equation then reads,

$$\partial_t v_i + \partial_j(v_j v_i) = -\partial_i p + \nu \partial_{jj} v_i \tag{2.64}$$

To obtain energy conservation, we multiply this expression with v_i,

$$\partial_t v_i v_i + \partial_j(v_j v_i v_i) = -v_i \partial_i p + \nu v_i \partial_{jj} v_i \tag{2.65}$$

The first term on the right-hand side can be rewritten as $(\partial_i v_i)p$ from the relation $\langle(\partial_i f)g\rangle = -\langle f(\partial_i g)\rangle$. Due to the incompressibility condition, this term drops out of the equation. The second term on the right-hand side can be transformed into $\nu\langle-(\nabla\times\mathbf{u})\cdot(\nabla\times\mathbf{u})\rangle$, following the vector identity $\langle\mathbf{u}\cdot\nabla^2\mathbf{v}\rangle = -\langle(\nabla\times\mathbf{u})\cdot(\nabla\times\mathbf{v})\rangle$ [157]. The advection term, which is the second term on the left-hand side, also drops out due to the incompressibility condition. Navier-Stokes equation then reduces to

$$\frac{\mathrm{d}}{\mathrm{d}t}\Big\langle\frac{1}{2}v^2\Big\rangle = -\nu\langle|w|^2\rangle = -\frac{1}{2}\nu\Big\langle\sum_{i\neq j}(\partial_i v_j + \partial_j v_i)^2\Big\rangle \tag{2.66}$$

which is a manifestation of energy conservation. In the absence of forcing, the rate of change of energy is set by viscosity and enstrophy on the right-hand side of the energy conservation equation. Now we inject energy to the system by adding a forcing term $\mathbf{f}$ to the right-hand side of eq. 2.64. This turns into $\langle\mathbf{v}\cdot\mathbf{f}\rangle$ on the right-hand side of eq. 2.66 following the same steps. The Navier-Stokes equation then reads

$$\frac{\mathrm{d}}{\mathrm{d}t}\Big\langle\frac{1}{2}v^2\Big\rangle = -\nu\langle|w|^2\rangle + \langle\mathbf{v}\cdot\mathbf{f}\rangle \tag{2.67}$$

The forcing term causes a change in the energy flux, which is dissipated by viscosity. However, in the limit of $Re \to \infty$, where viscosity vanishes, it is not possible to dissipate the energy caused by forcing. When enstrophy is conserved (which is the case in 2D), there is no mechanism for energy dissipation in the limit of vanishing viscosity. In other words, as the dissipation term $\nu\langle|w|^2\rangle$ is fixed, energy injection cannot be dissipated. Therefore, the simultaneous conservation of kinetic energy and enstrophy creates problems in inviscid two-dimensional systems. This is a problem that cannot be solved by Onsager's conjecture on conservative systems.

The solution is proposed by Kraichnan and Montgomery who conjectured that injected energy and enstrophy should cascade towards opposite length scales [106]. We can understand this by comparing the scaling of kinetic energy and enstrophy in terms of length scale. Kinetic energy per unit mass is $E = v^2/2$, and the enstrophy per unit mass is $\varOmega = |w|^2/2 = k^2E/2$ as vorticity is the curl of velocity and in Fourier space the curl becomes multiplication with k. Therefore, an inverse energy cascade which would transfer energy from the forcing length scale k_f to higher modes would increase the enstrophy of higher modes. As a result, an inverse energy cascade should be accompanied with a direct enstrophy cascade which would carry enstrophy from higher modes to lower modes such that enstrophy conservation holds at the same time with energy conservation. A direct enstrophy cascade thus accompanies the inverse energy cascade in 2D. As a result, injected energy escapes to the small wavenumbers/large length scales (inverse energy cascade) while the enstrophy goes down towards large wavenumbers/small length scales (direct enstrophy cascade) in inviscid 2D systems. We extend the handwaving argument presented here in somewhat more detail in Appendix D on Fjortoft's theorem by exploring the role of nonlinearities coming from the advection term on the phenomenology of turbulent cascade.

The double cascade picture does not hold in three dimensions, as enstrophy is not conserved. If we go back to the Navier-Stokes equation written in terms of vorticity, in eq. 2.63, we can see that $\mathbf{w} \cdot \nabla \mathbf{v}$ term does not drop out of the equation, as $\mathbf{w}$ and $\mathbf{v}$ are no longer orthogonal. Therefore, instead of having the relation $\mathrm{D}w/\mathrm{D}t = 0$, which leads to enstrophy conservation, we have an exponentially changing vorticity in 3D. Without enstrophy conservation, injected energy by forcing can be dissipated by increasing enstrophy. Therefore, energy and enstrophy are allowed to be transferred down towards the same length scales. Indeed, injected energy cascades down to large wavenumbers/small length scales (direct energy cascade) in 3D and enstrophy increases by vortex stretching [9].

After discussing energy cascades, we turn to Kolmogorov theory to explore the properties and scaling relations of turbulence. Kolmogorov phenomenology is based on the idea of separation of length scales at high Re. The intermediate length scale, between the large length scale of energy injection and the small length scale of dissipation, is referred as the inertial range. Eddies falling inside this inertial range are neither affected by the forcing nor the dissipation. Therefore, the properties of a turbulent eddy with a length scale of d at the inertial range depends solely on the length scale d, and the energy flux rate ϵ. This is to say, the eddy only knows how long it is, at what rate energy is supplied to it from the next longer eddy, and at what rate it is supplying energy to the next smaller eddy. Mathematically, the velocity of the eddy at the inertial range is solely determined by d and ϵ. The only way for this dependence to hold from a dimensional perspective is to have

$$v(d) = A(\epsilon d)^{1/3} \tag{2.68}$$

with d having units of length, ϵ having units of energy per unit time per unit mass, and v having units of length per time. This relation shows that smaller eddies are slower. It also includes a prediction on the scaling of velocity structure factors. Velocity structure factors are the statistical moments of the spatial velocity correlation projected on the parallel or perpendicular direction of the spatial separation vector. For example,

$$\delta v_{||}(\mathbf{r}) = [\mathbf{v}(\mathbf{r} + \mathbf{R}, t) - \mathbf{v}(\mathbf{R}, t)] \cdot \frac{\mathbf{r}}{r} \tag{2.69}$$

is the velocity difference between two points separated with a vector of $\mathbf{r}$, and the velocity difference is projected parallel upon the separation vector $\mathbf{r}$. Parallel velocity structure factor is then the nth moment of this velocity difference,

$$S_n(r,t) = \langle (\delta v_{||}(r))^n \rangle \tag{2.70}$$

By eq. 2.68, the parallel velocity structure factor is expected to scale with $S_n(r,t) = C(\epsilon r)^{n/3}$.

This way of dimensional arguments based on self-similarity of the inertial range is first proposed by Kolmogorov in 1941, and it is referred as K41 after him. There are other ways of establishing the same scaling exponents. For scaling of velocity, Landau suggested the following physical picture: The energy turnover time of an eddy is given by $r/\delta v_r$. Assuming that the eddy loses a significant portion of its energy during the turnover time, the energy flux goes as $\delta v_r^2/(r/\delta v_r)$ [60]. Therefore, $\delta v_r \approx (\epsilon r)^{1/3}$, which is the same result as eq. 2.68.

As the last step of our description of turbulence, we describe relevant scaling relations derived from K41 phenomenology.

The length of shortest eddies depends on dissipation, which depends on viscosity ν with dimensions L^2/t, and energy flux. Therefore, the shortest eddy lengths at the dissipation range is set by $d_{\mathrm{min}} \approx \nu^{3/4}\epsilon^{-1/4}$. This length scale, where energy dissipation is dominant, is called the Kolmogorov scale, which is typically on the order of a few milimeters or shorter.

The kinetic energy per mass of fluid has the dimensions of L^2/t^2. The portion of the kinetic energy within the modes k to $k + dk$ is defined as $dE = E_k \mathrm{d}k$. The quantity E_k is known as the kinetic energy spectrum. It is the kinetic energy accumulated at the length scale k and it has the units of energy per length scale L^3/t^2. At the inertial range, it depends on the energy flux and the length scale, and dimensional requirement suggests a scaling of the form,

$$E(k) = C_K \epsilon^{2/3} k^{-5/3} \tag{2.71}$$

Therefore, the energy cascade scales as $k^{-5/3}$. Such scaling has been observed to hold well experimentally at intermediate length scales remote from longest and shortest scales. Its spatial range becomes broader with increasing *Re*. It is interesting to note the same scaling holds with different interpretations in 3D and 2D. It is a forward or direct cascade in case of 3D systems, as it carries the injected energy from large scales to smaller scales where the energy is dissipated by viscosity. While it is a backward or inverse cascade in the case of 2D systems, with energy transfer from small scales to larger scales.

To get the scaling for the direct enstrophy cascade, we again apply dimensional analysis: E_k depends on the enstrophy flux η, which has the dimensions of $1/t^3$ as it goes with $k^2\epsilon$, and the length scale set by k,

$$E(k) = C' \eta^{2/3} k^{-3} \tag{2.72}$$

Physically, the enstrophy cascade is the elongation of a fluid part in the flow direction when it is under a larger scale velocity strain. The fluid part will be elongated in the flow direction and compressed in the transverse direction to the flow. Since the vorticity of each fluid component is conserved, the result of compressed flow in the transverse direction will be a steepening of the transverse vorticity gradients, which yields a flux of vorticity towards smaller length scales. In this way, enstrophy is transferred from larger scales to smaller scales giving a picture of direct enstrophy cascade.

As we have seen before, according to Kraichnan conjecture, in a 2D system at high *Re*, a constant injection of energy to the flow at a rate ϵ at an intermediate length scale d will be transferred towards longer length scales until the longest length scales are attained [2] [106].

---

[2] Note that this focusing of energy on low k-modes (*spectral condensation*) is similar to Bose-Einstein condensation. This can be understood on the grounds that Gross-Pitaevskii equation which describes the ground

This inverse energy cascade follows the $k^{-5/3}$ scaling. Vortices start to appear once the inverse cascade carries the energy to the longest scales and the $k^{-5/3}$ scaling is disrupted. In the case of a periodic simulation box, the longest scale is half of the box length. Both k^{-3} and $k^{-5/3}$ scalings are observed in the atmosphere, corresponding to the enstrophy and the energy cascades, respectively. This is a result of the stratified nature of the atmosphere which renders certain parts of it quasi-2D.

The inverse energy cascade of two-dimensional inertial turbulence is observed experimentally in 1980s. A grid of an array of cylinders, with 0.2 cm in diameter and 0.2 cm spacing in between, was towed through a soap film [31]. A soap film is a thin layer of water bounded by surfactant monolayers that reduce the surface tension. In this experiment, the thickness of the film is on the order of a few micrometers, while it extended centimeter squares laterally, which renders the velocity field of the water perpendicular to the surface. Small vortices generated at the length scales of the cylinders merge to form larger vortices, and the flow becomes dominated by vortices [31]. The towing speed is held constant about $60cm/s$ with $Re \approx 1200$.

Besides soap films, two-dimensional turbulence is also observed in thin layers of conducting liquids driven with a spatiotemporally varing magnetic field. In a pioneering experiment, Sommeria, *et. al.* observed inverse cascade when a thin layer of mercury on a solid substrate is forced via electrical currents and a static vertical magnetic field [179].

In 3D, energy is turned into heat by viscosity at the smallest length scales. However, as the energy is carried towards the longest length scales, a friction term to damp the energy is necessary in 2D systems. With the addition of a linear friction term, which can be added to the Navier-Stokes equation $-\gamma v$ (this term is known as *Ekman friction*), the scaling behaviour changes. Friction damps energy from all lengths scales the same way. Once the energy is at the longest scales, it will still be damped by friction. Therefore, the nonlinear energy transfer via advection must be balanced now with friction. Friction is found to have a regularizing effect on the flow with a depletion of small-sized structures [60]. It causes a steeper spectrum of the form,

$$E(k) \approx k^{-3-a} \tag{2.73}$$

Diffusion in turbulent flow can be obtained via the time evolution of the mean square distance between two tracer particles. From eq. 2.68, we get the scaling for time as $t \approx \epsilon^{-1/3} d^{2/3}$. When a pair of particles initially separated a distance of d apart are released inside a turbulent flow, the rate of change of the squared distance between them scales with $d^2/t \approx \epsilon^{1/3} d^{4/3}$. This scaling is first discovered by Richardson around 20 years before Kolmogorov.

There are two assumptions that led to the K41 phenomenology. First is the assumption of scale invariance at the inertial range, which is a result of the separation of energy injection and dissipation scales at high Re. The second assumption is the localness of the interactions,

---

state of identical boson ensembles is a generalized diffusion equation similar to Navier-Stokes equation in form.

that is energy of an eddy is only affected by eddies of similar sizes. We only described pheonomenological properties of turbulence based on these assumptions. Indeed, the putative universality of turbulence based on the theory of Kolmogorov adequately describes a large body of experimental evidence. However, it is far from being complete. There is no way of proving its universality from first principles as yet, and at best it remains at an approximate universality providing a useful phenomenological picture of seemingly universal phenomena. We describe here one of the earliest objections to K41 that is raised as early as 1962 to exemplify its shortcomings.

Kolmogorov theory relies on a self-similar turbulent flow with a Gaussian distribution of spatial velocity differences. The Gaussian distribution assumption holds well across large scales. However, at small scales, the distribution starts to develop tails departing from Gaussian. This phenomenon is known as *intermittency*, which is nothing but the statistical tendency of a random variable to have an unusual distribution of very large and very small values in comparison its typical values. Experimental data from the time series of velocities in turbulent flow suggests a picture with intermittent behaviour where there are periods of intense fluctuations and also periods where velocity is not changing much [137]. Thus, at small spatial and time scales, velocity fluctuations show intermittent character. As a result, higher order statistical moments of certain functions like the velocity structure factor do not follow predictions of K41. To solve this intermittency problem, Kolmogorov modified his global scale-invariance assumption, by suggesting a local scale-invariance instead, such that the velocity field can take on different dimensions on a fractal set [60]. However, this multifractal approach brings about as many questions as it answers. This is at best another approximation, which does not answer the fundamental question of, how to justify a universality or a multifractality assumption starting from the Navier-Stokes equations.

Turbulence is a pheonomenological problem, and in this regard our general definition at the beginning of this section remains relevant after our discussion. We close this section by giving a formal -albeit still general- definition. In order to be characterized by turbulence, a flow must be unpredictable in the sense that a small change in initial conditions amplify significant changes in the dynamical behaviour of the flow. Turbulent flow should lead to increased mixing when compared with diffusive mixing. It must have flow patterns that involve a wide range of length scales with rotational patterns [60]. This set of phenomenological rules will be useful when we discuss the possibility of turbulent behaviour in other systems later in the text. As some of the key results of this thesis pertain to turbulence at low Re, we give a detailed literature review highlighting key results on low Re or active turbulence in Appendix D.

3. Collective Dynamics of Dense Cell Monolayers

3.1. Introduction

Epithelial tissue lines the internal and external sides of organs and blood vessels in the body. To function as a lining barrier, cells in epithelial tissue are spatially well-ordered and non-motile. However, under a variety of circumstances, epithelial cells can become motile and create a disordered and fluid-like tissue. In wound healing, cells become motile within a moving sheet to close the wound [108]. Metastasing cells turn into an invasive and migratory phenotype when undergoing cancer metastasis [144, 7]. During vertebrate embryonic development, cells move to facilitate structural rearrangements [212]. In each of these instances, an initially non-motile tissue undergoes a motility transition upon which it becomes motile and fluid-like. The reverse transition from a fluid-like phase to a solid-like phase can also occur. Experiments on Madin Darby canine kidney cells (MDCK) showed that after the epithelial cell monolayer reaches confluency upon successive cell divisions, dynamics of the monolayer significantly slows down [4]. Furthermore, in this regime, cell motion is found to be correlated with swirl-like patterns similar to the jamming of dense suspensions of inert matter like colloids, emulsions and foams.

Motility transitions of cell monolayers present an intriguing physical problem. In inert matter at mesoscales, jamming is mainly driven by density. Cell monolayers, on the other hand, can display different phases of motility despite remaining at a density of unity after reaching confluency. During vertebrate embryonic development ectoderm and mesendoderm layers display different motility phases despite sharing the same densities [13]. Other parameters are proposed to accommodate such density-independent motility transitions. Experiments on human bronchial epithelial cells (HBEC) found the velocity correlations to be proportional to cell-cell adhesion and cell-substrate adhesion instead of density. Therefore, after the monolayer reaches confluency, the glass-like dynamics does not correlate with density, but instead correlates with growing adhesion [62]. In HBEC monolayers from the airway epithelium, the onset of jamming is found to be delayed due to asthma [151]. Bronchial cells are compressed during asthma, which unjams the tissue. Therefore, mechanical properties like compressibility and cell-cell adhesion also play a role in the jamming of tissues.

After the experimental findings highlighted the role of mechanical parameters in motility transitions, simulations gained traction in a bid to pin down the physical origins of this phenomena. Confluent monolayers are usually simulated with variants of vertex and cellular Potts models, as they take advantage of the confluency of the monolayer to reduce the computational costs [76, 22]. In the cellular Potts model, the monolayer is made up of fixed lattice positions and cells are the lattice sites with the same spin. Cells then move via spin exchanges between neighbouring lattice sites. Desirable single cell and interaction properties (including cell motility) are encoded in the energy function, which determines the spin exchanges [22].

The vertex model is different from the cellular Potts model in that lattice sites are not fixed in the vertex model. In this model, cells are described as polygons. Equations of motion (which may also include cell motility) propagate the vertices. Interactions between cells are described by energy functions that govern vertex exchanges [58].

In the Voronoi model, polygons that describe cells are determined from a Voronoi tessellation of space. This model is different from the vertex model in that the equations of motion apply to the center of cells. Motility can then be added by treating the center as a soft self-propelled particle. Softness is determined via energy functions governing cell-cell interactions. This model captures motility transitions as a function of cell shape and motility [14, 13, 151]. When the cortical tension dominates over the cell-cell adhesion, the monolayer displays solid-like characteristics. When the cell-cell adhesion is dominant, the monolayer exhibits fluid-like dynamics. Therefore, this model predicts that increasing adhesions fluidize the monolayer. The cellular Potts model also accounts for motility transitions as a function of cell motility and adhesion [28]. In this model, increasing motility, or decreasing adhesion is found to fluidize the monolayer.

A jamming phase diagram of cell monolayers, akin to that of inert matter, remains far from complete. Here we present a novel model of simulating dense cell monolayers in a bid to understand the role of mechanical properties of single cells in motility transitions. We map the transitions based on independent single cell parameters. Specifically, we capture constant-density motility transitions based on the deformability, compressibility, motility of cells and cell-cell adhesions. Our findings further underline the role of cell shape and deformability in the dynamics of 2D cell monolayers. In addition, we identify an active turbulence regime at the interface between the jamming and completely fluid-like phases.

3.2. Structure of the Monolayer

We start our description of cell monolayers by exploring their structural properties. We can identify the material properties through structural characterization. The monolayer is at a packing fraction ϕ of 1.5, well above the close packing limit 0.907 of hard disks, where all disks make immediate contacts [85]. Monodisperse hard disks undergo freezing at a packing fraction of ~ 0.68 [86, 160]. However, addition of polydispersity disrupts the spatial order[1].

---

[1] For colloidal suspensions, introducing a radii polydispersity of $s > 2\%$ is shown to destabilize the crystal phase [55]. It is interesting to note that synthetic colloids have usually a polydispersity of at least $s \approx 2\%$ in their radii distribution, which alters the freezing point slightly [6].

This is because it is entropically more advantegeous to distribute the different sized disks into different sized spaces than to pack them all at certain lattice points. In our system, cells have a polydispersity of $s \sim 7.4\%$ in their area distribution, that is, there is a standard deviation of $\sim 7.4\%$ of the mean cell area in the distribution. As a result, in the thermal limit of $Pe \to 0$, crystalline ordering is disrupted towards amorphous phases. We look for signatures of such amorphous phases by calculating the pair correlation function and the static structure factor. In the ensuing analysis, we will vary a single parameter (for example, ξ_p/R) and choose the remaining fixed parameters ($\epsilon/\mathrm{k_B}T$, Pe, and κ_A in this case) in a way that would enhance ordering to dissect the effect of the chosen parameter.

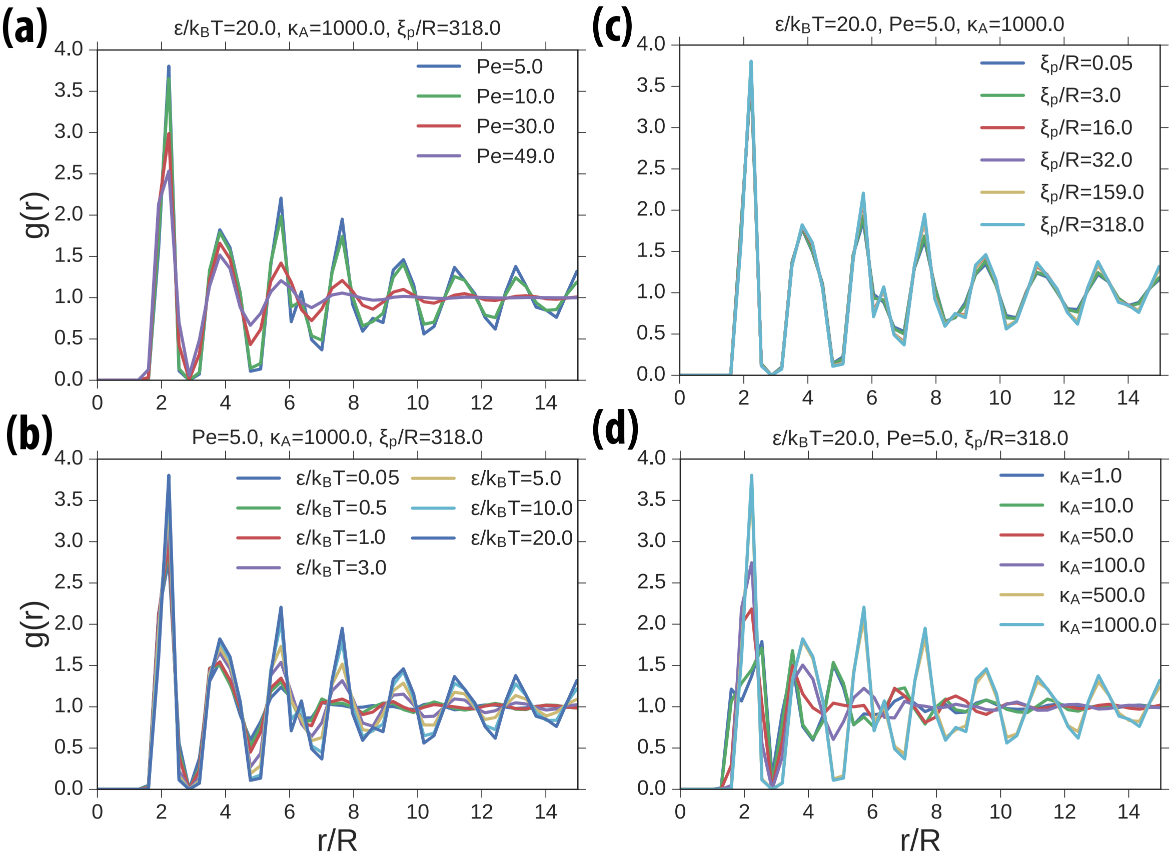

Figure 3.1.: Pair correlation function as a function of distance: (a) For various Pe at $\epsilon/\mathrm{k_B}T = 20$, $\kappa_\mathrm{A} = 1000$, $\xi_p/R = 49$, (b) for various ξ_p/R at $\epsilon/\mathrm{k_B}T = 20$, $Pe = 5$, $\kappa_\mathrm{A} = 1000$, (c) for various $\epsilon/\mathrm{k_B}T$ at $Pe = 5$, $\kappa_\mathrm{A} = 1000$, $\xi_p/R = 318$, and (d) for various κ_A at $\epsilon/\mathrm{k_B}T = 20$, $Pe = 5$, $\xi_p/R = 318$.

The pair correlation function, defined as

$$g(r) = \frac{1}{2\pi r}\frac{1}{N_c \rho}\sum_{i \neq j}\langle \delta(r - |\boldsymbol{r}_j - \boldsymbol{r}_i|)\rangle, \tag{3.1}$$

describes the variation of density around the center of mass of cells (assuming isotropy). The static structure factor

$$S(k) = \frac{1}{N}\left\langle \Big| \sum_{j=0}^{N} \mathrm{e}^{-i\boldsymbol{k}\cdot\boldsymbol{r}} \Big|^2 \right\rangle, \tag{3.2}$$

is the density autocorrelation in Fourier space. These two functions are measures of spatial order.

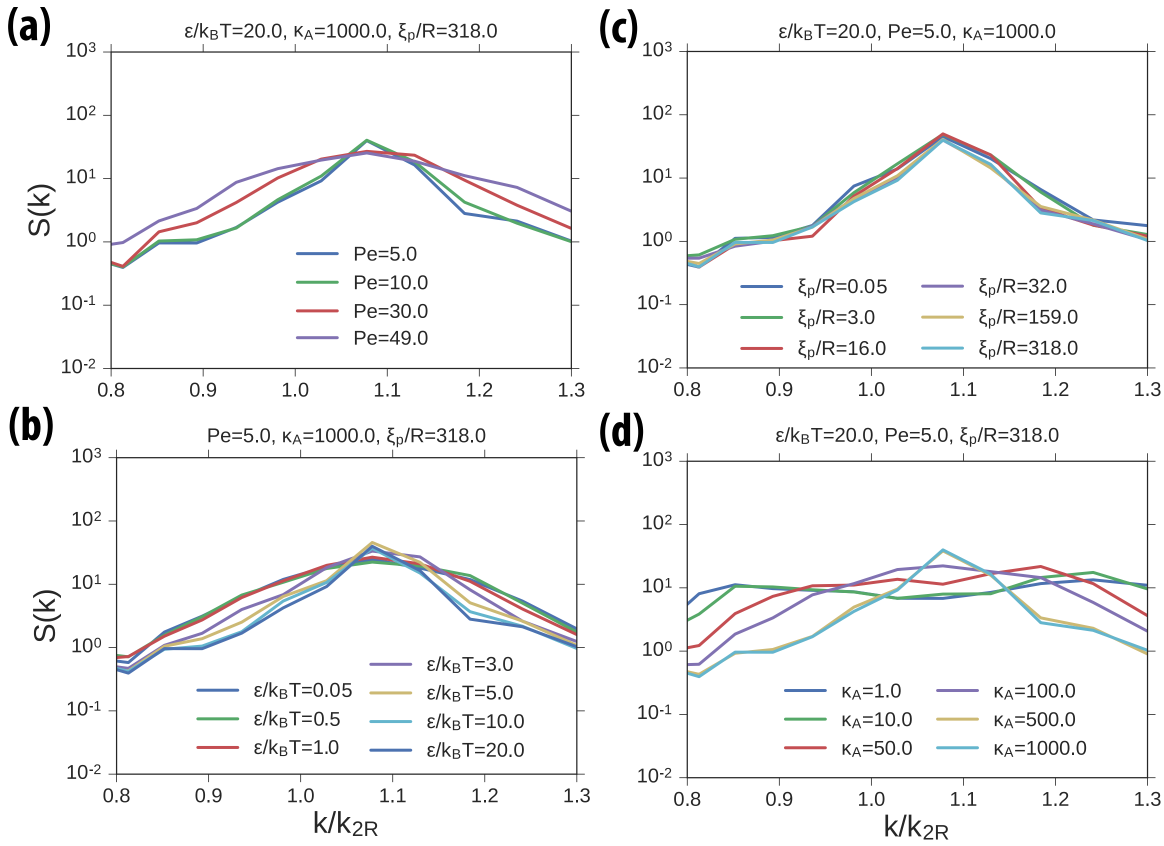

Figure 3.2.: Static structure function as a function of wavenumbers: (a) For various Pe at $\epsilon/\mathrm{k_B}T = 20$, $\kappa_\mathrm{A} = 1000$, $\xi_p/R = 49$, (b) for various ξ_p/R at $\epsilon/\mathrm{k_B}T = 20$, $Pe = 5$, $\kappa_\mathrm{A} = 1000$, (c) for various $\epsilon/\mathrm{k_B}T$ at $Pe = 5$, $\kappa_\mathrm{A} = 1000$, $\xi_p/R = 318$, and (d) for various κ_A at $\epsilon/\mathrm{k_B}T = 20$, $Pe = 5$, $\xi_p/R = 318$. The wavenumber axis is normalized by the wavenumber corresponding to the average cell diameter $k_{2R} = 2\pi/2R$.

The observed pair correlation functions indicate the absence of crystalline order (Fig. 3.1). Instead, the observed ordered phases are similar to amorphous solids, or dense liquids (with peaks decaying over distances longer than half the box size) and disordered phases are similar to dilute liquids (with peaks decaying over a few cell radii). Spatial order increases with decreasing Pe (as stronger motility forces help the cells in breaking out of cages, see Fig. 3.1-a), or increasing $\epsilon/\mathrm{k_B}T$ (as increasing $\epsilon/\mathrm{k_B}T$ sticks the cells stronger together, see Fig. 3.1-b), κ_A (as increasing κ_A makes the cells more resistant to area fluctuations, which hinders structural rearrangements, see Fig. 3.1-d). We observe that changing ξ_p/R does not alter the structural order significantly, indicating that deformability is a lesser-order effect in terms of monolayer structure (see Fig. 3.1-c).

A common feature of glass-like systems is the existence of peaks in pair correlation function that are broken into two [10]. Such broken peaks correspond to slightly shifted neighbour distances. During jamming, cells become caged by their neighbours. When one of the cells breaks out of the cage, other cells around it can follow the hole created by the freed cell, thereby moving the group of cells from one cage to another. These slight cooperative rearrangements are reflected as double peaks. One such distinctive broken peak is seen in the third neighbour distance of $Pe = 5$, $\xi_p/R = 318$, $\kappa_\mathrm{A} = 1000$, and $\epsilon/\mathrm{k_B}T = 20$ (Fig. 3.1).

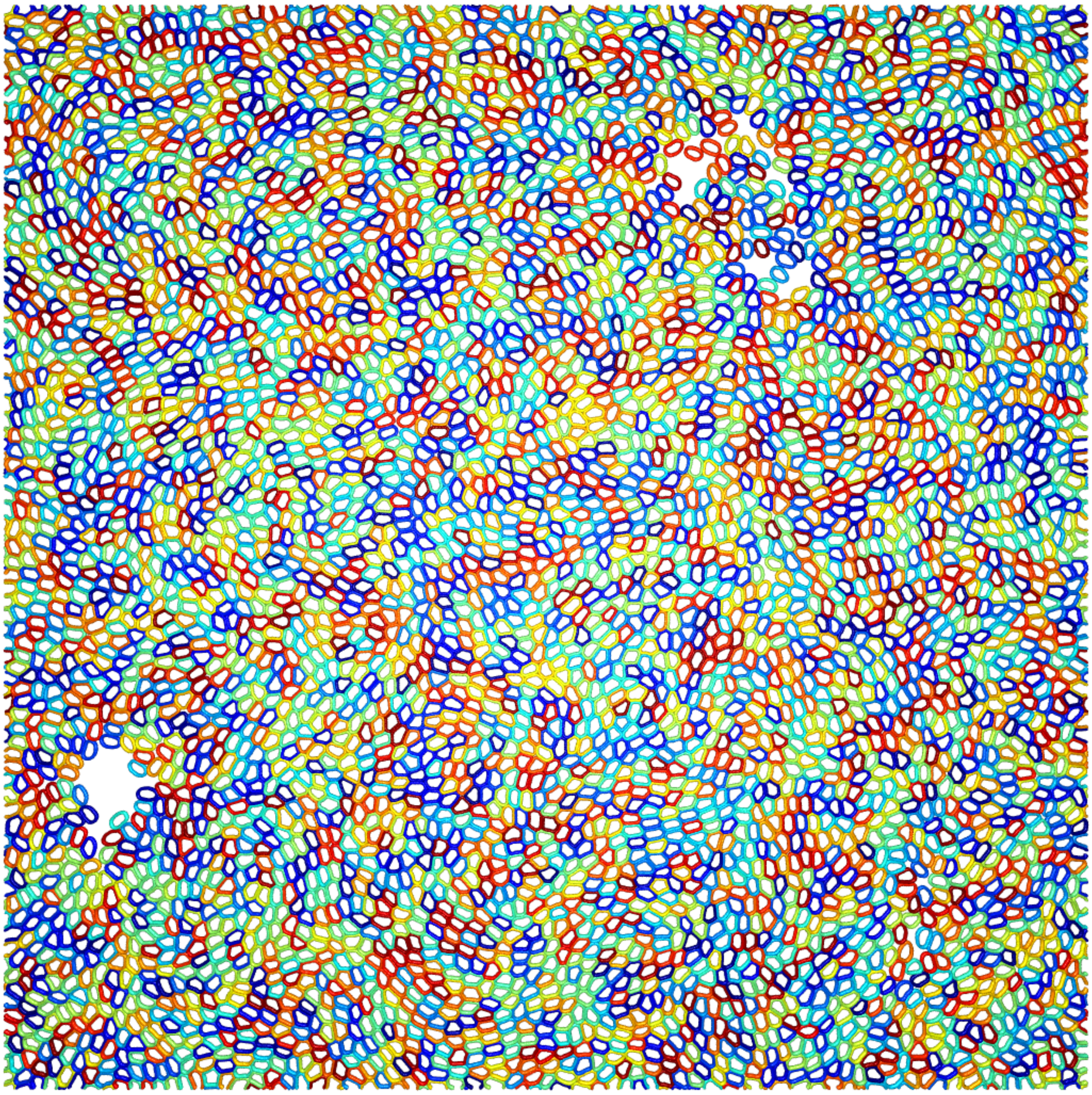

Figure 3.3.: Snapshot of the cell monolayer showing density inhomogeneities due to opening up of gaps. The parameters are $\epsilon/\mathrm{k_B}T = 0.05$, $Pe = 5$, $\kappa_\mathrm{A} = 10$, $\xi_p/R = 3$.

In static structure factor, order is marked by a sharp peak in wavenumbers corresponding to the ordered length scale. We observe peaks on the order of a cell diameter that differ from each other by their broadness. In the disordered states, the peak is very broad. In the well-ordered states, the peak is sharp and has a higher magnitude. Consistently with $g(r)$, decreasing Pe (Fig. 3.2-a), or increasing $\epsilon/\mathrm{k_B}T$ (Fig. 3.2-b), κ_A (Fig. 3.2-d) increases the spatial order and changing ξ_p/R does not lead to a significant change (Fig. 3.2-c).

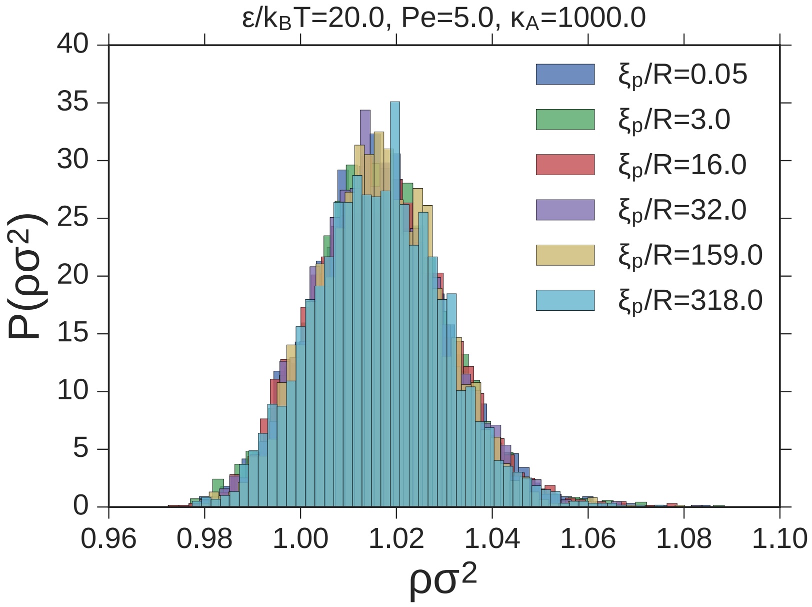

Figure 3.4.: Density histogram for varying ξ_p/R at $\epsilon/\mathrm{k_B}T = 20$, $Pe = 5$, $\kappa_\mathrm{A} = 1000$. Note that the number density of the system is $\rho = 1.015$.

In terms of structure, $g(r)$ and $S(k)$ indicate the existence of two types of structure: An amorphous solid-like ordering and a less ordered dilute liquid type of ordering. Visual inspections of the monolayer reveals that the disordered phases are accompanied with opening up of gaps within the monolayer (Fig. 3.3). This results in dynamics that is similar to motility-induced phase separation, in which dense liquid and gas phases coexist [23]. The ordered phases, on the other hand, are accompanied with minimal density variations. To quantify, we calculate the density histogram. We divide the simulation box into smaller boxes of length $4R$ and make a histogram of the number density inside the boxes. For structurally ordered phases, the density histogram is approximately a Gaussian, centered around the number density of the system ($\rho = 1.015$), indicating a spatially homogeneous distribution of cells (Fig. 3.4).

In order to quantify density inhomogeneities, we calculate the average number of contacting cells. We consider two cells as contacting, if they share a single bead within the interaction range. The average number of contacting neighbours for a cell changes slightly between 5.8 and 6 depending on the parameters (Fig. 3.5-a). Therefore, the number of neighbours does not show a significant variation due to the high density of the monolayer. We then compute the number of surface cells. We consider a cell is to be an ”orphan cell when” it has no connection to a cluster or a ”surface cell” when it is at the perimeter of a cluster, and it has less than or equal to 4 contacting neighbours. Increasing Pe and decreasing $\epsilon/\mathrm{k_B}T$ generates more surface cells, and orphan cells that are detached from the bulk (Fig. 3.5-b).

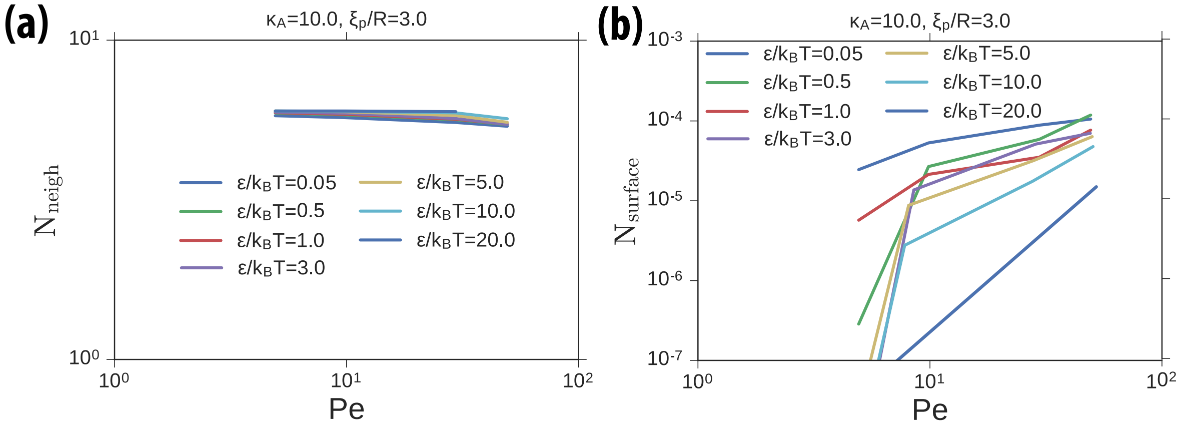

Figure 3.5.: (a) Average number of neighbours, and (b) average number of surface cells as a function of Pe for varying $\epsilon/\mathrm{k_B}T$ at $\kappa_\mathrm{A} = 10$ and $\xi_p/R = 3$.

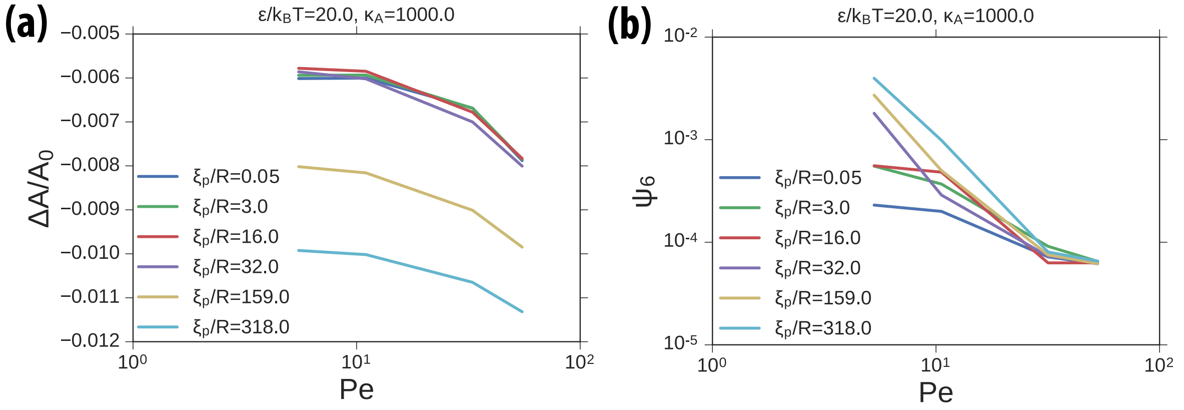

Figure 3.6.: (a) Effective stress $\Delta A/A_0$, and (b) hexagonal order parameter ψ_6 as a function of Pe for varying ξ_p/R at $\epsilon/\mathrm{k_B}T = 20$, $\kappa_\mathrm{A} = 1000$.

Density inhomogeneities are facilitated by compressibility of cells which allows them to adjust their area. Due to the energetic penalty of area changes, the degree of change in cell area is effectively an indicator for the degree of stress on the cell. We calculate this effective stress by $\langle \Delta A\rangle = \langle (A_c(t) - A_0)/A_0\rangle$ where $A_c(t)$ is the area of the cell at time t and A_0 is the initial area of the cell. As the filling ratio is larger than 100%, we find that cells are under compressive stress with a negative sign in ΔA on average. Compressive stress is rather small, that is the average cell area change is minimal. However, the degree of compressive stress increases with increasing Pe and increasing ξ_p/R (The curves become more negative in Fig. 3.6-a). Cells are compressed more as they push stronger against each other with increasing motility forces. With reducing bending rigidity, cells can deform more, which opens up more possibilities for collective motion. As a result, area changes have a wider distribution, both positive and negative, throughout the monolayer resulting in less compressive stress overall at lower bending rigidities.

Cells are found to have on average approximately 6 neighbours (Fig. 3.5-a). This suggests a possible hexagonal bond ordering. We quantify such ordering by calculating the bond order parameter

$$\psi_6 = \frac{1}{6}\left\langle \left| \sum_{j=1}^{6} \mathrm{e}^{i6\theta_{jk}} \right| \right\rangle, \tag{3.3}$$

where θ_{jk} is the bond angle between the center of mass of cell k and its 6 nearest neighbours j. The global hexagonal order is calculated by averaging over all the cells in each time frame. A value of 1 indicates perfect hexagonal bond order, while a value of 0 indicates the absence of hexagonal ordering. For all the parameters, we find a hexagonal order value that is very small $\sim 10^{-2} - 10^{-3}$, indicating the absence of hexagonal ordering. However, the hexagonal order increases with decreasing Pe and increasing ξ_p/R, both of which are indicators of growing structural order (Fig. 3.6-b).

3.3. Dynamics of the Monolayer

Dynamical behaviour of the monolayer is determined by the magnitude and cooperativity of cell displacements. Both of these properties are reflected directly in the displacement field. Therefore, we start by describing the phase dynamics in terms of the displacement field of cells (Fig. 3.7).

The motion of individual cells is constrained by neighbouring cells due to the high density of the monolayer. Fast-moving cells can move independently from each other. Such fast motion with disordered and uncorrelated displacement patterns resembles the dynamics of a gas (see Fig. 3.7-a for the displacement field of the monolayer at $\epsilon/\mathrm{k_B}T = 1$, $Pe = 10$, $\kappa_\mathrm{A} = 10$, and $\xi_p/R = 0.5$). As ξ_p/R increases, cells slow down and correlation length increases. At this regime of intermediate speeds and correlations, cells move in vortices and swirls, which renders a displacement field reminiscent of turbulent motion (see Fig. 3.7-b for the displacement field with increased $\xi_p/R = 159$). As ξ_p/R increases further, cell motion is further restrained. This dramatic slowing down of dynamics corresponds to a jamming phase (see Fig. 3.7-c for the displacement field with increased $\xi_p/R = 318$). Correlations increase towards the system size in the laboratory frame inside the jamming phase.

We thus identify three phases: A gas phase with fast speeds and low correlations, a turbulent phase with fast speeds and strong correlations, and a jamming phase with low speeds and high correlations. Therefore, we can distinguish the jamming phase from the gas phase in terms of the correlations in cell motion, or from the turbulent phase in terms of the cell speeds or the degree of cell motion.

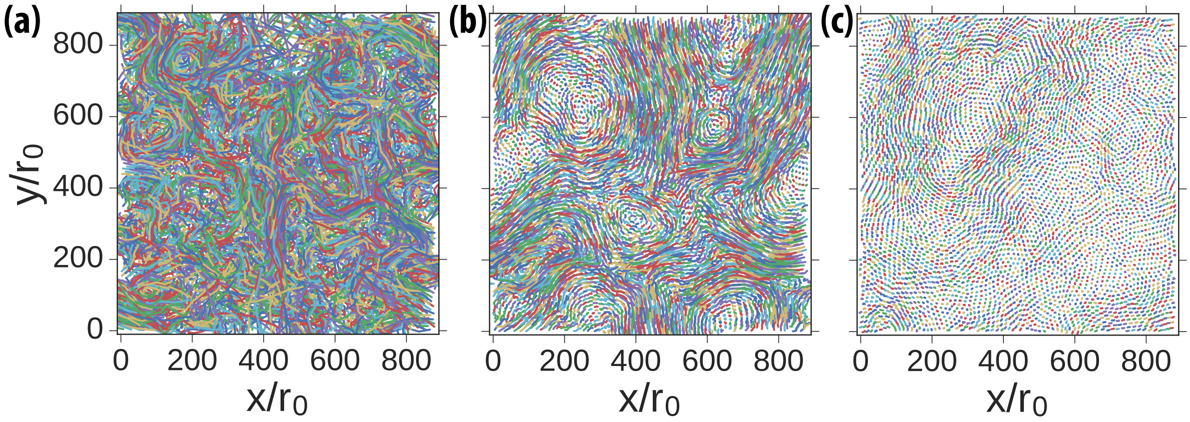

Figure 3.7.: Time trace of the trajectory of the center of mass of cells at $\epsilon/\mathrm{k_B}T = 1$, $Pe = 10$, $\kappa_\mathrm{A} = 10$, for various ξ_p/R: (a) a gas-like phase with $\xi_p/R = 0.5$, (b) a turbulent-like phase with $\xi_p/R = 159$, and (c) a jammed phase with $\xi_p/R = 318$. The trajectory is recorded for a duration of $4\tau_D$.

3.4. Jamming Transition

In glass transition, cooling a viscous liquid rapidly spikes the viscosity of the liquid up to ≈ 17 times higher, while the liquid-like spatial order is maintained [36]. The glass phase is consequently characterized with spatial disorder and extremely high relaxation times. The jamming phase is very similar to the glass phase. The idea of jamming applies to mesoscopic systems, such as colloids, foams, and emulsions. As such, the driving factors behind jamming are different from glass transition [198]. Increasing density, reducing shear forces, or increasing interparticle attractions increases the energy barriers for structural rearrangements in jamming of mesoscopic systems, which then increases the relaxation time. Similar jamming transitions are also observed in active systems [12, 134, 11]. Activity increases the critical density for jamming of hard spheres closer towards the close packing limit [139].

The main characteristic of jamming is the slowing down of dynamics. To quantify, we calculate the mean square displacement (MSD) of cells in the center-of-mass frame of the monolayer

$$\Delta r^2(t) = \frac{1}{N_c}\sum_j (\boldsymbol{\delta r}_j(t+t_0) - \boldsymbol{\delta r}_j(t))^2, \tag{3.4}$$

with $\boldsymbol{\delta r} = \boldsymbol{r} - \boldsymbol{r}_\mathrm{cm}$ and N_c is the number of cells. As cells are strongly adhering to one another in the jamming phase, the whole monolayer appears to move as a single rigid body. To eliminate this finite-size effect, we consider cell displacements relative to the center-of-mass motion of the monolayer. We thus disregard the rigid body degree of freedom by subtracting the drift of the entire monolayer from the individual cell displacements.

In the gas and turbulent phases, cells cover decades more distances in comparison to the jamming phase. Furthermore, inside the jamming phase, cells move subdiffusively (with MSD exponent smaller than 1) at intermediate time scales (corresponding to the crossover regime

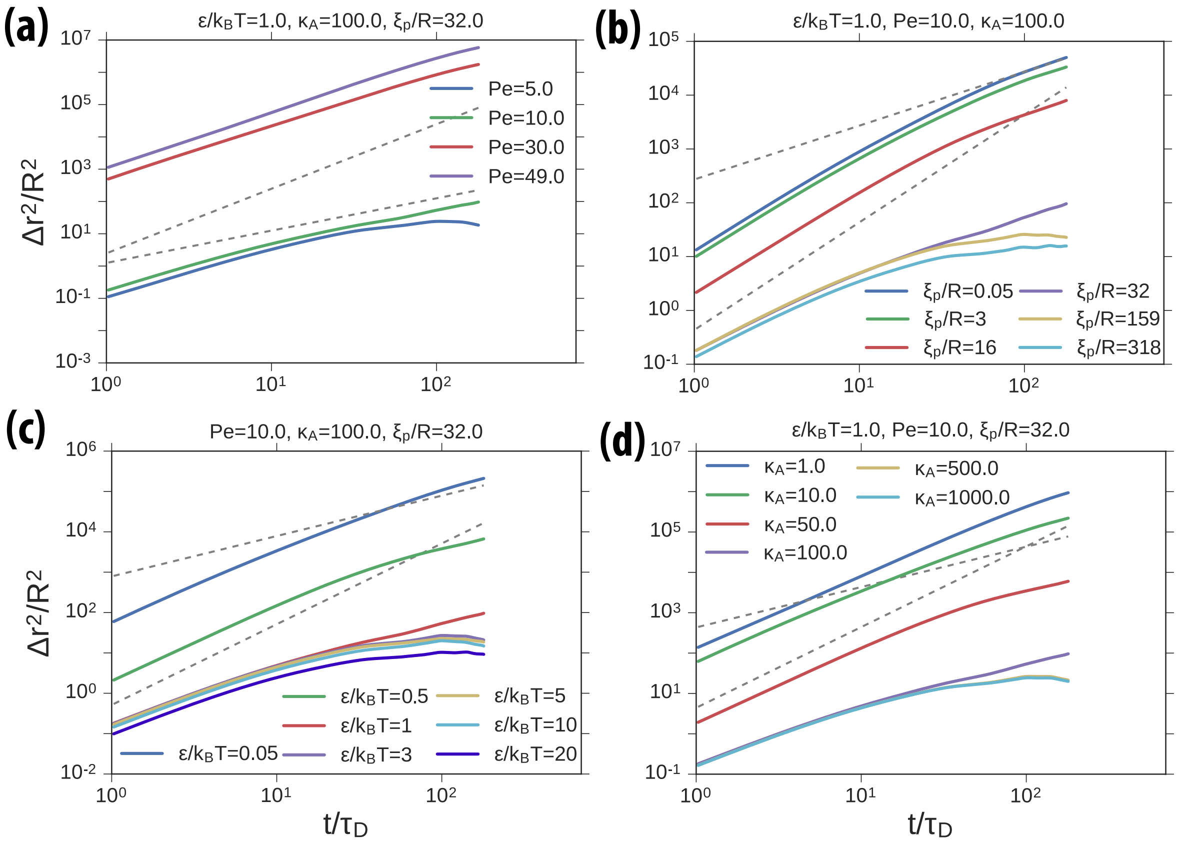

Figure 3.8.: Mean square displacement in the center of mass frame of the monolayer: (a) For varying Pe, (b) for varying ξ_p/R, (c) for varying $\epsilon/\mathrm{k_B}T$, and (d) for varying κ_A. The fixed parameters are chosen as $\epsilon/\mathrm{k_B}T = 1$, $Pe = 10$, $\kappa_\mathrm{A} = 100$, and $\xi_p/R = 32$. The gray dashed lines indicate slopes of 1 and 2, corresponding to diffusive and ballistic motion, respectively.

from an initial ballistic motion to a late-time diffusive motion). Such a subdiffusive plateau also appears in the MSD of binary liquids undergoing glass transition [105]. It indicates the time scale wherein cells are caged by their neighbours. Upon successive cage breaking events, the dynamics turns diffusive in longer-time scales[2]. Gas- and turbulent-like dynamics are marked with superdiffusive motion at the crossover regime with MSD exponents larger than 1.

At low $Pe \sim 5-10$, cells move $\sim 10R$ during $4\tau_D$ and the intermediate time slope of MSD is $\sim 0.7-0.97$. As Pe is increased ($Pe \sim 30-49$), the slope becomes superdiffusive at ~ 1.6 (Fig. 3.8-a). Thus, increasing Pe fluidizes the tissue. Conversely, increasing ξ_p/R slows down the dynamics of the monolayer leading to jamming as ξ_p/R is increased from 0.05 towards 318. At $\xi_p/R = 159-318$, MSD is subdiffusive with a slope of $\sim 0.75-0.8$ (Fig. 3.8-b). Increasing $\epsilon/\mathrm{k_B}T$ makes the cells more sticky, which leads to a jamming monolayer. Cells move subdiffusively for $\epsilon/\mathrm{k_B}T > 1$ with slopes ~ 0.65 – 0.8 (Fig. 3.8-c). Increasing κ_A also jams the monolayer. The monolayer is jammed for $\kappa_\mathrm{A} \geq 500$ with slopes ~ 0.62 (Fig. 3.8-d).

---

[2] Note that we do not simulate the monolayer until we see late-time diffusive motion due to the high computational costs.

Probability distribution of displacements in diffusive motion is Gaussian by the central limit theorem. Non-Gaussian distributions arise in sub- or super-diffusive motion. To identify such non-Gaussian distributions, we turn to the cumulants of displacements $\boldsymbol{\Delta r} = \boldsymbol{\delta r}(t+t_0) - \boldsymbol{\delta r}(t_0)$. The cumulants are defined from the logarithm of the Fourier transform of the displacements [3]. Assuming isotropy, it is given by

$$\begin{aligned} P(k) &= \langle \mathrm{e}^{-i\boldsymbol{k}\cdot\boldsymbol{\Delta r}} \rangle \\ &= 1 - \frac{(\boldsymbol{k}\cdot\boldsymbol{\Delta r})^2}{2} + \frac{(\boldsymbol{k}\cdot\boldsymbol{\Delta r})^4}{24} + O(k^6) \end{aligned} \tag{3.5}$$

where we expanded the exponential in the short wavenumber limit. The odd terms of the expansion vanish due to symmetry. The cosine terms coming from the dot products can be calculated by averaging over a circle, which yields $\langle \cos^2(\theta) \rangle = 1/2$, and $\langle \cos^4(\theta) \rangle = 3/8$ [5]. As a result, the characteristic function is given by

$$P(k) = 1 - \frac{k^2}{4} \Delta r^2 + \frac{k^4}{64} \Delta r^4 + O(k^6) \tag{3.6}$$

and the cumulants are the logarithm of this function:

$$\begin{aligned} \ln(P(k)) &= -\frac{k^2}{4}\Delta r^2 + \frac{k^4}{64}\Delta r^4 - \frac{k^4(\Delta r^2)^2}{32} + O(k^6) \\ &= -\frac{k^2}{4}\Delta r^2 + \frac{k^4(\Delta r^2)^2}{32}\left(\frac{\Delta r^4}{2(\Delta r^2)^2} - 1\right) + O(k^6) \end{aligned} \tag{3.7}$$

where the first term on the right-hand side is the Fourier transform of the displacement distribution for diffusive motion. For Gaussian distributions, cumulants above the second cumulant Δr^2 vanish, leaving only the first term on the right-hand side [56]. As a result, we can use the second term on the right-hand side as a dimensionless indicator of non-Gaussian distributions

$$\alpha_2(t) = \frac{1}{2} \frac{\langle \Delta r^4(t) \rangle}{\langle \Delta r^2(t) \rangle^2} - 1, \tag{3.8}$$

where the subscript indicates that similar quantities can be derived for higher-order moments as well [82, 114]. This dimensionless quantity, known simply as the *non-Gaussian parameter*, is used to identify subdiffusive plateaus in the glass transition literature [105]. For diffusive motion, the mean quartic displacement is $\langle \Delta r^4 \rangle = 2\langle \Delta r \rangle^2$, which yields $\alpha_2 = 0$ [82]. For ballistic motion, $\langle \Delta r^4 \rangle = \langle \Delta r^2 \rangle^2$ (simply from $\Delta r^2 = v_0^2 t^2$), which yields $\alpha_2 = -0.5$.

We expect α_2 to relax to zero as the late-time diffusive regime is approached. However, as we do not reach this regime, it is almost always non-zero as a function of time (Fig. 3.9). Increasing Pe, or decreasing ξ_p/R, $\epsilon/\mathrm{k_B}T$, κ_A is observed to shift α_2 towards the ballistic limit. Going in the opposite direction in the phase space shifts α_2 towards the diffusive limit.

---

[3] See Appendix B for a discussion on characteristic functions and cumulants.

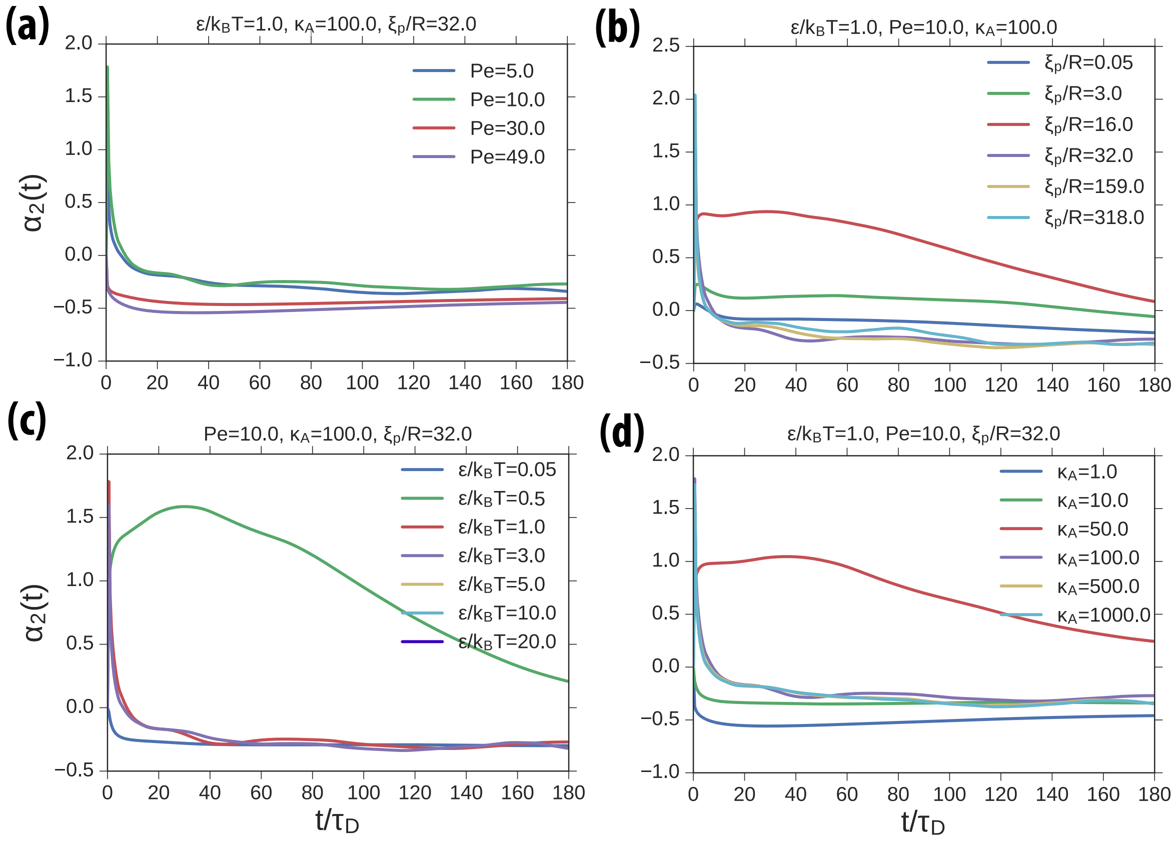

Figure 3.9.: Non-Gaussian parameter $\alpha_2(t)$ as a function of lag time: (a) For varying Pe, (b) for varying ξ_p/R, (c) for varying $\epsilon/\mathrm{k_B}T$, and (d) for varying κ_A. The fixed parameters are chosen as $\epsilon/\mathrm{k_B}T = 1$, $Pe = 10$, $\kappa_\mathrm{A} = 100$, and $\xi_p/R = 32$.

Monolayers deep inside the turbulent phase show a particularly different behaviour of α_2 as a function of lag time with curves staying positive for extended durations ($\xi_p/R = 16$, $\epsilon/\mathrm{k_B}T = 0.5$, and $\kappa_\mathrm{A} = 50$ in Fig. 3.9-b, c, and d, respectively). This indicates the strong deviations of squared displacements from Gaussian distribution inside the turbulence regime.

As indicated in eq. 3.5, the displacement distribution depends on the wavenumber. To quantify this, we calculate the self-part of the intermediate scattering function

$$F_s(k,t) = \left\langle \frac{1}{N_c} \sum_j \mathrm{e}^{i\mathbf{k}\cdot\mathbf{\Delta r(t)}} \right\rangle, \tag{3.9}$$

which characterizes the cell displacements relative to a threshold displacement magnitude. We choose $k = 2\pi/2R$, so that the threshold distance is the average cell diameter. Self intermediate scattering function goes from 1 to 0, as all cells displace an amount that is equal to or larger than $2R$. We can extract a relaxation time scale, that is the time scale over which there are configurational relaxations, by computing the time $F_s(t)$ drops to e^{-1}.

Increasing Pe, or decreasing ξ_p/R, $\epsilon/\mathrm{k_B}T$, κ_A reduces the relaxation time from $\sim 8\tau_D$ to $< 1\tau_D$ (Fig. 3.10). Therefore, in the gas phase, cells rearrange faster than the time it takes

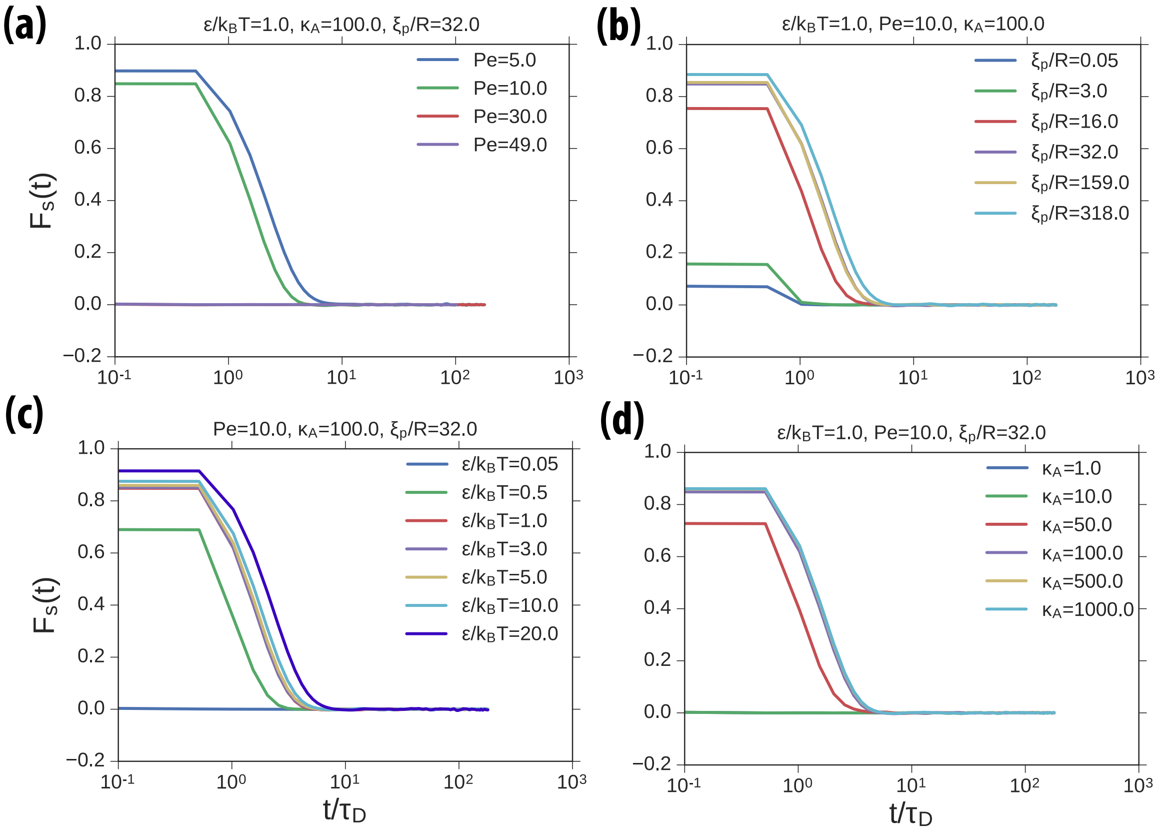

Figure 3.10.: Self-part of the intermediate scattering function $F_s(t)$ as a function of lag time at $k = \pi/R$: (a) For varying Pe, (b) for varying ξ_p/R, (c) for varying $\epsilon/\mathrm{k_B}T$, and (d) for varying κ_A. The fixed parameters are chosen as $\epsilon/\mathrm{k_B}T = 1$, $Pe = 10$, $\kappa_\mathrm{A} = 100$, and $\xi_p/R = 32$.

for a cell to diffuse its own radius. Inside the jamming phase, on the other hand, structural rearrangements take a few diffusive time scales.

One of the characteristics of glass transition is the development of intermediate-time plateaus that indicate the time scale of rattling motion inside cages [105]. We observe similar double-scale relaxations (as can be seen, for example, by comparing $\epsilon/\mathrm{k_B}T = 0.5$ to $\epsilon/\mathrm{k_B}T = 20$ in Fig. 3.10-c). However, instead of flat plateaus, we only observe slopes that become smaller in the intermediate time scales. In this regard, instead of glass transition, the monolayer displays characteristics of *yield stress materials*, like mayonnaise, tooth paste, or paint. When these complex fluids are jammed, they cease moving to a larger extent than glasses. However, under the application of a force larger than a material-specific force threshold, they start flowing rather easily [4] [17]. Therefore, the intermediate scattering function points to a rather sharp transition from the jamming phase to the flowing phase that is similar to a yielding transition [5].

---

[4] The difference between mayonnaise and syrup underlines the properties of yield stress materials in a clear way: Both are fluids that do not flow easily. When a spoon is passed through both of them, the syrup appears like the more viscous fluid. However, when the spoon is out, the syrup will flatten readily whereas the mayonnaise will keep the same shape, making it look like the mayonnaise is the more viscous fluid at

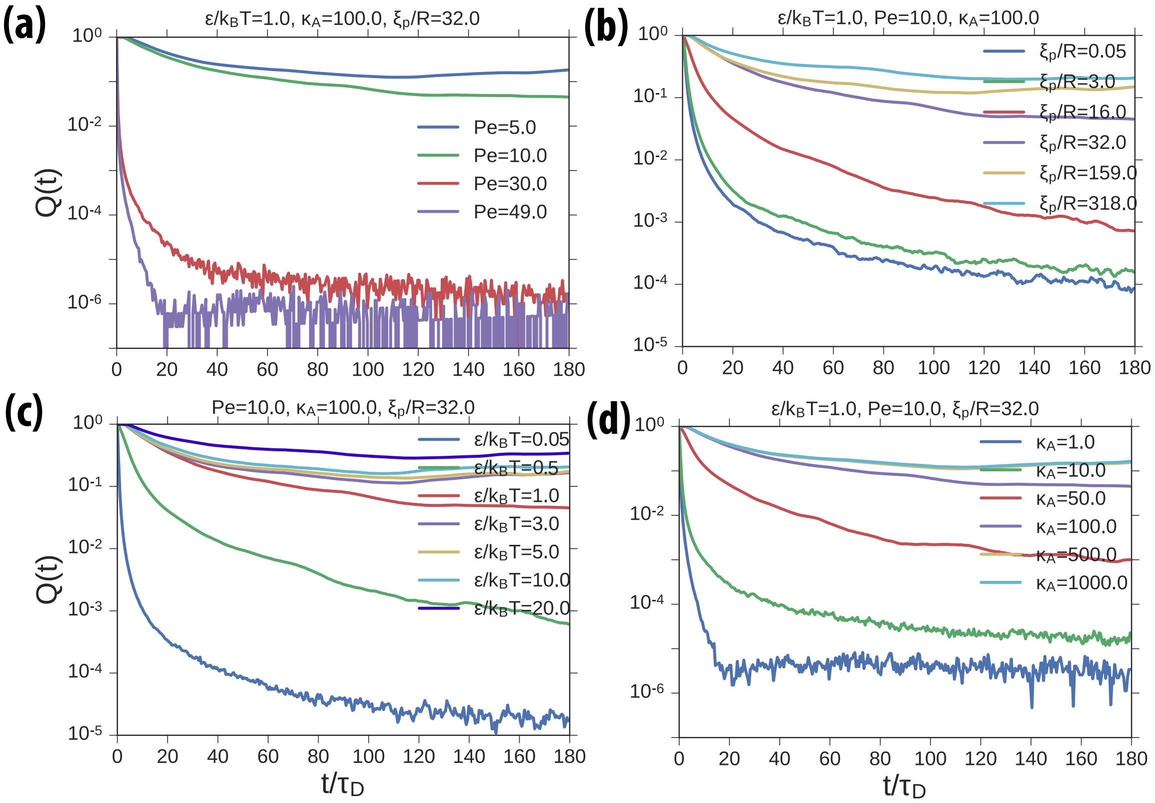

Figure 3.11.: Self-overlap function $Q(t)$ as a function of lag time at a threshold amplitude of $2R$: (a) For varying Pe, (b) for varying ξ_p/R, (c) for varying $\epsilon/\mathrm{k_B}T$, and (d) for varying κ_A. The fixed parameters are chosen as $\epsilon/\mathrm{k_B}T = 1$, $Pe = 10$, $\kappa_\mathrm{A} = 100$, and $\xi_p/R = 32$.

A real-space analogue of intermediate scattering function is provided by the self-overlap function Q

$$Q(t) = \frac{1}{N_c}\sum_j w_j, \tag{3.10}$$

where $w_j = 1$ if $|r_j(t + t_0) - r_j(t_0)| < a$ and $w_j = 0$, otherwise and N_c is the number of cells. The threshold amplitude a is set to the the average cell diameter $2R$. Similar to $F_s(t)$, the self-overlap function Q will go from 1 to 0 as all cells displace an amount that is equal to or larger than $2R$. Therefore, Q measures the degree of overlapping of cell trajectories in time.

---

the longer time scale. The solution to this ”paradox” is that a syrup is a Newtonian liquid with a single viscosity, whereas a mayonnaise is not a fluid, but a yield stress material [17].

[5] In the literature on jamming of cell monolayers, it is often the case that the words jamming and glass-like transitions are used interchangeably. We follow this convention, as our main aim is to identify the motility transitions. However, recent works focusing on the physical nature of these transitions in cell monolayers suggest the existence of a yielding transition instead of jamming [193].

If the cell is staying in the same place, its position is overlapping with its initial position, and thus it will have a higher value of Q. On the contrary, for a cell displacing an amount more than $2R$, Q will vanish.

Increasing Pe, or decreasing ξ_p/R, $\epsilon/\mathrm{k_B}T$, κ_A decreases the overlap function, indicating that cells are displacing more than the average cell diameter (Fig. 3.11). We note that the regimes we identified earlier as the deeply turbulent phases display intermediate level overlapping in between the high overlaps of jamming phases and extermely low overlaps of gas phases (parameters of $\xi_p/R = 16$, $\epsilon/\mathrm{k_B}T = 0.5$, and $\kappa_\mathrm{A} = 50$).

Mean square displacement, intermediate scattering function, and self-overlap function display the slowing-down dynamics aspect of jamming transition in a consistent manner. They all suggest that increasing motility forces, or making the cells more deformable, or decreasing compressibility, or cell-cell adhesions drives the monolayer towards fluidization. However, slow dynamics is not the only aspect of jamming. As the energy barries to break out of cages independently become too high in jamming, it becomes more favourable for cells to rearrange cooperatively. At the thermal limit of $Pe \to 0$, the displacement of one cell faciliates the displacement of others around it, which generates patterns that look like strings [185, 169]. Then the conjecture in thermal limit is that most of the cells are stuck, and the cells that are able to break out, move cooperatively. This is known as the *dynamic heterogeneties* of glass transition. It is *dynamic*, because displacing cells and stuck cells change in time and space. As such, regions of cooperative motion and caging are dynamic.

We quantify the dynamic heterogeneties in the displacement field by calculating the 4-point susceptibility χ_4, which is the variance of overlap function. Since Q measures the degree of stuck cells with respect to displacing cells as a function of time, taking its variance gives the distribution of stuck cells, which is then an indicator of the size of heterogeneties. Thus, when calculated as a function of various displacement times, χ_4 measures the size and rearrangement times of displacement heterogeneties. It is calculated as

$$\chi_4(t) = N_c\big[\langle Q(t)^2\rangle - \langle Q(t)\rangle^2\big], \tag{3.11}$$

where N_c is the number of cells. The peak time and the peak magnitude indicate the rearrangement time and the number of rearranging cells approximately.

Increasing Pe, or decreasing ξ_p/R, $\epsilon/\mathrm{k_B}T$, κ_A homogenizes the displacements, because χ_4 increases (Fig. 3.12). In the regime dominated by heterogenous displacements, approximately 20% of the cells take place in cooperative packs (with a peak magnitude around 1000 cells in a system of 5000 cells). The peak times, corresponding to the rearrangement times of cooperative packs, occur at very early times ($\leq 5\tau_D$) and slightly shift towards $5\tau_D$ as heterogeneous displacements become more dominant.

We characterize the cooperative motion by calculating the velocity correlation function as a function of distance $C_v(r)$

$$C_v(r) = \left\langle \frac{2\delta\mathbf{v}(r+r_0)\cdot\delta\mathbf{v}(r_0)}{\delta\mathbf{v}(r+r_0)\cdot\delta\mathbf{v}(r+r_0) + \delta\mathbf{v}(r_0)\cdot\delta\mathbf{v}(r_0)} \right\rangle, \tag{3.12}$$

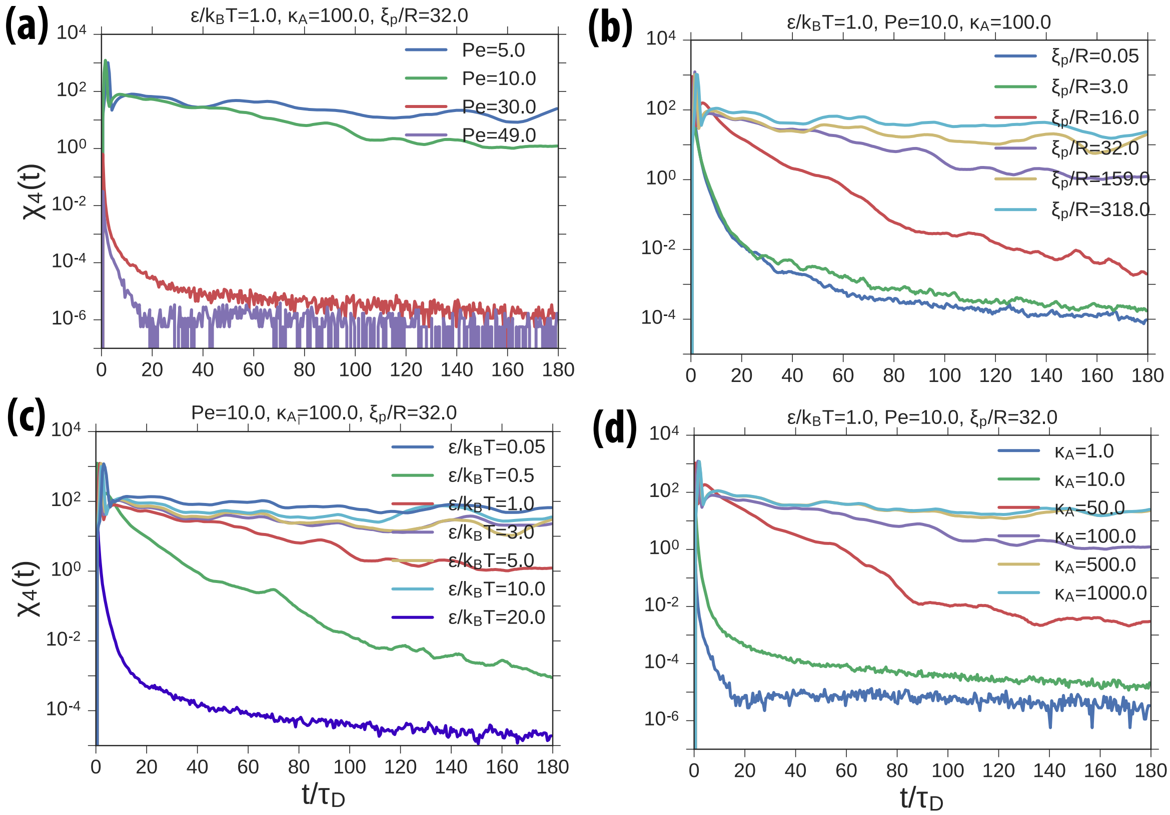

Figure 3.12.: 4-point susceptibility $\chi_4(t)$ as a function of lag time at a threshold amplitude of $2R$: (a) For varying Pe, (b) for varying ξ_p/R, (c) for varying $\epsilon/\mathrm{k_B}T$, and (d) for varying κ_A. The fixed parameters are chosen as $\epsilon/\mathrm{k_B}T = 1$, $Pe = 10$, $\kappa_\mathrm{A} = 100$, and $\xi_p/R = 32$.

where $\delta\mathbf{v}(r_0) = \mathbf{v}(r_0) - \mathbf{v}_\mathrm{cm}$ indicates the cell velocities in the center-of-mass reference frame. A value of 1 indicates polar alignment, −1 antipolar alignment, and 0 corresponds to disorder.

The velocity correlation length increases dramatically from a few cell radii to $\sim 30R$ as Pe is decreased below 30 (Fig. 3.13-a). Furthermore, at high Pe, correlations decay to zero as a function of increasing distance. At low Pe, correlations have a negative tail. This indicates that cells move in opposite directions on average at long distances, pointing to a vortex- or swirl-like flow. At $\xi_p/R = 0.05 - 3$, correlations decay to zero with correlation lengths of ~ 20 cells. As ξ_p/R is increased, the correlations decay to negative values with correlation lengths extended up to ~ 30 cells (Fig. 3.13-b). In case of $\epsilon/\mathrm{k_B}T$, increasing $\epsilon/\mathrm{k_B}T$ beyond 0.05 increases the correlation length from a few cells towards > 30 cells and causes negative correlations at long distances (Fig. 3.13-c). For κ_A, the correlation length is on the order of a few cells for $\kappa_\mathrm{A} = 1$, while higher values show longer correlations with negative tails (Fig. 3.13-d).

Jamming is thus characterized with a significant slowing down of dynamics and a dynamically heterogeneous displacement field in which some cells perform correlated displacements

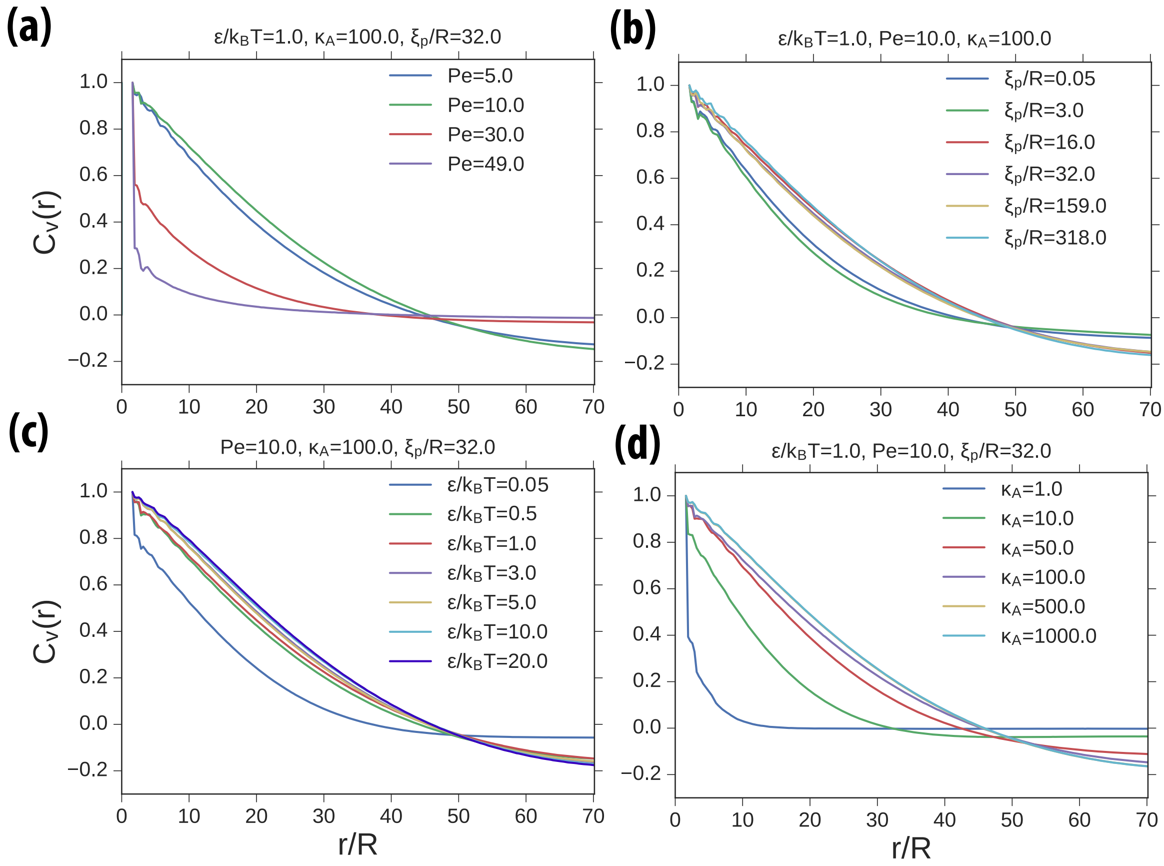

Figure 3.13.: Spatial velocity correlation in the center-of-mass reference frame as a function of distance: (a) For varying Pe, (b) for varying ξ_p/R, (c) for varying $\epsilon/\mathrm{k_B}T$, and (d) for varying κ_A. The fixed parameters are chosen as $\epsilon/\mathrm{k_B}T = 1$, $Pe = 10$, $\kappa_\mathrm{A} = 100$, and $\xi_p/R = 32$.

while some cells get stuck in cages formed by their neighbours. Jamming occurs when the energy barrier for cells to break out of cages becomes too high. Therefore, increasing Pe, or decreasing $\epsilon/\mathrm{k_B}T$, ξ_p/R, κ_A fluidizes the monolayer as each of them facilitate lower energy barriers for rearrangements.

3.5. Active Turbulence

Negative-tailed displacement correlations indicate the possibility of formation of very large vortices or swirls in the jamming phase. As cells are driven out of jamming, the displacement correlation lengths, and thereby the vortex sizes, get smaller until they disappear completely as cells move faster and faster (see Fig. 3.14). The limit of long correlation lengths corresponds to the jamming phase, while that of small correlation lengths is the gas phase. In between these two phases, at intermediate correlation lengths, the collective dynamics is determined with vortex motion, as the number of vortices increases with decreasing correlation lengths.

Such dynamics is reminiscent of inertial turbulence.

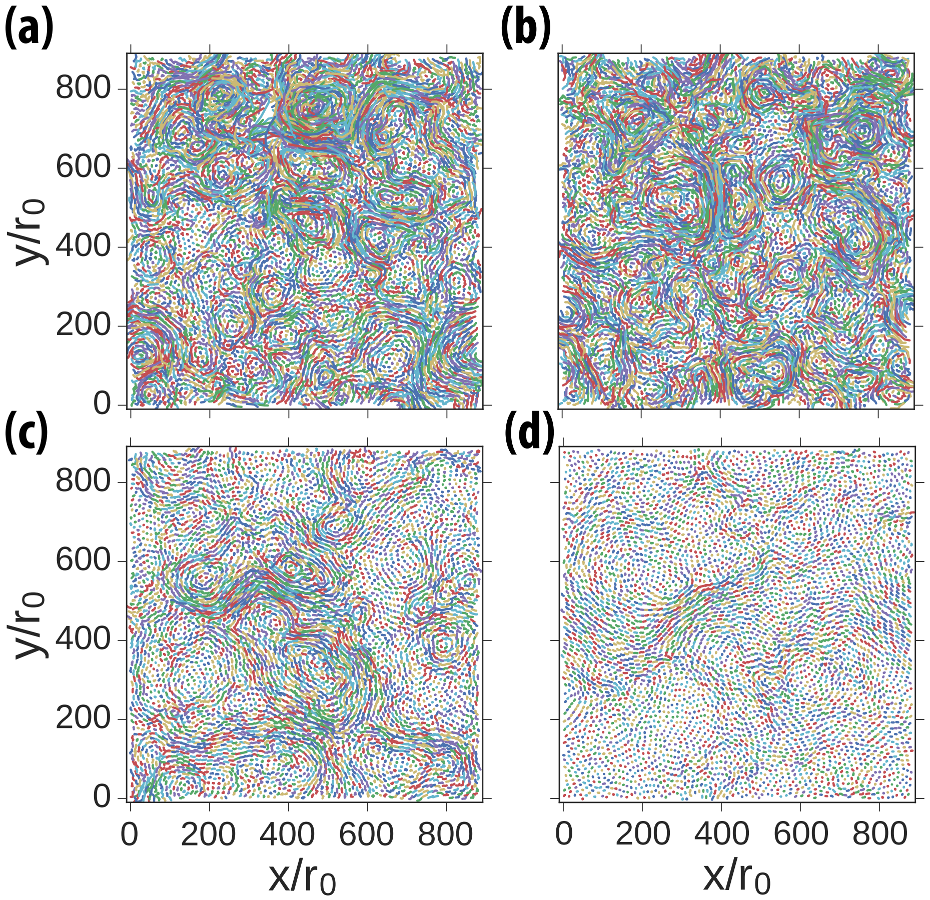

Figure 3.14.: Time trace of the trajectory of the center of mass of cells at $\epsilon/\mathrm{k_B}T = 1$, $Pe = 5$, $\kappa_{\mathrm{A}} = 10$, for various ξ_p/R: (a) $\xi_p/R = 3$, (b) $\xi_p/R = 16$, (c) $\xi_p/R = 32$, and (d) $\xi_p/R = 159$. The trajectory is recorded for a duration of $4\tau_D$.

Turbulence is characterised by occurrence of vortices and swirls. It is based on the idea that at high Re numbers, the length scales over which energy injection and energy dissipation occur are separated. This implies the existence of length scales which are neither affected by energy injection (forcing) nor energy dissipation. These length scales (the so-called *inertial scale*) display universal or self-similar characteristics.

There are multiple differences for cell motion that differ from the assumptions that lead to the characteristic phenomenology of inertial turbulence. Namely, cells move at low Re numbers and the energy injection occurs at the level of a single cell. Both of these differences are overcome by the fact that cells move in a correlated way. The correlation length becomes effectively the length scale of forcing. As a result, the effective Re number (at the length scale of correlations) is higher and the forcing length scale is long compared to the dissipation length scale.

To characterize vortices, we calculate the vorticity $w = \nabla \times \boldsymbol{v}$, which is a pseudo-scalar in 2D.

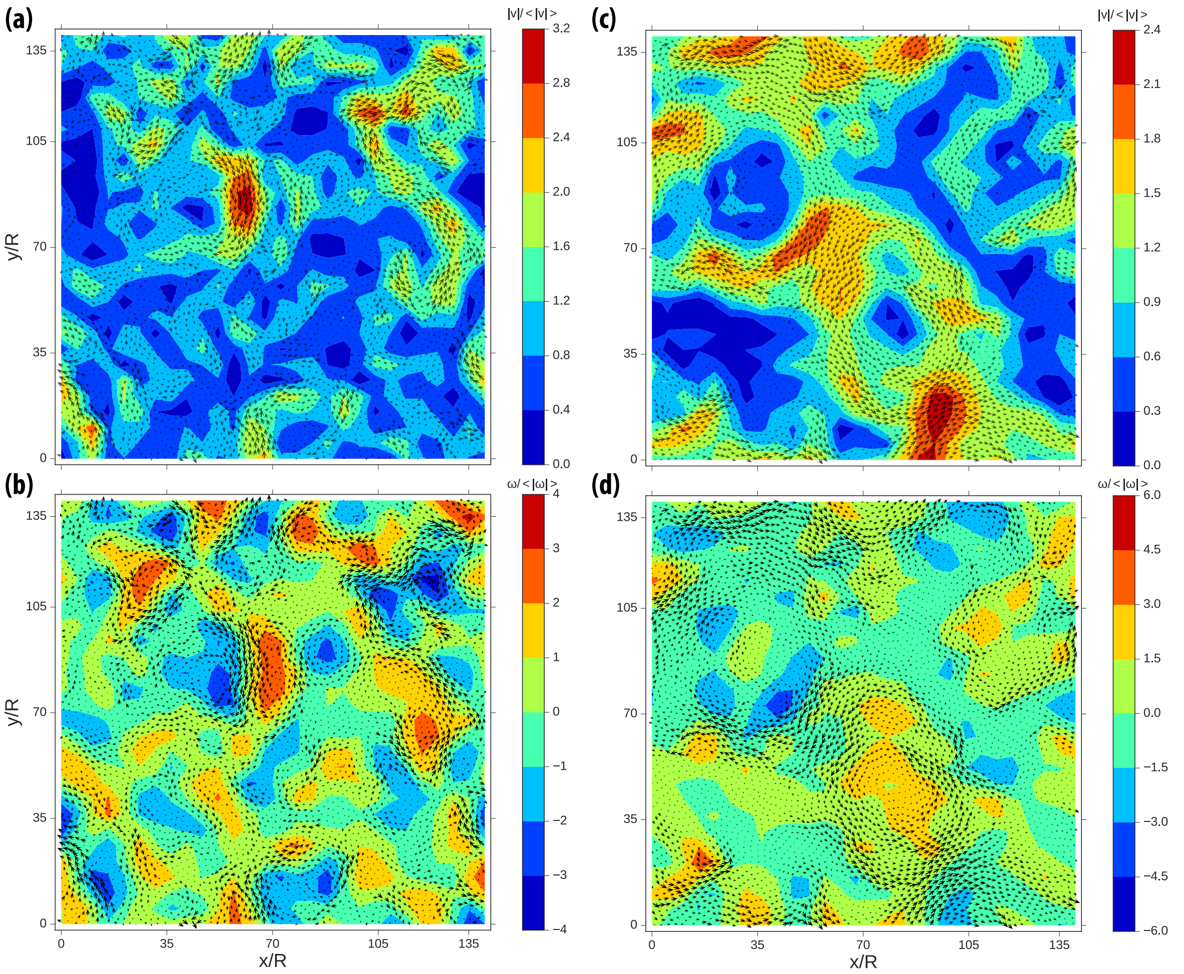

Figure 3.15.: (a) Velocity magnitude field, (b) vorticity field of cells at $\epsilon/\mathrm{k_B}T = 1$, $Pe = 5$, $\kappa_\mathrm{A} = 10$, and $\xi_p/R = 3$ in the turbulence phase. (c) Velocity magnitude field, (d) vorticity field at $\epsilon/\mathrm{k_B}T = 1$, $Pe = 5$, $\kappa_\mathrm{A} = 10$, and $\xi_p/R = 159$ in the jamming phase. The velocity fields are depicted with the black arrows in the background.

To get a smooth velocity field, we take the average of cell velocities inside bins that overlap 75% with the neighbouring bins (which is similar to particle image velocimetry). We calculate the vorticity field by taking the curl of the binned velocities. The resultant velocity magnitude and vorticity fields are depicted in Fig. 3.15. Cell velocities are largely correlated inside the jamming phase with a vorticity map of large vortices. The correlation length decreases, vortex sizes get smaller and their number increases inside the turbulence phase. An important distinction is to note that vortex sizes are heterogenously distributed (Fig. 3.15-b). Thus, the inertial range where motion is expected to be self-similar, is mixed with the forcing length scale. The forcing length scale is also mixed with the energy dissipation length scale due to activity. Therefore, we expect a smaller inertial range in comparison to inertial turbulence.

Velocity and vorticity statistics are different than inertial turbulence due to the heterogenous

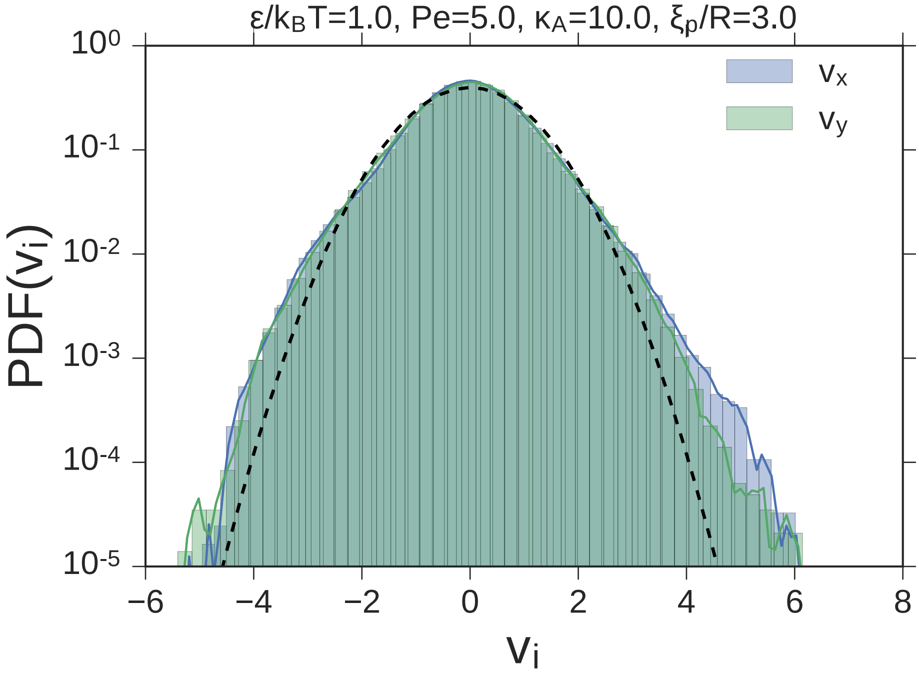

Figure 3.16.: Probability density function for Cartesian components of velocity, $v_i = (v_i - \langle v_i \rangle)/(\langle v_i^2 \rangle - \langle v_i \rangle^2)^{1/2}$. Velocities are calculated inside bins that overlap 75% with the neighbouring bins. The set of parameters, as given in the title, corresponds to the turbulence phase. The dashed black line depicts a Gaussian function with zero mean and unit variance.

distribution of vortex sizes. Unlike in inertial turbulence wherein velocity components are indepedent random variables, we observe a non-Gaussian distribution of Cartesian velocity components with heavy tails in the active turbulence phase (Fig. 3.16). Velocity components display correlations, which can be attributed to the mixed inertial ranges emanating from the heterogeneous distribution of vortex sizes.

The probability density of vorticity is approximately Gaussian inside the active turbulence phase (Fig. 3.17), implying that vorticities are not correlated. We observe similar dynamics to the discrete vortex theory of Onsager with opposite-signed vortices remaining bound together like forming a dipole, while same signed vortices clumping together in time (see Appendix D for a discussion on Onsager phenomenology). However, due to the small system sizes and relatively short accessible simulation times, we do not see signatures of such vortex dynamics in the statistics of velocity components and vorticities.

Active turbulence shares the essential features of two-dimensional inertial turbulence. Intertial turbulence in two-dimensions is characterised by conservation of energy and enstrophy at the same time. The injected energy at the intermediate length scales escapes to longer length scales, while the enstrophy cascades down to the smaller length scales where it is dissipated into heat by viscosity. Energy and enstrophy transfer are coupled. In fact, enstrophy transfer

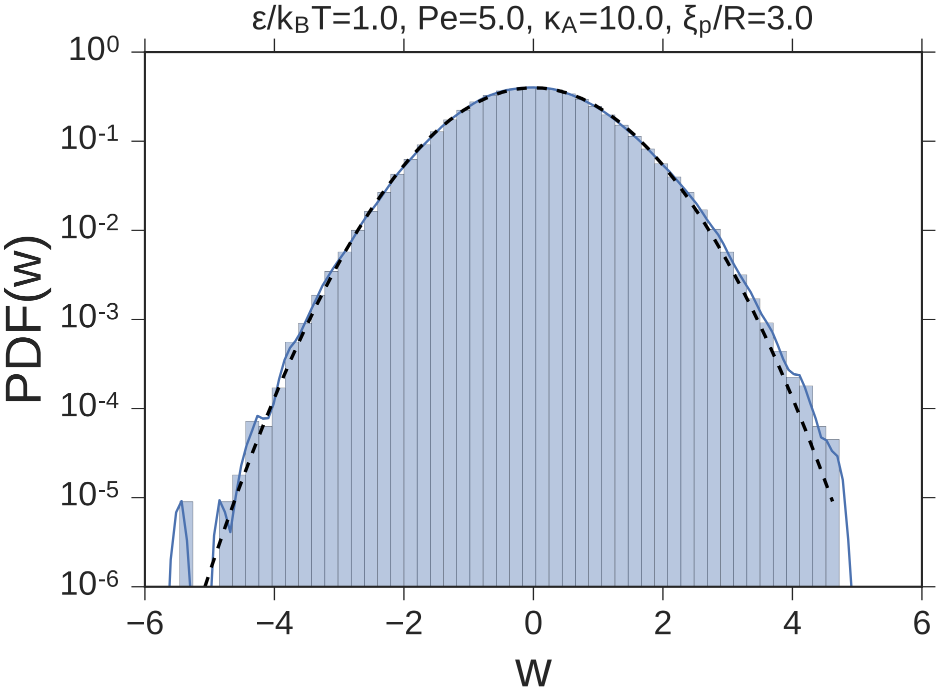

Figure 3.17.: Probability density function for vorticity, $w = (w - \langle w\rangle)/(\langle w^2\rangle - \langle w\rangle^2)^{1/2}$. Vorticities are calculated from binned velocities. The set of parameters, as given in the title, corresponds to the turbulence phase. The dashed black line depicts a Gaussian function with zero mean and unit variance.

over length scales (scaling with $\approx k^2 E(k)$) is faster than energy transfer $E(k)$. Therefore, an increase in energy towards longer lengths caused by forcing, necessitates a reverse enstrophy transfer (see Chapter 2).

The correlation length of cells corresponds to the forcing length scale. According to the phenomenology of 2D inertial turbulence, energy is cascaded up in length from the correlation length to the largest length scale which is half the length of the simulation box with an inverse cascade. The kinetic energy per length scale $E(k)$ from the correlation length to half the simulation box size depends on the energy flux π (with units of energy per unit time and per unit mass), and on the length scale k (with units of inverse length). By dimensional analysis *a la* Kolmogorov, we get the scaling relation of $E(k) = C\pi^{2/3}k^{-5/3}$ for the inverse cascade.

We look for Kolmogorov scaling relations by calculating the kinetic energy spectrum. By Wiener-Khincin theorem, the Fourier transform of spatial velocity correlations gives the kinetic energy spectrum

$$E(k) = \frac{k}{2\pi}\int \mathrm{d}^2\mathbf{r}\mathrm{e}^{-i\mathbf{k}\cdot\mathbf{r}}\langle\mathbf{v}(\mathbf{r}+\mathbf{r}_0)\mathbf{v}(\mathbf{r_0})\rangle, \tag{3.13}$$

which quantifies the accummulation of kinetic energy across length scales [9, 204].

We find that the spectral behaviour changes with the correlation length. We observe three different scaling regimes. At length scales longer than half of the simulation box size, kinetic

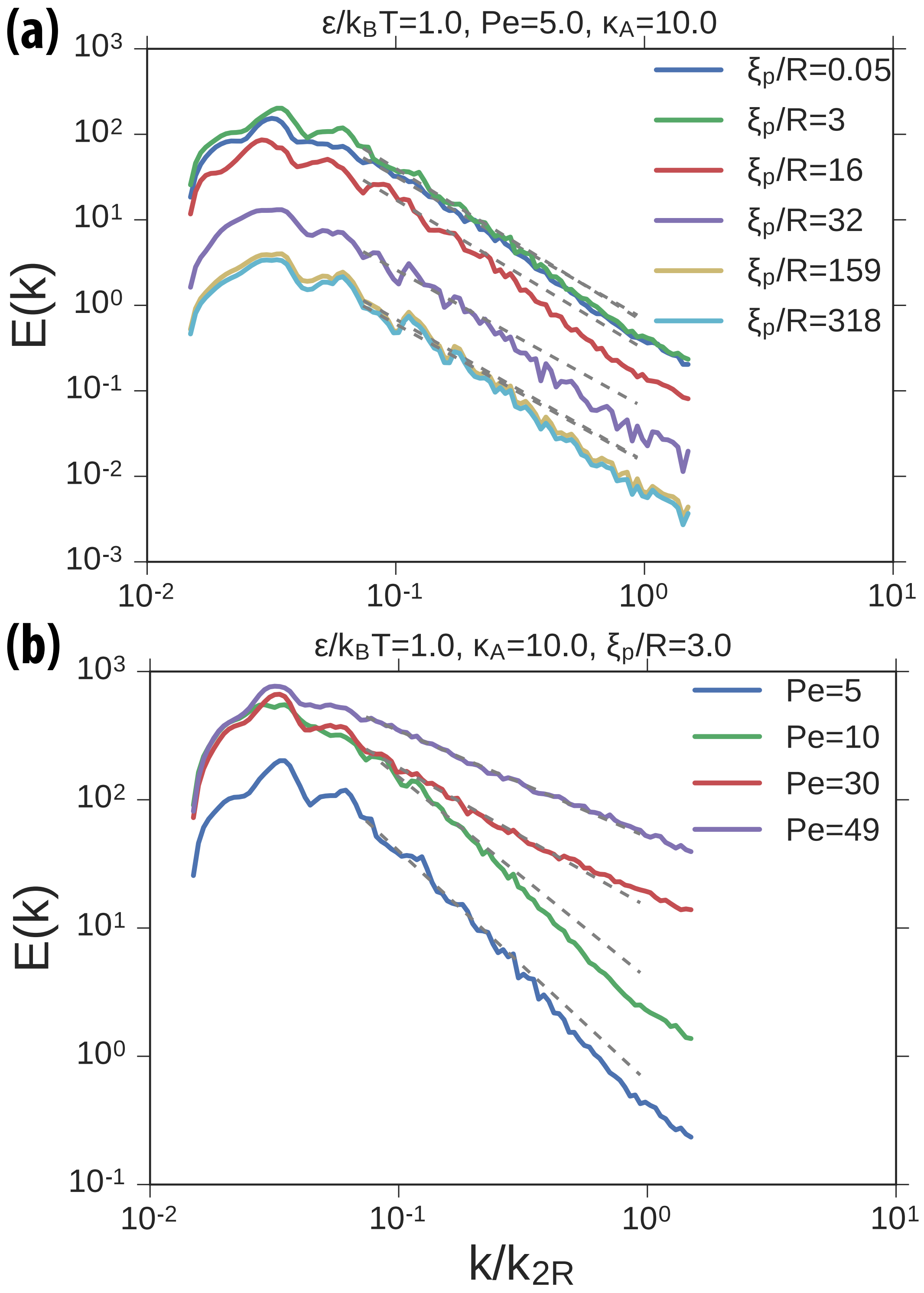

Figure 3.18.: Energy spectrum as a function of wavenumbers: (a) For various ξ_p/R at $\epsilon/\mathrm{k_B}T = 1$, $Pe = 5$, $\kappa_\mathrm{A} = 10$, and (b) for various Pe at $\epsilon/\mathrm{k_B}T = 1$, $\kappa_\mathrm{A} = 10$, $\xi_p/R = 3$. The gray dashed lines are power law fits with slopes as given in the text.

energy increases with increasing k. Since the number of data points is low at this very long regime, we are not able to determine a scaling relation here. From half the simulation box size, where kinetic energy is at maximum, to the correlation length of the system, kinetic energy decreases as $\approx k^{-\alpha}$ with a slope α that is close to $5/3 = 1.66$. The slopes vary from 1.61 to 1.72. These values are similar to the expected inverse energy cascade of Kraichnan-Kolmogorov conjecture. From the correlation length to the average cell radius, the kinetic energy decreases as $\approx k^{-\alpha}$ with a slope α ranging between 2.8 to 3.9, corresponding to the direct enstrophy cascade (which has a slope of 3).

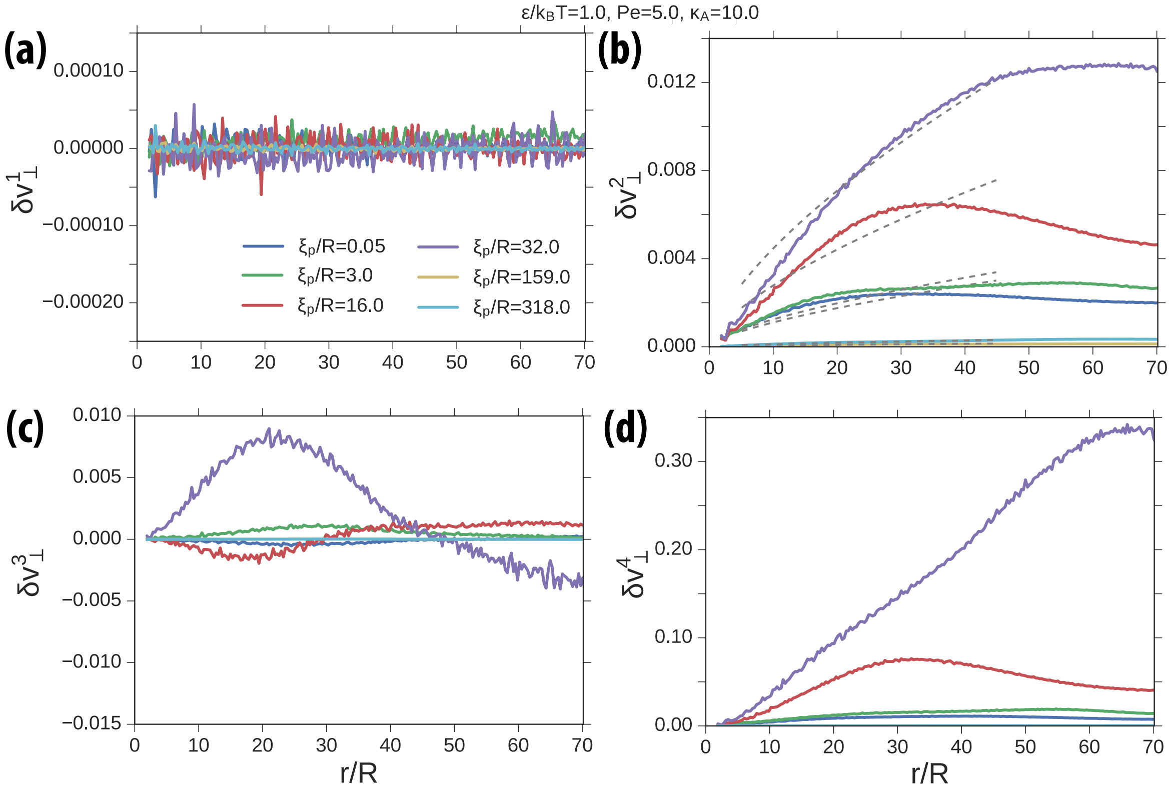

Figure 3.19.: Perpendicular velocity structure functions $(\delta v_\perp)^n$, normalized by $\langle v^2 \rangle^{n/2}$, as a function of distance at $\epsilon/\mathrm{k_B}T = 1$, $Pe = 5$, $\kappa_\mathrm{A} = 10$ for various ξ_p/R: (a) First moment, (b) second moment with gray dashed lines showing power law fits with a power of 2/3, (c) third moment, and (d) fourth moment.

As correlation length is a dynamic parameter that changes with the simulation parameters, the forcing length scale shifts dynamically. Increasing correlation length shifts the forcing length scale towards the smaller wavenumbers. In case of jamming with system-wide correlations, the inverse energy cascade completely disappears as the forcing occurs in the largest length scale of the system. Thus, in jamming, we only see the direct enstrophy cascade with steep slopes (see Fig. 3.18 as a function of increasing ξ_p/R in a, or decreasing Pe in b). The forcing scale shifts towards the higher wavenumbers with decreasing correlation lengths. As a result, in the gas phase, we only see the inverse energy cascade.

In the inverse energy cascade scaling, we get slopes that are close to $-5/3$, but not exactly it. This is because the forcing length scale has a relatively broad spectrum as the correlation length is not uniform.

According to the Kolmogorov phenomenology, the velocity statistics should be universal in the energy dissipation range. The kinetic energy, in the dissipation range, depend on the enstrophy flux η (which has units of $1/t^3$) and the length scale, which leads to a scaling of $E(k) = C\eta^{2/3}k^{-3}$ by dimensional requirements. However, we get a slope that varies broadly in the dissipation regime. This is due to the mixing of the dissipation regime with energy injection of cells at their own length scales.

The main unique property of active turbulence is its self-organizing nature. The cooperative motion of cells generates a self-organized effective forcing length scale, which then renders the turbulent dynamics we observe. However, there are many different aspects of active turbulence in comparison to fully developed inertial turbulence, as we pointed out with the different spectral behaviour. We finish our discussion on active turbulence by comparing its properties further with inertial turbulence.

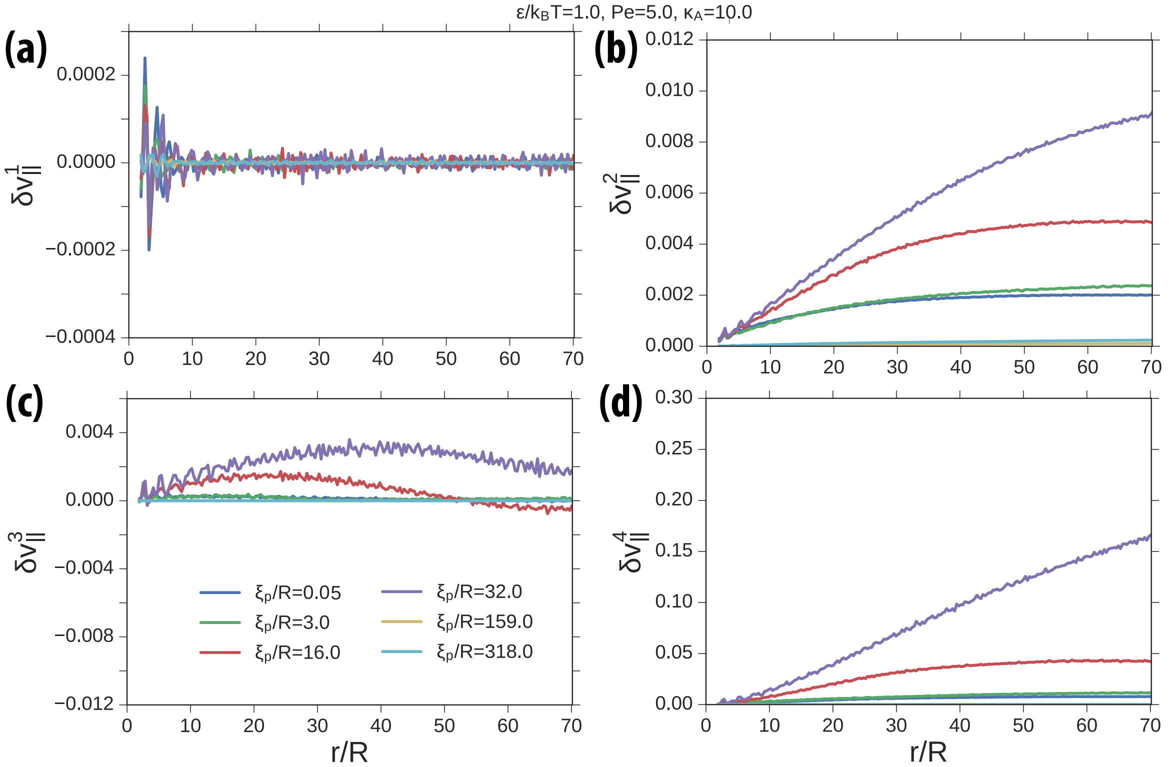

Figure 3.20.: Parallel velocity structure functions $(\delta v_{||})^n$, normalized by $\langle v^2\rangle^{n/2}$, as a function of distance at $\epsilon/\mathrm{k_B}T = 1$, $Pe = 5$, $\kappa_\mathrm{A} = 10$ for various ξ_p/R: (a) First moment, (b) second moment, (c) third moment, and (d) fourth moment.

The Kolmogorov phenomenology can be elucidated in real space via the velocity structure functions from velocity increments $\delta\mathbf{v}(\mathbf{r}) = \mathbf{v}(\mathbf{r}+\mathbf{r}_0) - \mathbf{v}(\mathbf{r}_0)$ that is projected in the parallel or perpendicular direction with respect to the separation vector $\mathbf{r}$,

$$\begin{aligned}(\delta \mathbf{v}_{\|})^n &= \big((\mathbf{v}(\mathbf{r}+\mathbf{r}_0) - \mathbf{v}(\mathbf{r}_0)) \cdot \hat{r}\big)^n \\ (\delta \mathbf{v}_{\perp})^n &= \big((\mathbf{v}(\mathbf{r}+\mathbf{r}_0) - \mathbf{v}(\mathbf{r}_0)) \cdot \hat{T}\big)^n\end{aligned} \tag{3.14}$$

where $\hat{r} = \mathbf{r}/|\mathbf{r}|$, and $\hat{T} = \epsilon_{ij}\hat{r}_j$. ϵ_{ij} is the Levi-Cevita symbol.

The perpendicular velocity structure function signifies the structure of vortices (Fig. 3.19). The first moment of the perpendicular structure functions is close to zero for all ξ_p/R. The maximum of the second moment signals the typical size of the vortices. The second moment of the structure function increases up to the vortex diameter, and then either flattens, or decreases. As we increase ξ_p/R, we go from the gas phase to the turbulence phase, and vortex sizes increases with the maximum of the second moment of the structure function shifting towards longer lengths. As we increase ξ_p/R further, we go form the turbulence phase to the jamming phase, and vortices disappear. This is indicated by a sudden drop in second moment of the structure function. Inside the jamming phase, correlation length of the velocity becomes too large to sustain a vortex, instead within this regime, the movement patterns become swirl-like. In the turbulence phase, the increase of $(\delta v_{\perp})^2$ up to the vortex size follows a power-law behaviour. According to K41 theory, the power law should scale with 2/3 based on dimensional arguments. Just like the scaling relations in Fourier space, the power is slightly different than 2/3 due to the mixed inertial scales in active turbulence.

The third moment of the perpendicular velocity structure function points to heterogeneity of vortex sizes in the turbulence phase. Inside the turbulence phase, the third moment has a maximum or a minimum at half the vortex size, which is due to the formation of vortices at different sizes. The fourth moment is similar to the second moment in behaviour. It grows larger with perpendicular vortex-like correlations between velocities, and then decreases or flattens. When the heterogeneity in vortex sizes grow, the fourth moment increases further in distance in comparison to the second moment before starting to flatten. Although when the flow is dominated by uniformly sized vortices, then the peaks occur in the same distances corresponding to the rather uniform vortex diameter.

The parallel velocity structure functions give information about velocity correlations along the vortices (Fig. 3.20). The first moment is zero by symmetry. The even moments are increasing functions of distance in the turbulence phase, reflecting the parallel-oriented correlations in velocity as we move along a vortex.

3.6. Phase Space

We observe three distinct phases of the monolayer as a function of $\epsilon/\mathrm{k_B}T$, Pe, ξ_p/R and κ_A. The gas phase is characterized with disordered and independent motion of cells. The jamming phase is marked by slowed down motion and long-range displacement correlations. The active turbulence phase is characterized by swirl- and vortex-like motion of cells.

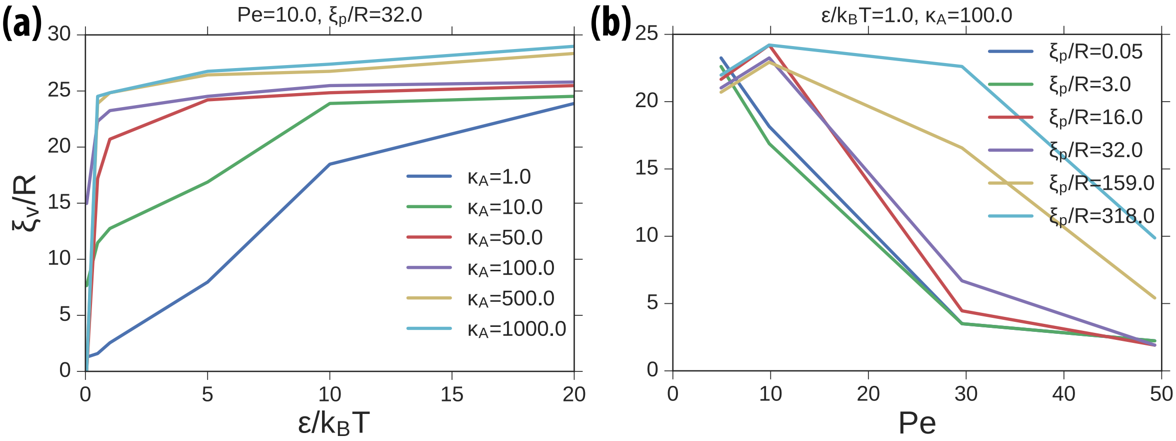

Figure 3.21.: Velocity correlation length ξ_v/R (a) for various $\epsilon/\mathrm{k_B}T$ and κ_A at $Pe = 10$ and $\xi_p/R = 32$, (b) for various Pe and ξ_p/R at $\epsilon/\mathrm{k_B}T = 1$ and $\kappa_\mathrm{A} = 100$.

We can distinguish the jamming phase from the gas and active turbulence phases by looking at the degree of cell motion. Hindered cell motion indicates a jamming state, while fast dynamics correspond to fluid states. Once the jamming phase is identified, we can differentiate the gas phase from the active turbulence phase by looking at the correlation length of displacements. Cells move correlated in the active turbulence phase, while the gas phase is accompanied with uncorrelated motion.

The correlation length is on the order of a few cell radii ($< 5R$ approximately) in the gas phase. Correlation lenghts that are larger than $5R$ correspond to jamming and active turbulence phases. There is not a significant difference between the jamming and turbulence phases in terms of the correlation length. The gas phase occurs at low $\epsilon/\mathrm{k_B}T$, κ_A, ξ_p/R and high Pe. We choose intermediate regimes of each of these parameters at $\epsilon/\mathrm{k_B}T = 1$, $Pe = 10$, $\kappa_\mathrm{A} = 100$, $\xi_p/R = 32$ and study the phase dynamics as a function of these parameters individually. This analysis reveals that the gas phase occurs only at very low $\epsilon/\mathrm{k_B}T$ ($\epsilon/\mathrm{k_B}T < 5$) and κ_A ($\kappa_\mathrm{A} < 10$). Correlation lengths increase from the order of a few cell radii to $29R$ with increasing $\epsilon/\mathrm{k_B}T$ and κ_A (Fig. 3.21-a). The gas phase occurs at $\xi_p/R < 32$ and $Pe > 30$. Increasing ξ_p/R and decreasing Pe increases the correlation length towards $25R$ (Fig. 3.21-b).

To distinguish the jamming phase from the active turbulence phase, we calculate the intermediate-time exponents of the mean square displacement, which reveal the degree of motion in comparison to diffusive motion. An exponent of $\alpha > 1$ indicates superdiffusive motion, $\alpha < 1$ indicates subdiffusive motion, while $\alpha = 1$ is diffusive motion. We consider the monolayer as jammed when $\alpha < 0.92$. Jamming takes place for $Pe < 20$. Increasing Pe fluidizes the monolayer. Increasing ξ_p/R hinders cell motion, decreasing α from 1.2 to 0.9, thus leading to a jamming transition from a fluid state (Fig. 3.22-a). Increasing $\epsilon/\mathrm{k_B}T$ decreases α from 1.63 to 0.2 causing a jamming transition along the way, while decreasing κ_A from 1000 to 1 increases α from 0.8 to 1.56 leading to fluidization from a jammed state (Fig. 3.22-b). Therefore, decreasing $\epsilon/\mathrm{k_B}T$ and decreasing ξ_p/R fluidizes the monolayer.

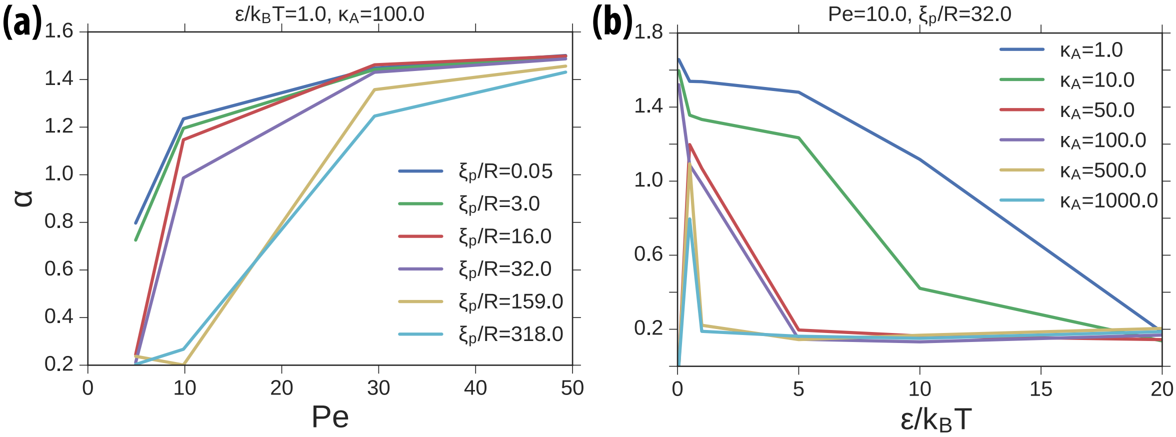

Figure 3.22.: Intermediate-time exponents of mean square displacement α (a) for various Pe and ξ_p/R at $\epsilon/\mathrm{k_B}T = 1$ and $\kappa_\mathrm{A} = 100$, (b) for various $\epsilon/\mathrm{k_B}T$ and κ_A at $Pe = 10$ and $\xi_p/R = 32$.

3.7. Discussion

Non-motile epithelial cells can become motile with a biological trigger during embryonic development, cancer metastasis and wound healing. Despite the underlying biological origin, motility transitions are also physical events at their core. The properties of each motility phase and the transition between these phases are both similar to their counterparts in inert matter and at the same, they are also unique in that there can be novel properties of these phases with novel triggering mechanisms. Therefore, the study of motility transitions offers an interesting perspective into the jamming transition and fluidization of inert matter at the mesoscale.

The gas phase consists of fast-moving cells performing uncorrelated motion. In this phase, the correlation length is smaller than 5 cell radii and as a result, cells move to a large degree independently from each other leaving behind a disordered trajectory pattern. The degree of cell motion is largest in the gas phase. Small gaps occur across the monolayer, akin to motility-induced phase separation, as cells are compressed.

As the correlation length increases, cells form vortices and swirls. Such displacement patterns are reminiscent of inertial turbulence, despite cells operating at a low Re regime. In this regime, inertia, an essential ingredient of turbulence, is neglected over high viscosity. We observe turbulence in regimes of Peclet number Pe as low as 5. With a Schmidt number $Sc = \nu/D = 30$, we have a Reynolds number of $Re = 0.16$, which points to a regime where viscosity dominates over inertia. However, once we consider correlations in cell motion, with a typical correlation length of 15 cells, Pe increases 225 times, which increases Re to 36 locally at the correlation length scale. Therefore, even though single cells operate at low Re, due to the cooperative motion Re could increase to a level where turbulence sets in.

Active turbulence is different from inertial turbulence in the mechanism of energy injection.

In inertial turbulence, an external forcing is assumed to take place in a narrow length spectrum. In contrast, cells move through internal means which corresponds to an energy injection at the level of a single cell in active turbulence. In addition, cells move correlated in a multitude of length scales which mixes the length spectrum further. Therefore, we have multiscale forcing in active turbulence, which sets a contrast with inertial turbulence.

Active turbulence and inertial turbulence are similar on a phenomenological level. The dynamics in both cases is determined by the simultaneous conservation of energy and enstrophy in $2D$. Enstrophy transfer scales with k^2 times the energy transfer $E(k)$. Thus, to conserve both quantities at the same time in $2D$, they should be transferred towards opposite length scales. Kinetic energy increases towards the larger length scales (small wavenumbers), while enstrophy is transferred down to smaller length scales (large wavenumbers). According to the Kolmogorov-Kraichnan phenomenology of $2D$ inertial turbulence, kinetic energy spectrum scales as $k^{-5/3}$ for energy injection scales and as k^{-3} for enstrophy transfer scales. We find similar exponents for directly energy cascade that are only slightly different from their inertial counterparts due to the multiscale mixing. The enstrophy transfer scaling is found to be especially different from k^{-3} due to stronger mixing at smaller scales.

As the correlation length determines the scale of forcing, the enstrophy transfer is shifted towards larger length scales with increasing correlation lengths. Once the correlation length is increased to system size, energy escapes to the largest length scales (which is half the simulation box length) and the entire dynamics is dominated by enstrophy transfer.

In terms of displacement patterns, jamming and active turbulence phases are somewhat similar in formation of vortex- and swirl-like patterns. This is due to the escape of energy towards long length scales in both systems. The main distinguishing feature of jamming phase is instead the significant slowing down of dynamics. The degree of cell motion is dramatically lowered in the jamming phase as cells become caged by their neighbours.

We observe that, starting from a jamming phase, increasing cell motility (set by the strength of motility force) and decreasing cell-cell adhesion (set by the Lennard-Jones interaction strength), deformability (set by the bending rigidity), and area fluctuations (set by the area compression modulus) fluidizes the tissue. This fits well with the current jamming phase diagram of inert and living matter [168]. Our model, thus, has the advantage of producing the jamming transition independently as a function of these four parameters related to mechanical properties of single cells. In addition, we predict a new pathway for the motility transitions in deformability of cells. Making the cells more deformable fluidizes the tissue. Therefore, deformability acts as a source of energy injection effectively.

Cell deformability measurements (using microfluidics and atomic force microscopy) revealed that malignant breast cells have a significantly lower Young's modulus than non-malignant breast cells [116, 83]. Therefore, cancer cells might be softer (that is, more deformable) than their healthy counterparts. In light of our findings, this may be rationalized by the argument that softer cells lead to a disordered, fluid-like tissue where more migrations occur.

Cells change volume during self-propulsion via actomyosin contraction. Single-cell volume fluctuations of amplitude 20% and timescale of 4 h are observed *in vitro* for MDCK cells and zebrafish primordial germ cells [184, 214]. It has recently been shown that volume fluctuations can lead to collective motion [193]. In our model, increased area fluctuations due to reduced bending rigidity, or area compression modulus lead to fluidization.

In between the jamming and the gas phases, we predict an active turbulence phase. A turbulent phase is very recently observed in experiments on epithelial cell monolayers in quasi-$2D$ geometries [101, 171]. In these experiments, the turbulent dynamics is dominated by half-integer topological defects, which point to a picture of epithelial tissue as a nematic medium. In our simulations, we used polar cells, which create turbulent dynamics with vortices (+1 defects). Therefore, it may be possible to observe active turbulence dominated by vortex formation for cells with smaller aspect ratio, *i.e.*, lower nematic symmetry. Half-integer defects are observed for relatively high aspect ratio cells such as spindle-shaped cells (like smooth muscles cells, sarcomas and mouse embryo fibroblasts) and Madin-Darby canine kidney cells [101, 171, 48]. For smaller aspect ratio cells, like endothelial cells (which line the blood vessels), long-range and long-lived vortices occur as cell divisions act as local sources of energy injection stirring the fluid [167]. Similarly, cancerous human breast epithelial cells are observed to have high vorticities, as divisions of cancer cells act effectively as energy injection [207]. However, the vortex sizes are much smaller for cancer cells in comparison to the vortices observed in healthy endothelial cells.

3.8. Summary

Inspired by motility transitions in epithelial cell monolayers, we studied the collective cell motility in $2D$ by modelling a single cell as an active vesicle. We identify gas, active turbulence and jamming phases in terms of the degree and correlations of cell motion and map the phases to individual cell parameters. Increasing cell motility (measured by Peclet number Pe) and decreasing cell-cell adhesion (measured by pair interaction strength $\epsilon/\mathrm{k_B}T$), area fluctuations (measured by area compression modulus κ_A), and deformability (measured by the thermal persistence length ξ_p/R) fluidizes the tissue. As such, we pin the motility transitions down to mechanical properties of cells. Our results are in agreement with the current findings of jamming transition in inert and living matter. In addition, we predict that deformability could lead to motility transitions and an active turbulence phase dominated by vortices.

4. Collective Dynamics of Self-propelled Semiflexible Filaments

4.1. Introduction

Living systems often self-organize into functional structures by consuming energy. Biopolymers and filamentous objects like actin filaments, microtubules and slender bacteria exhibit particularly interesting examples of self-organization [100, 109, 125, 32, 165, 136, 158, 54, 162], as their extended nature makes the collective dynamics inherently complex. Microtubules display loops when gliding on motility assays of kinesin-1 motors [119] or on dynein-coated surfaces confined at an air-buffer interface [95]. Likewise, large-scale vortices of microtubules on dynein carpets emerge due to inelastic collisions [182, 91]. Actin filaments self-organize into swirls at high densities when propelled by immobilized heavy meromyosin molecular motors in a planar geometry [174]. Besides these cytoskeletal filaments, other filamentous objects like slender bacteria [117] and synthetic particles such as vibrated granular rods are also found to self-organize into swirls [15, 111]. Understanding how these structures emerge from the underlying dynamics could shed light on their function. Cytoplasmic streaming of microtubules in the cortical arrays of plant cells provides an example, where the organization of microtubules into a swirl provides function in furnishing cell-wall growth [25]. This type of self-organization can also play a useful role in micro- and nano-technology such as in nanofabrication and in drug delivery [80], in addition to its biological function.

Theoretical studies of active and flexible filaments have investigated different ways of invoking activity [88, 90, 92, 94, 93, 97, 52, 53, 102]. Activity, introduced as colored noise acting tangentially on a single filament, is shown to result in a net longitudinal drift of the filament accompanied by anomalous diffusion [120]. In an ensemble of filaments with active colored noise acting over the normal direction of the bonds, the collective dynamics is observed to become superdiffusive with increasing levels of activity [64]. Such activity-caused anomalous diffusion can be rationalized with effective-temperature models [123, 124].

Here we study the collective behaviour of self-propelled semiflexible filaments with a focus on self-organization and dynamical pattern formation. We employ the self-propelled worm-like chain model, introduced recently to study the dynamics of a single semiflexible filament [88, 90]. The self-propulsion is introduced as a constant magnitude force acting homogenously in the tangential direction along the contour of the filament. The effect of self-propulsion has been shown to differ markedly for rigid and flexible filaments. It drives the rigid filaments into a directed translational motion; in contrast, it leads to an increase of rotational diffusion for flexible filaments. Furthermore, longer filaments that are strongly propelled form stable spirals at low rigidities [88]. For a dilute suspension, we find that filaments cluster with increasing propulsion. Rigid filaments behave almost like rods, forming large clusters at intermediate propulsion. However, as propulsion increases, flexibility starts to play a role, and clusters break apart into smaller and highly motile clusters. At low rigidity filaments coil up into a gas of isolated spirals if propulsion is sufficiently strong, as expected from single filament dynamics.

4.2. Single Filament Dynamics

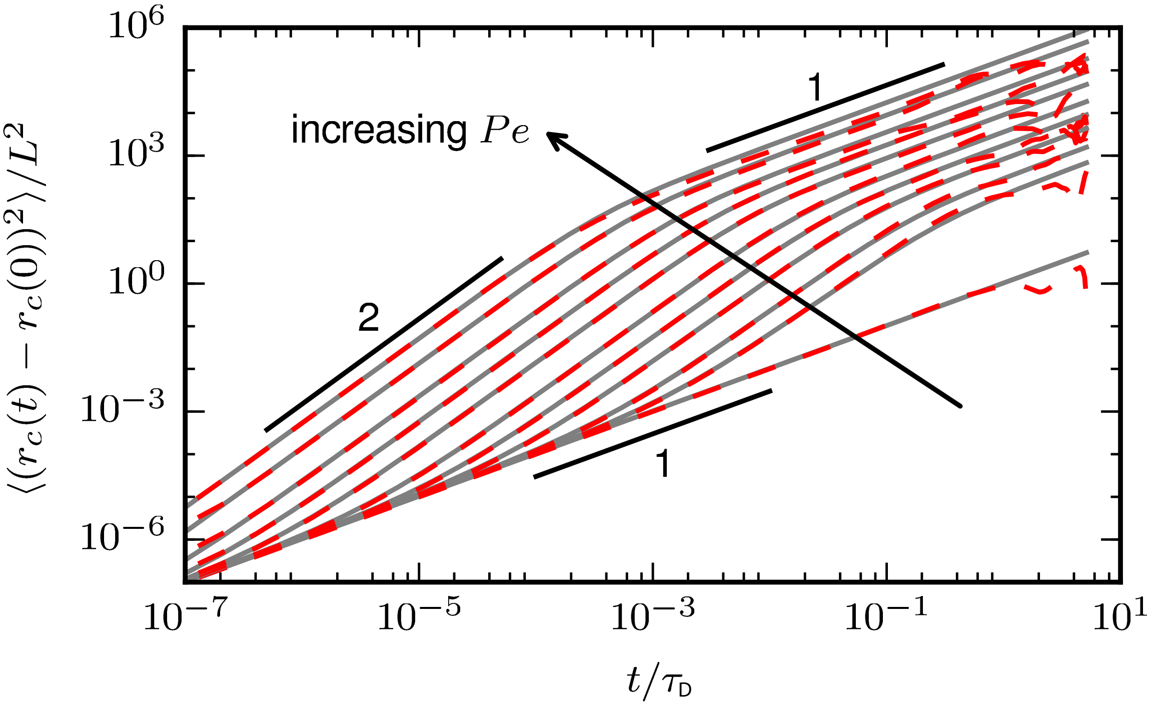

Figure 4.1.: Mean square displacement of the center of mass of filament at $\xi_p/L = 4$ with increasing Pe from 0 to 10^5. Dashed colored lines are the simulation results. Gray solid lines are the theoretical predictions as defined in eq. E.5. Adapted from ref. [87].

Structural and dynamical properties of a single filament is determined by the strength of self-propulsion characterized by Peclet number $Pe = f_p L^2/\mathrm{k_B}T$, and the stiffness characterized by the dimensionless thermal persistence length $\xi_p/L = \kappa/\mathrm{k_B}TL$. We find that two other parameters related to the shape of the filament play a role. The aspect ratio $a = L/\sigma$ characterizes the extension of the filament in its long axis. Furthermore, discretization, defined by the number of monomers making up the filament, characterizes the degree of polymerization.

At large ξ_p/L and low Pe, an individual filament has an elongated structure that resembles a passive filament or a rigid rod in shape. Increasing Pe drives the filament along its contour into a directed translational motion. In this regime, the dynamics of the filament, as determined from its center of mass motion, is analogous to the motion of a single active point particle with matching mean square displacements (see eq. E.5 and fig. 4.1). Filament motion thus can be characterized with an effective translational diffusion coefficient with $D_t' = D_t + v_c^2/2D_r^2$. The relation $v_c = f_p/\gamma$ indicates that the translational diffusion of the filament is enhanced due to active forces f_p.

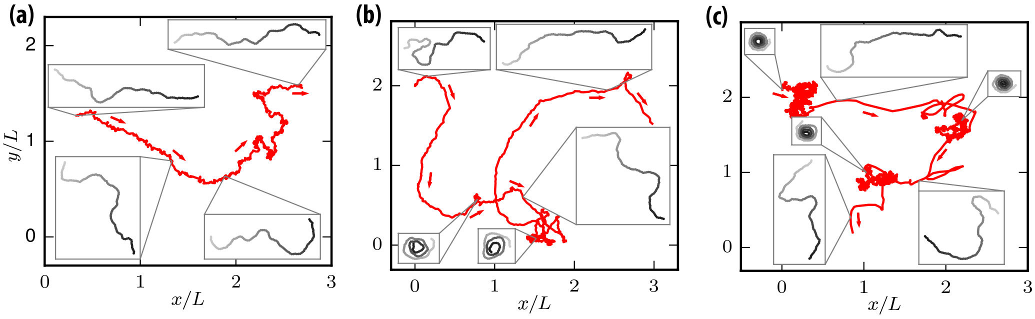

Figure 4.2.: Filament trajectories with shapes in the inset, for filaments at $\xi_p/L = 0.2$, $a = 100$, and changing Pe: (a) Polymer regime for a filament at $Pe = 200$. (b) Weak spiral regime at $Pe = 1000$. (c) Strong spiral regime at $Pe = 5000$. Adapted with slight modifications from ref. [87].

Active forces enhance the filament dynamics when the dynamics is reduced to center of mass motion. However, activity also alters the effective persistence length of the filament. The persistence length determines the decay of tangent-tangent correlations along the filament. The unit tangent vector can be written as the sum of tangent vectors of bonds along the filament

$$\hat{t}_e(t) = \frac{1}{L}\int_0^L \hat{t}(s(t))\mathrm{d}s, \tag{4.1}$$

The autocorrelation then becomes,

$$\begin{aligned}\langle \hat{t}_e(t)\cdot\hat{t}_e(0)\rangle &= \frac{1}{L^2}\int_0^L\int_0^L \mathrm{d}s'\mathrm{d}s\langle \hat{t}(s(t))\cdot\hat{t}(s'(0))\rangle \\ &= \frac{1}{L^2}\int_0^L\int_0^L \mathrm{d}s'\mathrm{d}s\exp\big(-(s+v_ct-s')/\xi_p\big) \\ &= -\frac{\xi_p^2}{L^2}\Big(\mathrm{e}^{-v_ct/\xi_p}\big(2-\mathrm{e}^{L/\xi_p}-\mathrm{e}^{-L/\xi_p}\big)\Big) \\ &= \mathrm{e}^{-v_ct/\xi_p}\end{aligned} \tag{4.2}$$

where we assumed that the filament is elongated so that $s(t) = s(0) + v_ct$ and the autocorrelation is exponentially decaying (see Appendix C for an extended discussion). The effective persistence length, or equivalently, the rotational diffusion of the filament, is set by the relation $D_r = v_c/\xi_p$. Therefore, active forces increases the rotational dynamics of the filament. Note that we can combine this dependence in terms of the flexure number with $D_r = \mathfrak{F}/4\tau$.

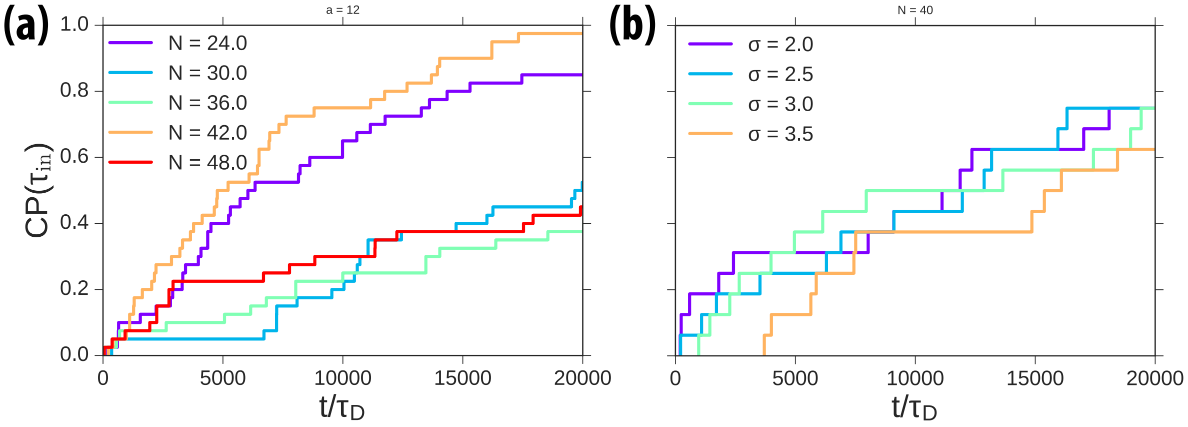

Figure 4.3.: Cumulative probability distribution of spiral formation times: (a) For various discretization at $a = 12$, (b) for various σ at $N = 40$. For both sets of simulations $\xi_p/L = 0.1$ and $Pe = 10000$.

The resultant filament trajectory is shown in fig. 4.2-a. As both the filament itself and its trajectory resembles a passive polymer, this regime is referred as *the polymer regime*. The polymer regime occurs at high ξ_p/L and low Pe.

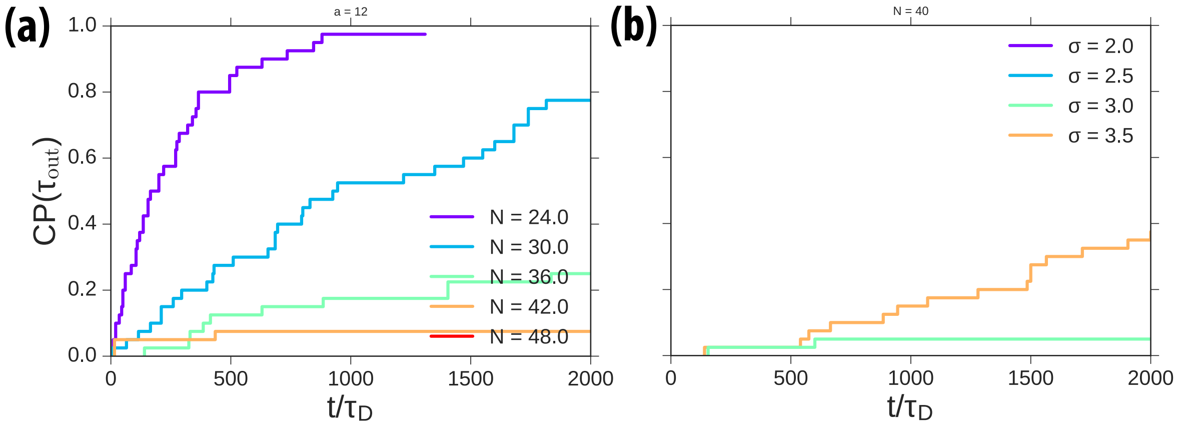

Figure 4.4.: Cumulative probability distribution of spiral breakout times: (a) For various discretization at $a = 12$, (b) for various σ at $N = 40$. For both sets of simulations $\xi_p/L = 0.1$ and $Pe = 10000$.

As we increase the activity further from the polymer regime, increased rotational dynamics renders the excluded-volume interactions more and more important. When the head of the filament hits a subsequent part of its body due to increased rotational dynamics, it winds up on itself, hindering its translational motion. If the active forces are not too strong, filament can break out of the cage by thermal diffusion. This phase, referred as *the weak spiral regime* is depicted in fig. 4.2-b.

When the active forces become stronger, the filament spirals on itself, resulting in a coiled configuration. In this regime, the filament stays locked for extended durations. The head body of the filament does ballistic rotations while the center of mass of the filament performs diffusive motion. This phase where the filament is coiled is referred as *the strong spiral regime* and it is depicted in fig. 4.2-c.

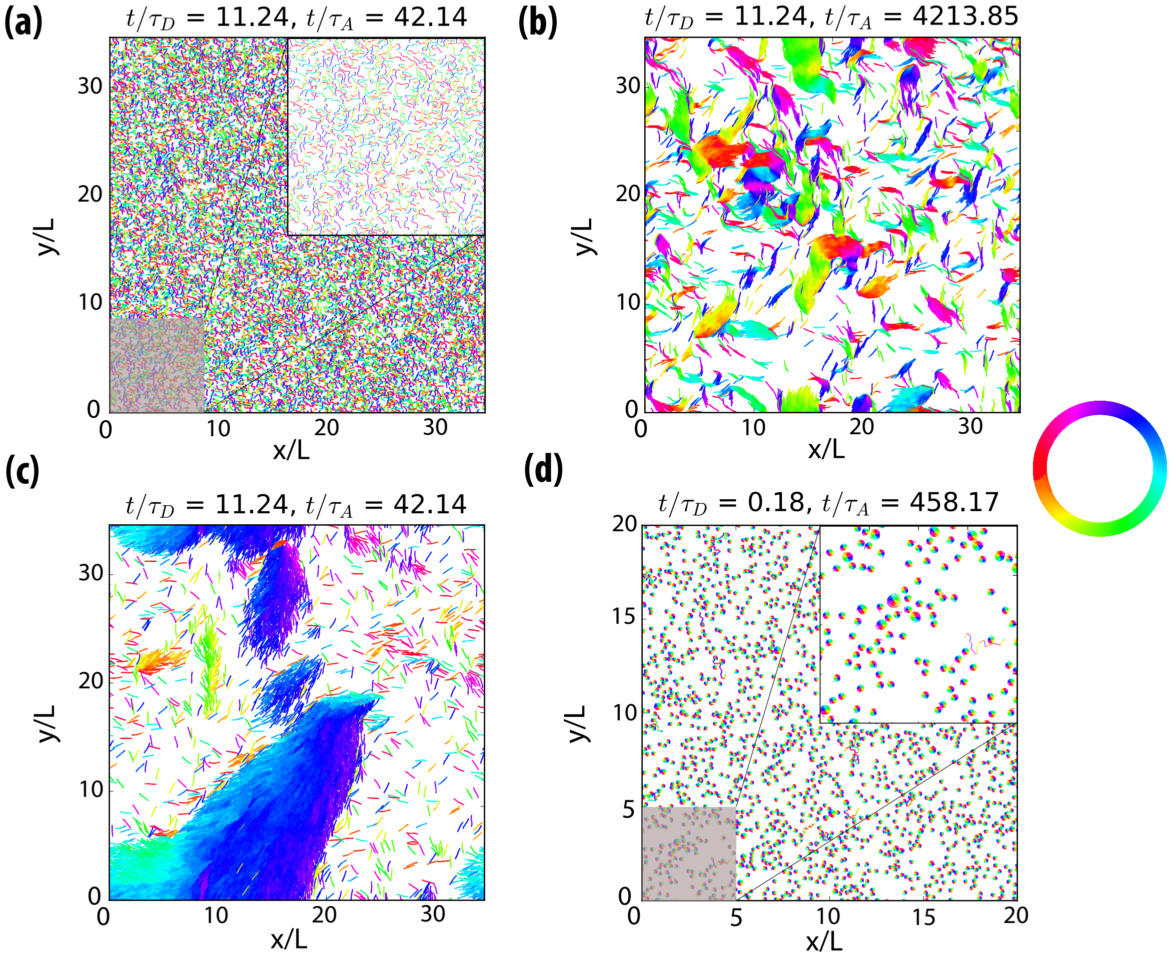

Figure 4.5.: Snapshots of the distinct phases: (a) melt phase characterized with a homogeneous distribution of filaments performing thermal motion (ξ_p/L = 0.1, Pe = 15, a = 25), (b) gas of clusters phase characterized with formation of small and transient clusters of filaments (ξ_p/L = 16, Pe = 1500, a = 25), (c) giant clusters phase characterized with formation of large and persistent clusters (ξ_p/L = 16, Pe = 15, a = 25), and (d) gas of spirals phase characterized with weakly interacting coiled filaments performing translational diffusion (ξ_p/L = 0.1, Pe = 10000, a = 100). Color wheel denotes orientation of each bond. Insets in (a) and (d) show zoomed areas shaded in grey.

Spiralling starts with the head of the filament hitting its body. Therefore, the onset of spiralling is set by the rotational dynamics of the filament, which depends on ξ_p/L and Pe. Decreasing ξ_p/L and increasing Pe increases the probability of spiralling as they enhance the rotational dynamics. We quantify this by calculating the cumulative probability distribution of spiral formation times. Starting from an initial configuration of a straight filament, we calculate the time it takes for the filament to form a spiral for the first time and calculate its cumulative distribution over 40 simulations. Spiral formation times do not depend neither on discretization nor on aspect ratio in a consistent manner. At fixed aspect ratio at $a = 12$, filaments tend to form spirals for discretization changing in the range of $24 - 48$ (Fig. 4.3-a). However, we do not identify a general trend for spiral formation times as a function of discretization. We then change the aspect ratio by fixing discretization at $N = 40$ (with $r_0 = 1$, so that $L = 40$) and changing σ between $2 - 3.5$. Increasing σ reduces the aspect ratio a from 20 to 11.4. We find that the spiral formation times are similar for different aspect ratio values without a consistent trend as a function of aspect ratio (Fig. 4.3-b). Therefore, spiral formation is not affected by discretization or aspect ratio, as these quantities do not affect rotational dynamics of the filament.

We next calculate the probability distribution of spiral breakout times by starting from a coiled initial configuration. Spirals break apart at longer times with increasing discretization (Fig. 4.4-a). At $N = 36{-}42$, spiral breakout events become dramatically reduced and at $N = 48$ they completely cease. Therefore, increasing discretization stabilizes the spirals. For aspect ratio $a = 16{-}20$, spirals do not break apart. With reduced aspect ratio down to $a = 11.4$, spirals start to break apart with break out times decreasing with decreasing aspect ratio. Therefore, increasing aspect ratio also stabilizes the spirals once they are formed. Filaments can wind up over themselves more with increased aspect ratio, which renders them more stable.

4.3. Collective Dynamics at Finite Densities

The collective dynamics of self-propelled semiflexible filaments is dictated by the dynamics of intra- and inter-filament collisions, which are in turn dependent on the properties of a single filament. The dynamical behavior of a single filament is determined by its thermal persistence length ξ_p/L, Peclet number Pe and aspect ratio a [88]. At high ξ_p/L, the active forces drive the filament along its contour leading to directed translational motion. At low ξ_p/L, increasing Pe increases the rotational diffusion of the filament. High aspect ratio filaments spontaneously form spirals in this regime of high Pe combined with low ξ_p/L [88]. We distinguish four distinct phases in the collective dynamics at finite filament concentration (see Fig. 4.5). The region of stability of each of these non-equilibrium phases is depicted in the phase diagram in Fig. 4.6. At low ξ_p/L and Pe, the ensemble behaves like a passive homogeneous melt (Fig. 4.5-a). Increasing Pe leads to the formation of clusters. Clusters of low ξ_p/L filaments are transient and small (Fig. 4.5-b), while clusters of high ξ_p/L filaments are large, persistent and rotating (Fig. 4.5-c). However, we find that cluster sizes do not monotonically grow in Pe,

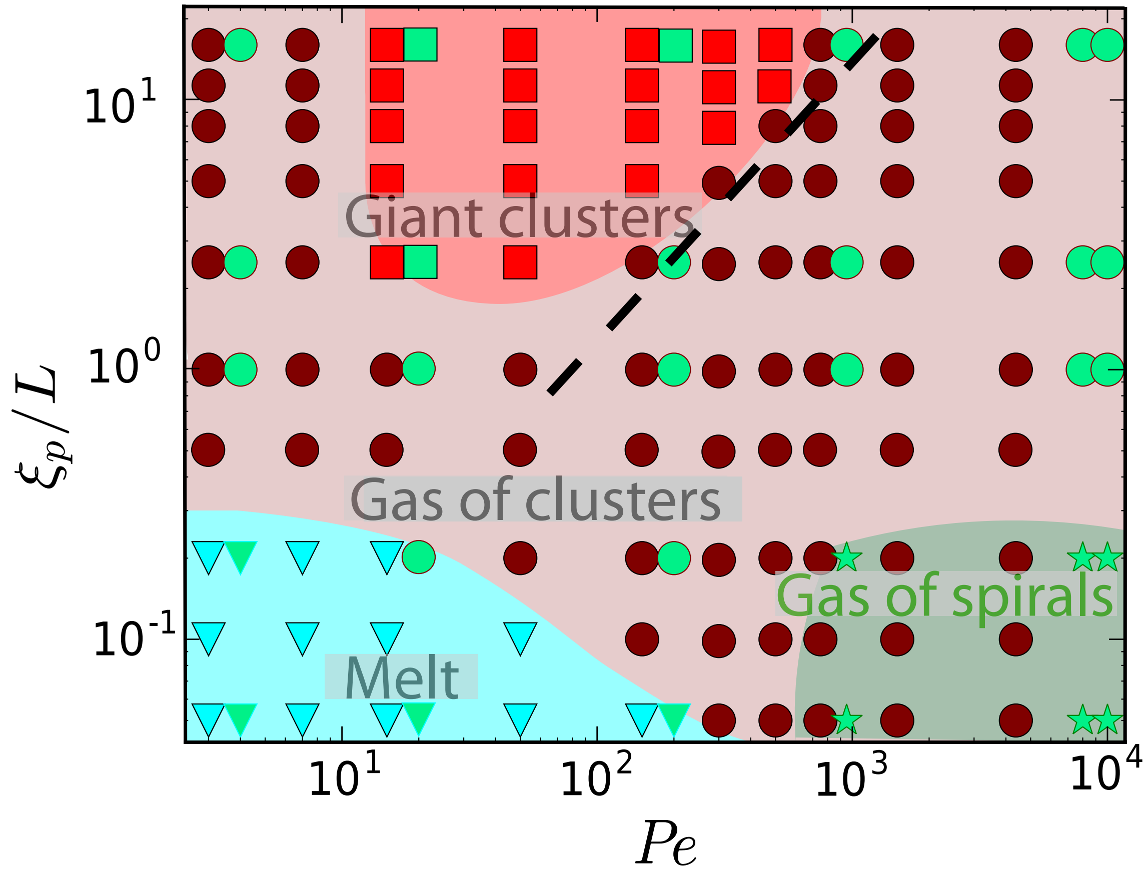

Figure 4.6.: Phase diagram as a function of ξ_p/L and Pe. Symbols encode the distinct phases. Cyan triangles display the melt phase, magenta circles are the gas of clusters phase and the red squares are the giant clusters phase. The background colors are guides to the eye. Phases are identified with the average cluster size. Points with an average cluster size smaller than 10 filaments are marked as the melt phase, while those larger than 200 filaments are marked as the giant clusters, with everything in between falling into the category of gas of clusters. Green filled symbols depict the simulations with high aspect ratio filaments (at $a = 100$, while every other points denote simulations with $a = 25$). The only different phase for high aspect ratio filaments is the gas-of-spirals phase, which is depicted with stars with every other symbol remaining the same as before. The black dashed line marks the phase boundary between the giant clusters and gas of clusters phases with a linear slope in $\xi_p/L \sim Pe$.

but instead peak at moderate propulsion strengths.

Strong propulsion alters the structure and dynamics of high aspect ratio filaments. At a higher aspect ratio a, filaments with low ξ_p/L and high Pe spontaneously wind up on themselves, or on other filaments, to form spirals (Fig. 4.5-d).

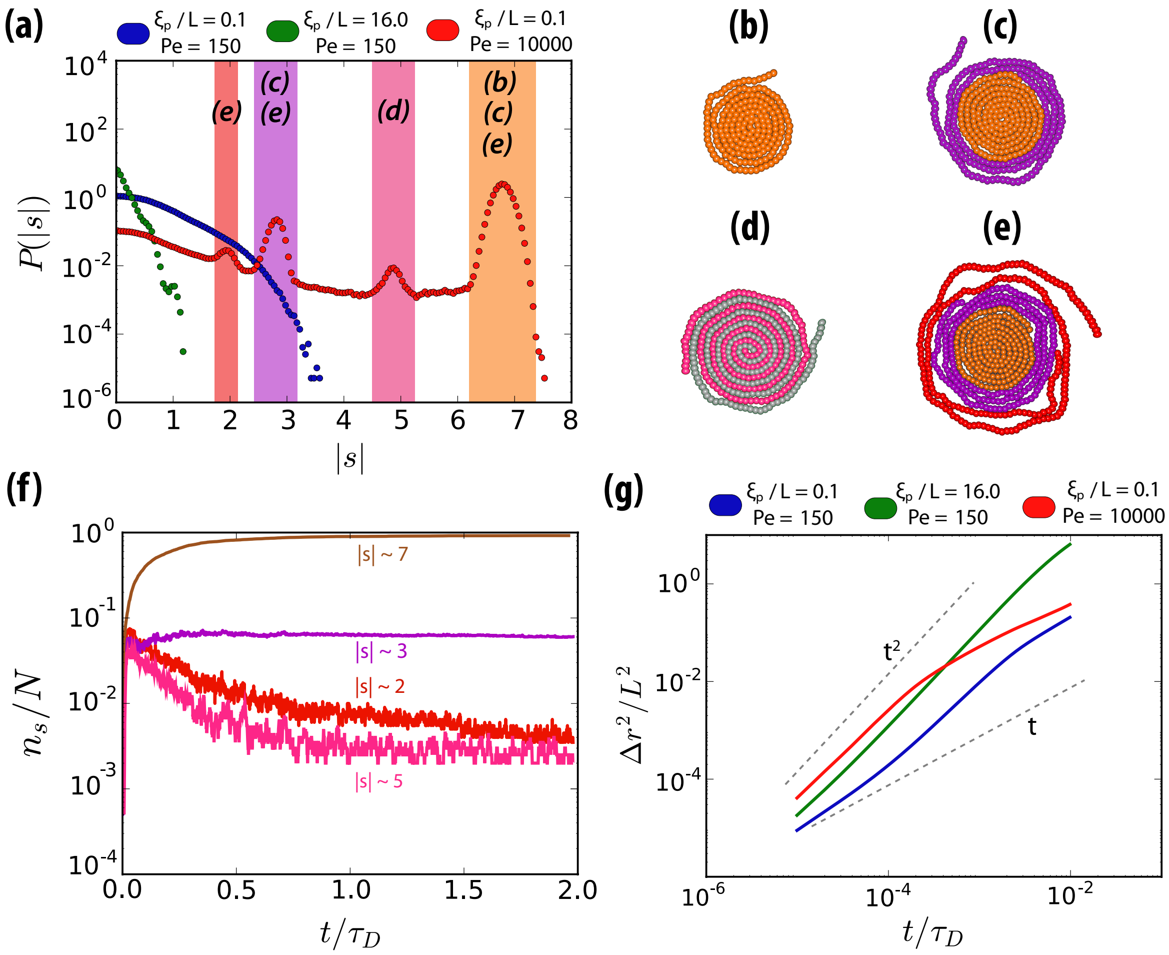

Figure 4.7.: (a) Probability distribution of the absolute value of the spiral number. (b-e) Distinct spiral configurations observed in the system: (b) A single coiled filament with $|s| \approx 7$, (c) a filament wrapped around a coiled filament, with $|s| \approx 3$, (d) two intertwined filaments each with $|s| \approx 5$, and (e) two filaments wrapped around a coiled filament, with $|s| \approx 3$ and $|s| \approx 2$, respectively. The color codes of filaments are consistent with the colors of the bars around the peaks in (a). (f) Time evolution of number of filaments with approximately the given spiral numbers. The intervals for each $|s|$ value are colored with a bar around each peak of (a). (g) Mean squared displacement of the center of mass of filaments. Aspect ratio is $a = 100$.

4.3.1. Spiral Formation

Isolated filaments wind up in spirals at strong propulsion and low rigidities. The onset of spiral formation is dictated by the head of the filament hitting a subsequent part of its body.

For strongly propelled long filaments with low rigidity, we observe the formation of several configurations of spirals. To elucidate spiral formation and spiral structure, we calculate the spiral number

$$s = \sum_{j=1}^{N_f} \frac{\theta_j(L) - \theta_j(0)}{2\pi N_f} \tag{4.3}$$

where $\theta_j(l)$ is the bond orientation at position l along the contour of the filament. It is a quantitave measure of the number of times the filament has wrapped around its head bead.

For filaments with low propulsion and low rigidity (at $\xi_p/L = 0.1$, $Pe = 150$), the probability distribution of the absolute value of the spiral number resembles a Gaussian distribution (see Fig. 4.7-a). With increasing rigidity (at $\xi_p/L = 16$, $Pe = 150$), the distribution becomes exponential with the development of a small peak around $|s| \approx 1$. Stiff filaments are bent into circles (corresponding to $|s| \approx 1$) due to the extensile stress generated by self-propulsion. However, such circular loops are transient in dynamics, so that the peak is small.

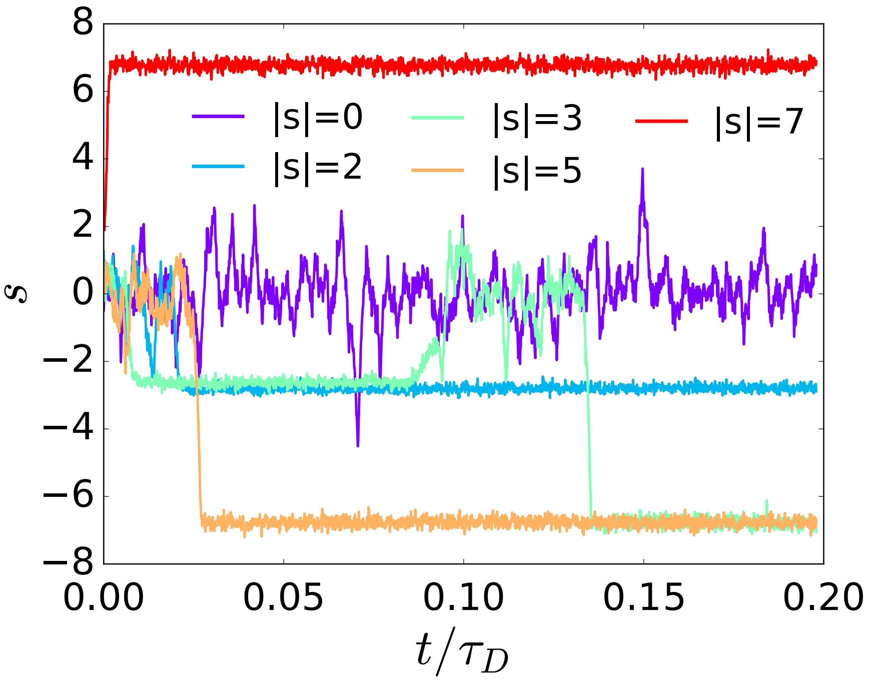

Figure 4.8.: The time evolution of the spiral number of a tagged filament with the average spiral number depicted in the legend. Filaments are picked from the same simulation instance.

Strongly propelled filaments with low rigidity (at $\xi_p/L = 0.1$, $Pe = 10000$) self-organize into spirals of different configurations. This results in multiple peaks in the proability distribution of $|s|$. Each peak denotes a different type of spiral configuration that are highlighted in Fig. 4.7-b to e. The most pronounced peak, coinciding with the most common type of spiral in the ensemble, is around $|s| \approx 7$, corresponding to a single coiled filament. When the leading tip of a filament hits a subsequent part of its own body, the volume exclusion force bends the leading tip, thereby causing it to wind onto itself. After the winding process, the filament stays locked in the coiled form for an extended duration. The number of spirals consisting of a single filament increases up to a value close to unity in time (see Fig. 4.7-f), rendering the dynamics of the ensemble analogous to a gas of spirals. This is consistent with the dynamics of a single filament [88].

As a direct result of collective motion, there are multiple spiral configurations corresponding to the different peaks in the distribution. The second important peak occurs at $|s| \approx 3$. The configuration it represents is involved in two types of spirals (in double-wrapped and triple-wrapped filament configurations in Figs. 4.7-c and e). The double-wrapped filament configuration consists of a single coiled filament with another filament wrapped around it. Another filament can wind itself around these two filaments to form the configuration with three filaments. The spiral number of the third wrapping filament coincides with the first peak of the distribution. It is relatively easier to break up this state. As a result, number of filaments with $|s| \approx 2$ decreases in time, reducing the triple-wrapped filament state to that of double wrapped filaments.

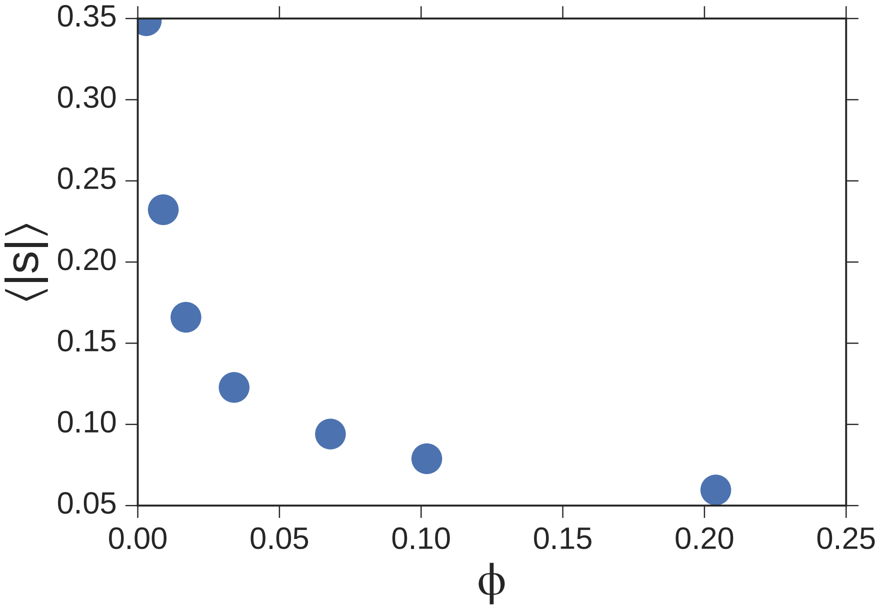

Figure 4.9.: Average of the absolute value of the spiral number as a function of density at $\xi_p/L = 0.1$, $Pe = 4552$, and $a = 25$. The average is taken per filaments and per time frame.

Finally, the smallest peak represents the configuration with two intertwined filaments (Fig. 4.7-d). Two filaments interlock when one of them hits the other one before winding itself over it. This type of formation has the least likelihood to occur. It is also easy for the filaments to break out of this interlock, as a free filament can widen the tail of one of the interlocking filaments, thereby facilitating the break-up. As a result, the observed peak around $|s| \approx 5$ is small.

In terms of dynamical behaviour, spirals rotate without a preferred direction, with the center

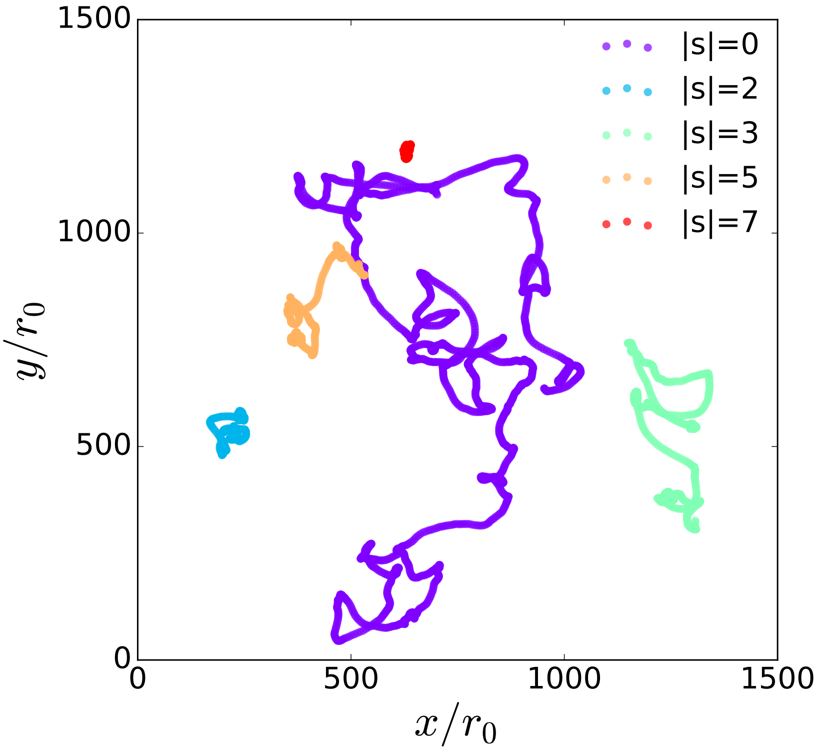

Figure 4.10.: The trace of the center of mass of filaments with average spiral numbers depicted in the legend. The color code and the tagged filaments are the same as in Fig. 4.8.

of mass performing thermal motion. The mean square displacement (MSD) of the center of mass of long filaments in the spiralling phase is marked by an initial ballistic behaviour ($\sim t^2$) that makes a transition into a diffusive behaviour ($\sim t$) at late lag times (see Fig. 4.7-g). The initial ballistic regime is a result of filaments performing directed motion at early lag times. Therefore, the transition time from ballistic to diffusive motion gives a time scale for spiralling on average. The movement of the filaments is significantly hindered in the spiralling regime, despite the strong propulsion.

The time evolution of a typical filament in given spiral numbers is plotted in Fig. 4.8 for tagged filaments and their corresponding trajectories are given in Fig. 4.10. Single wrapped filaments are the most dominant spiral configurations, and filaments stay in this configuration for extended durations. The trajectory of single coiled filament is the most confined in space in comparison to the other spiral configurations. Spiral numbers of 2 and 3 correspond to filaments that are either slightly wound up, or on the outermost sites of multiple wrapped filament configurations. Therefore, they get out of this conformation easier as they are not interlocked on themselves as the single wrapped ones. Their motion is also somewhat hindered as can be observed from the trajectory.

As discussed for a single filament, aspect ratio plays an important role in the stability of

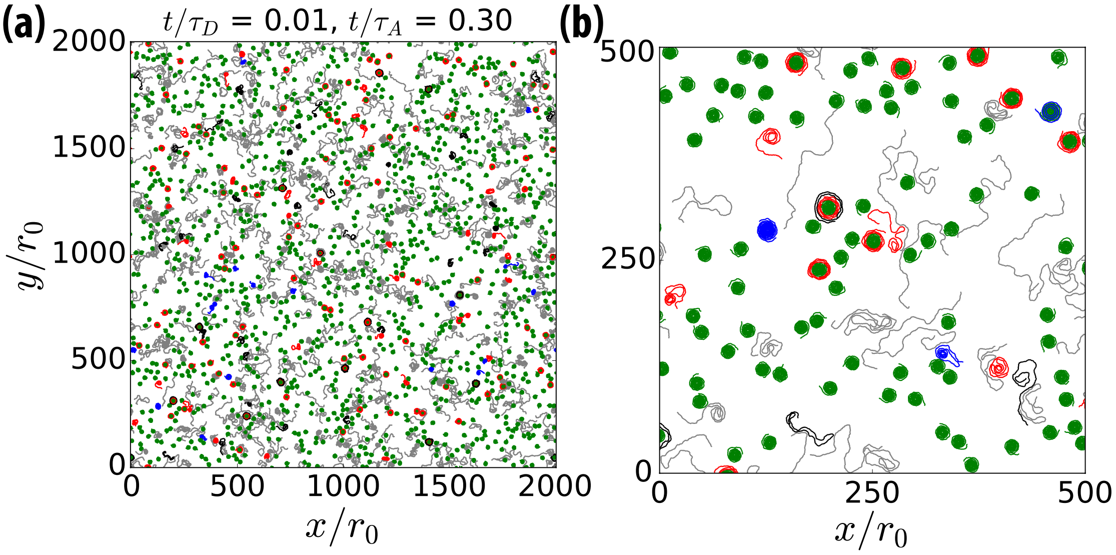

Figure 4.11.: A snapshot from a simulation instance depicting the gas of spirals phase for $\xi_p/L = 0.1$ and $Pe = 10000$: (a) Snapshot, and (b) zoomed in version of the snapshot. The color code denotes the spiral number of individiual filaments with green $|s| \approx 7$, blue $|s| \approx 5$, red $|s| \approx 3$, and black $|s| \approx 2$.

spirals. Filaments can wrap around themselves more times with increasing aspect ratio, which stabilizes the spiralling configuration. We study two values of aspect ratio in our simulations with $a = 25$ and $a = 100$. We only observed a gas of spirals phase for $a = 100$. Thus, gas of spirals phase did not set in for $a = 25$, even though parts of the phase space we built cover filament parameters for spiralling at $a = 25$ in the infinite-dilution limit. This suggests a dynamics in which collective effects combined with reduced stability of spirals due to lower aspect ratio destroys the gas of spirals phase at $a = 25$. In order to quantify this effect, we calculate the average of the absolute value of the spiral number as a function of changing density by changing the number of filaments at fixed box size. We simulate the filaments at $Pe = 4552$, $\xi_p/L = 0.1$ and $a = 25$ where a single, isolated filament is expected to form spirals. The average absolute value of the spiral number decreases with increasing density (Fig. 4.9). Therefore, spirals become less stable at higher densities due to collisions with free filaments.

The gas of spirals phase is depicted in Fig. 4.11. The entire region is observed to be dominated by filaments with a spiral number of ≈ 7. Although there are still filaments that are not yet in any of the spiral configurations, we expect all of the filaments to be spiralled as the simulation reaches steady state. We could not reach such a complete gas of spirals state where all the filaments are coiled in one form due to the long simulation times it requires.

We quantify the rotational dynamics by calculating the mean square rotation of the end-to-end vector (see Fig. 4.12). At short times, rotations are influenced by the internal filament flexibility, which is reflected in superdiffusive rotation. Initial superdiffusive rotations relax into diffusive behaviour at long times. In the spiralling regime (for $\xi_p/L = 0.05$ and $Pe = 10000$),

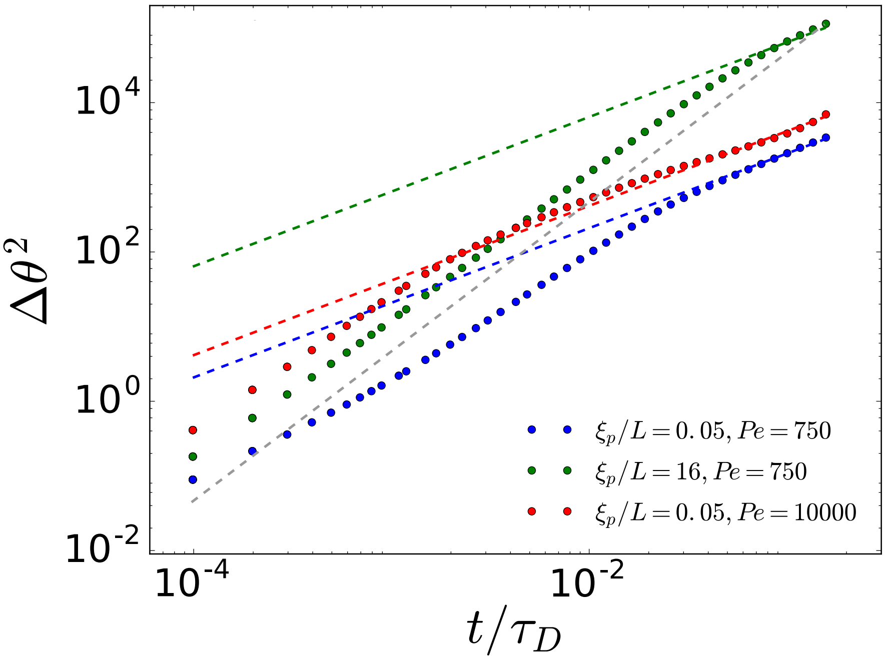

Figure 4.12.: Mean square rotation of the end-to-end vector as a function of different lag times. The dashed lines are linear fits for theoretical expectation of diffusive rotations. The gray dashed line indicate a slope of 2, corresponding to ballistic rotations.

filaments rotate ballistically at short times and then relax into diffusive rotations. However, stiff filaments curiously rotate ballistically for longer times. This phenomenon is associated with the formation of loops at high rigidities, as is also observed in spiral number distribution with an additional small peak at around $s \approx 1$. When filaments are contained in small spaces, they get bent into transient circular loops as shown in Fig. 4.13. These loops are unstable structures, and they relax into clusters or giant clusters depending on the filament rigidity.

We look for a signature of circular loops in the structural properties of the filaments by calculating the gyration tensor. It is defined as,

$$R^2_{\text{xy}} = \frac{1}{N_b+1}\begin{bmatrix} \sum_{i=0}^{N_b}(x_i^{(j)} - x_{cm}^{(j)})^2 & \sum_{i=0}^{N_b}(x_i^{(j)} - x_{cm}^{(j)})(y_i^{(j)} - y_{cm}^{(j)}) \\ \sum_{i=0}^{N_b}(x_i^{(j)} - x_{cm}^{(j)})(y_i^{(j)} - y_{cm}^{(j)}) & \sum_{i=0}^{N_b}(y_i^{(j)} - y_{cm}^{(j)})^2 \end{bmatrix} \tag{4.4}$$

where $N_b + 1$ is the number of beads per filament, i is the bead index, superscript j is the filament identity and subscripts cm indicate center of mass of the filament j. We calculate the average of the ratio of the large to small eigenvalue of the gyration tensor, which quantifies the structural extension of the filaments around their center of mass (see Fig. 4.14). We observe that formation of loops is associated with an increasing eigenvalue ratio in time (for $\xi_p/L = 16$ and $Pe = 750$). This is because initially filaments are confined in tight spaces which is only possible in circularly bent conformations. As time passes, they relax into their steady state configuration, which is reflected with the increase in the eigenvalue ratio. In case of melt and small cluster formation, the eigenvalue ratio does not change much. However, spiralling

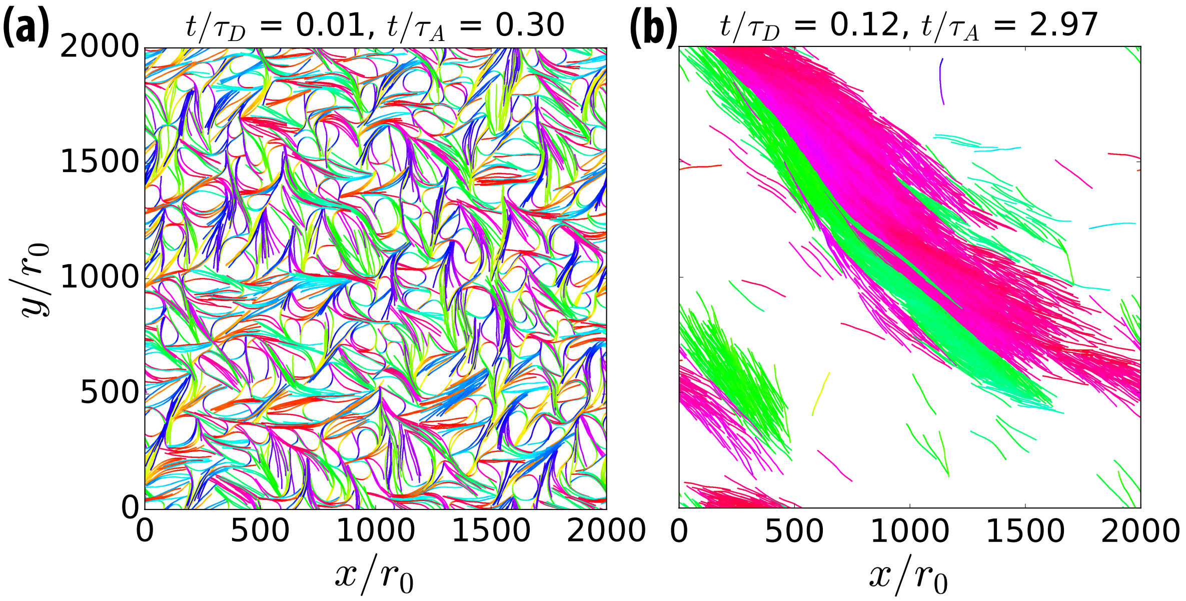

Figure 4.13.: Simulation snapshots at two different time instances for $\xi_p/L = 16$ and $Pe = 150$: (a) Formation of loops, and (b) formation of giant clusters. The color code is the bond orientation as defined earlier with the color wheel.

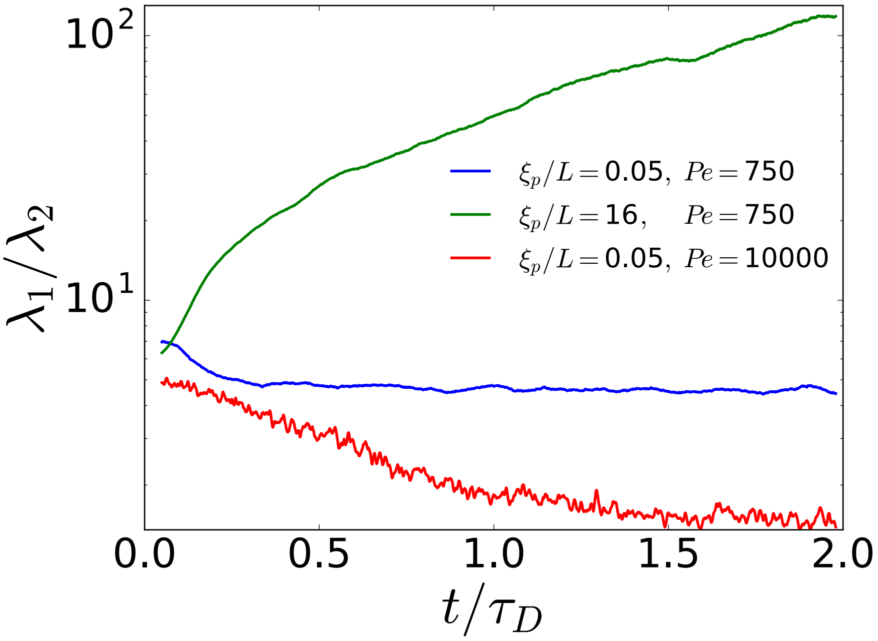

Figure 4.14.: The averaged ratio between the large and small eigenvalue of the gyration tensor as a function of time for different values of ξ_p/L and Pe as depicted in the legend.

coincides with a decrease in the eigenvalue ratio as a function of time, as spirals are roughly filaments that are tightly packed in a symmetric shape around the center of mass.

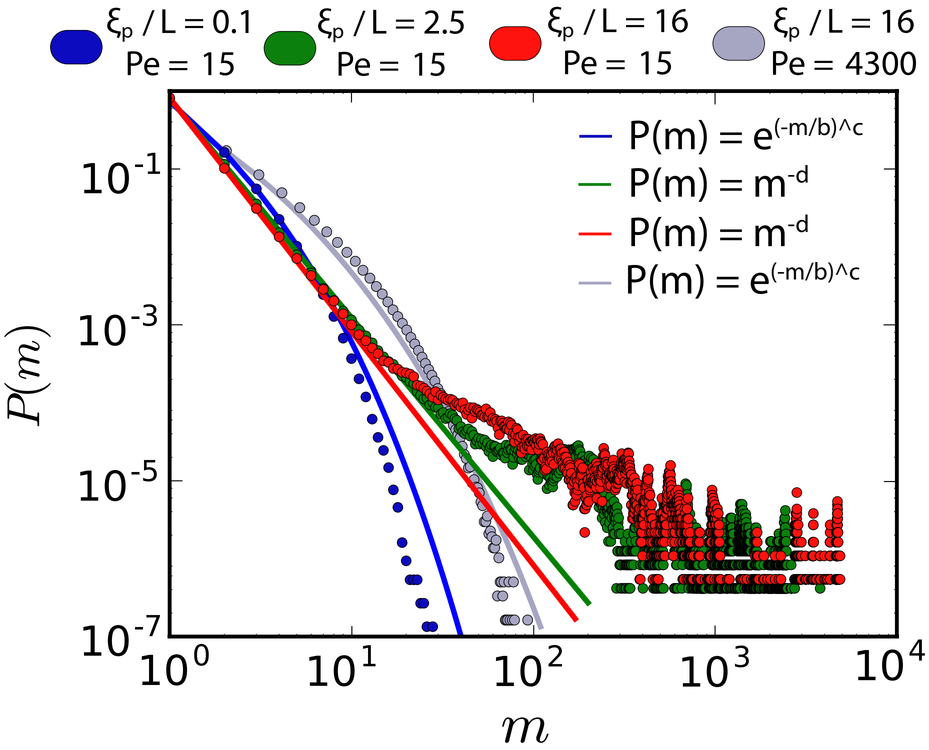

Figure 4.15.: Cluster mass distribution as a function of ξ_p/L at $Pe = 15$ and $Pe = 4300$ as depicted in the outer legend. Solid lines are fits as given in the inner legend.

4.3.2. Cluster Formation and Disintegration

Spiral formation is facilitated by self-interactions. As such, spiralling behaviour is affected by aspect ratio. At the spiral configuration, shorter filaments are winded a smaller number of times with a smaller spiral number, which renders them less stable. For such short filaments, the defining characteristic of the collective motion is instead the formation of clusters. We consider two filaments as part of the same cluster if they have closely spaced bonds that are pointing in the same direction. More specifically, if 30% of the body of two filaments are within a distance range of 2σ of each other, and point in the same direction $\pm\pi/6$, then we consider the filaments to be part of the same cluster.

To quantify the transition into clustering, we calculate the cluster mass distribution,

$$P(m,t) = \frac{m n_m(t)}{N_f}, \tag{4.5}$$

where $n_m(t)$ is the number of clusters of mass m present at time t and N_f is the total number of filaments in the system. The distribution fits a stretched exponential of the form $P(m) = \exp(-m/b)^c$ with $b = 0.02$ to 0.04 and $c = 0.2$ to 0.4 for filaments with low rigidity and low propulsion (see Fig. 4.15). The stretched exponential fit points to a dynamical clustering picture where clusters of different mass acquire and eject filaments at different characteristic rates [71]. With an increasing rigidity, the cluster mass distribution undergoes a transition to

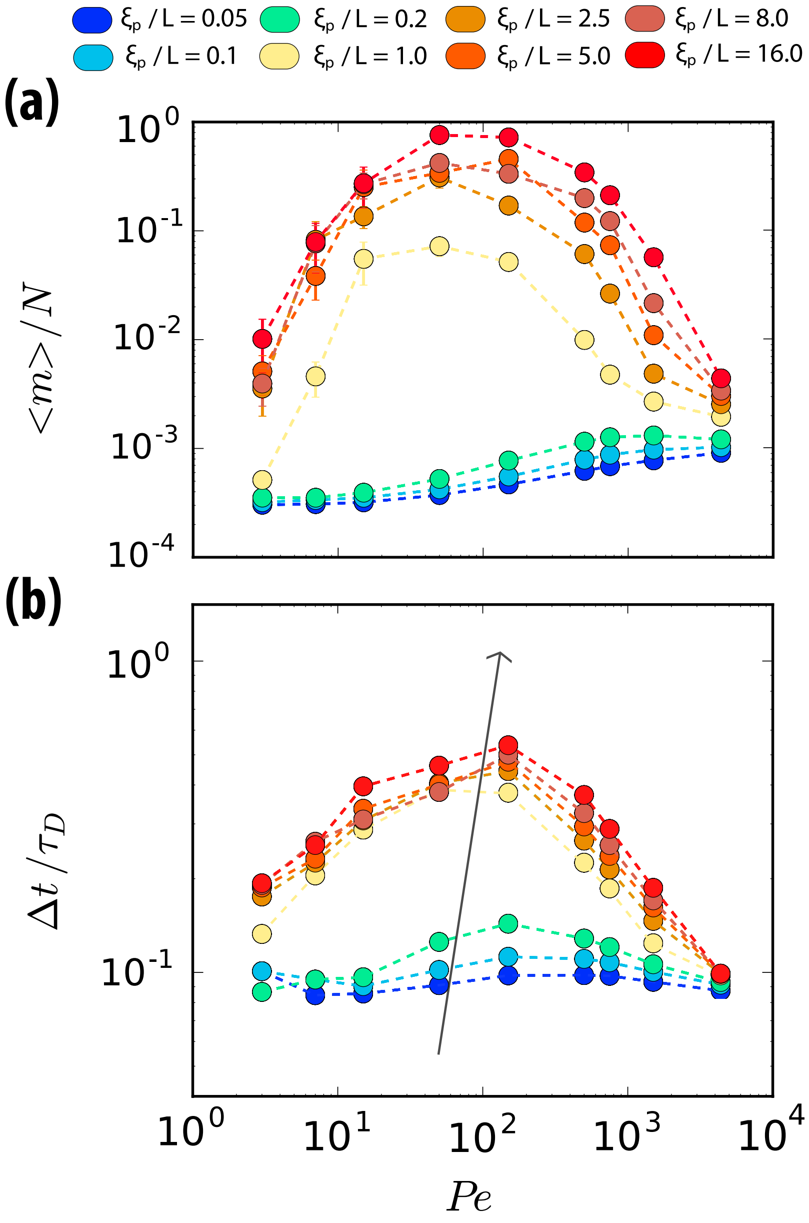

Figure 4.16.: (a) Average cluster mass (in terms of bead mass), and (b) average lifetime of clusters as a function of Pe. Different ξ_p/L values are denoted in the legend. The arrow direction indicates increasing ξ_p/L.

a power law distribution of the form $P(m) = m^{-d}$ with $d \approx 3$. Additionally, the distribution has a nonmonotonically decreasing tail with a shoulder at large mass values, indicating an increase in the probability of finding a filament in a larger cluster. This corresponds to the giant cluster regime in Fig. 4.6. However, as the activity is increased to $Pe = 4300$, the distribution turns back to a stretched exponential with $b \approx 0.07$ and $c \approx 0.3$. Remarkably, formation of large clusters disappear with increasing activity.

To elucidate the properties of the clusters further, we calculate the average cluster size and

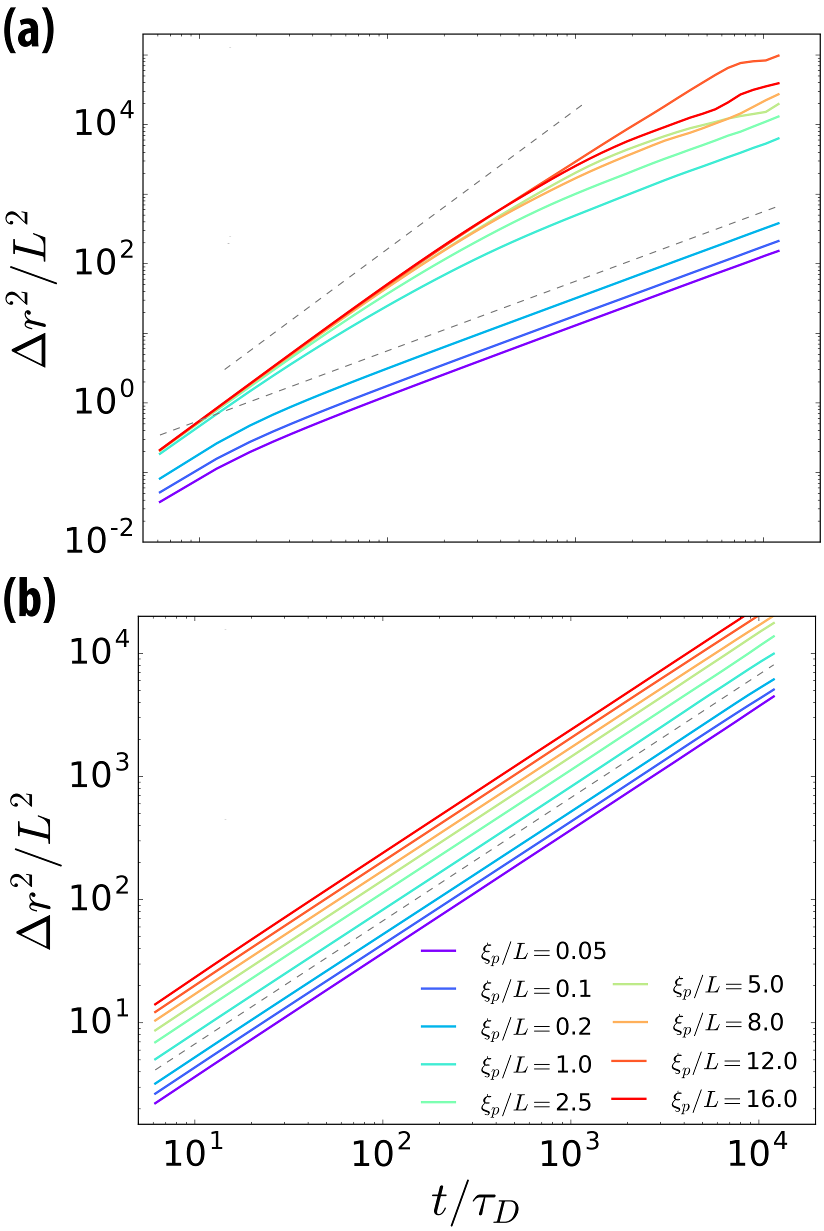

Figure 4.17.: Mean square displacement of the center of mass of filaments for changing ξ_p/L. (a) $Pe = 105$, (b) $Pe = 4300$. Slopes of 1 and 2 are given in the gray dashed lines as guides to the eye.

the average lifetime of clusters. The average cluster size is defined as $\langle m \rangle = \sum_m m \langle P(m,t) \rangle$ where the average is taken over time. For the average lifetime calculation, we label the clusters in time by comparing the identity of filaments in two successive time frames. The clusters with maximum overlapping filaments are labelled as the same cluster with a unique identity. A cluster is deemed to lose its identity when its size drops down to less than 10 filaments or when it merges with a larger cluster. The tendency of clustering decreases with decreasing rigidity.

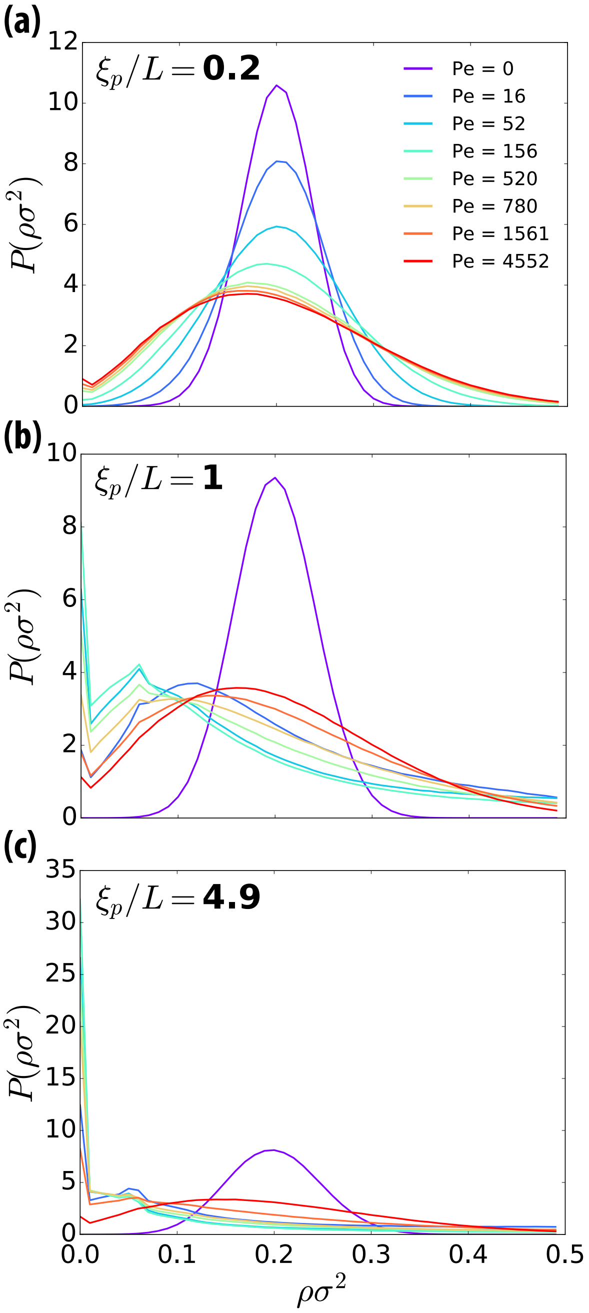

Figure 4.18.: Normalized density histogram as a function of densities for different activities: (a) $\xi_p/L = 0.2$, (b) $\xi_p/L = 1$, and (c) $\xi_p/L = 4.9$.

However, for increasing activity, it reaches a peak at intermediate values, after which it starts to decrease. Therefore, both average cluster size and average cluster lifetime have distinct peaks at intermediate Pe for stiff filaments (see Fig. 4.16). The maximum at intermediate activity level corresponds to the pocket of giant clusters in the phase diagram (Fig. 4.6).

We quantify the motion of filaments inside the clusters by calculating the mean square dis-

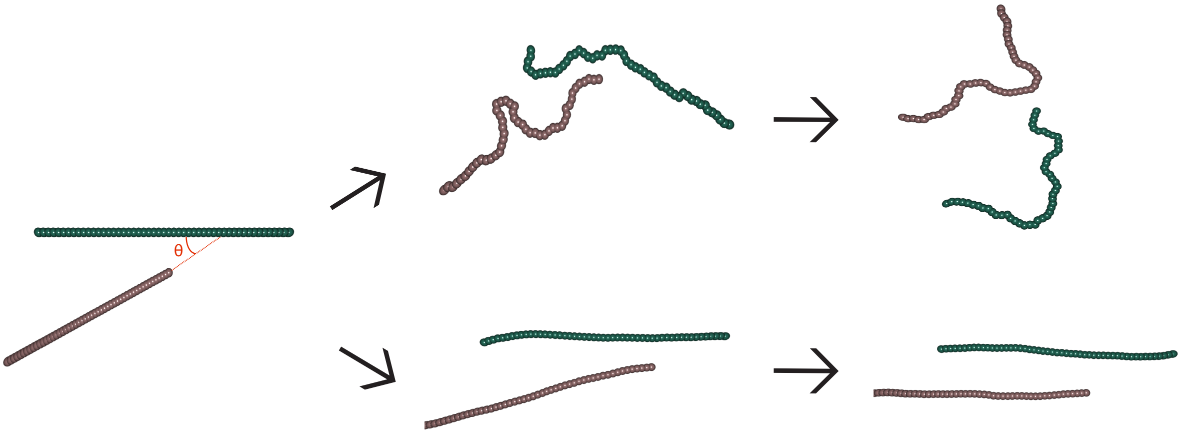

Figure 4.19.: Collisions between two filaments at a given angle θ. The initial configuration is given in the leftmost panel with arrows indicating the direction of increasing time towards right. The upper panel depicts collisions between filaments with $\xi_p/L = 0.2$, while the lower panel is for that of $\xi_p/L = 16$, both at fixed $Pe = 100$. The shapes are rendered from the simulation data.

placement of the center of mass of filaments (fig. 4.17). Persistence length creates a distinct deviation in dynamics of individual filaments. For $Pe = 105$, stiff filaments move ballistically for $\xi_p/L \geq 1$, while flexible filaments perform diffusive motion. This can be inferred as the inversely proportional relationship between the persistence length of a filament and its rotational diffusion. Flexible filaments with low persistence length have shorter rotational diffusion times, therefore they perform diffusive motion at earlier time scales. However, stiff filaments have longer rotational diffusion times, which makes them move in more straight trajectories. Note that this trend is in line with the single filament dynamics as depicted in fig. 4.1. It can be argued that filaments are able to move roughly independently despite the presence of other filaments. The nature of the dynamics (*i.e.* ballistic or diffusive motion) does not change with collective dynamics. For strongly propelled filaments (at $Pe = 4300$), filaments perform diffusive motion for different persistence lengths due to the activity-enhanced rotational diffusion. This fits to the picture of rotational diffusion scaling with flexure number. The translational diffusion of the filaments, on the other hand, is observed to scale with rigidity of the filaments.

To study the spatial distribution of filaments, we calculate the density histogram. We divide the entire simulation box into smaller boxes of size $8r_0$, and calculate the number density ρ for each boxes as the ratio of number of beads inside the box and the area of the box. The density histogram is then given by the histogram of the calculated number densities. For passive motion, the distribution is a Gaussian with a peak at the system density of $\phi = 0.2$, indicating that filaments are distributed homogeneously (Fig. 4.18). For $\xi_p/L = 0.2$, increasing activity leads to a wider distribution with an increasing skew towards lower densities. As the filaments cluster, they fill some boxes more than the others which creates a spatial heterogeneity in the distribution. For stiffer filaments, low density peak surpasses the peak of the Gaussian

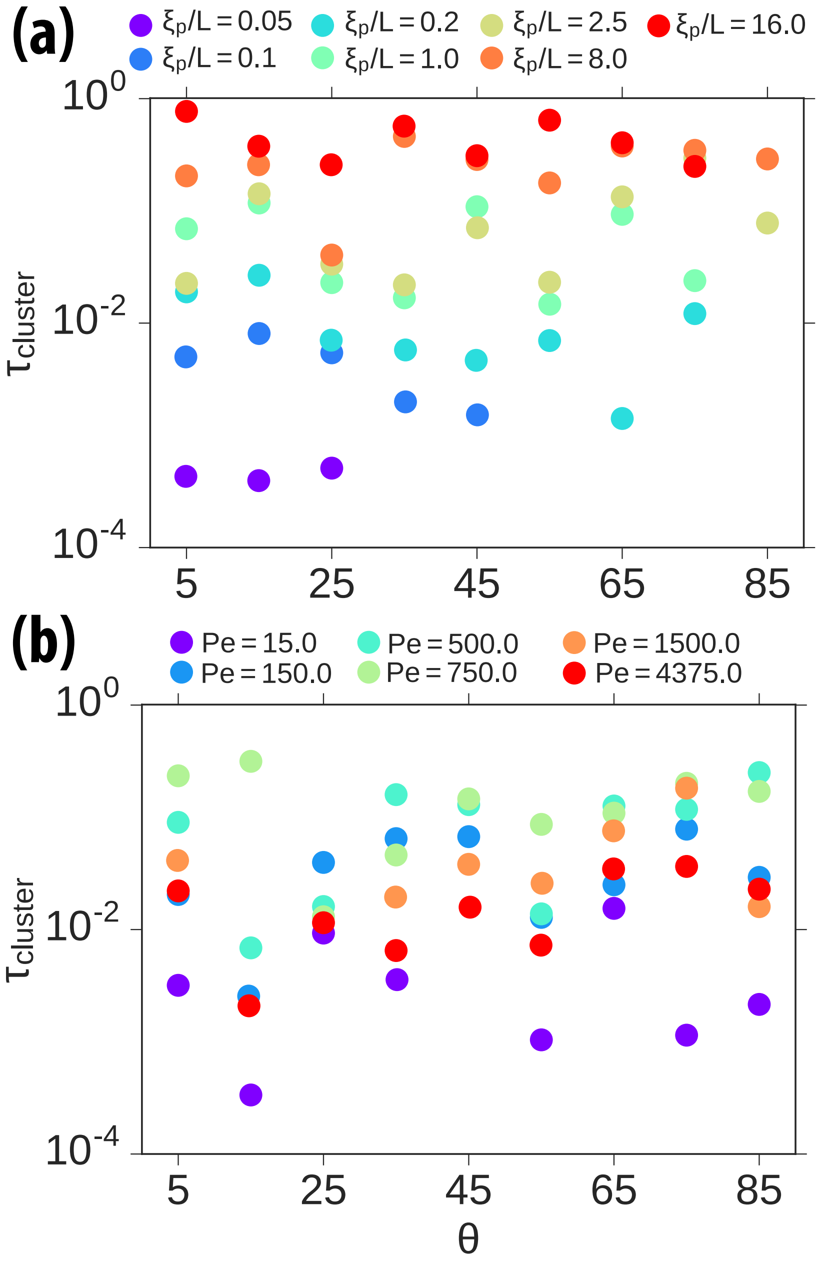

Figure 4.20.: The average time two filaments spend as part of the same cluster for different collision angles θ as depicted in Fig. 4.19. (a) $Pe = 100$, changing ξ_p/L as depicted in the legend, (b) $\xi_p/L = 8$, changing Pe as shown in the legend. The results are averaged over 100 simulations for each data point.

distribution. With a rigidity value that includes giant cluster formation, magnitude of the low density peak does not grow monotonically with activity, but instead peaks at moderate propulsion and then decreases with increasing activity further. It corresponds to the reentrant behaviour of giant clusters with activity.

Clusters are the results of inter-filament collisions. The outcome of collisions between fil-

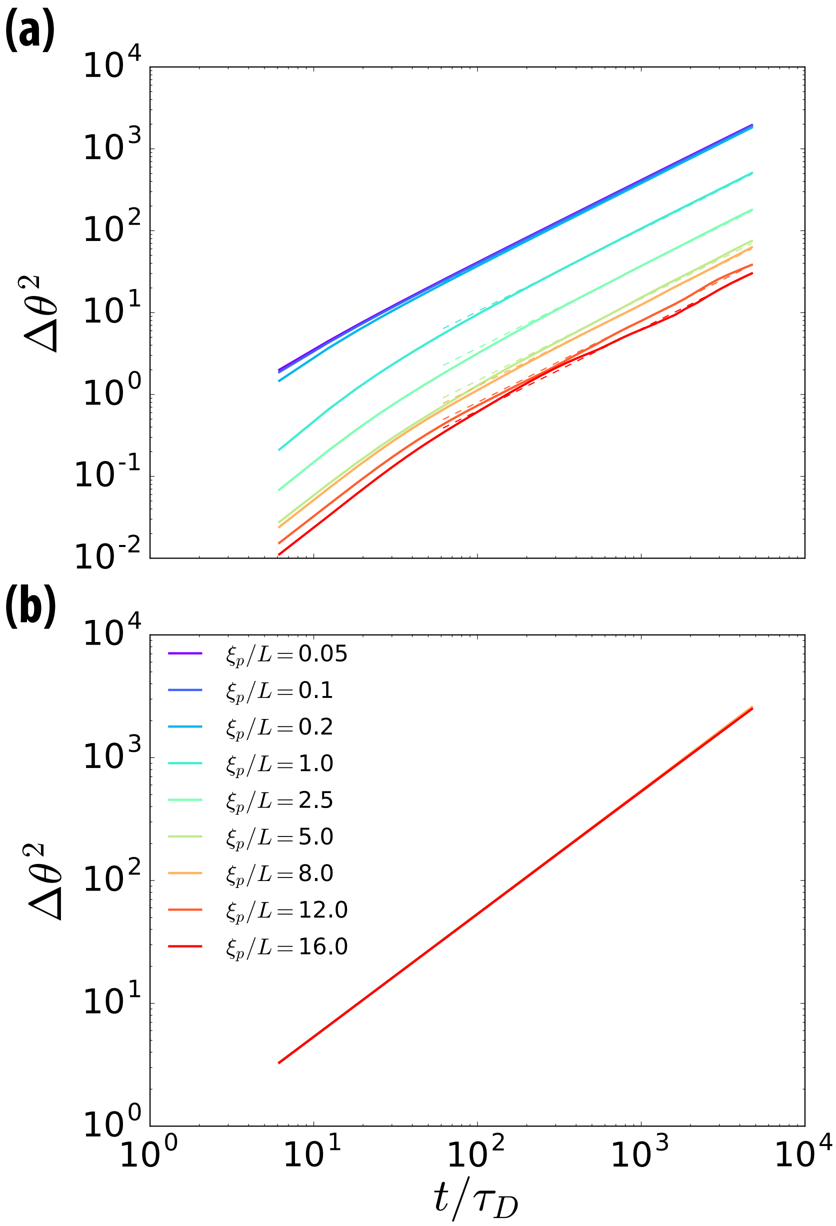

Figure 4.21.: Mean square rotation of the end-to-end vector: (a) For $Pe = 15$ and (b) $Pe = 4375$ with changing ξ_p/L as given in the legend.

aments is determined by the persistence length of the filament. Stiff filaments are spatially elongated with long persistence lengths. If two stiff filaments collide at an acute angle, then they start to move in the same direction after the collision due to the excluded volume interactions. As the persistence length is high, filaments move in their new common direction for extended durations. However, when the persistence length is short, then filaments form bent conformations, which hinders alignment upon collisions. Furthermore, short persistence lengths lead to more frequent deviations in the tangential orientations of the bonds. Therefore, rotational diffusion of the filaments increases effectively with reduced persistence length (note that the reduced persistence length is, by its very definition, nothing but reduced tangent tangent correlations between the bonds of a filament). The described collision mechanism is depicted in Fig. 4.19). Acute-angled collisions align the stiff filaments parallel to each other, while flexible filaments are bent even further upon collisions. As a result, stiff filaments and rigid rods form giant clusters with the same alignment mechanism of collisions. On the other hand, flexible filaments form only short-lived small clusters. For those filaments, cluster formation is a density-effect. When the density is high, filaments are trapped in small spaces which leads to cluster formation. As this effect does not depend on a specific conformation, it applies to other systems like self-propelled colloids too.

To quantify the outcome of filament collisions, we perform multiple simulations of two filaments (as given in Fig. 4.19) for different collision angles θ, and calculate the average time τ_{cluster} two filaments were considered as part of the same cluster with the cluster criteria remaining as before. In this way, we can quantify both if there is any alignment in tangential orientations of the filaments at all as well as the persistence of any possible alignment in time. In essence, this quantity measures the probability of finding the filaments at a clustered configuration. The probability of clustering increases with increasing persistence length at fixed activity (Fig. 4.20-a). At small angles, flexible filaments are part of the same cluster occasionally, while they almost never form any cluster when the collision angle is increased towards $\pi/2$. Stiff filaments seem to always form clusters in a more persistent manner. Although when the collision is close to being perpendicular, the probability of alignment falls down sharply. Therefore, even at the level of two filaments, acute angled collisions lead to polar alignment of filaments. Increasing density, or reducing noise would be predicted to have a more stabilizing effect for cluster formation, as they will make the filaments less likely to leave from the cluster.

When the persistence length is fixed at $\xi_p/L = 8$ with changing activity, the data becomes noisy indicating that activity does not necessarily effect the cluster formation for only two filaments within this configuration setup (Fig. 4.20). The only general trend to be observed is that the tendency of clustering increases initially with Pe, but then goes down again at higher Pe, but by no means it is significant. Therefore, we have to turn to the collective effects involving more than two filaments to investigate the origin of the melting of giant clusters at high Pe, which we turn to next.

4.3.3. Melting of Giant Clusters

In order to understand the disappearence of giant clusters at high Pe, we quantify the rotational dynamics of filaments. We first calculate the mean square rotation $\langle \Delta\theta^2 \rangle$ of the end-to-end vector. For diffusive rotations, mean square rotation is expected to be linear as a function of time with the proportionality constant given by the rotational diffusion coefficient via the relation $\Delta\theta^2 = 2D_r t$. Note that the rotations can be more than 2π. This is accounted for in our calculations by wrapping successive orientation differences between the bonds to the

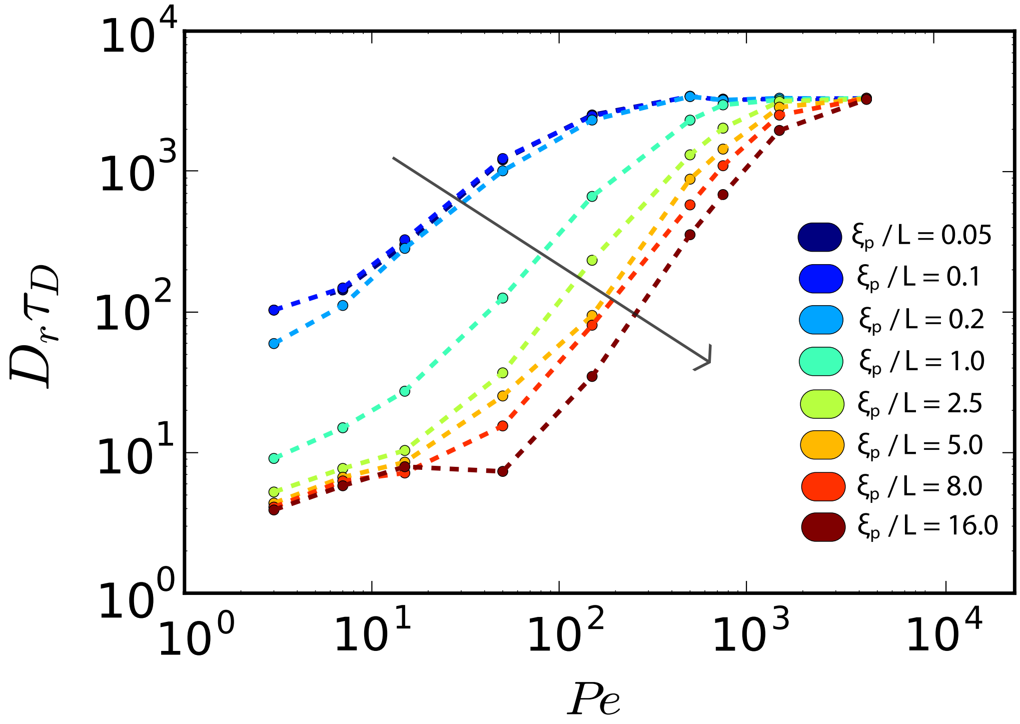

Figure 4.22.: Rotational diffusion coefficients as extracted from the MSR of the end-to-end vector of filaments a function of Pe. ξ_p/L values are given in the legend. The arrow indicates the direction of increasing ξ_p/L.

range of 0 to 2π. Then the total orientation of a filament is just the sum of the orientation differences across the bonds. Mean square rotation is then given by $\varDelta\theta^2(t) = \langle(\theta(t) - \theta(0))^2\rangle$. At intermediate propulsion, rotational diffusion of filaments increase with increasing rigidity (Fig. 4.21-a), while at high levels of propulsion the differences between rigidities disappear and mean square rotations fall onto the same curve (Fig. 4.21-b). The rotational dynamics of single filaments is observed to be dominated by internal flexibility of the filament at short lag times [88]. As shown for single filaments in eq. 4.2, the rotational diffusion coefficient is expected to grow linearly with the flexure number (*i.e.*, the ratio between the activity and the persistence length). This effect is diminished due to the collective motion effects, as the curves fall on top of each other for different ξ_p/L at high Pe. This can be attributed to an increase in the rotational motion of the filaments due to very frequent collisions at high Pe.

The rotational diffusion coefficients can be extracted from the average orientation of the end-to-end vector θ for each filament. Fitting its mean square rotation with $\varDelta\theta^2 = 2D_rt$ to the regime of the MSR with gradient unity in double-log scale yields the effective rotational diffusion coefficient D_r. As activity increases, the difference between D_r of different rigidities decreases until all the curves fall roughly onto the same point (Fig. 4.22). Filaments have a much shorter mean free path at high Pe, which causes them to rotate very frequently by bending upon collisions. As a result, rotational diffusion of filaments gets a significant activity-

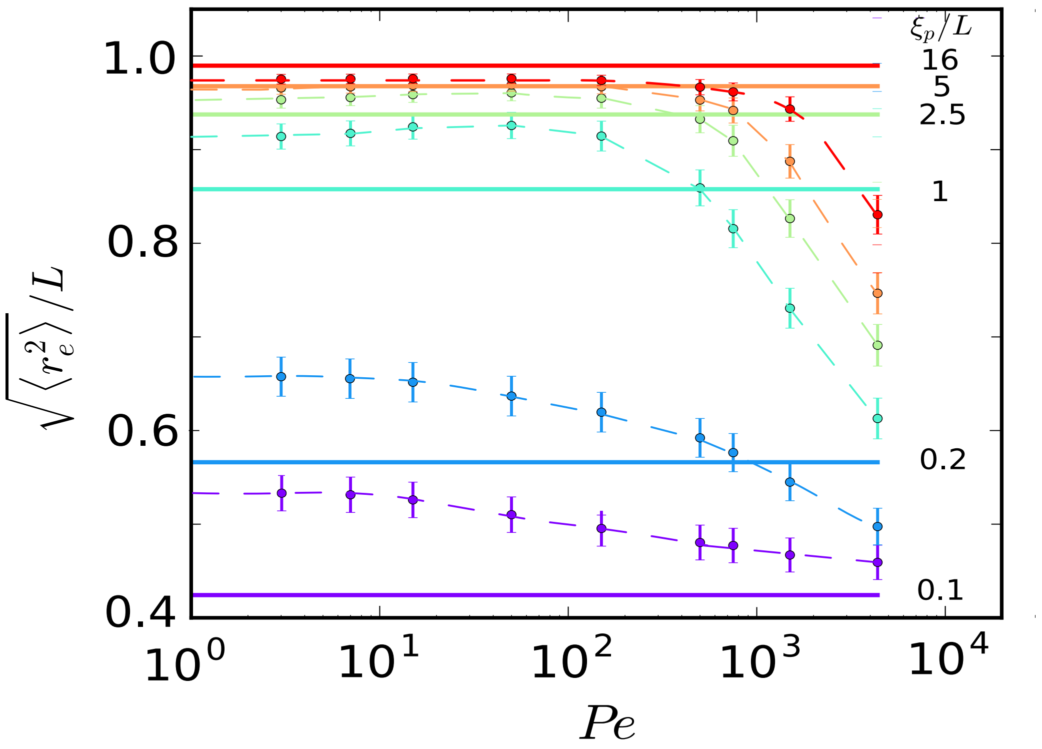

Figure 4.23.: Average end-to-end distance $\sqrt{\langle r_e^2 \rangle}$ of filaments with respect to Pe for different values of ξ_p/L. Solid lines show the theroretical values from the Kratky-Porod model.

enhanced contribution, which blurs the discrepancy between different rigidity regimes. In other words, the rotational diffusion coefficient no longer depends solely on the flexure number at high Pe due to the collective effects in the dynamical behaviour.

We calculate the average end-to-end distance $\sqrt{\langle r_e^2 \rangle}$ to quantify the structural properties of the filaments. The Kratky-Porod worm-like chain model, valid for passive filaments without volume exclusion, predicts[107]

$$\frac{\langle r_e^2 \rangle}{L^2} = 2\frac{\xi_p}{L} - 2\left(\frac{\xi_p}{L}\right)^2 \left(1 - \mathrm{e}^{-L/\xi_p}\right) \tag{4.6}$$

The end-to-end distances generally deviate from the Kratky-Porod prediction due to the excluded-volume interactions. However, for a single filament, the end-to-end distance is found to agree well with the Kratky-Porod prediction at high rigidities, whereas significant deviations occur at low rigidities due to spiral formation [88] For the collective dynamics, we find that the end-to-end distance $\sqrt{r_e^2}$ is nearly constant up to a critical Pe, then starts to decrease approximately logarithmically (Fig. 4.23). The critical Peclet number Pe_c decreases with decreasing ξ_p/L, roughly with a linear dependence, *i.e.* $Pe_c \sim \xi_p/L$. This behaviour is consistent with the dependence of the phase boundary of the giant-cluster phase at higher Pe in Fig. 4.6, which shows a similar linear dependence of $Pe \sim \xi_p/L$. Both of these observations

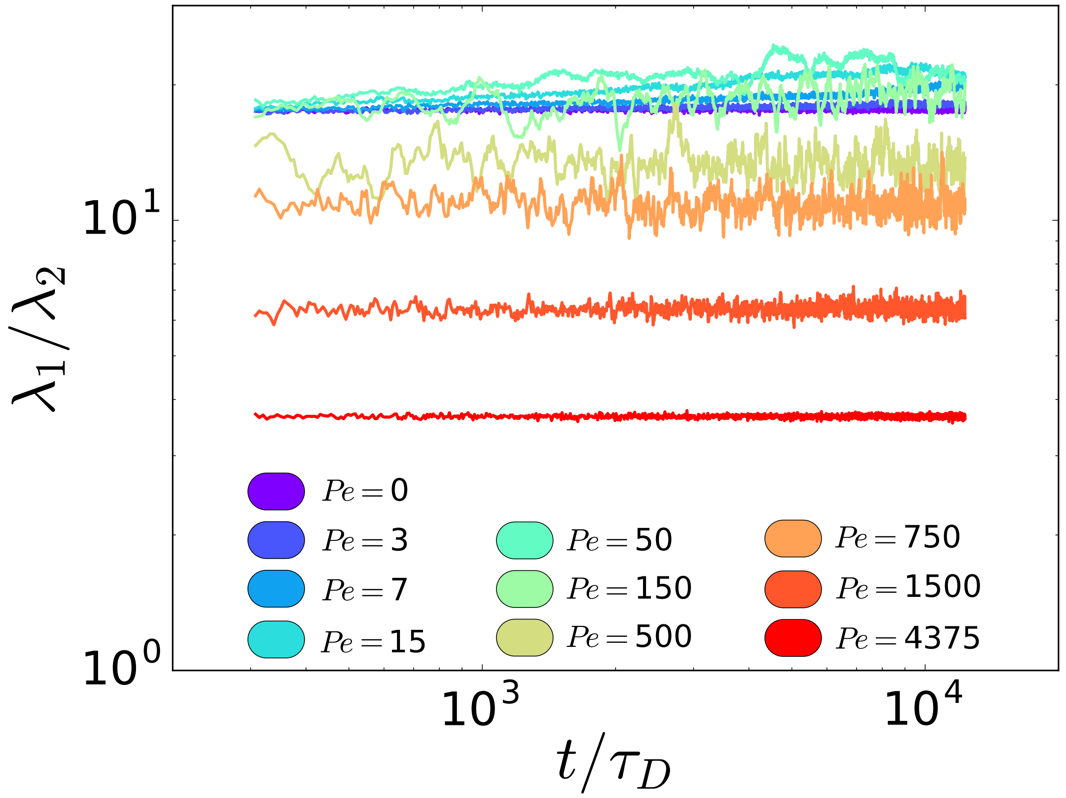

Figure 4.24.: Large to small eigenvalues ratio of the gyration tensor for $\xi_p/L = 200$ and changing Pe as depicted in the legend. Note that aspect ratio is $a = 25$.

indicate that the reentrant behaviour in Fig. 4.6 is due to a balance of propulsion and curvature forces. The giant clusters dissolve when propulsion forces ($\sim Pe$) become strong enough to significantly deform the filaments with bending-induced restoring forces ($\sim xi_p/L$).

We turn to the gyration tensor to further investigate the structural properties of the filaments. We calculate the ratio between the large and small eigenvalues of the gyration tensor and average it over filaments per time frame to characterize the shape of the filaments. When fixed at a high rigidity, the ratio increases first with increasing activity from $Pe = 0$ to $Pe \approx 150$, which corresponds to the mid-part of the giant clusters regime, and then starts to decrease (Fig. 4.24). It reaches its lowest value at the highest $Pe = 4375$. It indicates that giant cluster formation regime is associated with structurally elongated filaments, while melting of giant clusters into smaller clusters at high Pe is associated with bent-shaped filaments, which occur due to frequent collisions.

4.3.4. Dynamics of Giant Clusters

Giant clusters consist of polar ordered filaments. They occur in a part of the phase space wherein filaments are stiff ($\xi_p/L \geq 2$) and the propulsion force is at an intermediate value

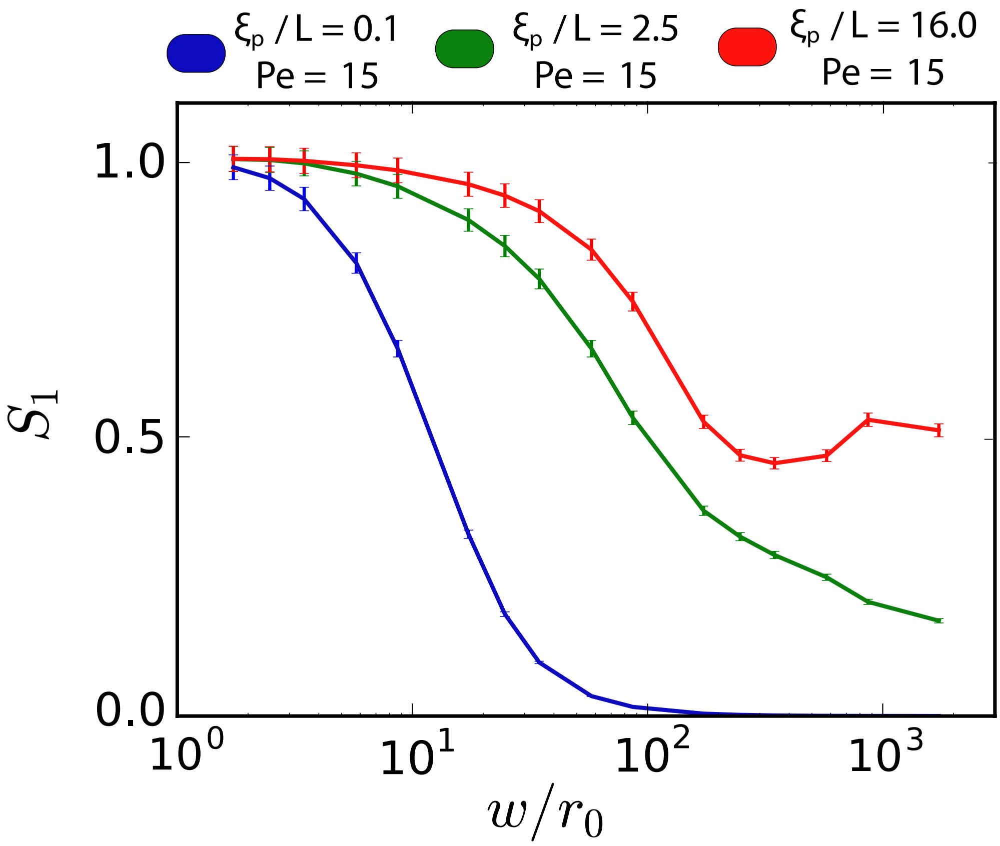

Figure 4.25.: Polar order parameter inside square boxes with respect to different box sizes. Colors correspond to different ξ_p/L values as given in the legend. $Pe = 15$ and $a = 25$ in all three curves.

($10^1 \leq Pe \leq 10^3$). We calculate the polar order parameter of the bond vectors,

$$S_1(w) = \langle |\langle e^{i\theta_j(t)} \rangle| \rangle, \tag{4.7}$$

where j denotes the bond identities within boxes of area w^2, and the averages are taken over bonds and time. In this way, we calculate the polar order locally inside square boxes and study it as a function of box size (see Fig. 4.25). As filaments become stiffer at intermediate activity, clusters of polar ordered filaments span larger and larger areas. The increase in polar ordering can be attributed to the alignment of stiff filaments upon collisions with the same mechanism as collision-induced alignment of self-propelled rigid rods [203].

Highly polar-ordered phases of self-propelled rods are observed to exhibit giant number fluctuations [65, 153, 152, 135]. Such fluctuations are given by the variance of the number of particles ($\Delta n^2 = \langle n^2 \rangle - \langle n \rangle^2$) within square boxes of varying sizes. For thermal motion accompanied with a homogeneous density distribution, the number fluctuations scale with $\Delta n^2 \approx n$, where n is the average number of particles (Fig. 4.26). We observe an increase in the power α in $\Delta n^2 \approx n^\alpha$ with increasing Pe when the rigidity is high ($\xi_p/L = 200$). It

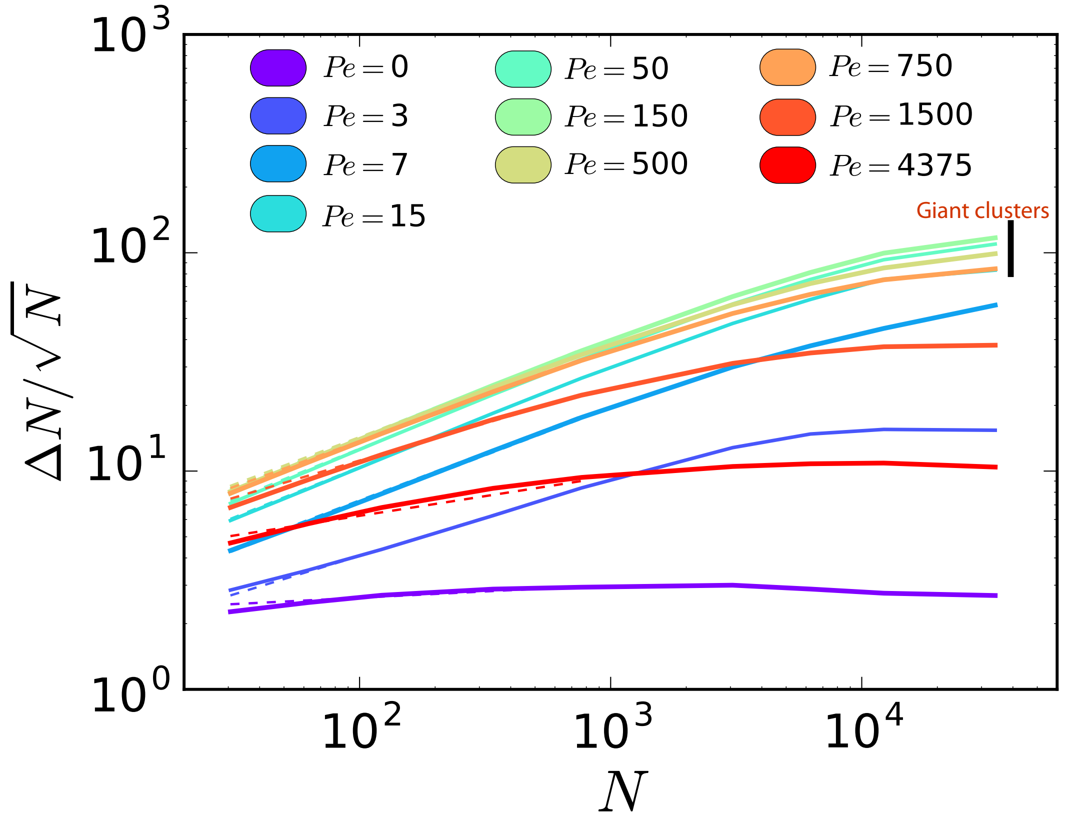

Figure 4.26.: Number fluctuations of beads in square boxes with respect to the average number of beads inside the box. The persistence length is fixed at $\xi_p/L = 16$ and aspect ratio at $a = 25$, while changing Pe is given in the legend. Power law fits are shown in the dashed lines. Giant clusters regime is marked with black line.

increases from $\alpha = 0.5$ at $Pe = 0$ up to $\alpha = 0.9$ at $Pe = 150$, which corresponds to the mid-part of the giant clusters regime. When Pe increases further, α decreases again all the way down to $\alpha = 0.6$ at $Pe = 4375$ (for comparison, a power of 0.8 is observed for rods in the giant-cluster regime) [65, 153]. Therefore, the giant-cluster regime is marked with giant number fluctuations due to the density inhomogeneities caused by clustering.

In forming giant clusters, active semiflexible filament ensembles behave similarly as ensembles of self-propelled rigid rods. However, even at high rigidities, flexibility plays a crucial role. One interesting manifestation of flexibility is in the collisions of giant clusters. For a dense system of active rigid rods, head-on collisions of large clusters are observed to lead to an accummulation of stress resulting in the formation of a jammed circular aggregate [203]. In an ensemble of active semiflexible filaments, on the other hand, filaments, either individually or in clusters, can open up channels inside the cluster they are hitting head on. They can bend their way through the antagonistic cluster until they escape (see Fig. 4.27).

Another interesting aspect of giant clusters is the ease of orientation-angle transmission between the filaments of a cluster. When the leading portion of filaments in the front part of

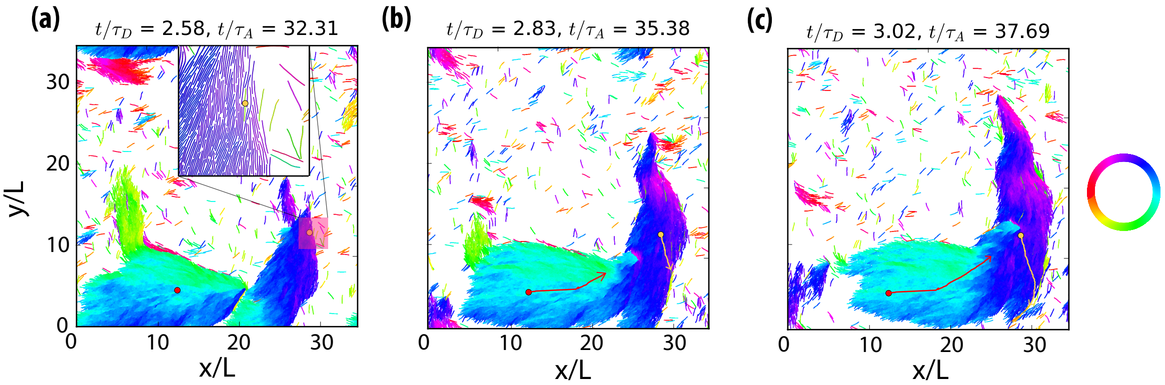

Figure 4.27.: Trajectory of the center of mass of a large cluster (red arrow) along with the trajectory of the center of mass of a filament moving upstream inside the same cluster (yellow arrow). The points denote the starting positions while the arrowa show the trajectory in time. The simulation pertains to the giant clusters regime with $\xi_p/L = 16$ and $Pe = 50$ and aspect ratio $a = 25$. Time increases from (a) to (c) with the color wheel indicating the bond orientations. Inset in (a) is a zoom-up to the antagonistic filament.

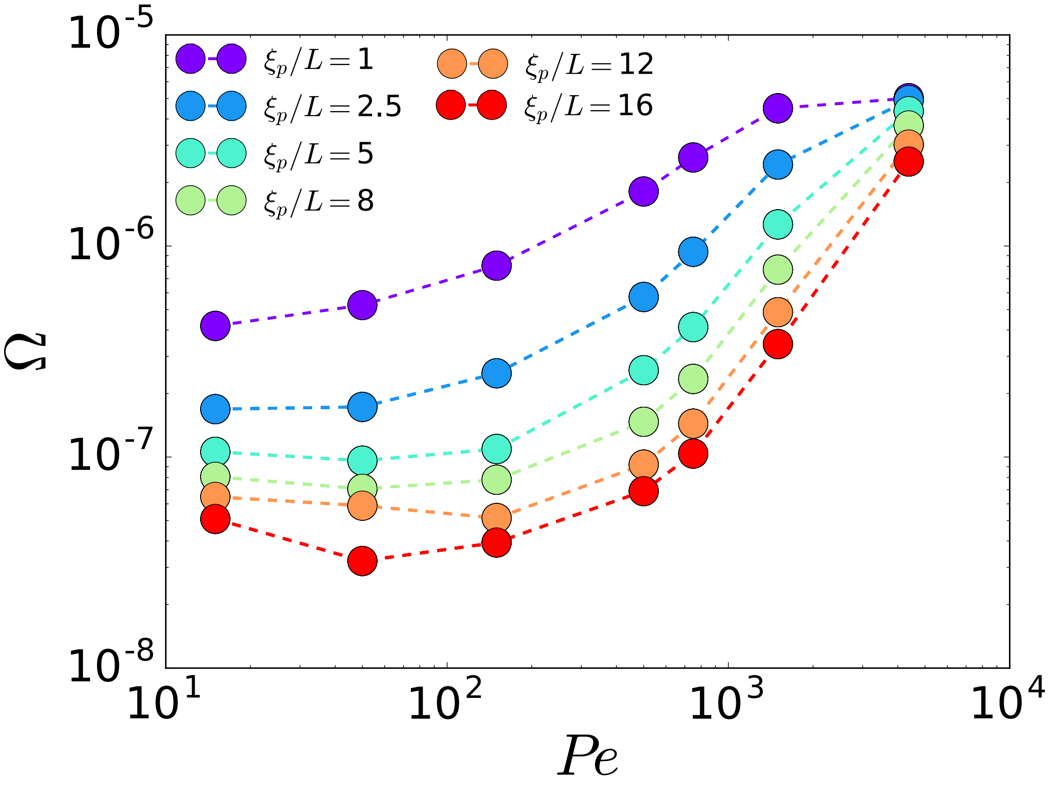

Figure 4.28.: Enstrophy Ω of the clusters as a function of Pe. ξ_p/L values are depicted in the legend. Dashed lines serve as guides to the eye.

a cluster change orientation, either due to a collision or thermal diffusion, the other filaments follow suit in reorienting themselves in the new direction and thereby they turn the entire cluster. As a result, giant clusters are rotating frequently and their shape is often curved and meandering (see Fig. 4.27).

We calculate the enstrophy per cluster (where clusters are identified as before) to quantify the rotational dynamics of clusters. We divide each identified cluster into small boxes of $2r_0$ and calculate its vorticity via $\omega = \partial_x v_y - \partial_y v_x$. Taking the square of the vorticity $|\omega|^2$ of each box and averaging it over the cluster yields the entrophy of the cluster. Averaging the enstrophy of each cluster per time and per cluster then gives an average enstrophy value of clusters for a given set of parameters. We do this calculation for the regime where reentrant clustering with activity is observed (see Fig. 4.28). As a general trend, enstrophy is observed to increase with increasing activity and decreasing rigidity, which corresponds with the scaling of rotational dynamics with the flexure number. However, as a deviation from this trend, the difference in enstrophy between different rigidities decrease with increasing activity. As activity is increased, filaments have shorter mean free paths, which makes them rotate more frequently upon collisions. This is a direct result of collective motion.

4.3.5. Isotropic-Nematic Transition

We investigate the isotropic-nematic transition properties of the passive semiflexible filament ensemble at $Pe = 0$ to compare with established analytical results. For an ensemble of passive impenetrable rigid rods, as there is no heat exchange and no work done on the ensemble, the only control parameter determining the phase behaviour is the density and the shape anisotropy. Onsager showed that with increasing density, rigid rod ensemble undergoes a phase transition from an initial isotropic state to a state with nematic ordering. The isotropic-nematic transition for rigid rods in $2D$ happens sharply at $\rho_c L^2 = 3\pi/2 = 4.712$ where ρ refers to the number density and L is the length of the rod [146].

To test this, for the passive semiflexible ensemble, we calculate the polar and nematic ordering for stiff filaments in the rigid rod limit (at $\xi_p/L = 16$). We make the calculation for two different densities. For a packing fraction of $\phi = 0.2$, we are very close to the Onsager transition with $\rho L^2 = 5$. For $\phi = 0.4$ with $\rho L^2 = 10$, we are well above the Onsager transition density. For each case, we find no polar ordering and very little nematic ordering at the level of the whole simulation box (see fig. 4.29). Nematic order parameter is significantly higher than polar ordering as collisions between filaments have only minor effects when filaments move without persistence in a given direction, and then the deciding factor in phase behaviour is entropically adventegous configuration of nematic ordered packing. Nematic order is observed to be high for short distances.

Polar order do not change in time while nematic order at the box level is increasing as time passes. Combining these two observations of nematic ordering at short length scales, and increasing nematic order with time, we expect that the system would eventually reach

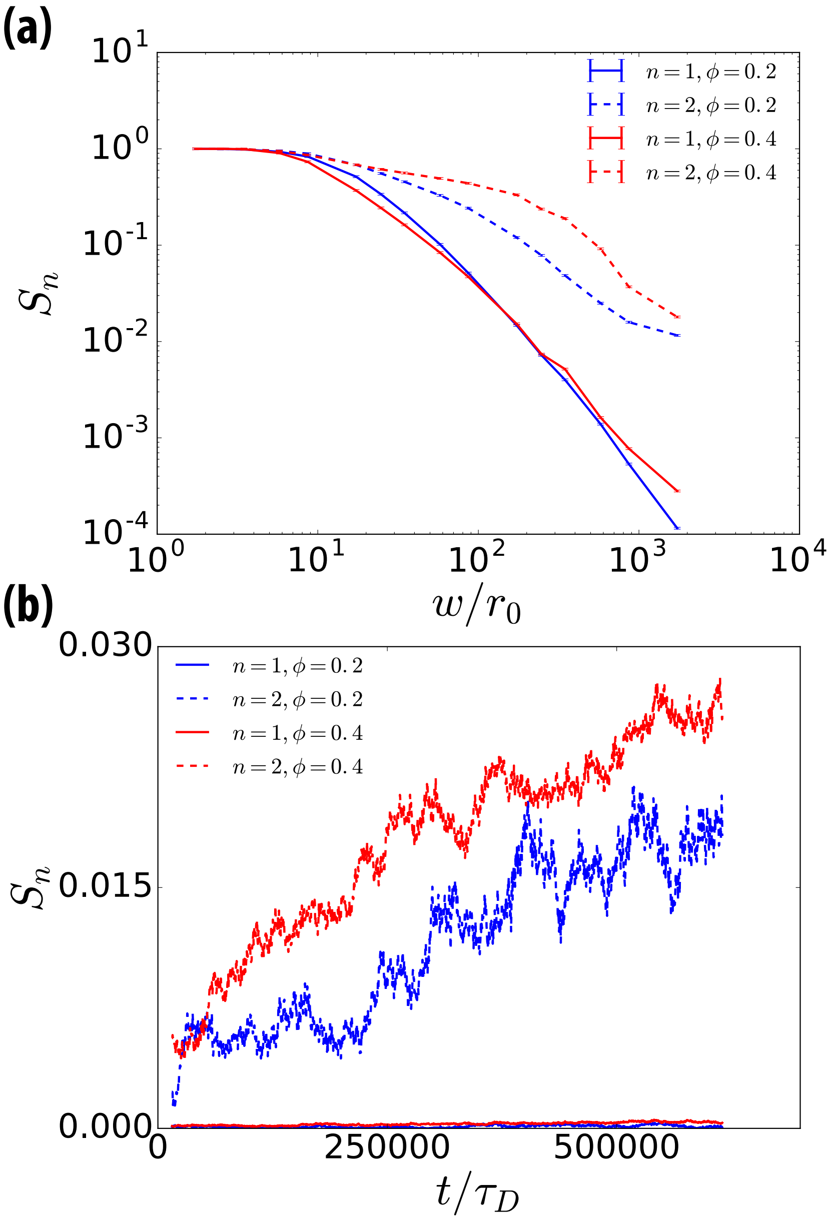

Figure 4.29.: Polar and nematic order parameters S_1 and S_2, respectively for $Pe = 0$ and $\xi_p/L = 16$. (a) Order parameters as a function of box size in which they are calculated. The legend shows the type of order parameter and the packing fraction. (b) Time evolution of the order parameters for different densities.

a globally nematically ordered state. However, we did not reach that stage in time due to the computational costs. We test this idea by looking at the simulation snapshots (see fig. 4.30). Nematic ordering is set up in small patches that slowly grow in time. Each patch with a curvature has an elastic energetic cost, so each curvature generates a current until all the curvatures disappear in a globally nematic ordered phase.

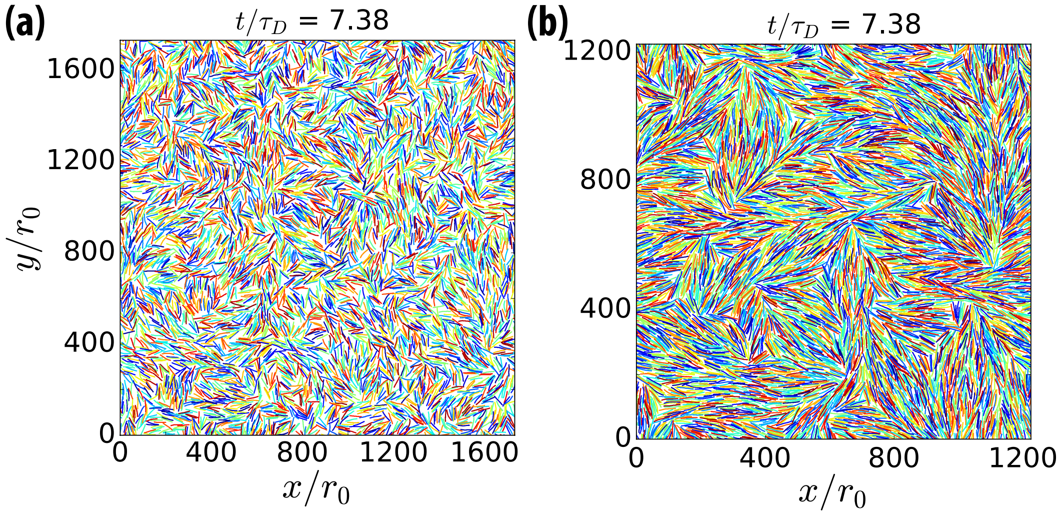

Figure 4.30.: Simulation snapshots of an ensemble of filaments at $Pe = 0$ and $\xi_p/L = 16$, for densities of (a) $\phi = 0.2$ and (b) $\phi = 0.4$, both above the isotropic-nematic transition density. The color code is the color wheel denoting bond orientations.

4.4. Collective Dynamics at High Densities

Density acts as an additional constraint on filament motion. Starting from finite densities, the number of collisions increases with increasing filament concentration. At high densities, motion of individual filaments becomes increasingly hindered by neighbouring filaments. At low ξ_p/L and Pe, filaments get jammed into a configuration where structural rearrangements become extremely rare. The jammed configuration consists of packs of filaments stacked around one another (Fig. 4.31-a). When Pe is increased to 9.3, packs of filaments push increasingly harder against other packs of filaments. Once a pack overcomes the energy barrier needed to break out of the jammed configuration, it moves by pushing the pack blocking it, which creates a propagating stress front. Such patterns of stress fronts with polar-aligned filaments pushing against perpendicularly oriented filaments resemble a +1/2 topological defect pattern. When these stress fronts collide at $\pi/3$ angle, their motion becomes hindered again. The collision centre constitutes a $-1/2$ topological defect. Stress in the system accummulates in the core of the defect. Nematic defect dominated dynamics of filaments is referred as the active turbulent phase. In this phase, a multitude of spatial and temporal scales are excited, which generates a displacement pattern resembling the spatiotemporal chaos associated with turbulent motion (Fig. 4.31-b). This chaotic motion is only transitory in time, and at late times, the system relaxes into a regime in which move in very large bands moving against each other, or in lanes where every filament moves in the same direction (Fig. 4.31-c). The active turbulence remains in the steady state only at higher Pe, wherein laning becomes instable. Therefore, the onset of steady-state active turbulence is determined by a balance between active forces and bending forces, which set a correlation length for the collective dynamics at high densities.

Increasing Pe, or reducing ξ_p/L decreases the effective persistence length of filaments, which then decrease the correlation length of the motion. At large correlation lengths, filaments form lanes, whereas at lower correlation lengths, laning becomes instable, and filaments move in turbulent patterns.

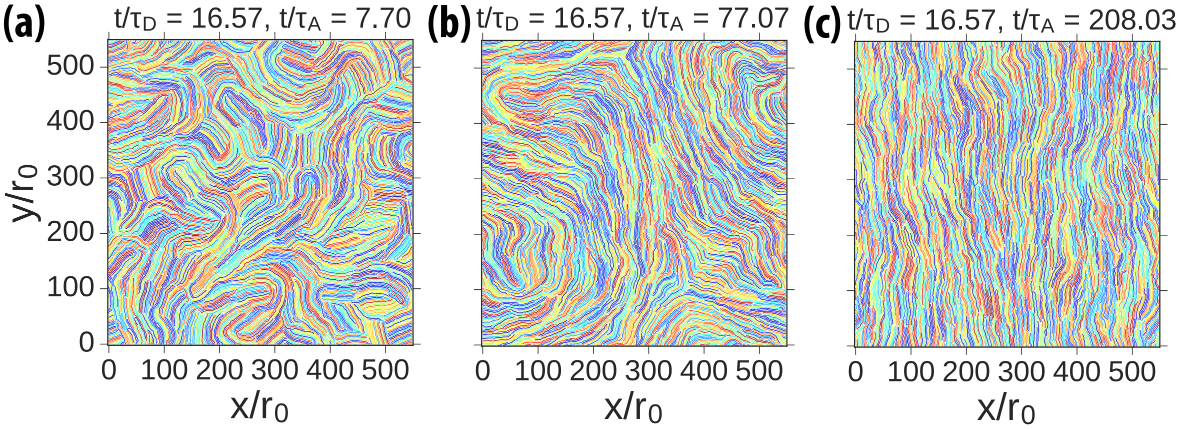

Figure 4.31.: Simulation snapshots of an ensemble of filaments depicting the phases observed at $\phi = 0.8$ for (a) jamming phase at $Pe = 0.93$, $\xi_p/L = 0.2$, (b) active turbulence at $Pe = 9.3$, $\xi_p/L = 0.2$, and (c) band formation at $Pe = 24$, $\xi_p/L = 0.2$.

The phase dynamics at high densities is determined with the extent and the correlations of filament motion. When filaments are stuck in their configuration, the dynamics is jammed. When filaments are able to break out of the cages formed by their neighbours, the dynamics is determined with the correlation length of displacements, which is set by Pe and ξ_p/L. Increasing Pe and ξ_p/L increases the correlation length, as the correlation length reaches the system size, the dynamics changes from defect-dominated spatiotemporal chaos of active turbulence to lane or band formation.

Mean square displacement is diffusive with a slope α of t^α close to 1 in the jamming phase. In this phase, filaments diffuse a distance smaller than their body length. At $\xi_p/L = 0.2$ and $Pe = 0.93$, filaments are jammed in stacks (Fig. 4.32-a). As Pe is increased to 9.3, MSD displays a staggered behaviour with early-time diffusive motion, intermediate-time superdiffusive motion which then relaxes to diffusive motion at late times. At early times, filament motion is hindered by the surrounding neighbour filaments which results in diffusive motion. Intermediate-time superdiffusive motion corresponds to the motion of a group of cooperatively moving filaments pushing other filaments. At later times, such cooperative motion becomes diffusive as the orientational memory of filaments is lost. Increasing Pe to 25.12 results in superdiffusive motion. In this regime, filaments break out of cages completely due to increased self-propulsion and the correlation length of motion increases to system size. As such, filaments move in the same direction in a system-wide lane, each filament performing directed motion. At $Pe = 93.03$, MSD is ballistic at early times and then diffusive at late times. Correlation length decreases from system size to an intermediate value as Pe is increased from 25.12 to 93.03. As a result, the dynamics is dominated by topological defects and spatiotemporal chaos.

With increased ξ_p/L to 0.79, the dynamics as a function of Pe remains similar (Fig. 4.32-b). The ensemble is jammed at $Pe = 0.93$. Filaments move in groups with significantly slowed down dynamics at $Pe = 9.3$ that result in a staggered MSD. $Pe = 25.12$ corresponds to laning with filaments performing directed motion. The main difference between $\xi_p/L = 0.2$ and $\xi_p/L = 0.79$ occurs at $Pe = 93.03$. At $\xi_p/L = 0.2$, the correlation length is at intermediate levels which results in active turbulence. The correlation length is longer for $\xi_p/L = 0.79$. Therefore, instead of a turbulent regime, filaments move ballistic in bands.

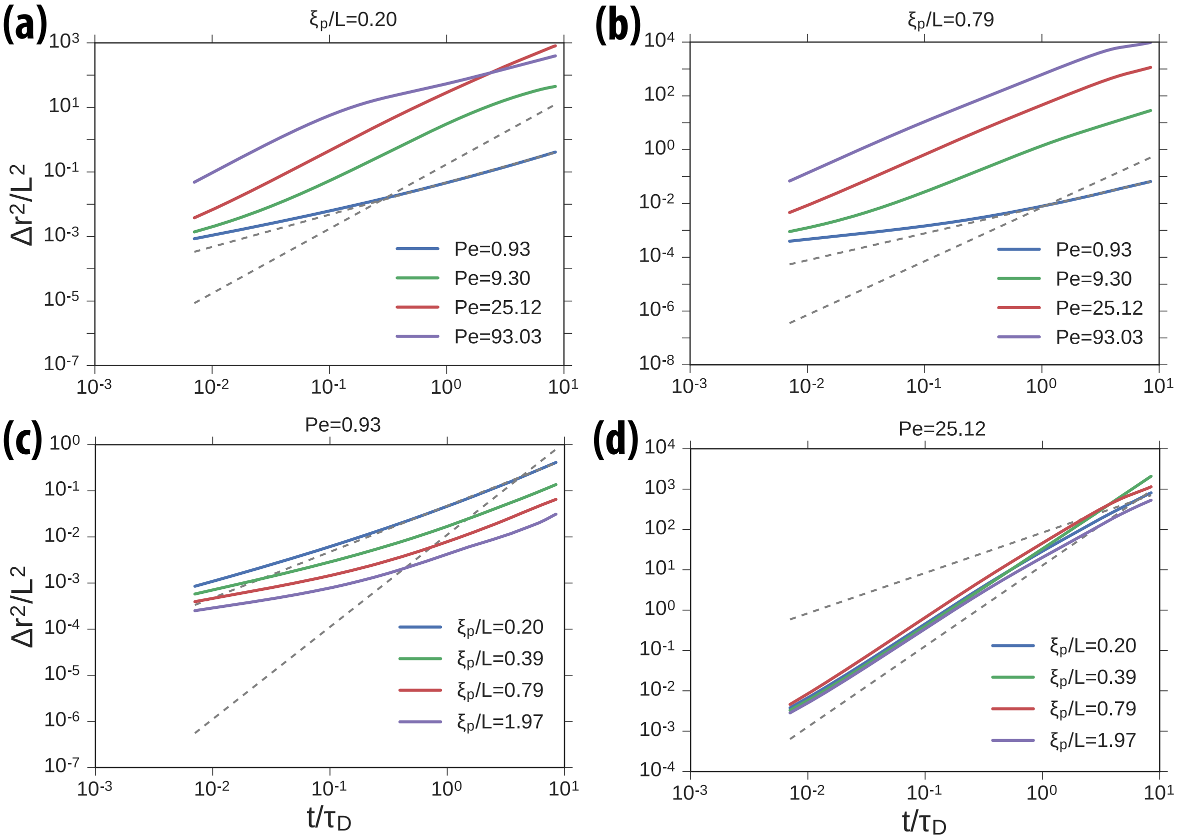

Figure 4.32.: Mean square displacement of the center of mass of filaments at $\phi = 0.8$ for (a) various Pe at $\xi_p/L = 0.2$, (b) various Pe at $\xi_p/L = 0.79$, (c) various ξ_p/L at $Pe = 0.93$, (d) various ξ_p/L at $Pe = 25.12$. The gray dashed lines indicate slopes of 1 and 2, indicating diffusive and ballistic motion, respectively.

At $Pe = 0.93$, filaments are jammed with diffusive and subdiffusive motion at ξ_p/L from 0.2 to 1.97 (Fig. 4.32-c). As Pe increases to 25.12, the ensemble undergoes a transition from jamming to laning or band formation (Fig. 4.32-d). With self-propulsion at intermediate values, the correlation length is long and as such, filaments move in very large groups in a cooperative manner.

The relaxation time of structural rearrangements in the ensemble can be characterized with self-part of the intermediate scattering function. We set a length threshold of $k = 2\pi/L$ for

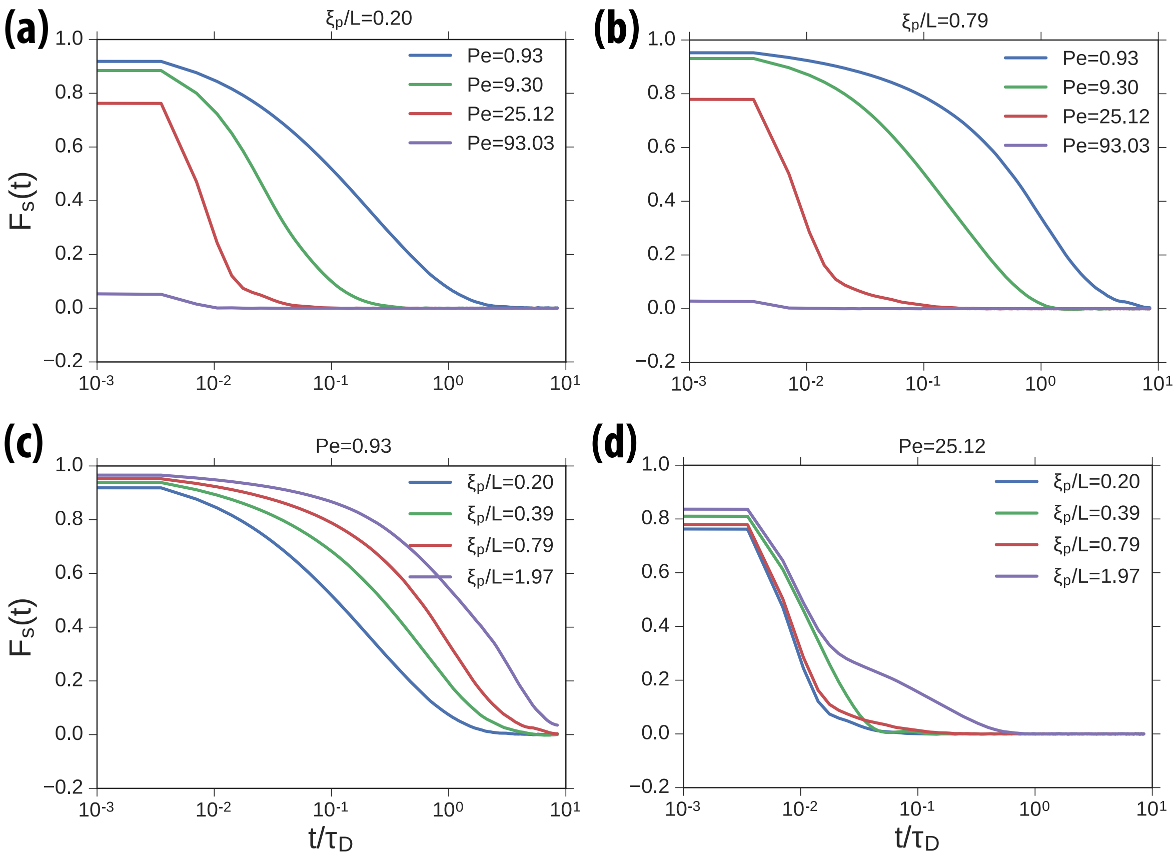

Figure 4.33.: Self-part of the intermediate scattering function of center of mass of filaments for $k = 2\pi/L$ at $\phi = 0.8$ for (a) various Pe at $\xi_p/L = 0.2$, (b) various Pe at $\xi_p/L = 0.79$, (c) various ξ_p/L at $Pe = 0.93$, (d) various ξ_p/L at $Pe = 25.12$.

rearrangements. The relaxation time increases dramatically from $< 0.001\tau_D$ to $0.5\tau_D$ as Pe is increased from 0.93 to 93.03 at $\xi_p/L = 0.2$ (Fig. 4.33-a). As ξ_p/L increases to 0.79, the maximum relaxation time we observe increases to $1.1\tau_D$ (Fig. 4.33-b). At $Pe = 0.93$, filaments are jammed with high relaxation times. The relaxation time increase from $0.5\tau_D$ to $1.3\tau_D$ as ξ_p/L increases from 0.2 to 1.97 (Fig. 4.33-c). At $Pe = 25.12$, there is lane and bands formation. As a result, the relaxation times are low $\sim 0.03 - 0.06$ (Fig. 4.33-d).

We quantify the structural properties of the ensemble by calculating the pair correlation function of the center of mass of filaments. Structural order is dominated by orientational order at high densities due to the extendedness of filaments. As such, we only find small peaks at first and second neighbour distances corresponding to multiples of body length of filaments in pair correlation function. The most significant peak occurs at the effective diameter σ of beads. The magnitude of the peak decreases as Pe increases at $\xi_p/L = 0.2$ and $\xi_p/L = 0.79$ with reducing structural order (Fig. 4.34-a-b). Structural order is highest at the jamming phase corresponding to low Pe. At $Pe = 0.93$, structural order decreases with increasing ξ_p/L (Fig. 4.34-c). At low ξ_p/L, filaments are able to bend and relax into their extended forms from their

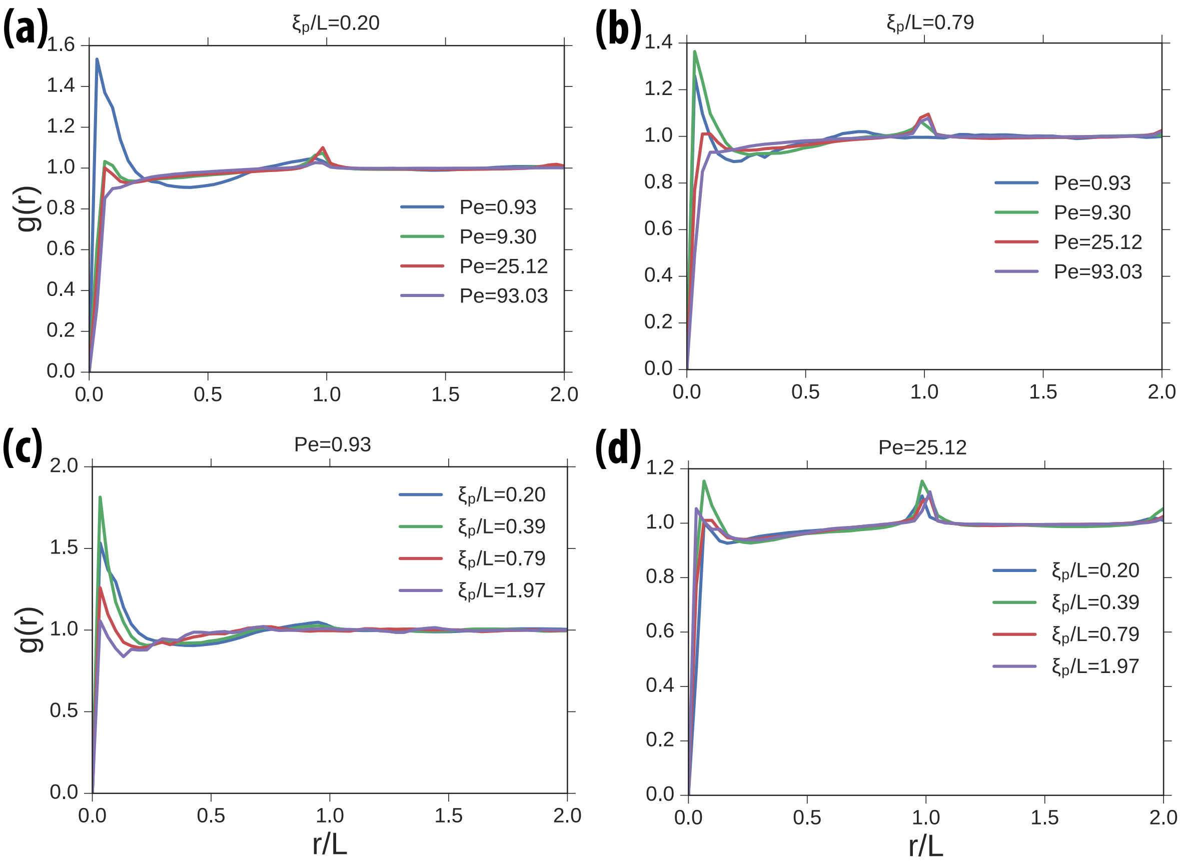

Figure 4.34.: Pair correlation function of center of mass of filaments at $\phi = 0.8$ for (a) various Pe at $\xi_p/L = 0.2$, (b) various Pe at $\xi_p/L = 0.79$, (c) various ξ_p/L at $Pe = 0.93$, (d) various ξ_p/L at $Pe = 25.12$.

initial configuration which increases the structural order. As ξ_p/L increases, bending costs more energy and filaments are stuck in compressed configurations. At $Pe = 25.12$, there are periodic small peaks at multiples of body lengths of filaments (Fig. 4.34-d). Filaments are spatially ordered in a lane structure at this regime. However, spatial order is not reflected as peaks of higher magnitude, because the order is anisotropic.

We calculate the spatial velocity correlation in the center of mass frame of the ensemble to analyse the length scales of correlations. At $\xi_p/L = 0.2$, the correlation length increases to 1 filament length as Pe increases 100 times from 0.93 (Fig. 4.35-a). In the jamming regime, velocity correlations span small distances and they relax to zero. Band formation is reflected as a negative tail in the spatial velocity correlation, as bands move opposite to one another. There is also a small peak in multiples of body lengths that arises from anisotropic spatial correlations. In the active turbulence phase, correlations are at an intermediate length and they decay to zero.

At $\xi_p/L = 0.79$, velocity correlations decay to zero with very small correlation lengths for $Pe = 0.93 - 9.3$ corresponding to jamming regime (Fig. 4.35-b). For $Pe \geq 25.12$, velocity

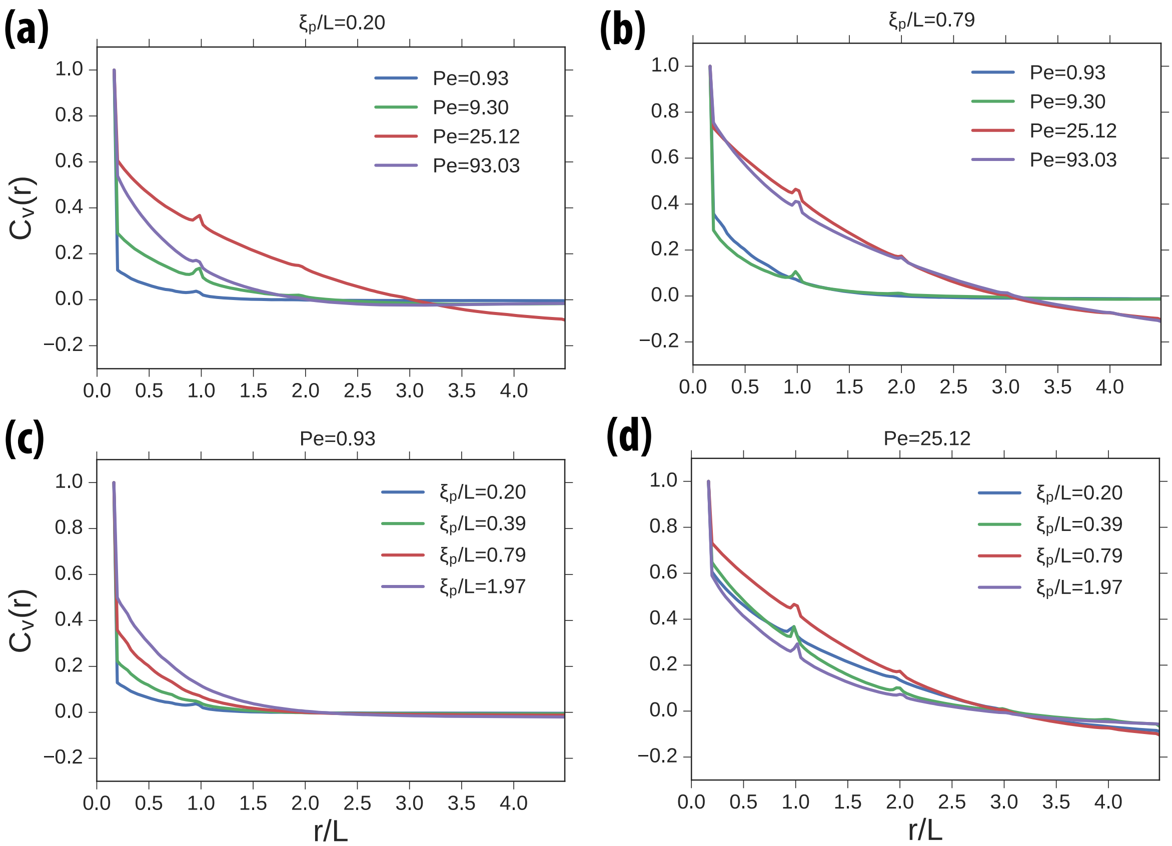

Figure 4.35.: Spatial velocity correlation of center of mass of filaments in the center of mass frame of the ensemble at $\phi = 0.8$ for (a) various Pe at $\xi_p/L = 0.2$, (b) various Pe at $\xi_p/L = 0.79$, (c) various ξ_p/L at $Pe = 0.93$, (d) various ξ_p/L at $Pe = 25.12$.

correlations are on the order of $1.4L$ with negative tails corresponding to laning and band formation regime. At $Pe = 0.93$, the ensemble is jammed and correlation length increases with increasing ξ_p/L (Fig. 4.35-c). At $Pe = 25.12$, the phase dynamics is determined with band formation and lanes that is reflected as long correlation lengths with negative tails (Fig. 4.35-d).

We identify the half-integer topological defects to characterize the active turbulence phase in somewhat more detail. To identify defects, we first choose random points in the system and calculate the average nematic director around the chosen point within a circle that is divided into 8. The rotation of the nematic director around the point gives the defect strength of the randomly chosen point. If the found defect strength is within 0.1 of 0.5 or −0.5, then we identify the point as a possible defect point and look at 10 more points around the possible point. If one of the neighbour points is a possible defect, then we look at 10 more points around the new possible point and so on. Once the recursive search for possible defect points is completed, we calculate the center of mass of possible defect points weighted by their defect strengths to pinpoint the defect core with more precision (Fig. 4.36).

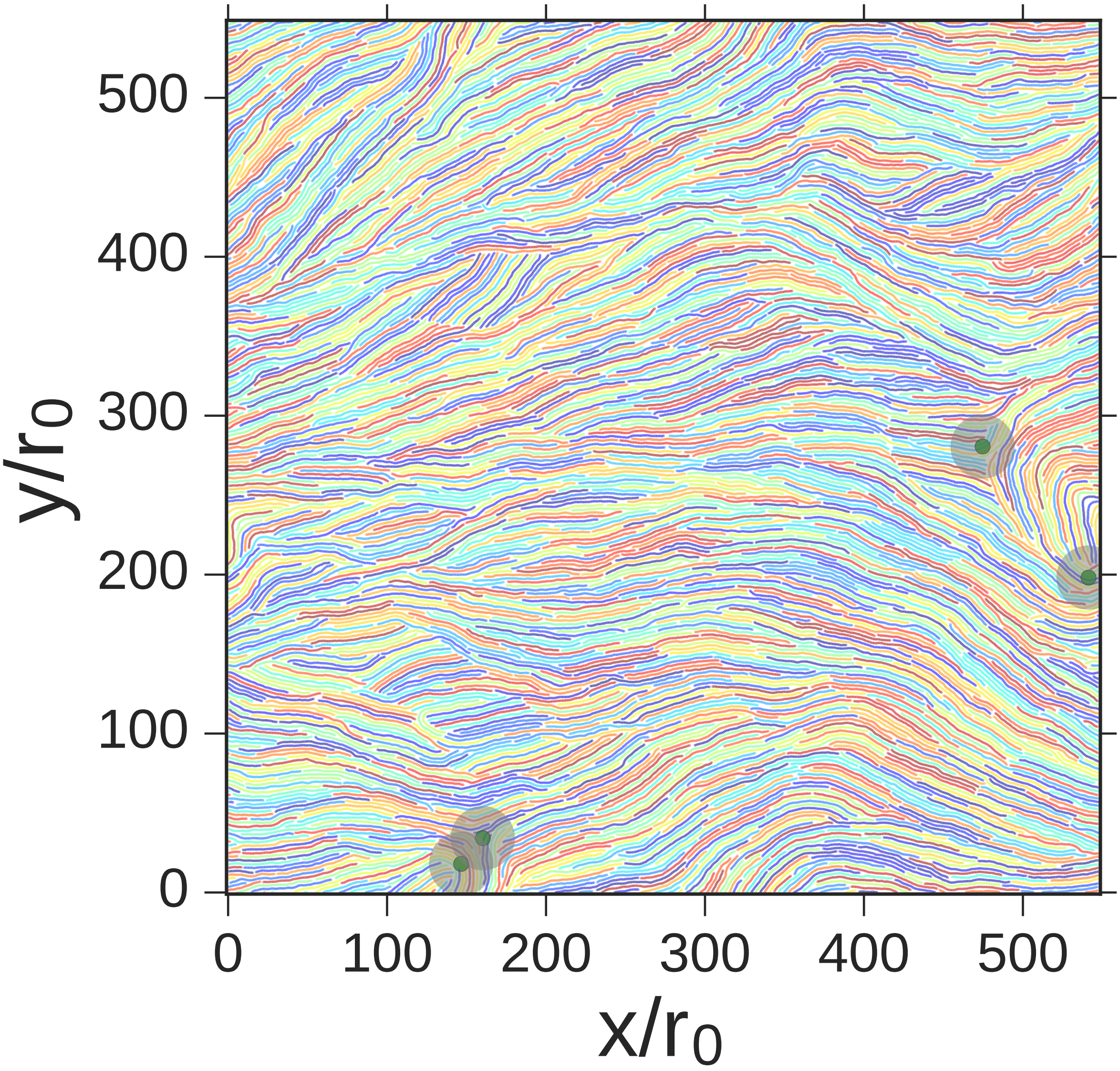

Figure 4.36.: Positions of half-integer topological defects for $Pe = 16$ and $\xi_p/L = 0.96$. The defect cores are colored green and the interrogation circle within which the rotation of the nematic director is calculated is shaded in gray.

The number of defects remain approximately constant in the active turbulence phase. In the laning phase, the number of defects decreases sharply once the steady state sets in (Fig. 4.37). Therefore, defect-dominated dynamics is only transient before filaments align either in lanes or in bands for the laning regime.

4.5. Discussion

The extended and flexible nature of filamentous objects allow deformations and self-interactions. This additional degree of freedom enhances the importance of individual filaments in the col-

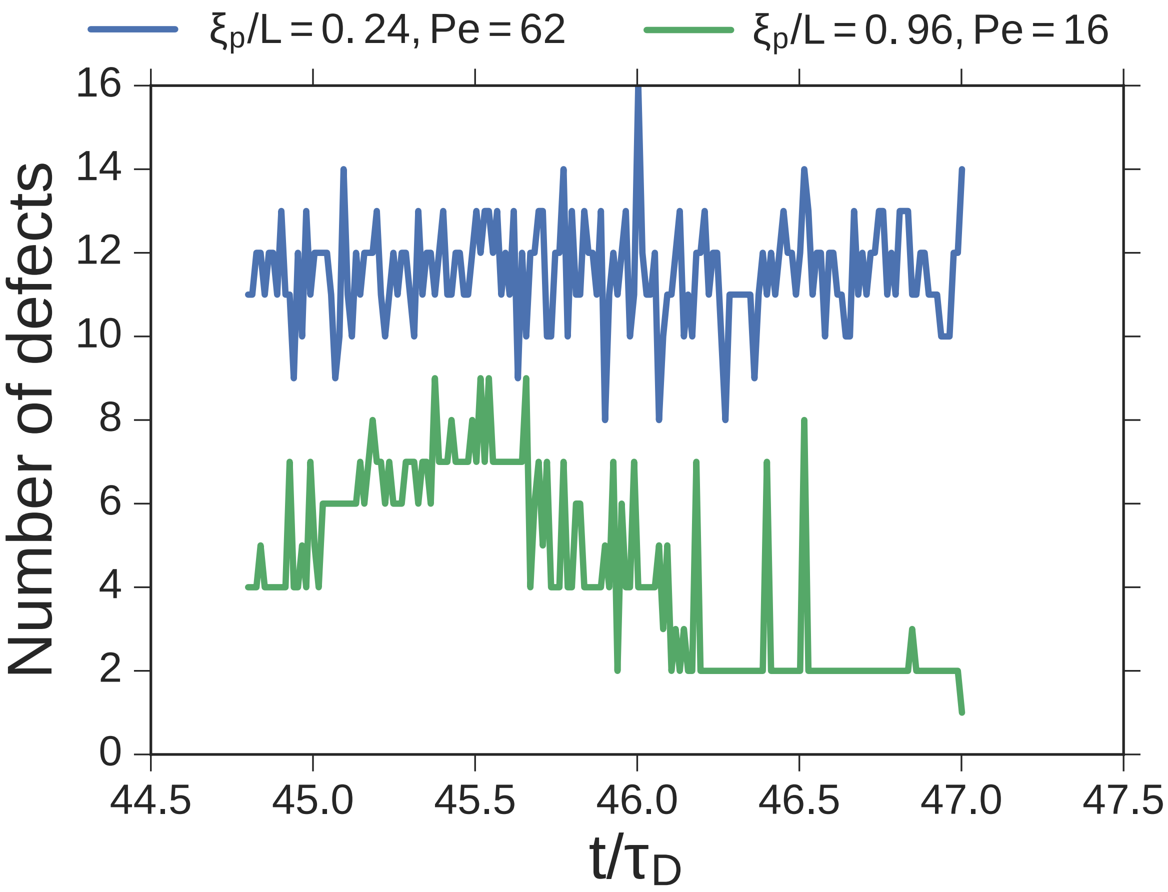

Figure 4.37.: Number of defects as a function of time for $\xi_p/L = 0.24$ and $Pe = 62$ and $\xi_p/L = 0.96$ and $Pe = 16$.

lective dynamics. When the individual filaments are at low rigidity, filaments are bent, inhibiting the filament extension and directionality of motion. The resulting ensemble is weakly interacting, akin to a gas, as embodied in the gas-like dynamics of spirals and gas of clusters regimes. Stiff filaments, on the other hand, have extended rod-like shapes. They form larger and more persistent clusters that are strongly cooperative in dynamics. Such filaments inside giant clusters not only point in the same direction, but also follow the change in orientation of other constituent filaments. In this way, spirals and giant clusters are results of the interplay between the extended and flexible nature of the filaments.

The change from the spiralling state, where filament motion is constrained, to the clustering state, where filaments move in groups in an aligned fashion, represents dramatically different routes as to how the propulsion force induces structure formation. In the clustering state, the propulsion force driving the system out of equilibrium is used for the movement of filaments whereas, in stark contrast, it is used for shape change to sustain a slowed-down steady state in the spiralling case. It is indeed peculiar for an active system to turn inactive by a shape change without the involvement of an external cue. Actin filaments and microtubules in motility assays are found to exhibit this type of frozen steady state notwithstanding their activity [173].

Activity enhances the ability of filaments to explore the rich configurational space provided by flexibility and aspect ratio. Therefore, the resultant phase space displays a spectrum of phases that mimic the behaviour of other non-equilibrium systems. In the gas of spirals phase, filaments effectively perform thermal motion analogous to an ensemble of passive point particles. In the gas-of-clusters regime, on the other hand, filaments organize in small and short-lived clusters, reminiscent of the dynamical clusters observed for self-propelled point particles [21, 1, 211]. Stiff filaments behave like self-propelled rigid rods in forming structures like giant clusters. In this respect, the collective dynamics of active semiflexible filaments provides a rich framework where different non-equilibrium behaviour can be accessed. This can prove useful both in experimental applications and in distinguishing the rich behaviour of biopolymers and filamentous structures in biology.

The changing cluster dynamics with activity and flexibility can be understood by analysing the collisions. An increase in activity leads to an increased number of collisions which trap filaments for a duration that is proportional with their persistence in orientation. As a result, filaments form clusters with increasing activity due to collision-mediated self-trapping. However, the effect of collisions depends strongly on the flexibility of filaments. When filaments are stiff, they are structurally more elongated. In this regime, colliding filaments align in parallel or anti-parallel directions depending on the angle of collision being acute or obtuse, respectively. Flexible filaments, on the other hand, are easier to be bent upon collisions, which makes them reorient frequently. Therefore, clustering gets enhanced with increasing rigidity, but decreases again at high levels of activity. It can be argued that the cluster formation is a density-driven effect for flexible filaments, hence the formation of small and transient clusters, whereas it is an alignment-driven effect for stiff filaments, hence the large and persistent clusters.

It is important to highlight the differences between self-propelled rigid rods and semiflexible filaments. Stiff filaments are elongated in a way that resembles rigid rods. Hence, both systems form giant clusters as a result of alignment upon collisions. However, flexibility of filaments still reflects itself even in the rigid rod limit. Filaments can penetrate through antagonistically oriented clusters, as they can bend, which alters the stress accummulation mechanism in the ensemble. Therefore, some of the phases observed for active rigid rods, like giant jammed structures,[203] disappear for semiflexible filaments. Another important difference is that, when the leading tip of a filament turns by bending, the body of the filament bends in the same direction. As a result of this ease in reorientation, stiffer filaments can easily rotate even at very high rigidities. Consequently, giant clusters of filaments are often in curved and meandering form and change their direction of motion frequently. Such clustering dynamics is very similar to the dynamics of bird flocks and fish schools, where the collective dynamics is set by a number of leaders [133, 24].

Individual filaments scatter and reorient too often to form larger and more persistent clusters at high levels of activity. Therefore, giant clusters disappear at high propulsion strengths, in contrast to impenetrable rigid rods [213]. Similar behaviour of non-monotic cluster size with self-propulsion is also observed in ensembles of self-propelled overlapping rods and self-propelled colloids with short-range attractive interactions [128, 132, 1].

The observed phases in the active semiflexible filament collective can be used in a tunable fashion. The system can be switched from a moving state with aligned filaments moving together to a frozen steady state with coiled filaments. This parameter-dependent effect can be used as a tunable switch in micro- and nano-technology, for which the first steps have already been made [80]. Besides the possible technological function, this type of self-organization also has a functional role in living matter. In a plant cell, microtubules form cortical arrays, which are curved and rotating structures in a two-dimensional plane along the cell wall, to provide stability and growth to the cell wall [25]. Slender bacteria are observed to form spiral structures through mechanical interactions when put in a bath of shorter cells [117]. With their structural and dynamical resemblance to active semiflexible polymers, there is a plethora of biological systems like actin filaments and microtubules on molecular motor carpets, which can self-organize into spirals or into rotating clusters based on their level of rigidity, activity and aspect ratio. Our work can help in construction of such *in-vitro* experiments. Additional effects like hydrodynamic interactions may need to be included in the interpretation of experimental results on microtubules in motility assays [37]. Simulation studies of active polar semiflexible filaments in the dilute regime indicate a qualitatively similar behaviour with and without hydrodynamics [94, 93].

4.6. Summary

We have studied the collective dynamics of active semiflexible filaments in a low-density, two-dimensional system with steric interactions. With a minimal active polymer model, we are able to capture rich dynamical behaviour. The collective dynamics has the hallmarks of a passive homogenous melt for low propulsion strengths. Filaments organize in small and transient clusters similar to the dynamical clusters observed in active point particles when the propulsion is increased. As the rigidity is increased, we find that filaments form giant clusters like self-propelled rigid rods, when they are propelled at intermediate levels of activity. Compared with rods, clustering is not homogenous with activity due to the reorientation of filaments upon collisions. The aspect ratio of filaments plays an important effect in the dynamics of strongly propelled and flexible filaments. Such filaments self-organize in different configurations of spiral aggregates in which they perform diffusive motion.

5. Concluding Summary

Collective behaviour is a hallmark of life. From bird flocks to bacterial swarms, organisms across many length scales gather in many different ways and form moving groups that display a myriad of patterns. Although each pattern is different in the way it is generated, we can still gain valuable insight by dissecting pattern formation into its minimal ingredients. This enables us to generalize collective motion across length scales as well as domains between living and inert matter. In this thesis, we have studied the collective behaviour of motile cells and self-propelled semiflexible filaments with a minimal-model approach. By identifying the collective dynamics as functions of mechanical properties of individual constituents, we identify the role of simple mechanical rules that can give rise to complex collective motion.

We have developed a novel computational model of motile cells as active vesicles. The model allows to incorporate cell-cell adhesions, cell motility, compressibility, and deformability as independent parameters. We study the role of each single-cell parameter in the collective motion of dense cell monolayers. We identify three phases (gas, active turbulence, and jamming) in terms of the degree of cell motion and correlations. A decrease in adhesion, compressibility, or bending rigidity, or an increase of motility forces lead to an overall increase of cell motion and reduce the correlation length, resulting in an effective fluidization of the monolayer. At the completely fluid-like phase, cells displace large distances in an uncorrelated manner.

Going in the opposite direction of fluidization in the phase space reduces the degree of cell motion and increases the correlation length. At this intermediate regime, cells move in vortices and swirls resulting in dynamics reminiscent of inertial turbulence. We identify the origin of turbulent dynamics in the correlated motion of cells, which generates an effective inertial regime at the length scale of correlations. However, unlike inertial turbulence, this effective inertial regime is not universal, but changes with the correlation length. As cells move correlated on a multitude of length scales, the spectrum of energy injection is broad in active turbulence. Therefore, we observe a kinetic spectrum that deviates from Kolmogorov scaling.

Driving cells further away from fluidization by decreasing motility, or increasing adhesion, compressibility, or self-deformability leads to a jamming state in which cell motion is significantly hindered. The correlation length increases towards the system size inside the jamming phase.

In-vitro experiments on Madin Darby canine kidney cells, zebrafish embyonic cells, and human bronchial cells revealed jamming transitions of cell monolayers that are driven by various factors such as density, cell-cell adhesion, and cell shape [4, 175, 151, 62]. Our results provide a phase diagram of motile cell monolayers in terms of single-cell properties. In particular, we identify a deformability-driven jamming transition and an active turbulence phase in between the jamming and completely fluid-like phases.

As a second example of collective motion, we have studied ensembles of self-propelled semiflexible filaments. Inspired by the gliding motility assays of microtubules and actin filaments with a homogeneous motor distribution, we introduce self-propulsion to semiflexible filaments as a constant magnitude force acting tangentially along the bonds. We find that filaments form clusters with increasing activity. Rigidity of filaments alters the cluster dynamics. Filaments organise into large and long-lived clusters at high rigidity, whereas they form small and transient clusters at low rigidity. The clustering of filaments displays a reentrant phase behaviour as a function of activity, as large clusters of high rigidity filaments melt into smaller and transient clusters due to increasing self-propulsion forces enhancing the rotational dynamics of filaments. At values of low rigidity and high aspect ratio, we identify a transition from a free-swimming phase to a frozen steady state where strongly propelled filaments form stable spirals.

In mapping out the collective behaviour of polar active matter, our results particularly shed light on the role of shape and finite extent of individual constituents. Filaments and cells are both polar and active, but they differ in structure. Filaments, with higher aspect ratios than elliptically-shaped cells, display an effective nematic symmetry at high densities. As a result, we observe an active turbulence phase for filament suspensions that is dominated by the formation of half-integer nematic topological defects. Cells, on the other hand, display polar symmetry, which results in an active turbulence regime dominated by the formation of vortices and swirls.

Before concluding this thesis, we discuss some ideas related to our models that could be explored in the future. Models of cells and filaments presented in this thesis are minimalistic in terms of detail. Our minimal model approach can be extended step by step to include more and more complexity towards a more comprehensive modelling of motile cells and cytoskeletal filaments. We do not include hydrodynamics in both of the models. As cell migration is mediated through traction forces exerted at the substrate, frictional damping screens momentum propagation to a large extent, reducing the role of hydrodynamics in cell monolayers. However, for motility assays at finite densities, long-range hydrodynamic interactions among the filaments can play a role in collective dynamics. We expect that hydrodynamics would lead to quantitative changes in the phase space of filaments at finite densities. At the moment, a systematic study on the role of hydrodynamics remains an open question.

We presented preliminary results on high density suspensions of filaments in this thesis. We observed three phases as a function of activity and rigidity. At higher densities, jammed filaments relax into a chaotic active turbulence regime with increasing activity, or decreasing rigidity. Upon increasing the activity, or decreasing the rigidity further, filaments form lanes or bands. A quantitative study of establishing phase boundaries remains open. We are also studying the properties of active turbulence phase of filaments in more detail. In particular, a study of the defect dynamics with changing rigidity might provide valuable insight on liquid crystalline ordering of active semiflexible systems. Theoretical predictions suggest that for our case of an active nematic in the dry hydrodynamic limit, the ordering of topological defects should disappear [45]. It would be interesting to test these predictions by studying orientational ordering of defects. However, this requires much larger systems to simulate to gain statistically significant results.

Microtubules and actin filaments are dynamic in assembly and disassembly. Therefore, they have polydisperse size distributions. To study the effects of polydispersity on filament dynamics, we simulated bidisperse ensembles. So far, we observed a slight fractionation in terms of aspect ratio through visual inspection of simulations. A more systematic study of effects of polydispersity is also an interesting point for further research.

Our model of cells can be used, as it is, or with extensions, to model and predict new phenomena in wound healing, tumor progression, and embryogenesis. A group of cells that are sticking together with strong adhesion forces can be used to study formation of fingers in wound healing. Having a large value of polydispersity may create leader cells that push the smaller cells along into finger-like protrusions. However, alignment rules might need to be added to study this phenomenon. Changing only the mechanical properties of a few cells (for example, making some of the selected cells more deformable, or more motile) could generate interesting toy models to study fluidization associated with tumor progression.

Bibliography

[1] Masoud Abkenar et al. “Collective behavior of penetrable self-propelled rods in two dimensions”. In: *Phys. Rev. E.* 88.6 (2013), p. 062314.

[2] Silvanus Alt, Poulami Ganguly, and Guillaume Salbreux. “Vertex models: from cell mechanics to tissue morphogenesis”. In: *Phil. Trans. R. Soc. B* 372.1720 (2017), p. 20150520.

[3] Thomas E Angelini et al. “Cell migration driven by cooperative substrate deformation patterns”. In: *Phys. Rev. Lett.* 104.16 (2010), p. 168104.

[4] Thomas E Angelini et al. “Glass-like dynamics of collective cell migration”. In: *Proc. Natl. Acad. Sci. USA* 108.12 (2011), pp. 4714–4719.

[5] George B Arfken and Hans J Weber. *Mathematical methods for physicists.* AAPT, 1999.

[6] Stefan Auer and Daan Frenkel. “Suppression of crystal nucleation in polydisperse colloids due to increase of the surface free energy”. In: *Nature* 413.6857 (Oct. 2001), pp. 711–713. ISSN: 0028-0836. DOI: `10.1038/35099513`. URL: `http:https://doi.org/10.1038/35099513`.

[7] Johannes Bange et al. “Cancer progression and tumor cell motility are associated with the FGFR4 Arg388 allele”. In: *Cancer research* 62.3 (2002), pp. 840–847.

[8] Markus Basan et al. “Alignment of cellular motility forces with tissue flow as a mechanism for efficient wound healing”. In: *Proc. Natl. Acad. Sci. USA* 110.7 (2013), pp. 2452–2459.

[9] George K. Batchelor. *The Theory of Homogeneous Turbulence.* 1st ed. New York: Cambridge University Press, 1982.

[10] Clemens Bechinger, Francesco Sciortino, and Primož Ziherl. *Physics of complex colloids.* Vol. 184. IOS Press, 2013.

[11] Ludovic Berthier. “Nonequilibrium glassy dynamics of self-propelled hard disks”. In: *Phys. Rev. Lett.* 112.22 (2014), p. 220602.

[12] Ludovic Berthier, Elijah Flenner, and Grzegorz Szamel. “How active forces influence nonequilibrium glass transitions”. In: *arXiv preprint arXiv:1708.04259* (2017).

[13] Dapeng Bi et al. “A density-independent glass transition in biological tissues”. In: *arXiv preprint arXiv:1409.0593* (2014).

[14] Dapeng Bi et al. “Motility-driven glass and jamming transitions in biological tissues”. In: *Phys. Rev. X* 6.2 (2016), p. 021011.

[15] Daniel L Blair, T Neicu, and A Kudrolli. “Vortices in vibrated granular rods”. In: *Phys. Rev. E.* 67.3 (2003), p. 031303. ISSN: 2470-0053. DOI: `10.1103/PhysRevE.67.031303`.

[16] C Blanch-Mercader et al. “Turbulent dynamics of epithelial cell cultures”. In: *arXiv preprint arXiv:1711.01568* (2017).

[17] Daniel Bonn et al. “Yield stress materials in soft condensed matter”. In: *Reviews of Modern Physics* 89.3 (2017), p. 035005.

[18] Vasil Bratanov, Frank Jenko, and Erwin Frey. “New class of turbulence in active fluids”. In: *Proc. Natl. Acad. Sci. USA* 112.49 (2015), pp. 15048–15053.

[19] Vasil Bratanov et al. “Nonuniversal power-law spectra in turbulent systems”. In: *Phys. Rev. Lett.* 111.7 (2013), p. 075001.

[20] Thomas Brettschneider et al. “Force measurement in the presence of Brownian noise: Equilibrium-distribution method versus drift method”. In: *Phys. Rev. E* 83 (4 Apr. 2011), p. 041113. DOI: `10.1103/PhysRevE.83.041113`. URL: `https://link.aps.org/doi/10.1103/PhysRevE.83.041113`.

[21] Ivo Buttinoni et al. “Dynamical clustering and phase separation in suspensions of self-propelled colloidal particles.” In: *Phys. Rev. Lett.* 110.23 (2013), p. 238301. ISSN: 0031-9007. DOI: `10.1103/PhysRevLett.110.238301`.

[22] Brian A Camley and Wouter-Jan Rappel. “Physical models of collective cell motility: from cell to tissue”. In: *Journal of Physics D: Applied Physics* 50.11 (2017), p. 113002.

[23] Michael E Cates and Julien Tailleur. “Motility-induced phase separation”. In: *Annu. Rev. Condens. Matter Phys.* 6.1 (2015), pp. 219–244.

[24] Andrea Cavagna et al. “Scale-free correlations in starling flocks”. In: *Proc. Natl. Acad. Sci. USA* 107.26 (2010), pp. 11865–11870.

[25] Jordi Chan et al. “Cortical microtubule arrays undergo rotary movements in Arabidopsis hypocotyl epidermal cells”. In: *Nat. Cell. Biol.* 9.2 (2007), pp. 171–175. ISSN: 1465-7392. DOI: `10.1038/ncb1533`.

[26] Hugues Chaté et al. “Modeling collective motion: variations on the Vicsek model”. In: *The European Physical Journal B-Condensed Matter and Complex Systems* 64.3 (2008), pp. 451–456.

[27] Leiming Chen, Chiu Fan Lee, and John Toner. “Mapping two-dimensional polar active fluids to two-dimensional soap and one-dimensional sandblasting”. In: *Nat. Comm.* 7 (2016).

[28] M Chiang and D Marenduzzo. “Glass transitions in the cellular Potts model”. In: *Europhys. Lett.* 116.2 (2016), p. 28009.

[29] Luke Coburn et al. “Tactile interactions lead to coherent motion and enhanced chemotaxis of migrating cells”. In: *Physical biology* 10.4 (2013), p. 046002.

[30] Matthew F Copeland and Douglas B Weibel. “Bacterial swarming: a model system for studying dynamic self-assembly”. In: *Soft matter* 5.6 (2009), pp. 1174–1187.

[31] Y Couder. “Two-dimensional grid turbulence in a thin liquid film”. In: *Journal de Physique Lettres* 45.8 (1984), pp. 353–360.

[32] Iain D Couzin et al. “Effective leadership and decision-making in animal groups on the move.” In: *Nature* 433.7025 (2005), pp. 513–6. ISSN: 0028-0836. DOI: `10.1038/nature03236`.

[33] Adama Creppy et al. “Turbulence of swarming sperm”. In: *Phys. Rev. E.* 92.3 (2015), p. 032722.

[34] Frenkel D. and B. Smit. *Understanding Molecular Simulation.* 2nd ed. San Diego: Academic Press, 2002.

[35] Debasis Dan et al. “Solving the advection-diffusion equations in biological contexts using the cellular Potts model”. In: *Phys. Rev. E.* 72.4 (2005), p. 041909.

[36] Pablo G Debenedetti and Frank H Stillinger. “Supercooled liquids and the glass transition”. In: *Nature* 410.6825 (2001), pp. 259–267.

[37] Stephen J DeCamp et al. “Orientational order of motile defects in active nematics”. In: *Nat Mater* 14.11 (2015), pp. 1110–1115. ISSN: 1476-1122. DOI: `10.1038/nmat4387`.

[38] Maxime Deforet et al. “Emergence of collective modes and tri-dimensional structures from epithelial confinement”. In: *Nat. Comm.* 5 (2014), p. 3747.

[39] Markus Deserno. “Fluid lipid membranes: From differential geometry to curvature stresses”. In: *Chemistry and Physics of Lipids* 185 (2015). Membrane mechanochemistry: From the molecular to the cellular scale, pp. 11–45. ISSN: 0009-3084. DOI: `https://doi.org/10.1016/j.chemphyslip.2014.05.001`. URL: `http://www.sciencedirect.com/science/article/pii/S000930841400053X`.

[40] J. K. G. Dhont. *An Introduction to Dynamics of Colloids.* 1st ed. New York: Elsevier Science, 1996.

[41] M. Doi and S. F. Edwards. *Differential Geometry: Curves, Surfaces, Manifolds.* 2nd ed. New York: American Mathematical Society, 2005.

[42] M. Doi and S. F. Edwards. *The Theory of Polymer Dynamics.* 1st ed. New York: Oxford University Press, 1986.

[43] Christopher Dombrowski et al. “Self-concentration and large-scale coherence in bacterial dynamics”. In: *Phys. Rev. Lett.* 93.9 (2004), p. 098103.

[44] Amin Doostmohammadi et al. “Onset of meso-scale turbulence in active nematics”. In: *Nat. Comm.* 8 (2017).

[45] Amin Doostmohammadi et al. “Stabilization of active matter by flow-vortex lattices and defect ordering”. In: *Nat. Comm.* 7 (2016).

[46] Ruben van Drongelen et al. “Collective dynamics of soft active particles”. In: *Phys. Rev. E.* 91.3 (2015), p. 032706.

[47] XinXin Du, Miriam Osterfield, and Stanislav Y Shvartsman. “Computational analysis of three-dimensional epithelial morphogenesis using vertex models”. In: *Physical biology* 11.6 (2014), p. 066007.

[48] Guillaume Duclos et al. “Topological defects in confined populations of spindle-shaped cells”. In: *Nature Physics* 13.1 (2017), pp. 58–62.

[49] Jörn Dunkel et al. “Fluid dynamics of bacterial turbulence”. In: *Phys. Rev. Lett.* 110.22 (2013), p. 228102.

[50] Jörn Dunkel et al. “Minimal continuum theories of structure formation in dense active fluids”. In: *New Journal of Physics* 15.4 (2013), p. 045016.

[51] Albert Einstein. *Investigations on the Theory of the Brownian Movement.* Courier Corporation, 1956.

[52] Thomas Eisenstecken, Gerhard Gompper, and Roland G. Winkler. “Conformational Properties of Active Semiflexible Polymers”. In: *Polymers* 8.8 (2016), p. 304. DOI: `http://dx.doi.org/10.3390/polym8080304`. URL: `http://http://www.mdpi.com/2073-4360/8/8/304/htm`.

[53] Thomas Eisenstecken, Gerhard Gompper, and Roland G Winkler. “Internal dynamics of semiflexible polymers with active noise.” In: *J Chem Phys* 146.15 (2017), p. 154903. ISSN: 0021-9606. DOI: `10.1063/1.4981012`.

[54] Jens Elgeti, Roland G Winkler, and Gerhard Gompper. “Physics of microswimmers—single particle motion and collective behavior: a review”. In: *Reports on progress in physics* 78.5 (2015), p. 056601.

[55] Moreno Fasolo and Peter Sollich. “Fractionation effects in phase equilibria of polydisperse hard-sphere colloids”. In: *Phys. Rev. E.* 70 (4 Oct. 2004), p. 041410. DOI: `10.1103/PhysRevE.70.041410`. URL: `https://link.aps.org/doi/10.1103/PhysRevE.70.041410`.

[56] William Feller. *An introduction to probability theory and its applications, volume II.* Vol. 2. Wiley, New York, 1971.

[57] Yaouen Fily and M Cristina Marchetti. “Athermal phase separation of self-propelled particles with no alignment”. In: *Phys. Rev. Lett.* 108.23 (2012), p. 235702.

[58] Alexander G Fletcher et al. “Vertex models of epithelial morphogenesis”. In: *Biophys. J.* 106.11 (2014), pp. 2291–2304.

[59] Matthew J Footer et al. “Direct measurement of force generation by actin filament polymerization using an optical trap”. In: *Proc. Natl. Acad. Sci. USA* 104.7 (2007), pp. 2181–2186.

[60] Uriel Frisch. *Turbulence: The Legacy of A. N. Kolmogorov.* 1st ed. New York: Cambridge University Press, 1995.

[61] Tong Gao and Zhaorui Li. "Self-Driven Droplet Powered By Active Nematics". In: *Phys. Rev. Lett.* 119.10 (2017), p. 108002.

[62] Simon Garcia et al. "Physics of active jamming during collective cellular motion in a monolayer". In: *Proc. Natl. Acad. Sci. USA* 112.50 (2015), pp. 15314–15319.

[63] Mikhail M Genkin et al. "Topological defects in a living nematic ensnare swimming bacteria". In: *Phys. Rev. X* 7.1 (2017), p. 011029.

[64] A. Ghosh and N.S. Gov. "Dynamics of Active Semiflexible Polymers". In: *Biophys J* 107.5 (2014), pp. 1065–1073. ISSN: 0006-3495. DOI: `10.1016/j.bpj.2014.07.034`.

[65] Francesco Ginelli et al. "Large-Scale Collective Properties of Self-Propelled Rods". In: *Phys. Rev. Lett.* 104 (18 May 2010), p. 184502. DOI: `10.1103/PhysRevLett.104.184502`. URL: `https://link.aps.org/doi/10.1103/PhysRevLett.104.184502`.

[66] Luca Giomi. "Geometry and topology of turbulence in active nematics". In: *Phys. Rev. X* 5.3 (2015), p. 031003.

[67] Luca Giomi et al. "Defect annihilation and proliferation in active nematics". In: *Phys. Rev. Lett.* 110.22 (2013), p. 228101.

[68] Luca Giomi et al. "Defect dynamics in active nematics". In: *Phil. Trans. R. Soc. A* 372.2029 (2014), p. 20130365.

[69] L Giomi et al. "Banding, excitability and chaos in active nematic suspensions". In: *Nonlinearity* 25.8 (2012), p. 2245.

[70] James A Glazier and François Graner. "Simulation of the differential adhesion driven rearrangement of biological cells". In: *Phys. Rev. E.* 47.3 (1993), p. 2128.

[71] Sharon C. Glotzer et al. "Dynamical heterogeneity in the Ising spin glass". In: *Phys. Rev. E.* 57 (6 June 1998), pp. 7350–7353. DOI: `10.1103/PhysRevE.57.7350`. URL: `https://link.aps.org/doi/10.1103/PhysRevE.57.7350`.

[72] Chris Goddard, Ortwin Hess, and Siegfried Hess. "Low Reynolds number turbulence in nonlinear Maxwell-model fluids". In: *Phys. Rev. E.* 81.3 (2010), p. 036310.

[73] François Graner and James A Glazier. "Simulation of biological cell sorting using a two-dimensional extended Potts model". In: *Phys. Rev. Lett.* 69.13 (1992), p. 2013.

[74] A Groisman and VV Steinberg. "Elastic turbulence in a polymer solution flow". In: *Nature* 405.6782 (2000), pp. 53–55.

[75] Robert Großmann et al. "Vortex arrays and mesoscale turbulence of self-propelled particles". In: *Phys. Rev. Lett.* 113.25 (2014), p. 258104.

[76] Vincent Hakim and Pascal Silberzan. "Collective cell migration: a physics perspective". In: *Reports on progress in physics* 80.7 (2017), p. 076601.

[77] EJ Hemingway et al. “Active viscoelastic matter: From bacterial drag reduction to turbulent solids”. In: *Phys. Rev. Lett.* 114.9 (2015), p. 098302.

[78] Ewan J Hemingway et al. “Correlation lengths in hydrodynamic models of active nematics”. In: *Soft matter* 12.38 (2016), pp. 7943–7952.

[79] Silke Henkes, Yaouen Fily, and M Cristina Marchetti. “Active jamming: Self-propelled soft particles at high density”. In: *Phys. Rev. E.* 84.4 (2011), p. 040301.

[80] Martin G van den Heuvel and Cees Dekker. “Motor proteins at work for nanotechnology.” In: *Science* 317.5836 (2007), pp. 333–6. ISSN: 0036-8075. DOI: 10.1126/science.1139570.

[81] Stefan Hoehme and Dirk Drasdo. “A cell-based simulation software for multi-cellular systems”. In: *Bioinformatics* 26.20 (2010), pp. 2641–2642.

[82] Felix Höfling and Thomas Franosch. “Anomalous transport in the crowded world of biological cells”. In: *Reports on Progress in Physics* 76.4 (2013), p. 046602.

[83] Han Wei Hou et al. “Deformability study of breast cancer cells using microfluidics”. In: *Biomedical microdevices* 11.3 (2009), pp. 557–564.

[84] Rongxin Huang et al. “Direct observation of the full transition from ballistic to diffusive Brownian motion in a liquid”. In: *Nat. Phys.* 7.7 (2011), pp. 576–580. ISSN: 1745-2473. DOI: 10.1038/nphys1953. URL: https://www.nature.com/nphys/journal/v7/n7/pdf/nphys1953.pdf.

[85] Adrián Huerta, Douglas Henderson, and Andrij Trokhymchuk. “Freezing of two-dimensional hard disks”. In: *Phys. Rev. E.* 74.6 (2006), p. 061106.

[86] Gary L Hunter and Eric R Weeks. “The physics of the colloidal glass transition”. In: *Reports on Progress in Physics* 75.6 (2012), p. 066501. URL: http://stacks.iop.org/0034-4885/75/i=6/a=066501.

[87] Rolf E. Isele-Holder, Jens Elgeti, and Gerhard Gompper. “Self-propelled worm-like filaments: spontaneous spiral formation, structure, and dynamics.” In: *Soft Matter* 11.36 (2015), pp. 7181–90. ISSN: 1744-683X. DOI: 10.1039/c5sm01683e.

[88] Rolf E. Isele-Holder, Jens Elgeti, and Gerhard Gompper. “Self-propelled worm-like filaments: spontaneous spiral formation, structure, and dynamics.” In: *Soft Matter* 11.36 (2015), pp. 7181–90. ISSN: 1744-683X. DOI: 10.1039/c5sm01683e.

[89] Rolf E. Isele-Holder et al. “Dynamics of self-propelled filaments pushing a load”. In: *Soft Matter* (2016). ISSN: 1744-683X. DOI: 10.1039/C6SM01094F.

[90] Rolf E. Isele-Holder et al. “Dynamics of self-propelled filaments pushing a load”. In: *Soft Matter* (2016). ISSN: 1744-683X. DOI: 10.1039/C6SM01094F.

[91] Masaki Ito et al. “Formation of ring-shaped microtubule assemblies through active self-organization on dynein”. In: *Polym. J.* 46.4 (2014), pp. 220–225. ISSN: 0032-3896. DOI: 10.1038/pj.2013.89.

[92] G Jayaraman et al. “Autonomous motility of active filaments due to spontaneous flow-symmetry breaking”. In: *Phys. Rev. Lett.* 109.15 (2012), p. 158302.

[93] H Jiang and Z Hou. “Motion transition of active filaments: rotation without hydrodynamic interactions”. In: *Soft Matter* 10.46 (2014), pp. 1012–1017. DOI: `10.1039/C3SM52291A`.

[94] Huijun Jiang and Zhonghuai Hou. “Hydrodynamic interaction induced spontaneous rotation of coupled active filaments”. In: *Soft Matter* 10.46 (2014), pp. 9248–9253. ISSN: 1744-6848. DOI: `10.1039/C4SM01734J`.

[95] Arif Kabir et al. “Formation of ring-shaped assembly of microtubules with a narrow size distribution at an air– buffer interface”. In: *Soft Matter* 8.42 (2012), pp. 10863–10867. ISSN: 1744-683X. DOI: `10.1039/C2SM26441B`.

[96] A Kaiser and H Löwen. “Vortex arrays as emergent collective phenomena for circle swimmers”. In: *Phys. Rev. E.* 87.3 (2013), p. 032712.

[97] Andreas Kaiser et al. “How does a flexible chain of active particles swell?” In: *J. Chem. Phys.* 142.12, 124905 (2015), p. 124905. DOI: `http://dx.doi.org/10.1063/1.4916134`. URL: `http://scitation.aip.org/content/aip/journal/jcp/142/12/10.1063/1.4916134`.

[98] Andreas Kaiser et al. “Transport powered by bacterial turbulence”. In: *Phys. Rev. Lett.* 112.15 (2014), p. 158101.

[99] N. G. van Kampen. “Itô versus Stratonovich”. In: *Journal of Statistical Physics* 24.1 (1981), pp. 175–187. ISSN: 1572-9613. DOI: `10.1007/BF01007642`. URL: `http://dx.doi.org/10.1007/BF01007642`.

[100] Eric Karsenti. “Self-organization in cell biology: a brief history”. In: *Nat. Rev. Mol. Cell Bio.* 9.3 (2008), pp. 255–262. ISSN: 1471-0072. DOI: `10.1038/nrm2357`.

[101] Kyogo Kawaguchi, Ryoichiro Kageyama, and Masaki Sano. “Topological defects control collective dynamics in neural progenitor cell cultures”. In: *Nature* 545.7654 (2017), pp. 327–331.

[102] J. Kierfeld et al. “Active dynamics of filaments in motility assays”. In: *The European Physical Journal Special Topics* 157.1 (2008), pp. 123–133. ISSN: 1951-6401. DOI: `10.1140/epjst/e2008-00635-9`. URL: `http://dx.doi.org/10.1140/epjst/e2008-00635-9`.

[103] Wook Kim et al. “Swarm-cell differentiation in Salmonella enterica serovar Typhimurium results in elevated resistance to multiple antibiotics”. In: *Journal of bacteriology* 185.10 (2003), pp. 3111–3117.

[104] P. Kloeden and E. Platen. *Numerical solution of stochastic differential equations.* 1st ed. Berlin: Springer-Verlag, 1992.

[105] Walter Kob. “Supercooled liquids, the glass transition, and computer simulations”. In: *arXiv preprint cond-mat/0212344* (2002).

[106] R H Kraichnan and D Montgomery. “Two-dimensional turbulence”. In: *Reports on Progress in Physics* 43.5 (1980), p. 547. URL: `http://stacks.iop.org/0034-4885/43/i=5/a=001`.

[107] O Kratky and G Porod. “Diffuse small-angle scattering of x-rays in colloid systems”. In: *J. Colloid Sci.* 4.1 (1949), pp. 35–70. ISSN: 0095-8522. DOI: `http://dx.doi.org/10.1016/0095-8522(49)90032-X`. URL: `http://www.sciencedirect.com/science/article/pii/009585224990032X`.

[108] Walter S Krawczyk. “A pattern of epidermal cell migration during wound healing”. In: *The Journal of cell biology* 49.2 (1971), pp. 247–263.

[109] K Kruse et al. “Asters, vortices, and rotating spirals in active gels of polar filaments.” In: *Phys. Rev. Lett.* 92.7 (2004), p. 078101. ISSN: 0031-9007. DOI: `10.1103/PhysRevLett.92.078101`.

[110] R. Kubo. “The fluctuation-dissipation theorem”. In: *Rep. Prog. Phys.* 29 (255 1966). DOI: `10.1088/0034-4885/29/1/306`. URL: `http://iopscience.iop.org/article/10.1088/0034-4885/29/1/306/`.

[111] Arshad Kudrolli et al. “Swarming and swirling in self-propelled polar granular rods.” In: *Phys. Rev. Lett.* 100.5 (2008), p. 058001. ISSN: 0031-9007. DOI: `10.1103/PhysRevLett.100.058001`.

[112] Dirk Alexander Kulawiak, Brian A Camley, and Wouter-Jan Rappel. “Modeling Contact Inhibition of Locomotion of Colliding Cells Migrating on Micropatterned Substrates”. In: *PLoS computational biology* 12.12 (2016), e1005239.

[113] R. Kupferman, G. A. Pavliotis, and A. M. Stuart. “Itô versus Stratonovich white-noise limits for systems with inertia and colored multiplicative noise”. In: *Phys. Rev. E* 70 (3 Sept. 2004), p. 036120. DOI: `10.1103/PhysRevE.70.036120`. URL: `https://link.aps.org/doi/10.1103/PhysRevE.70.036120`.

[114] Christina Kurzthaler, Sebastian Leitmann, and Thomas Franosch. “Intermediate scattering function of an anisotropic active Brownian particle”. In: *Scientific reports* 6 (2016), p. 36702.

[115] Tung-Chun Lee et al. “Self-propelling nanomotors in the presence of strong Brownian forces”. In: *Nano letters* 14.5 (2014), pp. 2407–2412.

[116] QS Li et al. “AFM indentation study of breast cancer cells”. In: *Biochemical and biophysical research communications* 374.4 (2008), pp. 609–613.

[117] Szu-Ning Lin, Wei-Chang Lo, and Chien-Jung Lo. “Dynamics of self-organized rotating spiral-coils in bacterial swarms”. In: *Soft Matter* 10.5 (2013), pp. 760–766. ISSN: 1744-683X. DOI: `10.1039/C3SM52120F`.

[118] Szu-Ning Lin, Wei-Chang Lo, and Chien-Jung Lo. “Dynamics of self-organized rotating spiral-coils in bacterial swarms”. In: *Soft matter* 10.5 (2014), pp. 760–766.

[119] Lynn Liu, Erkan Tüzel, and Jennifer Ross. “Loop formation of microtubules during gliding at high density”. In: *J. Phys. Condens. Matter* 23.37 (2011), p. 374104. ISSN: 0953-8984. DOI: `10.1088/0953-8984/23/37/374104`.

[120] Tanniemola Liverpool. “Anomalous fluctuations of active polar filaments”. In: *Phys. Rev. E.* 67.3 (2003), p. 031909. ISSN: 2470-0053. DOI: `10.1103/PhysRevE.67.031909`.

[121] Jakob Löber, Falko Ziebert, and Igor S Aranson. “Collisions of deformable cells lead to collective migration”. In: *Scientific reports* 5 (2015).

[122] Harvey Lodish et al. *Molecular cell biology.* Vol. 3. Scientific American Books New York, 1995.

[123] Davide Loi, Stefano Mossa, and Leticia Cugliandolo. “Effective temperature of active complex matter”. In: *Soft Matter* 7.8 (2011), pp. 3726–3729. ISSN: 1744-683X. DOI: `10.1039/C0SM01484B`.

[124] Davide Loi, Stefano Mossa, and Leticia Cugliandolo. “Non-conservative forces and effective temperatures in active polymers”. In: *Soft Matter* 7.21 (2011), pp. 10193–10209. ISSN: 1744-683X. DOI: `10.1039/C1SM05819C`.

[125] Martin Loose et al. “Spatial regulators for bacterial cell division self-organize into surface waves in vitro.” In: *Science* 320.5877 (2008), pp. 789–92. ISSN: 0036-8075. DOI: `10.1126/science.1154413`.

[126] Gisela Lorente, Emilio Syriani, and Miguel Morales. “Actin filaments at the leading edge of cancer cells are characterized by a high mobile fraction and turnover regulation by profilin I”. In: *PloS one* 9.1 (2014), e85817.

[127] Enkeleida Lushi, Hugo Wioland, and Raymond E Goldstein. “Fluid flows created by swimming bacteria drive self-organization in confined suspensions”. In: *Proc. Natl. Acad. Sci. USA* 111.27 (2014), pp. 9733–9738.

[128] Ethayaraja Mani and Hartmut Löwen. “Effect of self-propulsion on equilibrium clustering”. In: *Phys. Rev. E.* 92 (3 Sept. 2015), p. 032301. DOI: `10.1103/PhysRevE.92.032301`. URL: `https://link.aps.org/doi/10.1103/PhysRevE.92.032301`.

[129] M Cristina Marchetti et al. “Hydrodynamics of soft active matter”. In: *Reviews of Modern Physics* 85.3 (2013), p. 1143.

[130] Johan Mattsson et al. “Soft colloids make strong glasses”. In: *Nature* 462.7269 (2009), pp. 83–86.

[131] Andreas M Menzel and Takao Ohta. “Soft deformable self-propelled particles”. In: *Europhys. Lett.* 99.5 (2012), p. 58001.

[132] B. M. Mognetti et al. “Living Clusters and Crystals from Low-Density Suspensions of Active Colloids”. In: *Phys. Rev. Lett.* 111 (24 Dec. 2013), p. 245702. DOI: `10.1103/PhysRevLett.111.245702`. URL: `https://link.aps.org/doi/10.1103/PhysRevLett.111.245702`.

[133] M Nagy et al. “Hierarchical group dynamics in pigeon flocks”. In: *Nature* 464.7290 (2010), pp. 890–893.

[134] Saroj Kumar Nandi and Nir S Gov. “Nonequilibrium mode-coupling theory for dense active systems of self-propelled particles”. In: *arXiv preprint arXiv:1708.05222* (2017).

[135] Vijay Narayan, Sriram Ramaswamy, and Narayanan Menon. “Long-Lived Giant Number Fluctuations in a Swarming Granular Nematic”. In: *Science* 317.5834 (2007), pp. 105–108. ISSN: 0036-8075. DOI: `10.1126/science.1140414`. eprint: `http://science.sciencemag.org/content/317/5834/105.full.pdf`. URL: `http://science.sciencemag.org/content/317/5834/105`.

[136] FJ Nédélec et al. “Self-organization of microtubules and motors.” In: *Nature* 389.6648 (1997), pp. 305–8. ISSN: 0028-0836. DOI: `10.1038/38532`.

[137] Mark Nelkin. “In What Sense Is Turbulence an Unsolved Problem?” In: *Science* 255.5044 (1992), pp. 566–570. ISSN: 0036-8075. DOI: `10.1126/science.255.5044.566`. eprint: `http://science.sciencemag.org/content/255/5044/566.full.pdf`. URL: `http://science.sciencemag.org/content/255/5044/566`.

[138] Sandrine Ngo et al. “Large-scale chaos and fluctuations in active nematics”. In: *Phys. Rev. Lett.* 113.3 (2014), p. 038302.

[139] Ran Ni, Martien A Stuart, and Marjolein Dijkstra. “Pushing the glass transition towards random close packing using self-propelled hard spheres”. In: *Nat Commun* 4 (2013). ISSN: 2041-1733. DOI: `10.1038/ncomms3704`.

[140] Daiki Nishiguchi and Masaki Sano. “Mesoscopic turbulence and local order in Janus particles self-propelling under an ac electric field”. In: *Phys. Rev. E.* 92.5 (2015), p. 052309.

[141] Kenechukwu David Nnetu et al. “The impact of jamming on boundaries of collectively moving weak-interacting cells”. In: *New Journal of Physics* 14.11 (2012), p. 115012.

[142] Takao Ohta and Takahiro Ohkuma. “Deformable self-propelled particles”. In: *Phys. Rev. Lett.* 102.15 (2009), p. 154101.

[143] Bernt Oksendal. *Stochastic Differential Equations.* 6th ed. Berlin: Springer Berlin Heidelberg, 2003.

[144] Michael F Olson and Erik Sahai. “The actin cytoskeleton in cancer cell motility”. In: *Clinical & experimental metastasis* 26.4 (2009), p. 273.

[145] Lars Onsager. “Statistical hydrodynamics”. In: *Nuovo Cimento Suppl.* 6 (1949). DOI: `10.1111/j.1749-6632.1949.tb27296.x`.

[146] Lars Onsager. “The Effects of Shape on the Interaction of Colloidal Particles”. In: *Annals of the New York Academy of Sciences* 51.4 (1949), pp. 627–659. ISSN: 1749-6632. DOI: `10.1111/j.1749-6632.1949.tb27296.x`. URL: `http://dx.doi.org/10.1111/j.1749-6632.1949.tb27296.x`.

[147] Anand U Oza and Jörn Dunkel. “Antipolar ordering of topological defects in active liquid crystals”. In: *New Journal of Physics* 18.9 (2016), p. 093006.

[148] Anand U Oza, Sebastian Heidenreich, and Jörn Dunkel. “Generalized Swift-Hohenberg models for dense active suspensions”. In: *The European Physical Journal E* 39.10 (2016), p. 97.

[149] Eirikur Palsson. “A 3-D model used to explore how cell adhesion and stiffness affect cell sorting and movement in multicellular systems”. In: *Journal of Theoretical Biology* 254.1 (2008), pp. 1–13.

[150] Eirikur Palsson and Hans G Othmer. “A model for individual and collective cell movement in Dictyostelium discoideum”. In: *Proc. Natl. Acad. Sci. USA* 97.19 (2000), pp. 10448–10453.

[151] Jin-Ah Park et al. “Unjamming and cell shape in the asthmatic airway epithelium”. In: *Nature materials* 14.10 (2015), p. 1040.

[152] Fernando Peruani. “Active Brownian rods”. In: *The European Physical Journal Special Topics* 225.11 (2016), pp. 2301–2317. ISSN: 1951-6401. DOI: `10.1140/epjst/e2016-60062-0`. URL: `http://dx.doi.org/10.1140/epjst/e2016-60062-0`.

[153] Fernando Peruani et al. “Collective motion and nonequilibrium cluster formation in colonies of gliding bacteria.” In: *Phys. Rev. Lett.* 108.9 (2012), p. 098102. ISSN: 0031-9007. DOI: `10.1103/PhysRevLett.108.098102`.

[154] Giuseppe Pesce et al. “Stratonovich-to-Itô transition in noisy systems with multiplicative feedback.” In: *Nat Commun* 4 (2013), p. 2733. ISSN: 2041-1723. DOI: `10.1038/ncomms3733`.

[155] Alexander P Petroff, Xiao-Lun Wu, and Albert Libchaber. “Fast-moving bacteria self-organize into active two-dimensional crystals of rotating cells”. In: *Phys. Rev. Lett.* 114.15 (2015), p. 158102.

[156] Rob Phillips et al. *Physical biology of the cell.* Garland Science, 2012.

[157] Stephen B. Pope. *Turbulent Flows.* 1st ed. New York: Cambridge University Press, 2000.

[158] K Prathyusha, Silke Henkes, and Rastko Sknepnek. “Dynamically Generated Patterns in Dense Suspensions of Active Filaments”. In: *arXiv:1608.03305* (2016).

[159] Jacques Prost. *The physics of liquid crystals.* Vol. 83. Oxford university press, 1995.

[160] P. N. Pusey. *Liquids, Freezing and Glass Transition.* 1st ed. New York: Elsevier Science, 1991.

[161] Xiang Qiu et al. “Intermittency measurement in two-dimensional bacterial turbulence”. In: *Phys. Rev. E.* 93.6 (2016), p. 062226.

[162] J. Elgeti R. G. Winkler and G. Gompper. “Active Polymers: Emergent Conformational and Dynamical Properties”. In: *J. Phys. Soc. Jap.* 86.10 (2017), p. 101014.

[163] Amit Rabani, Gil Ariel, and Avraham Be’er. “Collective motion of spherical bacteria”. In: *PLoS One* 8.12 (2013), e83760.

[164] Sriram Ramaswamy. “The mechanics and statistics of active matter”. In: (2010).

[165] Ingmar H Riedel, Karsten Kruse, and Jonathon Howard. “A self-organized vortex array of hydrodynamically entrained sperm cells.” In: *Science* 309.5732 (2005), pp. 300–3. ISSN: 0036-8075. DOI: `10.1126/science.1110329`.

[166] Hannes Risken. *Fokker-Planck Equation.* 1st ed. Berlin: Springer-Verlag, 1984.

[167] Ninna S Rossen et al. “Long-range ordered vorticity patterns in living tissue induced by cell division”. In: *Nat. Comm.* 5 (2014).

[168] Monirosadat Sadati et al. “Collective migration and cell jamming”. In: *Differentiation* 86.3 (2013), pp. 121–125.

[169] Thomas Salez et al. “Cooperative strings and glassy interfaces”. In: *Proc. Natl. Acad. Sci. USA* 112.27 (2015), pp. 8227–8231.

[170] Devranjan Samanta et al. “Elasto-inertial turbulence”. In: *Proc. Natl. Acad. Sci. USA* 110.26 (2013), pp. 10557–10562.

[171] Thuan Beng Saw et al. “Topological defects in epithelia govern cell death and extrusion”. In: *Nature* 544.7649 (2017), pp. 212–216.

[172] Volker Schaller and Andreas R Bausch. “Topological defects and density fluctuations in collectively moving systems”. In: *Proc. Natl. Acad. Sci. USA* 110.12 (2013), pp. 4488–4493.

[173] Volker Schaller et al. “Frozen steady states in active systems.” In: *Proc. Natl. Acad. Sci.* 108.48 (2011), pp. 19183–8. ISSN: 0027-8424. DOI: `10.1073/pnas.1107540108`.

[174] Volker Schaller et al. “Polar patterns of driven filaments.” In: *Nature* 467.7311 (2010), pp. 73–7. ISSN: 0028-0836. DOI: `10.1038/nature09312`.

[175] Eva-Maria Schoetz et al. “Glassy dynamics in three-dimensional embryonic tissues”. In: *Journal of The Royal Society Interface* 10.89 (2013), p. 20130726.

[176] Ulrich Schwarz. *Theoretical Biophysics.* 2016. URL: `https://www.thphys.uni-heidelberg.de/~biophys/PDF/Skripte/TheoreticalBiophysics.pdf` (visited on 07/19/2016).

[177] Tyler N Shendruk et al. “Dancing disclinations in confined active nematics”. In: *Soft Matter* 13.21 (2017), pp. 3853–3862.

[178] Jonasz Słomka and Jörn Dunkel. “Generalized Navier-Stokes equations for active suspensions”. In: *The European Physical Journal Special Topics* 224.7 (2015), pp. 1349–1358.

[179] J Sommeria. “Experimental study of the two-dimensional inverse energy cascade in a square box”. In: *Journal of fluid mechanics* 170 (1986), pp. 139–168.

[180] Chaoming Song, Ping Wang, and Hernán A Makse. “Experimental measurement of an effective temperature for jammed granular materials”. In: *Proc. Natl. Acad. Sci. USA of the United States of America* 102.7 (2005), pp. 2299–2304.

[181] Malcolm S Steinberg. “Differential adhesion in morphogenesis: a modern view”. In: *Current opinion in genetics & development* 17.4 (2007), pp. 281–286.

[182] Yutaka Sumino et al. “Large-scale vortex lattice emerging from collectively moving microtubules”. In: *Nature* 483.7390 (2012), pp. 448–452. ISSN: 0028-0836. DOI: `10.1038/nature10874`.

[183] Balint Szabo et al. “Phase transition in the collective migration of tissue cells: experiment and model”. In: *Phys. Rev. E.* 74.6 (2006), p. 061908.

[184] Alessandro Taloni et al. “Volume changes during active shape fluctuations in cells”. In: *Phys. Rev. Lett.* 114.20 (2015), p. 208101.

[185] Elisa Tamborini, C Patrick Royall, and Pietro Cicuta. “Correlation between crystalline order and vitrification in colloidal monolayers”. In: *Journal of Physics: Condensed Matter* 27.19 (2015), p. 194124.

[186] M Tarama et al. “Individual and collective dynamics of self-propelled soft particles”. In: *The European Physical Journal Special Topics* 223.1 (2014), pp. 121–139.

[187] Victoria Tarle et al. “Modeling the finger instability in an expanding cell monolayer”. In: *Integrative Biology* 7.10 (2015), pp. 1218–1227.

[188] Sumesh P Thampi, Ramin Golestanian, and Julia M Yeomans. “Active nematic materials with substrate friction”. In: *Phys. Rev. E.* 90.6 (2014), p. 062307.

[189] Sumesh P Thampi, Ramin Golestanian, and Julia M Yeomans. “Instabilities and topological defects in active nematics”. In: *Europhys. Lett.* 105.1 (2014), p. 18001.

[190] Sumesh P Thampi, Ramin Golestanian, and Julia M Yeomans. “Velocity correlations in an active nematic”. In: *Phys. Rev. Lett.* 111.11 (2013), p. 118101.

[191] Sumesh P Thampi, Ramin Golestanian, and Julia M Yeomans. “Vorticity, defects and correlations in active turbulence”. In: *Phil. Trans. R. Soc. A* 372.2029 (2014), p. 20130366.

[192] Sumesh P Thampi et al. “Intrinsic free energy in active nematics”. In: *Europhys. Lett.* 112.2 (2015), p. 28004.

[193] Elsen Tjhung and Ludovic Berthier. "Discontinuous fluidisation transition in assemblies of actively-deforming particles: A new paradigm for collective motion in dense active materials". In: *arXiv preprint arXiv:1607.01734* (2016).

[194] John Toner and Yuhai Tu. "Flocks, herds, and schools: A quantitative theory of flocking". In: *Phys. Rev. E.* 58.4 (1998), p. 4828.

[195] John Toner and Yuhai Tu. "Long-range order in a two-dimensional dynamical XY model: how birds fly together". In: *Phys. Rev. Lett.* 75.23 (1995), p. 4326.

[196] John Toner, Yuhai Tu, and Sriram Ramaswamy. "Hydrodynamics and phases of flocks". In: *Annals of Physics* 318.1 (2005), pp. 170–244.

[197] Géza Tóth, Colin Denniston, and Julia M Yeomans. "Hydrodynamics of topological defects in nematic liquid crystals". In: *Phys. Rev. Lett.* 88.10 (2002), p. 105504.

[198] VERONIQUE Trappe et al. "Jamming phase diagram for attractive particles". In: *Nature* 411.6839 (2001), pp. 772–775.

[199] G. E. Uhlenbeck and L. S. Ornstein. "On the Theory of the Brownian Motion". In: *Phys. Rev.* 36 (5 Sept. 1930), pp. 823–841. DOI: `10.1103/PhysRev.36.823`. URL: `https://link.aps.org/doi/10.1103/PhysRev.36.823`.

[200] Javier Urzay, Amin Doostmohammadi, and Julia M Yeomans. "Multi-scale statistics of turbulence motorized by active matter". In: *Journal of Fluid Mechanics* 822 (2017), pp. 762–773.

[201] Tamás Vicsek et al. "Novel type of phase transition in a system of self-driven particles". In: *Phys. Rev. Lett.* 75.6 (1995), p. 1226.

[202] Giovanni Volpe et al. "Influence of Noise on Force Measurements". In: *Phys. Rev. Lett.* 104 (17 Apr. 2010), p. 170602. DOI: `10.1103/PhysRevLett.104.170602`. URL: `https://link.aps.org/doi/10.1103/PhysRevLett.104.170602`.

[203] Sebastian Weitz, Andreas Deutsch, and Fernando Peruani. "Self-propelled rods exhibit a phase-separated state characterized by the presence of active stresses and the ejection of polar clusters." In: *Phys. Rev. E.* 92.1 (2015), p. 012322. ISSN: 1539-3755. DOI: `10.1103/PhysRevE.92.012322`.

[204] Henricus H Wensink et al. "Meso-scale turbulence in living fluids". In: *Proc. Natl. Acad. Sci. USA* 109.36 (2012), pp. 14308–14313.

[205] HH Wensink and H Löwen. "Emergent states in dense systems of active rods: from swarming to turbulence". In: *Journal of Physics: Condensed Matter* 24.46 (2012), p. 464130.

[206] Rene Lefever Werner Hortshemke. *Noise-Induced Transitions.* 1st ed. Berlin: Springer Berlin Heidelberg, 1984.

[207] Ann-Katrine Vransø West et al. "Dynamics of cancerous tissue correlates with invasiveness". In: *Scientific Reports* 7 (2017), p. 43800.

[208] Hugo Wioland et al. "Confinement stabilizes a bacterial suspension into a spiral vortex". In: *Phys. Rev. Lett.* 110.26 (2013), p. 268102.

[209] Eugene Wong and Moshe Zakai. "On the Convergence of Ordinary Integrals to Stochastic Integrals". In: *Ann. Math. Statist.* 36.5 (Oct. 1965), pp. 1560–1564. DOI: `10.1214/aoms/1177699916`. URL: `http://dx.doi.org/10.1214/aoms/1177699916`.

[210] Kun-Ta Wu et al. "Transition from turbulent to coherent flows in confined three-dimensional active fluids". In: *Science* 355.6331 (2017), eaal1979.

[211] Adam Wysocki, Roland G Winkler, and Gerhard Gompper. "Cooperative motion of active Brownian spheres in three-dimensional dense suspensions". In: *EPL* 105.4 (2014), p. 48004. ISSN: 0295-5075. DOI: `10.1209/0295-5075/105/48004`.

[212] Jing Yang and Robert A Weinberg. "Epithelial-mesenchymal transition: at the crossroads of development and tumor metastasis". In: *Developmental cell* 14.6 (2008), pp. 818–829.

[213] Yingzi Yang, Vincent Marceau, and Gerhard Gompper. "Swarm behavior of self-propelled rods and swimming flagella". In: *Phys. Rev. E.* 82 (3 Sept. 2010), p. 031904. DOI: `10.1103/PhysRevE.82.031904`. URL: `https://link.aps.org/doi/10.1103/PhysRevE.82.031904`.

[214] Steven M Zehnder et al. "Cell volume fluctuations in MDCK monolayers". In: *Biophys. J.* 108.2 (2015), pp. 247–250.

[215] Juliane Zimmermann et al. "Contact inhibition of locomotion determines cell–cell and cell–substrate forces in tissues". In: *Proc. Natl. Acad. Sci. USA* 113.10 (2016), pp. 2660–2665.

[216] Robert Zwanzig. *Nonequilibrium Statistical Mechanics.* 1st ed. New York: Oxford University Press, 2001.

A. Biological Background

A.1. Microtubules

Microtubules are hollow cylinders with a circular cross section of 13 protofilaments and an external diameter of 25 nm. Each protofilament, making up a microtubule, is assembled from tubulin monomers. Tubulin is a dimer with α (which binds a nonhydrolyzable and stationary GTP molecule) and β (which binds a hydrolyzable and moveable GTP) subunits. $\alpha\beta$-tubulin dimers assemble into protofilaments with α subunit facing the $(-)$ end and β subunit facing the $(+)$ end of the protofilament. Tubulins repeat each other every 8 nm (Fig. A.1) [122]. Microtubules can exist in singlets, doublets and triplets. In doublet and triplets, protofilaments are shared side by side, with each additional microtubule having 10 protofilaments [122].

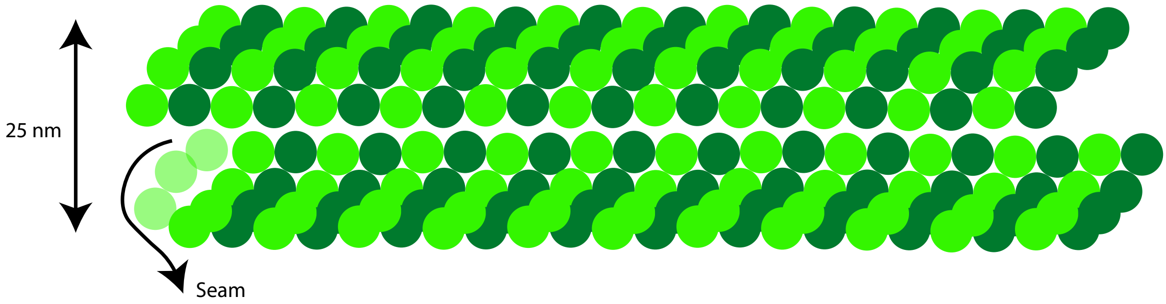

Figure A.1.: Sketch of a microtubule as a hollow cylinder: The circular cross section contains 13 protofilaments. Each protofilament is made of $\alpha\beta$-tubulin dimers. β subunit of the tubulin dimer is exposed at the $(+)$ end of the protofilament. α subunit is exposed at the $(-)$ end. Redrawn from ref. [122].

Unlike actin filaments, microtubules start assembling at specific sites. These nucleating sites are called microtubule-organizing centres (MTOC). After nucleation, microtubules usually remain anchored at MTOC with their $(+)$ ends extending outward. Centrosome is the MTOC responsible for nucleation of microtubules in nonmitotic cells. Spindle poles are MTOCs nucleating microtubules in mitotic spindles. In cilia and flagella, microtubules nucleate from the basal body [122].

Microtubule dynamics is determined by GTP hydrolysis. Monomers that bind GDP are more prone to dissociation than monomers that bind GTP. Therefore, GDP-tubulin at either end of a microtubule is more likely to detach in comparison to GTP-tubulin. As a result, growing (+) ends of microtubules are capped with GTP-tubulins [122]. However, if hydrolization along the microtubule catches up with the cap at the (+) end, protofilaments start disassembling by peeling outward from the microtubule. This can happen, for example, if the polymerization rate drops down, such that GTP-tubulins hydrolyze faster than monomer attachment to the (+) end. As a result of this disturbance, microtubules can grow and shrink dynamically inside the cell depending on GTP-tubulin capping. This is known as *dynamic instability* of microtubules. Due to the dynamic instability, microtubule lifetimes are relatively short with average lifetimes of less than a minute in mitotic cells and lifetimes of 5 – 10 minutes in nonmitotic cells. In axons, cilia and flagella, on the other hand, average lifetimes are much longer [156].

Cells make use of dynamic instability of microtubules as a search and capture strategy within the cytoplasm. Extending outward from the centrosome, growing and shrinking microtubules can search through the cytoplasm until an organelle stabilizes the extending (+) end [122]. In addition, microtubule dynamics can be altered by side-binding microtubule-associated proteins. *+TIPs* bind to the (+) end of microtubules and enhance their growth rate. Kinesin-13 and stathmin proteins faciliate shrinkage of microtubules [122].

As microtubules are structurally polar, motor proteins use them as tracks to transport cargo inside the cell. *Kinesin-1* motor protein transports organelles toward the membrane and it moves towards the (+) end of microtubules. It has a distinctive head domain consisting of two heavy chains, which is the motor domain; a flexible neck linker to the stalk domain, which is a long helical structure; and a tail domain, which is the cargo-binding domain consisting of two light chains.

Kinesin-1 uses ATP hydrolysis to generate conformational changes in the head domain with respect to the neck to move along the microtubule. At the first step, one of the heads of the motor domain, which will subsequently be the forward motor, binds β-tubulin and releases ADP. At the next step, ATP attaches to the forward motor causing a conformational change that swings the rear head forward. The new forward head releases ADP and the trailing head hydrolyzes ATP. After hydrolyzing ATP, the trailing head can dissociate from the microtubule. Thus, after the last step, the forward head is bound to the microtubule waiting for ATP binding and the trailing head is not attached to the microtubule, just like in the first step. Therefore, the cycle is ready to be repeated. As a result of one head always being attached to the microtubule, kinesin-1 is highly processive [122].

Cytoplasmic *dynein* is a motor that moves towards the (−) end of microtubules. With the help of the dynactin protein complex, it transports cargo from the membrane towards the center of the cell.

Kinesin and dynein work together inside a cell to transport organelles across the cytoplasm. Microtubules are generally used for long-range delivery of organelles, while actin filaments are used for shorter and more local delivery.

Microtubules facilitate motility of cells that make use of cilia and flagella for self-propulsion (such as sperm cells or *E.coli* that make use of flagella, or green algae that make use of cilia).

Cilia and flagella are microtubule-based extensions at the cell surface. They consist of radially arranged 9 doublet microtubules with 2 singlet microtubules at the center. These microtubules grow from the basal bodies, which are structures consisting of 9 triplet microtubules. Doublet microtubules along the flagella are attached together laterally. As dyneins move along the attachment site between the two doublet microtubules, they bend the cilia or flagella (Note that if the doublets were not attached, they would slide past one another instead of bending).

Microtubules also play an important role during mitosis. The separation of duplicated chromosomes prior to cell division into two daughter cells is facilitated by treadmilling of microtubules and the action of molecular motors.

A.2. Intermediate Filaments

Intermediate filaments constitute another type of cytoskeletal filaments. With a diameter of 10 nm, they fall between actin filaments (diameters of ~ 6 nm) and microtubules (diameters of ~ 25 nm) in size. They are made of 16 protofilaments made of dimers in the form of coiled-coils (coils joined together in a zipper-like structure). They have the characteristic feature of having high tensile strengths [122].

Unlike actin and microtubules, they are not found in plant and fungi cells. They are much more heterogenous than other cytoskeletal filaments as they are mostly tissue-specific. There is no intrinsic polarity associated with intermediate filaments, and as such, there are no molecular motors associated with them. They resemble F-actin and microtubules in having dynamic structures with subunit exchanges, however in comparison to actin and microtubules, they are much more stable [122].

There are five major classes of intermediate filaments. *Keratins* are class I and II filaments found in animal hair and nails. Keratins give epithelial cells structure and strength by associating with desmosomes (which link adjacent cells together), and hemidesmosomes (which link cells to the extracellular matrix) in epithelial tissue. *Vimentin*, *GFAP*, and *dermin* are class III filaments with structural roles in muscle cells [122]. *Neurofilaments* are class IV filaments. They are important for axonal structure in neurons. The class V filaments are the most common type of intermediate filaments. These filaments, known as *lamins*, are found in nucleus of cells and provide structure and facilitate transcriptional regulation in the nucleus [122].

A.3. Organisation of Cells into Tissues

In metazoans, cells organise into tissues and organs where they perform specialized functions. There are five different types of tissues in animals: epithelial tissue, connective tissue, muscular tissue, nervous tissue, and blood.

Cell-cell and cell-extracellular matrix interactions, in tandem with cytoskeleton, play a key role in organisation of cells into tissues. Cell-cell interactions are mediated by cell-adhesion molecules (CAMs), which bind cells together. There are four major CAM families: cadherins, integrins, selectins, and immunoglobulin (Ig) superfamily [122]. These molecules can be distributed randomly across the membrane or clustered in patches called cell junctions. CAMs can bind to the same type of CAM (homophilic binding) or to a different type of CAM (heterophilic binding) on the same or different cell. The part of CAM facing the cell inward use adapter proteins to link to the cytoskeleton directly or indirectly. By attachment to cytoskeleton and signalling pathways, the degree of cell-cell adhesion can alter cell shape and function [122].

To achieve cell-cell adhesion, parts of CAM outside of the cell form dimers with each other by making lateral connections. Then the dimers connect laterally together to form larger oligomers. These oligomers bind to other oligomers in other cells in a Velcro-like fashion to generate adhesion. Adhesion can be tight and long-lasting such as the adhesion between the nerve cells in the spinal cord or metabolic cells in liver, or weak and short-lasting such as the adhesion between the immune-system cells in the blood. The degree of adhesion is affected by a variety of factors such as binding affinity of molecules (thermodynamics), distribution and density of molecules (ensemble properties), activation rates of molecules (kinetics and biochemical) [122].

The extracellular matrix (ECM) can affect the cell shape and motility dramatically. ECM consists of proteins and polysaccharides with a density varying from tissue to tissue (Connective tissue is mostly ECM, whereas epithelium contains little ECM) [122]. The major classes of ECM components are proteoglycans, collagens, and multiadhesive matrix proteins like fibronectin and laminin. Through the expression of these components, ECM performs various duties such as giving strength in a tendon, tooth or bone [122]. ECM also serves as the basis for cell motility. Especially during morphogenesis, rearrangements between cells depend on the cell-ECM interactions [122].

A.4. Epithelial Cells

Epithelium consists of tightly-packed cells organised in sheetlike layers. It covers the inner and outer surfaces of tissues and organs and serves as a selective barrier. Its function is similar to that of plasma membrane of a cell. The membrane allows for specialization of the cell by separating the inner environment of the cell from outside. Epithelial tissue perform a similar function on a larger scale. They allow for compartmentalization in our bodies, so that different parts can perform different and specialized functions.

Epithelial cells are polarized due to the structural organization of their plasma membrane into apical (top), lateral (side), and basal (bottom) surfaces (Fig. A.2). They are normally in a sessile and non-motile state with adhesion molecules tightly attaching them to one another and to the extracellular matrix (ECM). They can be held together in a single layer (such as the epithelia lining the small intestine that moves digestion products towards the blood), or in multiple layers (such as in skin) [122].

Strong adhesive forces are needed to hold epithelial cells together. To generate such strong adhesion, adhesive molecules cluster into junctions. Tight junctions occur under the apical surface (which is extended by microvilli) and prevent the diffusion of macromolecules. They are made of thin bands of membrane proteins over the circumference of the cell. These proteins like occludin and claudin are in contact with similar thin bands in adjacent cells [122]. Cell polarity of epithelial cells is achieved through tight junctions, as they prevent the mixing of proteins and glycolipids of apical and basolateral surfaces.

Adherens junction lies under the tight junction. It connects the membranes of adjacent cells laterally. A belt of actin and myosin along the circumference of the cell serves as a tension cable in tandem with the adherens junction.

Gap junctions along the lateral surface of the cell allow rapid diffusion of small and water-soluble molecules across the cytoplasms of adjacent cells. They act as channels across cytoplasms of adjacent cells coupling them chemically or electrically (for example, neurons). Gap junctions are made of connexin proteins [122].

Some type of cells such as epithelial, smooth muscle and heart cells are further connected by desmosomes. Epithelial cells are also connected to the ECM from the basal surface via hemidesmosomes. Intermediate filaments connected to the desmosomes and hemidesmosomes give structure and stiffness to the cells. Through this stiffness, shear forces are distributed from cells to the entire tissue increasing the overall rigidity of the epithelium [122].

Cadherin family proteins are the main cell adhesion molecules in adherens junctions and desmosomes. Calcium ions rigidifies the cadherin oligomers, which bind laterally to cadherin oligomers of other cells to generate adhesion. Morphogenesis in vertebrates is accompanied by a transition of initially non-motile epithelial cells into motile precursor cells that are known as mesenchymal cells. This epithelial-mesenchymal transition is accompanied with a reduction of E-cadherin. Similarly, the transition of epithelial cells to malignant carcinoma cells is associated with a reduction in E-cadherin expression [122]. Reduced E-cadherin leads to reduced adhesion between cells, which then leads to increased cell motility and increased reorganizations between cells.

Epithelial cells make contacts with the basal lamina via adhesion receptors known as integrins. These are located both within and outside of hemidesmosomes [122]. Besides supplying adhesion of cells to the underlying ECM, integrin family proteins also faciliate signalling from outside of the cell to the inside and vice versa [122].

Other types of cells can also contain integrin-based aggregates (like focal adhesions) that bind cells to the underlying ECM. The environment in ECM can impact the cell dynamics dramatically through integrins. One example of this is in the movement of white blood cells (leukocytes) towards an infection site or a tissue damage site. Leukocytes normally circulate the blood unattached. Upon cues of infection or tissue damage, they must move rapidly to fight foreign invaders (like bacteria or viruses) or to clear away damaged tissue by trauma or inflammation. This movement of leukocytes is known as extravasation. Connections between leukocytes in the blood and endothelial cells in the blood vessel are maintained by selectin proteins. Extravasation is facilitated by breaking leukocyte-endothelia contacts through selectins,

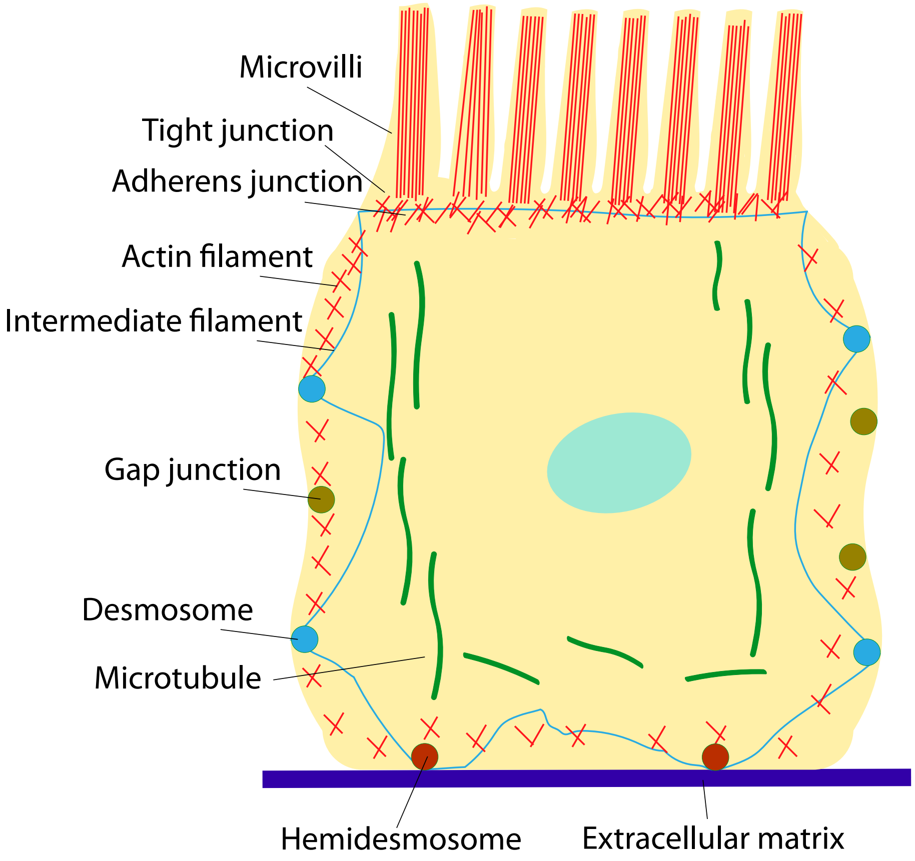
Microvilli
Tight junction
Adherens junction
Actin filament
Intermediate filament
Gap junction
Desmosome
Microtubule
Hemidesmosome
Extracellular matrix

Figure A.2.: Sketch of an epithelial cell from the small intestine. Epithelial cells have distinctive polarity. Nutrients are absorbed from the apical (top) domain and transported out across the basolateral (bottom and side) domain.

so that leukocytes can move from the blood to the underlying tissue [122].

B. Mathematical Background

B.1. Probability Density

The probability $P(x)$ to find the value η of a continuous stochastic variable within the interval $x \leq \eta \leq x + dx$ is defined as

$$dP = P(x + dx) - P(x) = \psi(x)dx \tag{B.1}$$

where $\psi(x)$ is the probability density, $\psi(x) = dP/dx$ [104]. The expectation value of a function $f(\eta)$ can be defined with the help of probability density as,

$$\langle f(\eta)\rangle = \int f(x)\psi(x)dx \tag{B.2}$$

Since the function on the left-hand side can be written as $f(\eta) = \int f(x)\delta(x-\eta)dx$, the average can be turned into,

$$\langle f(\eta)\rangle = \left\langle \int f(x)\delta(x-\eta)dx \right\rangle = \int f(x)\langle\delta(x-\eta)\rangle dx \tag{B.3}$$

Comparing eq. B.2 with eq. B.3 reveals that $\psi(x) = \langle\delta(x-\eta)\rangle$. For an r-dimensional distribution, the probability density can be defined as,

$$\psi_r(x_1, \ldots, x_r) = \langle\delta(x_1 - \eta_1)\ldots(x_r - \eta_r)\rangle \tag{B.4}$$

The probability density of the first $n < r$ variables can be calculated by integration over the remaining random variables with,

$$\psi_n(x_1, \ldots, x_n) = \int \psi_r(x_1, \ldots, x_r)dx_{n+1}\ldots dx_r \tag{B.5}$$

B.2. Characteristic Function

Fourier transform of the probability density is defined as the characteristic function of a probability distribution [166],

$$C_\eta(u) = \langle e^{iu\eta}\rangle = \int e^{iux}P_\eta(x)dx \tag{B.6}$$

Moments of a distribution can be calculated from the characteristic function via differentiation as,

$$M_n = \langle\eta^n\rangle = \frac{1}{i^n}\frac{d^n C_\eta(u)}{du^n} \tag{B.7}$$

Therefore, we can write the characteristic function in terms of the moments by Taylor expanding the characteristic function with [166],

$$C_\eta(u) = 1 + \sum_{n=1}^{\infty} (iu)^n \frac{M_n}{n!} \tag{B.8}$$

As a result, if all the moments of a distribution are known, then the characteristic function can be written. From the characteristic function, the probability density can be derived with an inverse Fourier transform,

$$\psi_\eta(x) = \frac{1}{2\pi} \int C_\eta(u) e^{-iux} du \tag{B.9}$$

Logarithm of the characteristic function defines the cumulants of a distribution as,

$$ln(C_\eta(u)) = ln\left(1 + \sum_{n=1}^{\infty} (iu)^n \frac{M_n}{n!}\right) = \sum_{n=1}^{\infty} (iu)^n \frac{K_n}{n!} \tag{B.10}$$

where K_n denotes the nth order cumulant [166]. From this equation, it can be seen that the first cumulant equals the first moment, $K_1 = M_1$. The second cumulant gives the variance with $K_2 = M_2 - M_1^2$.

B.3. Conditional Probability Density

Conditional probability density $P(x_1|x_2,\ldots,x_r)$ refers to the distribution of a single random variable x_1 within a r-dimensional distribution with all the other variables fixed. Then the total distribution is given by,

$$\psi_r(x_1,\ldots,x_r) = P(x_1|x_2,\ldots,x_r)\psi_{r-1}(x_2,\ldots,x_r) \tag{B.11}$$

We can extract the conditional probability density from this expression,

$$P(x_1|x_2,\ldots,x_r) = \frac{\psi_r(x_1,\ldots,x_r)}{\psi_{r-1}(x_2,\ldots,x_r)} = \frac{\psi_r(x_1,\ldots,x_r)}{\int \psi_r(x_1,\ldots,x_r)dx_1} \tag{B.12}$$

Conditional probability density can be used in the categorising stochastic processes. A process is defined to be a *purely random process*, if the conditional probability density P_n does not depend on the values of the stochastic variable at earlier times:

$$P(x_n,t_n|x_{n-1},t_{n-1},\ldots,x_1,t_1) = P(x_n,t_n) \tag{B.13}$$

The total distribution is then given by,

$$\begin{aligned} \psi_n(x_n,t_n,\ldots,x_1,t_1) &= P(x_n,t_n|x_{n-1},t_{n-1},\ldots,x_1,t_1)\psi_{n-1}(x_{n-1},t_{n-1},\ldots,x_1,t_1) \\ &= P(x_n,t_n)\ldots P(x_1,t_1) \end{aligned} \tag{B.14}$$

If the conditional probability density of a random variable depends on its value at the previous point in time, the stochastic process is defined as a *Markov process* with,

$$P(x_n,t_n|x_{n-1},t_{n-1},\ldots,x_1,t_1) = P(x_n,t_n|x_{n-1},t_{n-1}) \tag{B.15}$$

The probability distribution of a Markov process reads as,

$$\psi_n(x_n, t_n, \ldots, x_1, t_1) = P(x_n, t_n|x_{n-1}, t_{n-1})P(x_{n-1}, t_{n-1}|x_{n-2}, t_{n-2}) \ldots P(x_2, t_2|x_1, t_1)\psi_1(x_1, t_1) \tag{B.16}$$

For a Markov process, the relation

$$\psi_2(x_3, t_3, x_1, t_1) = \int \psi_3(x_3, t_3, x_2, t_2, x_1, t_1)dx_2 \tag{B.17}$$

implies that

$$P(x_3, t_3|x_1, t_1)\psi_1(x_1, t_1) = \int P(x_3, t_3|x_2, t_2)P(x_2, t_2|x_1, t_1)dx_2 \tag{B.18}$$

which leads to the Chapman-Kolmogorov equation

$$P(x_3, t_3|x_1, t_1) = \int P(x_3, t_3|x_2, t_2)P(x_2, t_2|x_1, t_1)dx_2 \tag{B.19}$$

B.4. Generalized Langevin Equation

Langevin equation as presented in eq. 2.1 is a linear inhomogenous differential equation, with an inhomogeneity coming from the fluctuating force. The discussion in the main text on time correlation functions and the fluctuation-dissipation theorem pertained to the solution of the linear Langevin equation. However, under an applied external potential, this equation can be nonlinear in a wide variety of situations.

Another problem comes from the assumption of white noise, or delta-correlated noise. In real life, noise is usually correlated in time and correspondingly friction does not depend on the instantenous velocity, but instead it is memory-dependent. In other words, friction often depends on a time interval rather than a single instantenous point in time. That is mathematically to replace the friction coefficient γ with a *memory function* $K(t)$, like

$$-\gamma v(t) \to -\int_{-\infty}^{t'} dtK(s-t)v(t) = -\int_{-\infty}^{t'} dtK(t)v(s-t) \tag{B.20}$$

The linear Langevin equation is Markovian, *i.e.*, the probability of fluctuating force at any given time depends only on its value at the previous time step (see Appendix for a general definition of Markov property). Problems of the kind with a time-dependent memory function like eq. B.20 are non-Markovian.

An example of non-Markovian Langevin equation is the motion of a Brownian particle under a harmonic potential of the form $U(x) = kx^2/2$. The force acting on the particle is $F = -kx$ and the corresponding equations of motion are given by

$$\begin{aligned} \frac{dx}{dt} &= v \\ \frac{dv}{dt} &= -\frac{\gamma}{m}v - w_0^2 x + \frac{1}{m}\eta_v(t) \end{aligned} \tag{B.21}$$

where $w_0 = \sqrt{k/m}$. The second equation can be solved by plugging a solution of the form $v(t) = e^{-(\gamma/m)t}u(t)$, which gives,

$$\begin{aligned} v(t) &= \int_{-\infty}^{t'} dt e^{-\gamma(s-t)/m}\big(- w_0^2 x(t) + \frac{1}{m}\eta_v(t)\big) \\ &= \int_{-\infty}^{t'} dt e^{-\gamma t/m}\big(- w_0^2 x(s-t) + \frac{1}{m}\eta_v(s-t)\big) \end{aligned} \tag{B.22}$$

If we now put this expression back into the first term in the equation of motion, we arrive at,

$$\frac{dx}{dt} = -\int_{-\infty}^{t'} dt K(t) x(s-t) + \eta_x(t) \tag{B.23}$$

where the kernel $K(t)$ and the fluctuation force for displacements η_x are given by

$$\begin{aligned} K(t) &= w_0^2 e^{-\gamma t/m} \\ \eta_x(t) &= \frac{1}{m}\int_{0}^{\infty} dt e^{-\gamma t/m}\eta_v(s-t) \end{aligned} \tag{B.24}$$

Therefore, the memory function of the velocity of the particle to the harmonic potential is observed to be an exponential decay with a characteristic timescale of $\tau_v = \gamma/m$, from the squared natural frequency of the harmonic potential w_0^2 [216]. As the potential is quadratic, by the equipartition theorem, we have $\langle x^2 \rangle = \frac{\mathrm{k_B}T}{m w_0^2}$ at equilibrium. In contrast with diffusive motion where $\langle x^2 \rangle$ scales with t or ballistic motion where scaling is with t^2, mean square displacement for Brownian motion inside a harmonic potential does not grow with time.

The concept of memory function can be generalised by rewriting the Langevin equation with memory function as,

$$m\frac{dv}{dt} = -\int_{0}^{t'} dt v(t) K(t'-t) + \eta(t) \tag{B.25}$$

Multiplying this equation with $v(0)$ and averaging in time, we get,

$$m\Big\langle \frac{dv(t)}{dt} v(0) \Big\rangle = -\int_{0}^{t'} dt \langle v(t) v(0) \rangle K(t'-t) \tag{B.26}$$

where the noise term drops out assuming it is uncorrelated with the initial velocity in average. If we take the Laplace transform $\mathscr{L}(s) = \int_0^\infty dt e^{-st} f(t)$ of both sides of this equation [110],

$$\begin{aligned} m\mathscr{L}\Big(\Big\langle \frac{dv(t)}{dt} v(0) \Big\rangle\Big) &= \mathscr{L}\Big(-\int_{0}^{t'} dt \langle v(t) v(0) \rangle K(t'-t)\Big) \\ m\big(s\mathscr{L}\big(\langle v(t) v(0) \rangle\big) - \langle v(0)^2 \rangle\big) &= -\mathscr{L}(K(t))\mathscr{L}\big(\langle v(t) v(0) \rangle\big) \end{aligned} \tag{B.27}$$

The first equation is rearranged by making use of two properties of Laplace transforms. Firstly, Laplace transform of derivative of a function is related to the function itself via $\mathscr{L}(dv(t)/dt) = s\mathscr{L}(v(t)) - v(0)$. Using this relation, we can rewrite the left-hand side of eq. B.27 in terms of the Laplace transform of the velocity autocorrelation function. Meanwhile right-hand side can be rearranged by noting that the integral is a convolution integral, and, just like the convolution property of Fourier transform, the Laplace transform of convolution in real space is multiplication of Laplace transform of each element of the kernel, $\mathscr{L}(f * g) = \mathscr{L}(f)\mathscr{L}(g)$. Making use of these two properties, Laplace transformed nonlinear Langevin quation, can be rearranged as depicted in eq. B.27.

Evaluating Langevin equation with memory function at $t = 0$ yields $mdv(0)/dt = \eta(0)$. Multiplying eq. B.25 with $mdv(0)/dt$ this time and averaging, gives,

$$m^2\left\langle \frac{dv(0)}{dt}\frac{dv(t)}{dt}\right\rangle = -m\int_0^{t'} dt\left\langle v(t)\frac{dv(0)}{dt}\right\rangle K(t'-t) + \langle \eta(t)\eta(0)\rangle \tag{B.28}$$

where $mdv(0)/dt$ is replaced with $\eta(0)$ in the last term. Now we can apply a similar procedure and take the Laplace transform of each side of the equation as before. However, to reduce complexity in expression, we will denote the Laplace transform of velocity autocorrelation with $C_v(s)$, Laplace transform of noise autocorrelation with $C_\eta(s)$, and Laplace transform of memory function with $K(s)$. Taking the Laplace transform gives,

$$-m^2\left(s^2C_v(s) - s\langle v(0)^2\rangle - \left\langle v(0)\frac{dv(0)}{dt}\right\rangle\right) = m(sC_v(s) - \langle v(0)^2\rangle)K(s) + C_\eta(s) \tag{B.29}$$

Extracting C_v from eq. B.27 and plugging it into eq. B.29, we get,

$$-m\langle v(0)^2\rangle K(s) + C_\eta(s) = 0 \tag{B.30}$$

From this expression, we arrive at the following relation between the memory function and the autocorrelation of noise:

$$\langle \eta(t)\eta(0)\rangle = m\langle v(0)^2\rangle K(t) = \mathrm{k_B}TK(t) \tag{B.31}$$

Therefore, the memory function is proportional with the autocorrelation function of the noise, which is a generalisation of the fluctuation-dissipation theorem for non-Markovian systems [110]. Indeed, comparing with Markovian form of the fluctuation-dissipation relation at eq. 2.11, we can see the equality of the two when $K(t) = 2\gamma\delta(t)$. In other words, in the limit of infinitely short memory function, non-Markovian processes can be approximated as Markovian.

The concept of memory function arises in the consideration of time-dependent friction. We can extend this idea to systems driven out of equilibrium by external forcing. To illustrate, we add an external force to the earlier example of damped harmonic oscillator. The equation of motion is,

$$m\ddot{x}(t) + \gamma\dot{x}(t) + kx(t) = F_e(t) \tag{B.32}$$

where F_e stands for an external force perturbing the system. We look for a spectral solution by taking the Fourier transforms of both sides of the equation,

$$(k - mw^2 - i\gamma w)x(w) = F_e(w) \tag{B.33}$$

Rewriting this expression as,

$$x(w) = \frac{1}{\chi(w)} F_e(w) \tag{B.34}$$

where $\chi(w) = k - mw^2 - i\gamma w$ is defined as the response function. We now take the inverse Fourier transform of B.34,

$$x(t) = \int_{-\infty}^{\infty} dt \chi(t' - t) F_e(t) \tag{B.35}$$

which reveals the idea behind the response function. It represents the response of the system to an external forcing that disturbs the equilibrium system for a duration in time.

Within the scope of linear response theory, which describes response of systems to small perturbations out of equilibrium such that the disturbant force can be approximated linearly, the real and imaginary parts of $\chi(w)$ can be transformed into one another with Kramers-Kronig relations and the imaginary part of the response function represents the dissipation in the system [110].

A memory dependent friction is not the only concept that makes the nonlinear Langevin equation harder to tackle. Another important issue arises with the introduction of nonlinearity as position-dependent noise. To see this, we start from the general form of the nonlinear Langevin equation,

$$\frac{dx}{dt} = h(x,t) + D(x,t)\eta(t) \tag{B.36}$$

where $h(x,t)$ is a drift term, $D(x,t)$ is a diffusion term and $\eta(t)$ is Gaussian noise with $\langle \eta(t) \rangle = 0$ and $\langle \eta(t)\eta(t') \rangle = g\delta(t - t')$. If the term D was a constant scalar, then the noise term as a whole is referred as *additive noise*. However, if it depends explicitly on the position x, which renders the equation nonlinear, then the noise term is referred as *multiplicative noise*.

Involving multiplicative noise creates a sly paradox. White noise is not a smooth, *i.e.*, continuous and differentiable, function; in other words, there is no infinitesimally small interval of time Δt in which its values are smooth. Furthermore, the noise is modelled to be delta-correlated in time. So if we were to discretize eq. B.36 from a point in time t to $t + \Delta t$, the noise term would still be uncorrelated between these two points by construction, that is, $\langle \eta(t)\eta(t + \Delta t) \rangle = 0$. The problem arises from coupling of the uncorrelated nature of noise in Δt with the position-dependent diffusion: When we are integrating the nonlinear Langevin equation, which value of the diffusion term should we take, $D(x,t)$ or $D(x, t + \Delta t)$, or some other point in between these two points? Each uncorrelated change in x due to the noise will induce a change between $D(x,t)$ and $D(x, t + \Delta t)$, which creates this ambiguity in where to define $D(x,t)$. The choice of choosing the diffusion term before the jump in time from t to $t + dt$, or after the jump, or some time in between, is ambiguous. This is to say, within a time interval Δt, the diffusion term can take on any value from $D[x(t)]$ to $D[x(t)+\alpha\Delta x]$, where $\alpha = [0,1]$ and $\Delta x = x(t+\alpha\Delta t) - x(t)$. Any α value is mathematically correct, due to the ambiguous nature of position-dependent diffusion.

A choice of $\alpha = 0$ indicates that we are taking the diffusion term at the point in time at the beginning of the time interval (at time t), in other words, we are taking the leftmost point in the time interval of Δt. This solution of $\alpha = 0$ is known as the Itô solution [143]. It is especially popular in economics, because of its so-called *martingale property.* The martingale property expresses a lack of information about future events. If we choose the beginning of the interval as our solution, then we do not have information about later points in time, hence the martingale property. The choice of $\alpha = 0.5$, the middle point of the interval at time $(t+\Delta t)/2$, is known as the Stratonovich solution [143]. It is most commonly used in physics and engineering. A choice with $\alpha = 1$, so the end of the interval at time $t+\Delta t$, is referred as the anti-Itô solution [143]. In principle, any other α value within the interval $[0,1]$ can be chosen, with each of them leading to different but consistent rules of calculus.

To see the significance of this ostensibly mathematical curiosity, we start by linearizing the diffusion term with a Taylor expansion in x as

$$D[x(t)+\alpha\Delta x] \approx D[x(t)] + \alpha\frac{dD[x(t)]}{dx}\Delta x \tag{B.37}$$

When this linearized term is plugged back into the integral of the noise term in eq. B.36, $\int_0^{t'} dtD[x(t)]\eta(t)$, we get different results based on the value of α. In the Itô interpretation with $\alpha = 0$, we have the following relation:

$$\int\limits_t^{t+\Delta t} dt' D[x(t')]\eta(t') \approx D[x(t)] \int\limits_t^{t+\Delta t} dt'\eta(t') \tag{B.38}$$

which vanishes upon taking the average as $\langle \int_t^{t+\Delta t} dt'\eta(t')\rangle = 0$. However, if we were to choose an α value that is not equal to 0, then we end up with

$$\int\limits_t^{t+\Delta t} dt' D[x(t')]\eta(t') \approx D[x(t)] \int\limits_t^{t+\Delta t} dt'\eta(t') + \alpha\frac{dD[x(t)]}{dx} \int\limits_t^{t+\Delta t} dt'\Delta x(t')\eta(t') \tag{B.39}$$

where the first term on the right-hand side vanishes as before [206]. However, the second term does not vanish as $\langle \Delta x(t')\eta(t')\rangle \neq 0$. In other words, we are adding an additional drift term to $\langle dx/dt\rangle$ in eq. B.36 that is proportional with the stochastic calculus choice α, as well as the spatial gradient of diffusion. This is known as *noise-induced drift* or *spurious drift* [206].

To derive equations on interpretation of stochastic calculus is beyond the scope of this manuscript, so we will suffice by a brief discussion on the literature. Volpe, *et.al.* observed these noise-induced forces experimentally for the motion of a particle in a fluid near a wall [202, 20]. The wall induces a gradient of diffusion due to hydrodynamical effects. They first calculate the forces on the particle from local drift velocity measurement (namely calculating velocities and then relating the velocity to the force via multiplication with the friction coefficient). They then go on to calculate the forces from particle-wall interaction potential $U(z) = -\mathrm{k_B}Tlnp(z)$, where $p(z)$ denotes the position distribution of the particle at thermal equilibrium. These forces are shown not to be in agreement, until the addition of noise-induced drift with the choice of $\alpha = 1$, the anti-Itô interpretation. This result emphasizes the importance of taking the noise-induced drift into account when diffusion gradients are present.

In interpreting the seeming dilemma in choice of stochastic calculus, Wong and Zakai argued that white noise serves only as an approximation in any real world system. All kinds of noise in the real world is somewhat correlated and is at least piecewise continuously differentiable in a small enough interval of time. They then approximated white noise as an Ornstein-Uhlenbeck process with a finite correlation time τ, with $\tau \to 0$. Within this approximation, one can define an infinitesimally small interval that is smooth. The finite but small correlation approximation of noise results in the Stratonovich interpretation and it reproduces the usual rules of calculus like the chain rule [209].

In directly tackling the dilemma, van Kampen famously called nonlinear Langevin equation in eq. B.36 a meaningless set of strings and that it is only a pre-equation until an interpretation rule is made [99]. To solve this ostensible dilemma, he makes a distinction between systems with internal noise and external noise. If the source of the noise is external, that is, when the source is not influenced by the system itself, for example, in the propagation of electromagnetic waves through the turbulent atmosphere, then if the autocorrelation time τ of noise is much shorter than the other time scales of the system, the Stratonovich rule should be chosen by the Wong-Zakai theorem. However, if the source of the noise is internal, then his suggestion is to construct the real equation on a case by case basis *a posteriori* after the system reaches a stable steady state [99].

Kupferman, *et.al.* show that, for systems with inertia and colored multiplicative noise, it is the interplay between the two which determines the stochastic calculus interpretation. Through an analytical treatment, they find that if the noise correlation time tends to zero faster than the particle relaxation time, then the correct interpretation should be Stratonovich interpretation, while if it is the other way round, then the interpretation should be Itô. However, they conclude that if the two time scales are comparable, then the stochastic differential equation cannot be interpreted with neither of the interpretations [113].

Taking the time-scale competition idea one step further, Pesce, *et.al* experimentally demonstrate that a noisy electrical circuit undergoes a transition from obeying Stratonovich calculus to obeying Itô calculus [154]. They build a simple RC-electric circuit driven with a noise that has a much shorter correlation time than the relaxation time of the circuit. The input noise is then multiplied with a state-dependent signal to induce multiplicative noise. For colored noise with a finite correlation time $\tau > 0$, Stratonovich interpretation holds as expected from the Wong-Zakai theorem. However, as the correlation time of noise decays, α starts to decay from 0.5 (Stratonovich) to 0 (Itô), which is an unexpected deviation from Wong-Zakai theorem, as shorter correlation times better suit its applicability. Instead, the origin of transition lies in the simple observation that feedback in an electrical circuit is not instantenously delivered, but instead it has a finite delay time. The transition is mapped with the ratio between the feedback delay time and the noise correlation time, δ/τ. When the delay time of feedback is high in comparison to the noise correlation time (in the limit of $\delta \gg \tau$), noise is randomized with respect to the state-dependent diffusion, which leads to a memoryless system in vein of martingale property of Itô interpretation. When $\delta/\tau \approx 1$, the state-dependence of diffusion on noise matters again, which gives back the Stratonovich interpretation [154].

Overall the question of which interpretation is correct is meaningless, as stressed by van Kampen. Nonlinear Langevin equation with multiplicative noise can be described either way. There is no new mathematical insight or content coming from choosing one interpretation over the other *per se* [206]. The dilemma has to do with modelling rather than a single correct mathematical definition. So the appropriate interpretation emanates from the properties and the details of the model itself *a posteriori*.

B.5. Fokker-Planck Equation

The discussion in the main text relied on Langevin equation in describing Brownian motion mathematically by adding a phenomenological random noise term to Newton's second law. By this token, expectation values of observables like displacement and velocity are derived by averaging over different realizations of the stochastic force. Alternatively, averages can also be calculated with the help of a probability distribution function, which comes as a result of a partial differential equation, known as *Fokker-Planck equation*.

As Brownian motion is a Markov process, probability density of the position of a Brownian particle at time $t + \Delta t$ depends on its value at the previous time point t:

$$P(x, t + \Delta t) = \int P(x, t + \Delta t | x', t) P(x', t) dx' \tag{B.40}$$

where $P(x, t + \Delta t | x', t)$ represents the conditional probability density, *i.e.*, the probability of the Brownian particle being at the position x at time $t + \Delta t$ given that it was at position x' at time t.

The nth moment of the distribution is given by,

$$M_n(x', t, \Delta t) = \langle [x(t + \Delta t) - x(t)]^n] \rangle = \int (x - x')^n P(x, t + \Delta t | x', t) dx \tag{B.41}$$

Assuming that all the moments of the distribution are known, we can write down the characteristic function in terms of the moments by a Taylor expansion,

$$C(u, x', t, \Delta t) = \int_{-\infty}^{\infty} e^{iu(x-x')} P(x, t + \Delta t | x', t) dx = 1 + \sum_{n=1}^{\infty} (iu)^n \frac{M_n(x', t, \Delta t)}{n!} \tag{B.42}$$

which is the Fourier transform of the probability density (for a more detailed discussion see the Appendix).

The probability density is the inverse Fourier transform of the characteristic function of the distribution, by construction,

$$\begin{aligned} P(x, t + \Delta t | x', t) &= \frac{1}{2\pi} \int_{-\infty}^{\infty} e^{-iu(x-x')} C(u, x', t, \Delta t) du \\ &= \frac{1}{2\pi} \int_{-\infty}^{\infty} e^{-iu(x-x')} \left[1 + \sum_{n=1}^{\infty} (iu)^n \frac{M_n(x', t, \Delta t)}{n!} \right] du \end{aligned} \tag{B.43}$$

Noting that $\frac{1}{2\pi} \int_{-\infty}^{\infty} (iu)^n e^{-iu(x-x')} du = -\left(\frac{\partial}{\partial x}\right)^n \delta(x - x')$ from the representation of the delta function and the identity $\delta(x - x') f(x') = \delta(x - x') f(x)$, we can rearrange the terms into,

$$P(x, t + \Delta t | x', t) = \left[1 + \sum_{n=1}^{\infty} \frac{1}{n!} \left(\frac{-\partial}{\partial x} \right)^n M_n(x, t, \Delta t) \right] \delta(x - x') \tag{B.44}$$

We can expand the moments around Δt,

$$M_n(x, t, \Delta t)/n! = D^n(x, t) \Delta t + O(\Delta t^2) \tag{B.45}$$

where the zeroth order terms are omitted, as for $\Delta t = 0$, the probability has the initial value $P(x, t | x', t) = \delta(x - x')$, which leads to vanishing moments. Combining eq. B.40 with eq. B.44 and eq. B.45, we end up with,

$$\frac{\partial P(x, t)}{\partial t} = \sum_{n=1}^{\infty} \left(\frac{-\partial}{\partial x} \right)^n D^{(n)}(x, t) P(x, t) = L_{KM} P(x, t) \tag{B.46}$$

where $L_{KM} = \sum_{n=1}^{\infty} \left(\frac{-\partial}{\partial x}\right)^n D^{(n)}(x, t)$ is known as the *Kramers-Moyal operator*, which acts on both $D^{(n)}(x, t)$ and $P(x, t)$. This is called *Kramers-Moyal forward expansion* [166].

There can be four different types of stochastic processes according to eq. B.46. If the expansion stops at $n = 0$, there is simply no dynamics. If it stops at $n = 1$, we have a deterministic equation in $\partial P / \partial t = -\partial D^{(1)} / \partial x$. This is nothing but *Liouville equation* of classical mechanics. If we include the $n = 2$ term, we have diffusion processes that are described by *Fokker-Planck equation* as,

$$\frac{\partial P(x, t)}{\partial t} = -\frac{\partial D^{(1)}(x, t)}{\partial x} + \frac{\partial D^{(2)}(x, t)}{\partial x^2} \tag{B.47}$$

If however the truncation stops at $n > 2$, the probability distribution would be smaller than zero by Pawula theorem [166].

Fokker-Planck equation[1] can be casted into a continuity equation for probability distribution in the form of $\partial P / \partial t = -\partial J / \partial x$, with the probability current $J(x, t)$ given as,

$$J(x, t) = \left[D^{(1)}(x, t) - \frac{\partial}{\partial x} D^{(2)}(x, t) \right] P(x, t) \tag{B.48}$$

---

[1] Fokker-Planck equation for position distribution is also known as *Smoluchowski equation.* While in mathematics, it is more commonly known as *Kolmogorov forward equation.*

For a Wiener process, which has a vanishing drift coefficient $D^{(1)} = 0$ and a constant diffusion coefficient $D^{(2)} = D$, by definition, the transition probability $P = P(x,t|x',t')$ is given by the diffusion equation,

$$\frac{\partial P}{\partial t} = D\frac{\partial^2 P}{\partial x^2} \tag{B.49}$$

with the initial condition $P(x,t'|x',t') = \delta(x-x')$. This equation can easily be solved by taking the Fourier transform of the probability distribution in space to get a linear equation in time, and then invoking the initial condition. The solution is found to be a Gaussian distribution,

$$P(x,t|x',t') = \frac{1}{\sqrt{4\pi D(t-t')}} exp\left(\frac{-(x-x')^2}{4D(t-t')}\right) \tag{B.50}$$

Thus, in the probability density expression, $P(x,t) = \int P(x,t|x',t')P(x',t')dx'$, the conditional probability serves as a Green's function.

For the Ornstein-Uhlenbeck process with a linear drift coefficient $D^{(1)} = -\gamma x$ and a constant diffusion coefficient $D^{(2)} = D$, we get the following Fokker-Planck equation,

$$\frac{\partial P}{\partial t} = \gamma\frac{\partial}{\partial x}(xP) + D\frac{\partial^2 P}{\partial x^2} \tag{B.51}$$

B.6. Numerical Accuracy of the Velocity Verlet Algorithm

In this appexdix, we extend the discussion on the accuracy of velocity Verlet algorithm further by looking at the propagation of points in phase space in time. To do so, we take the time derivative of a general function $f(r^N(t), p^N(t))$ that depicts the points in phase space. The time derivative is given by the chain rule as $\dot{f} = \dot{r}\partial f/\partial r + \dot{p}\partial f/\partial p = iLf$, where iL is the *Liouville operator*, defined as $iL = \dot{r}\partial/\partial r + \dot{p}\partial/\partial p$. The solution of this equation is simply,

$$f(r^N(t+\Delta t), p^N(t+\Delta t)) = \mathrm{e}^{iLt} f(r^N(t), p^N(t)) \tag{B.52}$$

We can rewrite the Liouville operator with Hamilton's equations of motion $\dot{r} = \partial H/\partial p$ and $\dot{p} = -\partial H/\partial r$ with a generic Hamiltonian of the form $H = p^2/2m + V$. Liouville operator thus turn into $iL = \frac{p}{m}\frac{\partial}{\partial r} + f\frac{\partial}{\partial p} = i(L_r + L_p)$. The problem with this expression is that L_r and L_p do not commute. Therefore, in calculation of eq. B.52, we cannot dissect the exponential into a simple multiplication of $\mathrm{e}^{iL_r t}\mathrm{e}^{iL_p t}$. However, we can approximate as,

$$\mathrm{e}^{iLt} = \mathrm{e}^{iL_p\Delta t/2}\mathrm{e}^{iL_r\Delta t}\mathrm{e}^{iL_p\Delta t/2} + O(\Delta t^3) \tag{B.53}$$

which is known as *Trotter identity* [34]. It can be confirmed by taking the Taylor expansion of exponentials in both sides of the equation.

Now we can propagate the exponentials one by one. The first exponential gives,

$$\begin{aligned} \mathrm{e}^{iL_p\Delta t/2} f(r(t),p(t)) &= \mathrm{e}^{if\frac{\Delta t}{2}\frac{\partial}{\partial p}} f(r(t),p(t)) \\ &= \sum_{n=0}^{\infty}\frac{1}{n!}\left(\frac{f\Delta t}{2}\right)^n \frac{\partial^n f(r(t),p(t))}{\partial p^n} \\ &= f(r(t), p(t) + f(t)\Delta t/2) \end{aligned} \tag{B.54}$$

which, following the same idea, can be further propagated to,

$$\begin{aligned} \mathrm{e}^{iL_r \Delta t} f(r(t), p(t) + f(t)\Delta t/2) &= \mathrm{e}^{i\frac{p\Delta t}{m}\frac{\partial}{\partial r}} f(r(t), p(t) + f(t)\Delta t/2) \\ &= f\left(r(t) + \frac{p\left(\frac{\Delta t}{2}\right)}{m}\Delta t, p(t) + f(t)\Delta t/2\right) \end{aligned} \tag{B.55}$$

which is finally propagated to,

$$\begin{aligned} \mathrm{e}^{iL_p \Delta t/2} f\left(r(t) + \frac{p\left(\frac{\Delta t}{2}\right)}{m}\Delta t, p(t) + f(t)\Delta t/2\right) &= \mathrm{e}^{if\frac{\Delta t}{2}\frac{\partial}{\partial p}} f\left(r(t) + \frac{p\left(\frac{\Delta t}{2}\right)}{m}\Delta t, p(t) + f(t)\Delta t/2\right) \\ = f\left(r(t) + \frac{p\left(\frac{\Delta t}{2}\right)}{m}\Delta t, p(t) + f(t)\Delta t/2 + f(t+\Delta t)\Delta t/2\right) \end{aligned} \tag{B.56}$$

In the end, the propagation of a point in phase space is established to evolve as,

$$\begin{aligned} r(t) &\to r(t) + \frac{p\left(\frac{\Delta t}{2}\right)}{m}\Delta t \approx r(t) + \frac{p(t)}{m}\Delta t + \frac{p(t+\Delta t)}{2m}\Delta t^2 \\ p(t) &\to p(t) + \frac{\Delta t}{2}(f(t) + f(t+\Delta t)) \end{aligned} \tag{B.57}$$

which describe nothing but the velocity Verlet integration steps. Therefore, we established that description of the time evolution of a point in phase space with velocity Verlet algorithm obeys Liouville formulation, which indicates that velocity Verlet scheme conserves area in phase space. In other words, energy is conserved within the approximation of velocity Verlet numerical integration without a long term energy drift unlike the Euler algorithm. The caveat is that we truncated the exponential expression in eq. B.53 via the Trotter identity. As a result, velocity Verlet is actually conserving a pseudo-energy that is slightly different than the true energy of the system.

C. Polymers

Polymers are long macromolecules made of repeating identical monomers. The structure and dynamics of a polymer is determined by the collective properties of monomers, which is why it is useful to think in terms of the larger structure instead of the individual monomer units. Likewise, in an ensemble of polymers, properties of polymers dominate the dynamics. Polymers are everywhere from DNA and proteins to plastic and rubber. Here we will give a brief description of polymer dynamics that is relevant within the scope of this thesis.

C.1. Freely Jointed Chain

Arguably the simplest idealisation of a polymer is a chain made of N bonds that are pointing in random directions independently from each other. Each bond has a length of b_0. This model depicted in fig. C.1-A is known as *freely jointed chain* model [42].

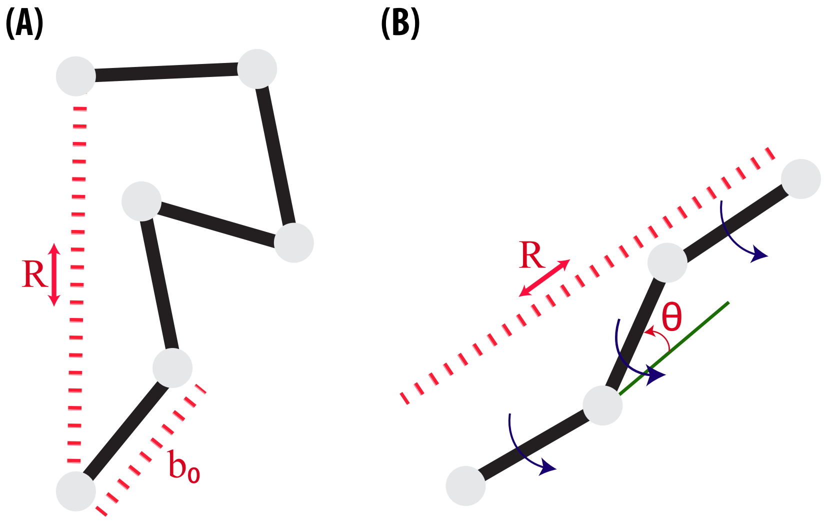

Figure C.1.: Sketches of simple discrete polymer models: (A) Freely jointed chain, and (B) freely rotating chain with end-to-end vector R and bond length b_0.

We can characterize the polymer by its end-to-end vector R. It is nothing but the sum of the bond vectors, $\boldsymbol{R} = \boldsymbol{R}_N - \boldsymbol{R}_0 = \sum_{n=1}^{N} \boldsymbol{r}_n$. As the bonds are independent from each other, $\langle \boldsymbol{r}_N \rangle = 0$ by the central limit theorem. Instead we calculate the mean square of the end-to-end vector with,

$$\langle R^2 \rangle = \sum_{n,m=1}^{N} \langle \boldsymbol{r}_n \cdot \boldsymbol{r}_m \rangle = \sum_{n=1}^{N} \langle \boldsymbol{r}_n^2 \rangle + 2 \sum_{n>m} \langle \boldsymbol{r}_n \cdot \boldsymbol{r}_m \rangle = N b_0^2 \tag{C.1}$$

where the cross term drops out as bonds are uncorrelated. Therefore mean square root of the end-to-end vector is given by $\langle R^2 \rangle^{(1/2)} = \sqrt{N} b_0$.

C.2. Freely Rotating Chain

Uncorrelated rotations of bonds indicate a flexible type of polymer. We can generate a semiflexible polymer by inducing correlations between successive bonds. One example of a discrete semiflexible polymer is the so-called *freely rotating chain* where bond n can rotate freely around the fixed bond $n-1$ with fixed angle θ [42]. This indicates a correlation between the bonds of the form $\langle \boldsymbol{r}_n \cdot \boldsymbol{r}_m \rangle = \cos\theta \langle \boldsymbol{r}_{n-1} \cdot \boldsymbol{r}_m \rangle$, with the initial condition $\langle r_0^2 \rangle = b_0^2$. By looking at the first few terms, $r_1 r_0 = \cos\theta r_0 r_0 = \cos\theta b_0^2$, $r_2 r_0 = \cos\theta r_1 r_0 = \cos\theta(\cos\theta b_0^2)$, we can deduce the general form of the recursion relation with $\langle \boldsymbol{r}_n \cdot \boldsymbol{r}_m \rangle = b_0^2 (\cos\theta)^{|n-m|}$. We can calculate the mean square end-to-end vector from this relation,

$$\langle R^2 \rangle = \sum_{n,m=1}^{N} \langle \boldsymbol{r}_n \cdot \boldsymbol{r}_m \rangle = \sum_{n=1}^{N} \sum_{m=1-n}^{N-n} \langle \boldsymbol{r}_n \cdot \boldsymbol{r}_{m+n} \rangle \tag{C.2}$$

where we substract n from the index of the second sum. In the limit of large N, we can change the index limits to infinity with,

$$\sum_{m=-\infty}^{\infty} \langle \boldsymbol{r}_n \cdot \boldsymbol{r}_{m+n} \rangle = b_0^2 \left(1 + 2 \sum_{m=1}^{\infty} \cos^m \theta \right) = b_0^2 \frac{1 + \cos\theta}{1 - \cos\theta} \tag{C.3}$$

Therefore, end-to-end distance is again proportional with $\sqrt{N}$ with $\langle R^2 \rangle = N b_0^2 (1 + \cos\theta)/(1 - \cos\theta)$.

C.3. Rouse Chain

Dependence of end-to-end vector to the bond length led the way to the idea of describing local structure of polymers by the bond length [42]. Such a generic description of structure is provided by the Gaussian chain in which the polymer is modelled to have Gaussian distributed bond lengths. Furthermore, the beads are assummed to be connected by harmonic springs with a spring constant $k_s = 3\mathrm{k_B} T / b^2$.

Rouse model builds on this idea of fixing the structure via bonds to describe the dynamics of the polymer. We can describe the dynamics of bonds with Langevin equations, by assumming a Gaussian chain where each bead feels the same friction. For N bonds, the equations in the overdamped limit read,

$$\begin{aligned}\frac{dr_0}{dt} &= \frac{-3\mathrm{k_B}T}{\gamma b^2}(r_0 - r_1) + \eta_0\\ \frac{dr_n}{dt} &= \frac{-3\mathrm{k_B}T}{\gamma b^2}(2r_n - r_{n-1} - r_{n+1}) + \eta_n\\ \frac{dr_N}{dt} &= \frac{-3\mathrm{k_B}T}{\gamma b^2}(r_N - r_{N-1}) + \eta_N\end{aligned} \tag{C.4}$$

where n runs over the bonds from 1 to $N-1$ and the properties of the noise term η is given with $\langle\eta_n(t)\rangle = 0$ and $\langle\eta_n(t)\eta_m(t')\rangle = 2D\delta_{nm}\delta(t-t')$, as before. This equation can be recognised as the discretised second derivative of the bond vectors with finite-time difference. So taking the continous limit, we end up with,

$$\gamma\frac{dr_n}{dt} = k\frac{\partial^2 r_n}{\partial n^2} + \eta_n \tag{C.5}$$

where the bonds at the beginning and the end provide the boundary conditions as $r_0 = r_1$, with $\frac{\partial r_n}{\partial n} = 0$ at $n = 0$, and $r_{N+1} = r_N$, with $\frac{\partial r_n}{\partial n} = 0$ at $n = N$.

The aim is to find the independent normal modes of this equation that describe the motion of the polymer. To do so, we make a linear transformation of the bond vector as $x_p(t) = \int_0^N dn\phi_{pn}r_n(t)$ and choose ϕ_{pn} such that the equation of motion becomes linear with [42],

$$\gamma_p\frac{\partial x_p}{\partial t} = -k_p x_p + \eta_p \tag{C.6}$$

The left-hand side of equation is $\gamma_p\partial x_p/\partial t = \gamma_p\int_0^N dn\phi_{np}\partial r_n/\partial t$. Plugging back eq. C.5, we obtain

$$\gamma_p\frac{\partial x_p}{\partial t} = \frac{\gamma_p}{\gamma}\int_0^N dn\phi_{pn}\left(k\frac{\partial^2 r_n}{\partial n^2} + \eta_n\right) \tag{C.7}$$

where the first term inside the paranthesis can be evaluated with integration by parts into

$$\begin{aligned}\int_0^N dnk\phi_{pn}\frac{\partial^2 r_n}{\partial n^2} &= \left[k\phi_{pn}\frac{\partial r_n}{\partial n}\right]_0^N - \int_0^N dnk\frac{\partial r_n}{\partial n}\frac{\partial\phi_{pn}}{\partial n}\\ &= \left[k\phi_{pn}\frac{\partial r_n}{\partial n}\right]_0^N - \left[k\frac{\partial\phi_{pn}}{\partial n}r_n\right]_0^N + \int_0^N dn\left[k\frac{\partial^2\phi_{pn}}{\partial n^2}r_n + \phi_{pn}\eta_n\right]\end{aligned} \tag{C.8}$$

where integration by parts is applied twice and the first terms on the right-hand sides vanish due to the boundary conditions. Plugging this expression back to eq. C.7 gives,

$$\gamma_p\frac{\partial x_p}{\partial t} = -\frac{\gamma_p}{\gamma}\left[k\frac{\partial\phi_{pn}}{\partial n}r_n\right]_0^N + \frac{\gamma_p}{\gamma}\int_0^N dn\left[k\frac{\partial^2\phi_{pn}}{\partial n^2}r_n + \phi_{pn}\eta_n\right] \tag{C.9}$$

By eq. C.6, we also have,

$$\gamma_p\frac{\partial x_p}{\partial t} = \int_0^N dn(-k_p\phi_{pn}r_n) + \eta_p \tag{C.10}$$

The only way eq. C.9 and eq. C.10 to hold together is to have the following relation:

$$\frac{\gamma_p}{\gamma} k \frac{\partial^2 \phi_{pn}}{\partial n^2} = -k_p \phi_{pn} \tag{C.11}$$

with the boundary conditions $\partial\phi_{pn}/\partial n = 0$ at $n = 0$ and $n = N$, and $\eta_p = \frac{\gamma_p}{\gamma} \int_0^N dn \phi_{pn} \eta_n$. This equation can assume an oscillatory solution of the form $\phi_{pn} = \frac{1}{N} \cos \frac{p\pi n}{N}$, with $p = 0, 1, 2, \ldots$ and $k_p = k \frac{\gamma_p}{\gamma} \left(\frac{p\pi}{n} \right)^2$. Therefore, the transformed coordinates become,

$$x_p = \frac{1}{N} \int\limits_0^N dn \cos\left(\frac{p\pi n}{N} \right) r_n(t) \tag{C.12}$$

with p representing each normal mode. The equation of motion for the transformed coordinates is the same as that of a Brownian particle under a harmonic spring potential, as depicted in eq. C.6. The mode-dependent spring constant is given by $k_p = 6\pi^2 \mathrm{k_B} T p^2/(Nb^2)$. We can write down the time correlations of the modes as that of harmonically trapped Brownian particle with a mode-dependent trap constant:

- For $p > 0$,

$$\langle x_{p\alpha}(t) x_{q\beta}(0) \rangle = \delta_{pq} \delta_{\alpha\beta} \frac{\mathrm{k_B} T}{k_p} e^{-t/\tau_p} \tag{C.13}$$

where $\tau_p = \tau_1/p^2$ and $\tau_1 = \gamma_1/k_1 = \gamma N^2 b^2/(3\pi^2 \mathrm{k_B} T)$.

- For $p = 0$,

$$\langle (x_{0\alpha}(t) - x_{0\alpha}(0))(x_{0\beta}(t) - x_{0\beta}(0)) \rangle = \delta_{\alpha\beta} \frac{2\mathrm{k_B} T}{\gamma_0} t = \delta_{\alpha\beta} \frac{2\mathrm{k_B} T}{N\gamma} t \tag{C.14}$$

To obtain the time correlations in terms of the bond vectors r, we can take the inverse transform of x_p with,

$$r_n = x_0 + 2 \sum_{p=1}^{\infty} x_p \cos\left(\frac{p\pi n}{N} \right) \tag{C.15}$$

From this relation, the average of the zero mode with $p = 0$ can be identified as the position of the centre of mass of the polymer via $\langle x_0 \rangle = \frac{1}{N} \int_0^N dn r_n$. The mean square displacement of the center of mass is then calculated with,

$$\langle (r_{cm}(t) - r_{cm}(0))^2 \rangle = \sum_{\alpha = x,y,z} \langle (x_{0\alpha}(t) - x_{0\alpha}(0))^2 \rangle = 6 \frac{\mathrm{k_B} T}{N\gamma} t \tag{C.16}$$

which is the same as that of a Brownian particle with a diffusion coefficient $D = \mathrm{k_B} T/(N\gamma)$.

The other mods with $p > 0$ represent the internal conformations of the polymer, and by that token, also the end-to-end vector. As cosine is an even function, the end-to-end vector is simply given by $\boldsymbol{R} = \boldsymbol{R}_N(t) - \boldsymbol{R}_0(0) = -4 \sum_{p=1,3,\ldots} x_p(t)$. Thus, the time correlation of the end-to-end vector is,

$$\langle \boldsymbol{R}(t) \cdot \boldsymbol{R}(0) \rangle = 16 \sum_{p=1,3,\ldots} \langle x_p(t) - x_p(0) \rangle = 16 \sum_{p=1,3,\ldots} \frac{3\mathrm{k_B} T}{k_p} e^{-t/\tau_p} = Nb^2 \sum_{p=1,3,\ldots} \frac{8}{p^2 \pi^2} e^{-tp^2/\tau_1} \tag{C.17}$$

Therefore, the first mode $p = 1$ mainly determines the dynamics of the end-to-end vector. Other modes correspond to the dynamics of a portion of the polymer with N/p segments within a length scale of $(Nb^2/p)^{1/2}$ [42]. Furthermore, rotational relaxation time τ_r of the polymer is defined as the longest relaxation time of the time correlation of the end-to-end vector, which equals to the relaxation time of the first mode τ_1. Thus, the rotational relaxation time of the polymer is given by $\tau_r = \gamma N^2 b^2/(3\pi^2 \mathrm{k_B} T)$.

We obtained $D \approx N^{-1}$ and $\tau_r \approx N^2$ within the approximations of the Rouse chain, wherein the description of the polymer immersed in a fluid pertains to a flexible polymer with bonds performing independent Brownian motion. However, experimental results for dilute suspensions suggest different relations with $D \approx N^{-1/2}$ and $\tau_r \approx N^{3/2}$, where N simply refers to the molecular weight of the polymer. The correct analytical relations are only obtained by considering hydrodynamic interactions. *Zimm model*, which extends Rouse model by taking hydroydynamics into account, yields the correct proportionality between the diffusion coefficient, relaxation time and the molecular weight of the polymer [42].

C.4. Kratky-Porod Worm-Like Chain

Flexiblity implies slightly different concepts depending on the type of the polymer. Flexiblity in flexible polymers refers to bonds that perform unhampered rotations. However, in semiflexible and stiff polymers, flexibility arises due to the fluctuations along the contour length.

The worm-like chain, introduced first by Kratky and Porod, is a continuous description of semiflexible polymers. It resembles the continuum version of the earlier introduced freely rotating chain for small bond angles. Therefore, just like the case for freely rotating chain, its end-to-end vector distance is an oscillatory decay with summations turned into integrals due to the continuous description,

$$\langle R^2 \rangle = \int_0^L \mathrm{d}s' \int_0^L \mathrm{d}s e^{(s-s')/\xi_p} \tag{C.18}$$

where ξ_p is the persistence length, s is the arc length along the contour of the polymer and L refers to the length of the polymer. The result of the integral yields,

$$\langle R^2 \rangle = 2L\xi_p - 2\xi_p^2(1 - e^{-L/\xi_p}) \tag{C.19}$$

The persistence length ξ_p is the length scale over which the bonds are correlated. Therefore, it describes an effective stiffness for the polymer. In the rigid rod limit with $L \ll \xi_p$, $\langle R^2 \rangle = L^2$, as the exponential term is important in this regime. Whereas in the flexible limit with $L \gg \xi_p$, $\langle R^2 \rangle = 2L\xi_p$, as the exponential term can be neglected.

For a stiff chain with constant contour length, the orientation of the unit tangent vector (defined as $\hat{u} = \partial \boldsymbol{r}(s)/\partial s$ where $\boldsymbol{r}(s)$ is the position vector at arc length s) varies slowly along the contour of the polymer. In general, for polymers with changing stiffness, the bending energy of the polymer is proportional with the change in orientation of the unit tangent vector with respect to the arc length variable, *i.e.* $\partial\hat{u}(s)/\partial s$, in other words,

$$H_b = \frac{\kappa_B}{2}\int_0^L \mathrm{d}s\left(\frac{\partial^2 \boldsymbol{r}(s)}{\partial s^2}\right)^2 \tag{C.20}$$

where κ_B is the bending rigidity, that is equal to $\kappa_B = \mathrm{k_B}T\xi_p$ (see the discussion on *Helfrich Hamiltonian* for an extended discussion on how to obtain bending energy).

Therefore, correlation of the unit tangent vector along the contour of the polymer provides a more formal way of distinguishing stiff polymers from flexible polymers. These correlations span longer and longer distances in the high stiffness limit.

C.5. Circular Chain

We captured mesoscopic dynamics of a linear polymer with Rouse model. We can apply the same approach to polymers with topological constraints by changing the boundary conditions. For example, the polymer can be made circular with the constraint of joining the first bond with the last bond. To accommodate the constraint, we change the boundary conditions in eq. C.5 to $r_0 = r_n$ and $\frac{\partial r_n}{\partial n}\big|_{n=0} = \frac{\partial r_n}{\partial n}\big|_{n=N}$. For this boundary condition to apply, we only need to change the frequency of the transform functiom x_p. Doubling the argument of cosine will make the values equal at the first and last points. So the new transform function is written as,

$$x_p(t) = \frac{1}{N}\int_0^N \mathrm{d}n \cos\left(\frac{2\pi n}{N}\right) r_n(t) \tag{C.21}$$

Applying the same procudere of Rouse model for linear polymers with the new transform function, the only difference will be in mode-dependent trap constant, which turns into $k_p = 24\pi^2\mathrm{k_B}Tp^2/(Nb^2)$ for $p = 0,1,2,\ldots$. It has a higher value for circular chain due to the doubling of cosine frequency. This changes the relaxation time of the polymer to

$$\tau_r = \frac{\gamma_1}{k_1} = \frac{\gamma N^2 b^2}{12\pi^2 \mathrm{k_B}T} \tag{C.22}$$

Therefore, the relaxation time is smaller in circular chains in comparison with the linear chain.

Circular chain with an energetic cost for bending as in eq. C.20 is an analog of 2D vesicles. It is thus interesting to calculate its fluctuation spectrum. By Wiener-Khinchine theorem, fluctuation spectrum corresponds with the autocorrelation in Fourier space. If mean square deviations in real space is denoted by $\langle h^2(x)\rangle$, then the fluctuation spectrum is given by $\langle h^2(k)\rangle$. We can calculate this by plugging $h(k) = \frac{1}{2\pi}\int \mathrm{d}x h(x)\exp(-ikx)$ to the bending energy, which results in,

$$\begin{aligned} H &= \frac{\kappa_B}{2}\int \mathrm{dx}\biggl(\int \mathrm{dk}(ik)^2 h(k)\mathrm{e}^{ikx}\biggr)\biggl(\int \mathrm{dk}'(ik')^2 h(k')\mathrm{e}^{ik'x}\biggr) \\ &= \frac{\kappa_B}{2}\int \mathrm{dk}\int \mathrm{dk}' k^2 k'^2 \delta(k-k')h(k)h(k') \\ &= \frac{\kappa_B}{2}\int \mathrm{dk} k^4 h^2(k) \end{aligned} \tag{C.23}$$

where we have used the Fourier representation of the delta function to eliminate the integrand with dx. We can invoke the equipartition theorem to find the Fourier transform of the mean square deviation as,

$$\langle h^2(k)\rangle = \frac{\mathrm{k_B}T}{\kappa_B k^4} \tag{C.24}$$

Therefore, spatial fluctuations at temperature T scale with k^4.

C.6. Helfrich Hamiltonian

Helfrich Hamiltonian describes the energy of nearly flat membranes. A membrane is essentially a 2D surface in 3D space, and as such, its description involves differential geometry. So we will start by a brief introduction of certain concepts in differential geometry that will be helpful in derivation of Helfrich Hamiltonian.

We start by parametrizing a curve in 3D by arc length,

$$s(t) = \int_{t_0}^{t_1} \mathrm{dt}' \frac{dr(t')}{dt} \tag{C.25}$$

The co-moving frame (or *Frenet frame*) of a curve can be described by three mutually orthogonal unit vectors:

$$\begin{aligned} \hat{t}(s) &= \frac{dr/dt}{|dr/dt|} = \frac{\frac{dr}{ds}\frac{ds}{dt}}{\frac{ds}{dt}} = \frac{dr}{ds} \\ \hat{n}(s) &= \frac{d\hat{t}}{ds}\left|\frac{d\hat{t}}{ds}\right|^{-1} = \frac{1}{\kappa}\frac{d\hat{t}}{ds} \\ \hat{b}(s) &= \hat{t}(s)\times\hat{n}(s) \end{aligned} \tag{C.26}$$

where the $\hat{t}(s)$ is the tangent vector, $\hat{n}(s)$ is the normal vector and $\hat{b}(s)$ is the binormal vector. We can see the emergence of the concept of *curvature* (denoted by κ) in the definition of the normal vector. It is defined as $\kappa = |d\hat{t}/ds|$. It is the magnitude of the rate of change of tangent vector along the arc length.

The curve can be geometrically characterized by the derivatives of these unit vectors,

$$\begin{aligned} \frac{d\hat{t}}{ds} &= \kappa\hat{n} \\ \frac{d\hat{n}}{ds} &= -\kappa\hat{t} + \tau\hat{b} \\ \frac{d\hat{b}}{ds} &= -\tau\hat{n} \end{aligned} \tag{C.27}$$

where a second definition is made by $\tau = -d\hat{b}/ds \cdot \hat{n} = d\hat{n}/ds \cdot \hat{b}$ where τ denotes *torsion* [39]. Mathematically it is the projection of the rate of change of the normal vector in the binormal direction. Intuitively it shows the propensity of the out of plane twist of the curve.

With these concepts in mind, we can turn from curves to surfaces. A surface in 3D can be parametrized with x and y. The tangent vectors $\partial_x \boldsymbol{f}$ and $\partial_y \boldsymbol{f}$ form the 2D tangent plane while the normal vector is simply defined as, $\hat{n} = \partial_x \boldsymbol{f} \times \partial_y \boldsymbol{f} / |\partial_x \boldsymbol{f} \times \partial_y \boldsymbol{f}|$, where the underscores indicate derivates with respect to the subscripted variable.

Curvature varies along the surface. The minimum (κ_1) and maximum (κ_2) curvatures are called *principal curvatures.* From these two, the followings definitions are made:

$$\begin{aligned} H &= \frac{\kappa_1 + \kappa_2}{2} = \frac{1}{2}\Big(\frac{1}{R_1} + \frac{1}{R_2}\Big) \\ K &= \kappa_1 \kappa_2 = \frac{1}{R_1 R_2} \end{aligned} \tag{C.28}$$

where H is the mean curvature and K is the Gaussian curvature. Gaussian curvature characterizes a point. If $K(x, y) > 0$, then the point is elliptic or sphere-like, if $K(x, y) < 0$, the point is hyperbolic or saddle-like, or if $K(x, y) = 0$, the point is parabolic or cylinder-like [41].

There are two important theorems associated with Gauss on Gaussian curvature [41]:

- **Theorema egregium** (or *the remarkable theorem*) states that Gaussian curvature K depends only on the inner geometry of the surface. Thus the normal vector $\hat{n}$ is not required to calculate it.
- **Gauss-Bonnet theorem** states that Gaussian curvature integrated over a closed surface is a topolotical constant, that is,

$$\oint \mathrm{dA}K = 2\pi\chi \tag{C.29}$$

where χ is called *Euler characteristic*, which is used to calculate the number of handles of a surface [1].

Metrics of differential geometry help in description of dA and K to describe integrals of the form $\int \mathrm{dA}K$ that appear in Gauss-Bonnet theorem. There are three metrics [41]:

- *Metric tensor* or *the first fundamental form* is defined as,

$$g_{ij} = \partial_i \boldsymbol{f} \cdot \partial_j \boldsymbol{f} \tag{C.30}$$

which only depends on the tangent plane. Therefore, it is useful in description of a surface:

$$A_S = \int \mathrm{dxdy} |\partial_x \boldsymbol{f} \times \partial_y \boldsymbol{f}| = \int \mathrm{dxdy} \sqrt{\det g} \tag{C.31}$$

- *The second fundamental form* is defined with $h_{ij} = \hat{n} \cdot \partial_{ij} \boldsymbol{f}$, which depends on the normal vector.
- Finally, *Weingarten matrix* is defined as $a = h \cdot g^{-1}$.

---

[1] It is calculated by the *Euler theorem* via the relation $\chi = F - E + V$ where F denotes the number of faces, E denotes the number of edges and V denote the number of vertices.

The principal curvatures for a surface is then defined in terms of the metrics as:

$$\begin{aligned} K &= \det(a) = \frac{\det(h)}{g} \\ H &= \frac{1}{2}\operatorname{Tr}(a) \end{aligned} \tag{C.32}$$

For a plane with parametrization $(x, y, 0)$,

$$g = \begin{pmatrix} 1 & 0 \\ 0 & 1 \end{pmatrix} \tag{C.33}$$

and

$$h = \begin{pmatrix} 0 & 0 \\ 0 & 0 \end{pmatrix} \tag{C.34}$$

Therefore, the area element is described by $dA = \sqrt{\det(g)}\mathrm{dxdy} = \mathrm{dxdy}$ and principal curvatures are zero.

To describe that of membranes, we first need to perform parametrization. One method is the so-called *Monge parameterization* where the membrane is described by a height function $h(x, y)$ in the z direction. This parametrization is valid for surfaces without overhangs. We will assume that the membrane is nearly flat, that is, $\nabla h(x, y) \ll 1$, then parametrization simply becomes $(x, y, h(x, y))$. The metric tensor is:

$$g = \begin{pmatrix} 1 + (\partial_x h)^2 & \partial_y h \cdot \partial_x h \\ \partial_x h \cdot \partial_y h & 1 + (\partial_y h)^2 \end{pmatrix} \tag{C.35}$$

The determinant becomes nicely $\det(g) = 1 + (\nabla h)^2$. Therefore, the area metric for the membrane is given by $dA = \sqrt{1 + (\nabla h)^2}\mathrm{dxdy} \approx (1 + (\nabla h)^2)\mathrm{dxdy}/2$.

The second fundamental form can be calculated as,

$$h = \frac{1}{\det(g)} \begin{pmatrix} \partial_{xx} h & \partial_{yx} h \\ \partial_{xy} h & \partial_{yy} h \approx a \end{pmatrix} \tag{C.36}$$

From these metrics, the principal curvatures can be calculated as [176],

$$\begin{aligned} H &\approx \frac{1}{2}\left(\frac{\partial^2 h}{\partial x^2} + \frac{\partial^2 h}{\partial y^2}\right) \\ K &\approx \frac{\partial^2 h}{\partial x^2} \cdot \frac{\partial^2 h}{\partial y^2} - \frac{\partial^2 h}{\partial x \partial y} \end{aligned} \tag{C.37}$$

Bending energy of a membrane is a function of the principal curvatures $H_b = \int \mathrm{dA} f(H, K)$. We can Taylor expand this expression in the limit of small curvatures,

$$H = \int \mathrm{dA}\left(\sigma + \kappa' K + 2\kappa(H - c_0)^2 + O(1/R^3)\right) \tag{C.38}$$

where we note that K or the Gaussian curvature goes as $1/R^2$ while H or the mean curvature goes with $1/R$ [176].

This equation is called as *Helfrich* or *Helfrich-Canham Hamiltonian.* Each term in the Hamiltonian corresponds to a different energetic contribution.

- σ in the first term is the surface tension. It can be thought of as a sort of chemical potential for the area. It is important in the description of liquid droplets and soap bubbles.
- κ' in the second term is the saddle-splay modulus and is related to the topology. It describes the tendency of the membrane to merge or split. It vanishes for closed surfaces [176].
- κ in the third term is the bending rigidity and c_0 is the spontaneous curvature describing any sort of asymmetry.

D. Additional Remarks on Turbulence

D.1. Onsager Phenomenology of Vortex Formation

Vorticity is a constant of motion in 2D. Therefore, Euler equation can be written in Hamiltonian form. Lars Onsager used this idea to explain vortex formation in turbulence in terms of equilibrium statistical mechanics [145]. He started with a representation of the fluid by a collection of point vortices,

$$w(\mathbf{r}) = \sum_i c_i \delta(\mathbf{r} - \mathbf{r}_i(t)) \tag{D.1}$$

that interact with each other via the Hamiltonian,

$$H = \sum_{i<j} c_i c_j V(\mathbf{r}_i, \mathbf{r}_j) \tag{D.2}$$

where $V(\mathbf{r}_i, \mathbf{r}_j) = -\ln(|\mathbf{r} - \mathbf{r}'|/2\pi)$ and the sum is over all vortex pairs i and j. He used this Hamiltonian to define a microcanonical ensemble of point vortices with an effective temperature given by,

$$\frac{1}{\theta} = \mathrm{k_B} \frac{\mathrm{d}\ln(\phi(E))}{\mathrm{d}E} = \frac{\mathrm{d}S}{\mathrm{d}E} \tag{D.3}$$

where $\phi(E)$ defines the multiplicity, θ and S are terms that describe the effective temperature and entropy, respectively. [1] For this system, Onsager pointed out to the possibility of negative effective temperature states [145]. When $1/\theta < 0$, entropy would be a decreasing function of the energy and high energy states would be favoured over the low energy states, which in turn favours the clustering of vortices of the same sign. Thus, Onsager predicted the spontaneous formation of large-scale, long-lived vortices in 2D inviscid fluids. His explanation provides an interpretation of coherent vortex formation in terms of an attractive interaction between the same-signed vortices with equilibrium statistical mechanics tools. Within this framework, no external forcing is required to sustain the vortex formation as long as viscosity is weak. However, the applicability of equilibrium statistical mechanics to an inherently dissipative pheonomenon like turbulence remains limited and in this regard, the theory of Onsager by construction applies only to two dimensional conservative systems.

D.2. Fjortoft's Theorem

We try to identify the origin of energy and enstrophy cascades in turbulent flow. We note that the advection term does not appear in the energy conservation equation at all. Instead its role is to redistribute the energy across different length scales. To see this, we introduce the concept of a length scale which is arguably most naturally done in Fourier space via filtering. Assuming a periodic box, we can decompose the velocity, pressure and force into a small wavenumber and a large wavenumber component with a cutoff wavenumber at **K** [60]. In Fourier space, velocity decomposes into:

---

[1] Note that the equations are very similar to those describing topological defects.

$$\mathbf{v}(\mathbf{r}) = \sum_{\mathbf{k}} \mathrm{v}_k \mathrm{e}^{\mathbf{ik}\cdot\mathbf{r}} = \mathbf{v}^S_{\mathbf{K}}(\mathbf{r}) + \mathbf{v}^L_{\mathbf{K}}(\mathbf{r}) \tag{D.4}$$

where $\mathbf{v}^S_{\mathbf{K}}(\mathbf{r}) = \sum_{\mathbf{k}\le\mathbf{K}} \mathrm{v}_k \mathrm{e}^{\mathbf{ik}\cdot\mathbf{r}}$ is the small wavenumber component representing the Fourier transform of the velocity with a sum truncated at the cutoff wavenumber **K** and $\mathbf{v}^L_{\mathbf{K}}(\mathbf{r}) = \sum_{\mathbf{k}>\mathbf{K}} \mathrm{v}_k \mathrm{e}^{\mathbf{ik}\cdot\mathbf{r}}$ is the large wavenumber component representing the same Fourier transform summed over wavenumbers larger than the cutoff wavenumber **K**. $\mathbf{v}^S_{\mathbf{K}}(\mathbf{r})$ acts like a low-pass filter for velocity. It sets all Fourier components of velocity smaller than **K** zero. Thus, it only contains information about large length scales. While $\mathbf{v}^L_{\mathbf{K}}(\mathbf{r})$ acts like a high-pass filter and it only contains small length scales. Now we apply the filtering operator to the Navier-Stokes equation,

$$\partial_t \mathbf{v}^S_{\mathbf{K}} + (\mathbf{v}^S_{\mathbf{K}} + \mathbf{v}^L_{\mathbf{K}}) \cdot \nabla(\mathbf{v}^S_{\mathbf{K}} + \mathbf{v}^L_{\mathbf{K}}) = -\nabla p^S_{\mathbf{K}} + \nu \nabla^2 \mathbf{v}^S_{\mathbf{K}} + \mathbf{f}^S_{\mathbf{K}} \tag{D.5}$$

High-pass filtered velocity is not written explicitly, as it is ortohogonal with low-pass filtered velocity and we next multiply by low-pass filtered velocity and take the spatial average as before,

$$\begin{aligned} \left\langle \partial_t \frac{|\mathbf{v}^S_{\mathbf{K}}|^2}{2} \right\rangle + \left\langle \mathbf{v}^S_{\mathbf{K}} \cdot (\mathbf{v}^S_{\mathbf{K}} + \mathbf{v}^L_{\mathbf{K}}) \cdot \nabla(\mathbf{v}^S_{\mathbf{K}} + \mathbf{v}^L_{\mathbf{K}}) \right\rangle = \\ - \left\langle \mathbf{v}^S_{\mathbf{K}} \cdot \nabla p^S_{\mathbf{K}} \right\rangle + \nu \left\langle \mathbf{v}^S_{\mathbf{K}} \cdot \nabla^2 \mathbf{v}^S_{\mathbf{K}} \right\rangle + \left\langle \mathbf{v}^S_{\mathbf{K}} \cdot \mathbf{f}^S_{\mathbf{K}} \right\rangle \end{aligned} \tag{D.6}$$

The first two terms on the right-hand side can be transformed by using the same identities as before. The first term vanishes due to incompressibility. The second term is equal to $\nu\langle |w^S_{\mathbf{K}}|^2 \rangle$. The nonlinear advection term does not vanish this time, because we are now considering interactions between distinct length scales. After expanding the advection term, the equation can be rearranged to a succinct form,

$$\partial_t \epsilon_K + \pi_K = -2\nu \varOmega_K + F_K \tag{D.7}$$

where $\epsilon_K = \sum_{k\le K} |v_k|^2/2$ is the cumulative energy, $\varOmega_K = \langle |w_k|^2/2 \rangle = \sum_{k\le K} k^2 |v_K|^2/2$ is the cumulative enstrophy, $F_K = \sum_{k\le K} f_k \cdot v_k$ is the cumulative energy injection by forcing, and π_K is the energy flux [60]. Therefore, in light of eq. D.7, the time rate of change of energy at length scales down to $1/K$ is determined by the energy injected to the given scale by the forcing (F_K) minus the energy dissipated at the given scale minus the flux of energy to smaller length scales due to nonlinear interactions.

The length scale L where energy injection is operating is set by the cumulative energy (ϵ_K), which in turn depends on the velocity (v_K), and the energy flux (π_K). The length scale l where energy dissipation plays an important role is determined with the cumulative enstrophy, which depends on ν, and the energy flux (π_K). Therefore, the ratio between the energy injection and the energy dissipation length scales L/l is proportional to v/ν, which is in turn proportional with Re. When $Re \gg 1$, $L/l \gg 1$ consequently. This is to say, in the limit of high Re, the energy injection is confined to large length scales, while the energy dissipation is confined to small length scales. The separation of length scales is central to the theory of turbulence as will be seen. To exemplify, the critical Reynolds number $Re = vD/\nu$ for the onset of turbulence (and separation of length scales) inside a circular pipe with circular Poiseuille flow is $Re \approx 2000$, where v is the average velocity of the flow, D is the tube diameter and ν is the molecular viscosity [157]. First we will illustrate how the nonlinearities in the advection term lead to the idea of energy cascade among length scales.

We consider the 2D Euler equation in Fourier space truncated such that there are only three modes k_1, k_2, and k_3. We assume for simplicity that $k_2 = 2k_1$ and $k_3 = 3k_1$, so that the modes are ordered as $k_1 < k_2 < k_3$, and the length scales as $\lambda_3 < \lambda_2 < \lambda_1$. The change in energy is given by $\delta E_i = E(k_i, t_2) - E(k_i, t_1)$. We consider a high Re regime wherein the energy injection and dissipation length scales are separated. Assuming that we are at an intermediate length scale away from the disturbance of forcing and dissipation, we can invoke energy and enstrophy conservation to get,

$$\begin{aligned} \delta E_1 + \delta E_2 + \delta E_3 &= 0 \\ k_1^2 \delta E_1 + k_2^2 \delta E_2 + k_3^2 \delta E_3 &= 0 \end{aligned} \tag{D.8}$$

which gives,

$$\begin{aligned} \delta E_1 &= -5\delta E_2/8 \\ \delta E_3 &= -3\delta E_2/8 \end{aligned} \tag{D.9}$$

and,

$$\begin{aligned} k_1^2 \delta E_1 &= -5k_2^2 \delta E_2/32 \\ k_3^2 \delta E_3 &= -27k_3^2 \delta E_2/32 \end{aligned} \tag{D.10}$$

This relation between the three modes (triads), known as *Fjortoft's theorem*, is a key result of 2D turbulence [9]. If the intermediate mode k_2 loses kinetic energy ($\delta E_2 < 0$), then more energy will go to k_1 than to k_3, and more enstrophy will go towards k_3 than to k_1. Now instead of three modes, we envisage a continuous range of wavenumbers, and an initial kinetic energy peaked around k_f. Due to the nonlinear interactions, the peak will spread out towards other modes, and consequently the amount of kinetic energy in the vicinity of k_f will decrease. More kinetic energy and less enstrophy will go towards $k < k_f$ (larger length scales) than towards $k > k_f$ (smaller length scales). The key assumption that led to this double cascade picture in opposite directions is the conservation of energy and enstrophy for 2D systems at high Re numbers.

D.3. Active Turbulence

Turbulence relies on the separation of energy injection and dissipation length scales and the redistribution of energy among different length scales via nonlinear advection, both of which are inherently inertial properties occuring at high Re. However, certain features of turbulent flows have been observed at low Re. As some of the key results of this thesis pertain to turbulence at low Re, we give here a detailed literature review highlighting key results.

A dilute solution of high molecular weight polyacrylamide in a viscous sugar syrup shows swirling flow inside a small tank [74]. The swirling flow is accompanied with more than a decade of power-law decay in the Fourier spectra of brightness profile along the diameter as well as the circumference of the tank. There is also a decade of power-law decay in the time spectra of velocity fluctuations, indicating that the fluid motion is excited at the length and time scales corresponding to power-law decay in the respective spectra. Despite the high viscosity, low velocity and the small tank (all features corresponding to low Re numbers), a wide range of length and time scales are excited and flow resistance is found to be increasing, similar to inertial turbulence. At low Re numbers, the nonlinear advection term in the Navier-Stokes equation that redistributes energy among different spatial scales drops out, leaving a linear equation. However, as polymers can stretch, stress does not drop to zero instantenously, but rather decays exponentially with a characteristic time λ that can have a value from seconds to minutes. This can be added to the Navier-Stokes equation for dilute polymer solutions as another linear term that describes elastic stress in a viscoelastic fluid. The stretching of polymers depends on the deformation of flow and is path dependent. Thus, the coupling between the elastic stress τ and the deformation rate of the flow is nonlinear. The degree of nonlinearity is given by the so-called Weissenberg number, $Wi = v\lambda/L$, multiplication of deformation rate and the relaxation time λ. It characterizes the ratio of elastic forces over the viscous forces. In viscoelastic flows, Wi is large and Re is small, with the ratio $Wi/Re = \lambda\nu/L^2$, rendering the equation of motion linear. However, mechanical properties of the flow is nonlinear, which gives rise to turbulent-like flow. Viscoelastic turbulence develops with the stretching of polymers in the primary shear flow, which makes the shear flow unstable and causes a secondary flow that is irregular. Thus, it is the nonlinearity in the back reaction of polymers to the primary shear flow that causes an irregular turbulent-like secondary flow.

Adding polymers to a Newtonian fluid reduces drag at high Re as polymers can stretch, which destroys turbulent behaviour [170]. However, adding polymers at low Re numbers leads to turbulent-like chaotic motion, as the dynamics of the flow is controlled by elastic stresses in that regime. This behaviour renders the viscoelastic turbulence solely a low Re number phenomenon, in stark contrast with inertial turbulence.

Viscoelastic turbulence can be treated semianalytically by supplementing the momentum conservation equation of generalized nonlinear Maxwell model of viscoelasticity with a non-linear stress term. For a lid-driven cavity flow, *i.e.* flow inside impermeable solid walls with a moving top lid, such models are found to exhibit both smooth laminar and turbulent regimes depending on the model parameters [72].

Experiments on high density suspensions of bacteria revealed that low Re number turbulence is not solely a viscoelastic phenomena. Dombrowski, *et. al.*, observed large-scale coherent motion for a microbial suspension with patterns of jet-like motion straddled with vortices [43].

Bacteria accummulate in a tightly packed cluster due to chemotactic interactions and the bacterial cluster exhibits jets and vortices.

One of the most consequential vortical motion at low Re numbers is the self-organization of sea urchin spermatozoa into a dynamic vortex array with local hexagonal order at planar surfaces above a critical density [165]. Spermatozoa gets trapped at planar surfaces and follows a circular trajectory with a preferred handedness. Hydrodynamic interactions lead to coupling of circularly swimming trapped spermatozoa which leads to vortex arrays. A typical vortex contains around 10 spermotozoa circulating clockwise with the center of mass of the vortex performing diffusive motion. The diffusion coefficient of the vortex is found to be larger than the thermal diffusion [165].

Petroff, *et. al.* observed the formation of a $2D$ hexagonal lattice of rotating fast-moving bacteria [155]. They used a species known as *Thiovolum majus* which is an order-of-magnitude faster than typical bacteria with speeds of up to $600 \mu m s^{-1}$ (It is a sulfur-oxidizing bacteria living in the diffusive boundary layer at the bottom of salt marshes. Thus, *T. majus* has to access the energy faster than the diffusive flux of sulfide from the mud and oxygen from the overlaying water. To be able to do that, it attaches to the surface and rotates a lot of flagella to generate fluid flow that transports oxygen and sulfide towards the cell.). It is also unusually large with a diameter of $8.5 \mu m$. It does not move with the typical run-and-tumble motion but rather performs smoother turns. As each bacteria rotates its flagella, it generates a tornado-like flow that pulls neighbouring cells around it. As cells rotate against their neighbours, they exert forces on each other, which rotates the crystal and reorganizes the bacteria. As a result, bacteria assemble into rotating crystals of ~ $10-1000$ cells. Crystals continually form, reorganize and move for $2h$ when the chamber eventually becomes anoxic and bacteria start to die.

In endothelial cell monolayers, cell divisions lead to the formation of long-range, well-ordered vortex patterns [167]. Endothelial cells are in the blood vessels, and as such, they are sensitive to fluid motion. They divide more often when there is no stress from the fluid, and adhere tightly to their neighbours to prevent leakage. High density and high intercell adhesion leads to a collective behaviour. A cell division event can be considered as a local injection of energy, which stirs the fluid over distances up to $140 \mu m$ (with a typical cell size of $40 \mu m$ and a total system size of $300 \mu m$) [167]. Long-range stirring of the fluid combined with correlated motion leads to the formation of long-range vortices 30 minutes after cell division, with a typical lifetime of ~ $4-5h$.

In a further experiment, vorticity in a cancerous tissue is found to be a good indicator of the invasive potential of the cancerous tissue [207]. Invasion here refers to a cancerous cell that does not respect the basal membrane or the tissue border and invades into the healhty tissue. The experiment, conducted on human breast epithelial cells, showed that invasive cells are faster than the non-invading cells, and the divergence of the velocity field and vorticity around a dividing cells correlates well with the invasiveness of the cell [207]. Two daughter cells move in opposite directions upon cell division, generating a pair of vortices that are visible for 4 minutes after division. Such vortices are small, unlike the ones observed in healthy endothelial cells, on the order of 1 cell diameter [207].

By using swarming bacteria *Vibrio alginolyticus* in an ensemble of ultra-long and short cells, Lin, *et. al.* showed that long cells sponatenously formed into stable spiral coils due to the frequent reorientations caused by collisions of long cells with the short cells.

Flow patterns dominated with vortices, jets and swirls in dense active matter is analysed within the frameworks of low Re numbers turbulence in comparison with inertial turbulence. The earliest work hinting at a turbulent regime for active matter found a regime of spatiotemporal chaos and relaxation oscillations for mutually propelled filaments suspended in a fluid inside a channel [69]. Their semianalytical modelling of mutually propelling filaments that leads to spatiotemporal chaos is particularly illuminating for the ensuing discussion. The model takes three fields into account in the filament concentration, hydrodynamic flow and the directional ordering of filaments. Onsager's consideration of a $2D$ ensemble of slender rods with head-tail symmetry revealed a directional ordering transition above a critical density of $c^O = 3\pi/2l^2$ where l is the length of the rods. The directional, or nematic order for apolar rods can be characterized with an order parameter Q_{ij} that is 1 when the rods i and j are ordered and 0 otherwise, $Q_{ij} = S(n_i n_j - \delta_{ij}/d)$ where $S = \langle (d|\hat{a}\cdot\hat{n}|^2 - 1)/(d-1)\rangle$ is the scalar nematic order parameter with $\hat{a}$ denoting the axis of the rod. Equivalently, the scalar nematic order parameters is given by $S = \sqrt{\mathrm{tr}(2Q^2)}$. It is proportional with the larger eigenvalue of Q and represents the average direction $\hat{n}$ over which the rods are oriented along.

The filament concentration field is governed by

$$\frac{\partial c}{\partial t} = -\nabla \cdot \big(c(\mathbf{v} + \mathbf{v}^a) - D\nabla c\big) \tag{D.11}$$

where $\mathbf{v}$ and $\mathbf{v}^a$ denote the fluid flow and active flow, respectively and $D_{ij} = D_0\delta_{ij} + D_1 Q_{ij}$ is the diffusion matrix with $D_0 = (D_{\|} + D_{\perp})/2$ and $D_1 = D_{\|} - D_{\perp}$. For polar filaments, the active flow would simply be $\mathbf{v}^a = v_0\hat{P}$ where $\hat{P}$ represents the polar direction of the filament. However, for mutually propelling filaments, it is a function of links between filaments. The number of such links increases linearly with increasing filament concentration, giving a speed of $v_0 = \alpha_1 c$. Therefore, active current is given by $\mathbf{j}^a = c\mathbf{v}^a = \alpha_1 c^2 \mathbf{v}^a$. For apolar rods with nematic symmetry, activity may lead to them $\hat{n}$ or $-\hat{n}$ equally likely. As a result, a uniform nematic director field $\hat{n}$ would not generate a flow. In the presence of a non-uniformity in the director field or nematic order parameter field, however, there woud be regions of filaments moving faster than the others leading to a flow. Thus, the active flow must also depend on the gradients of the nematic order parameter field Q_{ij}, which in the end yields the following active current: $\mathbf{j}^a = -\alpha_1 c^2 \partial_j Q_{ij}$. The minus sign accounts for the fact that the flux is from fast moving filaments to slower moving filaments. α_1 is a constant with units of inverse time. c^2 dependence arises from the mutual pair nature of the activity.

After establishing the concentration field, hydrodynamic equations for the nematic order parameter field Q_{ij} is constructed next:

$$\Big(\frac{\partial}{\partial t} + \mathbf{v}\cdot\nabla\Big)Q_{ij} = \Omega_{ij}^{(r)} + \Omega_{ij}^{(v)} + \Omega_{ij}^{(a)} \tag{D.12}$$

where Ω_{ij}, on the right-hand side, depict the relaxational dynamics of the nematic field, coupling of the nematic field to the flow, and the active contribution to the nematic field, respectively. The right-hand side is constructed by combining all possible symmetric-traceless tensors of the relevant fields (representing the degrees of freedom of the model). Such tensors are the strain-rate tensor $u_{ij} = (\partial_i v_j + \partial_j v_i)/2$, the vorticity tensor $w_{ij} = (\partial_j v_i - \partial_i v_j)/2$, and the molecular-field tensor $H_{ij} = -\delta F/\delta Q_{ij}$. F represents the Frank free energy,

$$F = \int \mathrm{dA}\bigg(\frac{1}{2}AQ_{ij}Q_{ij} + \frac{1}{4}C(Q_{ij}Q_{ij})^2 + \frac{1}{2}K(\partial_i Q_{jk}\partial_i Q_{jk})\bigg) \tag{D.13}$$

The parameters A and C parametrize the location of a second order phase transition and K is the Frank elastic energy under one-constant approximation (which assumes equal bend and splay moduli). Note that the above expression is equivalent to $A\mathrm{tr}(Q)^2/2 + C\mathrm{tr}(Q^2)^2/4 + K|\nabla Q|^2/2$ by definition. As $\mathrm{tr}(Q^2) = S^2/2$, at equilibrium (where the bending term -gradients of the nematic tensor- vanishes) we have $S = \sqrt{-2A/C}$. To set the phase transition in line with the Onsager isotropic-nematic transition, for which $S \sim 1$ at $c \gg c^O$ and $S \sim 0$ at $c \ll c^O$, one can choose the parameters as $A/K = (c^O - c)/2$ and $C/K = c$, such that $S = \sqrt{1 - c^O/c}$.

The relaxational dynamics of the nematic order field is governed by the molecular-field tensor H_{ij}:

$$\Omega_{ij}^{(r)} = \gamma^{-1}H_{ij} = -\gamma^{-1}\bigg((A + S^2C/2)Q_{ij} - K\nabla^2 Q_{ij}\bigg) \tag{D.14}$$

where γ is the rotational friction parameter for nematic order field (we make the replacement $Q_{ij}Q_{ij} = \mathrm{tr}(Q^2) = S^2/2$ when taking the derivative of the free energy with respect to the nematic order tensor).

The coupling between the nematic order field and the flow is found by constructing all possible traceless and symmetric tensors from the products u_{ij}, w_{ij} and Q_{ij} (with the rationale that traceless-symmetric tensors related to the flow field represent the degrees of freedom in the flow):

$$\Omega_{ij}^{(v)} = \beta_1 u_{ij} + \beta_2(w_{ik}Q_{kj} - Q_{ik}w_{kj}) \tag{D.15}$$

where the coefficients β_1 and β_2 are found by a comparison with Ericksen-Leslie theory, which gives $\beta_1 = \lambda S$ and $\beta_2 = -1$ (Ericksen-Leslie theory describes the stress associated with distortions in the nematic order in a flow in terms of the director field, see [69] for a more detailed discussion). λ, which is multiplied with the strain tensor, can be thought as a flow-aligning parameter. For $|\lambda| > 1$, the director is aligned with the flow direction at an angle θ such that $cos2\theta = 1/\lambda$ (flow-aligning regime). For $|\lambda| < 1$, the director forms rolls (flow-tumbling regime).

The active contribution to the nematic field is directly proportional with the nematic tensor, $\Omega_{ij}^{(a)} = \alpha_0 Q_{ij}$. The corresponding reactive elastic stress of the flow, in response to activity, is given by:

$$\sigma_{ij}^{(e)} = -\lambda S H_{ij} + Q_{ik}H_{kj} - H_{ik}Q_{kj} \tag{D.16}$$

which is essentially the elastic stress due to the elasticity of the nematic order field.

The flow velocity is determined by Navier-Stokes equation with the stress tensor,

$$\sigma_{ij} = 2\nu u_{ij} - p\delta_{ij} + \sigma_{ij}^{(e)} + \alpha_2 c^2 Q_{ij} \tag{D.17}$$

where ν is viscosity, p is pressure, and the last term on the right-hand side determines the extensile or contractile stress exerted by the active motion.

When all of the equations for each field is combined, the resulting hydrodynamic equations for an incompressible nematic suspension with mutually propelling filaments at low Re numbers is given by:

$$\begin{aligned}
&\rho\partial_t v_i = \nu\partial_i^2 v_i - \partial_i p + \partial_i \tau_{ij} \\
&(\partial_t + v_i\partial_i)c = \partial_i\big((D_0\delta_{ij} + D_1 Q_{ij})\partial_j c + \alpha_1 c^2 \partial_j Q_{ij}\big) \\
&(\partial_t + v_i\partial_i)Q_{ij} = \lambda S u_{ij} + Q_{ik}w_{kj} - w_{ik}Q_{kj} + \gamma^{-1}H_{ij}
\end{aligned} \tag{D.18}$$

where $\tau_{ij} = \sigma_{ij}^{(e)} + \alpha_2 c^2 Q_{ij}$. The nonlinear advection term drops out in the equation for flow velocity due to the negligence of inertia at low Re numbers (Assuming a length of $l \sim 1\mu m$ for a filament, with a velocity of $v \sim 1\mu m s^{-1}$, $\rho \sim 10^3 kg m^{-3}$, and $\eta = 10^{-3} Pas$ for water at room temperature, we get $Re = 10^{-6}$.).

The dynamics of the system is determined by the time scale of active forcing and passive structures. Active forcing τ_a^{-1} is proportional with activity parameters α_1 and α_2. Energy can either be stored or dissipated via passive structres in the solvent or in the nematic order field. The relaxational time scale of the nematic degrees of freedom $l^2/\gamma^{-1}K$, the diffusive time scale l^2/D_0, and the dissipation time scale of the solvent $\rho L^2 \nu$ give relaxational time of the passive structures τ_p. When $\tau_a \gg \tau_p$, the system behaves like a passive equilibrium ensemble with active forcing being irrelevant. When the time scales are comparable, the active and passive forcing balance each other leading to a stationary flow where active forces are accommodated via elastic distortion. When $\tau_a \ll \tau_p$, the active forcing dominates over passive structures as passive structures respond too slowly to accommodate active forces. This leads to a chaotic regime.

Increasing activity disturbs the stationary flow of a nematic suspension in a $2D$ channel towards non-uniform flow. Here it is explicitly shown that increasing activity further could lead to another type of oscillatory and possibly chaotic flow [69].

A later work making use of the same model inside a periodic box considered a linear stability analysis of the ordered state [68]. Flow-aligning nematics (with $|\lambda| > 1$) is found to be unstable to splay deformations under the effect of an extensile active stress, and to bending deformations under the effect of a contractile active stress. Flow-tumbling nematics (with $|\lambda| < 1$) is unstable to bending deformations under the effect of an extensile active stress, and to splay deformations under the effect of a contractile active stress. These instabilities lead to formation of topological defects [68].

Around the same time as the development of the outlined model, Schaller, *et. al.* observed the formation of topological defects on a high-density motility assay of actin filaments propelled by heavy meromyosin motor proteins within a quasi-2D geometry [172]. They observed large-scale and long-lived density fluctuations that are coupled to the topology of the velocity field. A sink in the velocity field (*i.e.*, $\nabla \cdot \mathbf{v} > 0$) causes a rise in density until the local density becoming high enough such that more filaments cannot be put in the same density. The sink is destroyed at this point as filaments move towards lower densities, which causes a source (*i.e.*, $\nabla \cdot \mathbf{v} < 0$) to develop. The decreased density, however, allows for stronger velocity fluctuations untile the density starts to rise again. The increase in density is followed by the emergence of a sink and the same process starts over again. They observed that such process span an area of $200\mu m$ in diameter with a lifetime of $30s$ [172]. Topological defects are observed at regions of low filament density. At these regions, filaments are less ordered which allows for stronger direction fluctuations, which in turn makes the formation of defects more likely.

Wensink, *et. al.* placed the spatiotemporal chaos associated with the vortical flow of dense bacterial suspensions within the context of *meso-scale turbulence* [204]. In their pioneering work, they established the general properties of meso-scale, or active turbulence, by studying it in relation with inertial turbulence. At high density and intermediate aspect ratio ($3 < a < 13$), the velocity field of *Bacillus subtilis* suspension confined in quasi-2D or 3D microfluidic chambers exhibits distinct vortices. The typical vortex size becomes substantially larger in 3D in comparison to quasi-2D, which could be facilitated by hydrodynamic interactions. The probability distribution of velocities and velocity increments are Gaussian with slight heavy tails due to collective motion. Unlike inertial turbulence, velocity structure functions have only a small power law regime and then flatten at longer distances. The energy spectrum is found to have two power law regimes, with an initial slope of $5/3$ that is followed by a slope of $-8/3$, that is quite different from the $-5/3$ direct energy cascade of 3D inertial turbulence. They capture similar behaviour with deterministic self-propelled rod simulations in 2D, which indicates that hydrodynamic interactions are not necessarily required for mesoscale turbulence, and that a rod-like shape and volume exclusion interactions are sufficient to induce turbulent states in active matter. Unlike in inertial turbulence where energy is supplied at a large scale, energy injection occurs at the level of a bacteria. However, excluded-volume interactions lead to an effective orientational alignment between bacteria (on the order of 10 bacterial lengths), which acts like an effective forcing at a large scale. Such behaviour is also captured with a minimal semianalytical model that extends Toner-Tu theory of polar active matter with pattern forming Swift-Hohenberg terms. These terms are essentially higher-order spatial partial differential equations. In Fourier space, chosen correctly, they can lead to amplification of the spatial frequencies. Thus, the rationale of adding higher order spatial partial differential equations is to select patterns at certain length scales.

Oza, *et. al.* recently generalized Swift-Hohenberg extension of Toner-Tu theory for minimal modelling of active-turbulent pattern formation [148]. For simplicity, let's assume a scalar field $\phi(t, \mathbf{x})$ that is equally likely to be $\pm\phi$ and has a characteristic $\pm\phi_c$ value. As it is sign-indepedent, only the even terms are included in a Taylor expansion of the time evolution of the field, $\partial_t \phi = a\phi + b\phi^3 + ...$ with $\phi_c = \sqrt{-a/b}$ with $a > 0$ and $b < 0$ to ensure stability of the fixed points $\pm\phi_c$. With this consideration, a is a driving drift term while b is a dissipation term, and as such, the dissipation should be growing larger in ϕ than the drift to ensure asymptotic stability. In order to be able to select a pattern of a certain wavelength, we can make the growth of the field depend on the wavenumber $\mathbf{k}$. If we assume isotropy, the wavenumber dependence will turn into a dependence on $|\mathbf{k}|$, such that, we have $\partial_t \hat{\phi} = (\alpha|\mathbf{k}|^2 + \beta|\mathbf{k}|^4 + ...)\hat{\phi}$ where $\hat{\phi}$ is the spatial Fourier transform of ϕ. The fixed points of the Fourier-transformed equation is given by $k_c = \sqrt{-\alpha/2\beta}$ with $\alpha > 0$ and $\beta < 0$ to ensure $\hat{\phi} \to 0$ as $|\mathbf{k}| \to \infty$, in other words, small-wavelength stability. We can write these two equations together in real space,

$$\partial_t \phi = a\phi + b\phi^3 - \alpha\nabla^2\phi + \beta(\nabla^2)^2\phi \tag{D.19}$$

which is also incidentally the Swift-Hohenberg equation describing the spatiotemporal chaos of Rayleigh-Benard convection in a heated fluid inside two parallel plates. This simple scalar field model can be used to capture turbulent pattern formation in two types of dense active suspensions. For polar active systems like bacteria, it can be generalized within a vector field, while for apolar suspensions like ATP-driven kinesin-microtubule suspensions, it can be generalized with a matrix field of apolar orientational order.

For polar active systems, like the dense *B. subtilis* suspension described earlier in [204], assuming constant density (or equivalently incompressibility), the dynamics can be described by a single field in polarization field $\hat{p}$, where $\mathbf{u} = \lambda_0 \hat{p}$ where $\mathbf{u}$ is the velocity field of bacteria, λ_0 is the velocity magnitude, and $\hat{p}$ is the polar orientation of bacteria. Incompressibility implies $\nabla \cdot \mathbf{u} = \nabla \cdot \hat{p} = 0$. Note that due to the incompressibility condition, this polarization-field based theory does not describe swarming or flocking regimes where density fluctuations are present. We can then describe the dynamics in terms of fluid dynamics with these assumptions,

$$(\partial_t + \mathbf{u} \cdot \nabla)\hat{p} = \frac{-\delta G}{\delta \hat{p}} \tag{D.20}$$

where G is an effective free energy from which forces are derived. It is modelled as,

$$G = \int \mathrm{d}^2 x \big(-q(\nabla \cdot \hat{p}) - \frac{\alpha}{2}\hat{p}^2 + \frac{\beta}{4}\hat{p}^4 + \frac{\gamma_0}{2}(\nabla\hat{p})^2 + \frac{\gamma_2}{2}(\nabla\nabla\hat{p})^2 \big) \tag{D.21}$$

where the last two terms inside paranthesis on the right-hand side can be rewritten in Eulerian notation as $(\partial_i p_j)(\partial_i p_j)$ and $(\partial_i \partial_j p_k)(\partial_i \partial_j p_k)$, respectively. Taking the derivative to combine eq. D.20 and eq. D.21, we get,

$$\begin{aligned} &\nabla \cdot \hat{p} = 0 \\ &(\partial_t + \lambda_0 \hat{p} \cdot \nabla)\hat{p} = -\nabla q + (\alpha - \beta|\hat{p}|^2)\hat{p} + \gamma_0 \nabla^2 \hat{p} - \gamma_2 (\nabla^2)^2 \hat{p} \end{aligned} \tag{D.22}$$

where the left-hand side represent the material derivative of the polarization field. The first term on the right-hand side is the pressure gradient. The second term emerges out of a quartic double-well potential (as depicted in eq. D.21) for the polarization field that describes the directional order-disorder transition of active materials with Toner-Tu theory [194, 195, 196]. $\alpha, \beta > 0$ leads to an effective polar alignment. The solution $\hat{p} = 0$ corresponds to an unstable isotropic fixed point, while the solutions $\hat{p} = \pm\sqrt{\alpha/\beta}$ are stable fixed points corresponding to globally polar ordered states with an arbitrary uniform orientation. As before, $\gamma_2 > 0$ for short-wavelength stability. The sign of γ_0 plays a critical role in determining the dynamics. With $\gamma_0 > 0$, γ_0 acts like viscosity in Navier-Stokes equation, damping the system into a stable homogeneous polar state. With $\gamma_0 < 0$, the system destabilizes into turbulent-like patterns with a characteristic length of $\sqrt{\gamma_2/-\gamma_0}$ and lifetime of γ_2/γ_0^2. Increasing density may cause such negative γ_0 values, thus increasing density may lead to turbulent behaviour within this model.

The same modelling approach can be extended to apolar active systems like kinesin-microtubule suspensions by treating them as active incompressible liquid crystal ensembles. The polarization vector field $\hat{p}$ turns into a matrix field of nematic order field Q,

$$\partial_t Q + \nabla \cdot (\mathbf{u}Q) - K[Q, \Omega] = \frac{-\delta G}{\delta Q} \tag{D.23}$$

where $\Omega = (\nabla\mathbf{u} - (\nabla\mathbf{u})^T)/2$ is the vorticity tensor, K represents a coupling with $[A, B] = AB - BA$ the matrix commutator (vanishing commutator indicates that the two fields are indepedent, that is, one can find common eigenbasis for both tensors; while a nonvanishing commutator indicates that the fields are coupled, that is, they are not indepedent from each other. In this regards, matrix commutator identifies the degree of coupling between two fields.). Note that $\nabla \cdot (\mathbf{u}Q) \neq \mathbf{u} \cdot \nabla Q$ when the incompressibility condition does not hold, *i.e.*, $\nabla \cdot \mathbf{u} \neq 0$. That is the case for kinesin-microtubule experiments in thin fluid layers wherein the fluid can enter and leave the interface, thus destroying the incompressibility assumption. Additional terms that aligns microtubules with the flow may be added with a term of the form Q, E where $\{A, B\} = AB + BA$ is the matrix anticommutator and $E = (\nabla\mathbf{u} + (\nabla\mathbf{u})^T)/2$ is the strain-rate tensor of the flow.

The nematic order parameter field Q can be related to the flow $\mathbf{u}$ via the Stokes equation,

$$-\mu\nabla^2\mathbf{u} + \nu\mathbf{u} = -\xi\nabla \cdot Q \tag{D.24}$$

where μ is an effective viscosity and ν is an effective damping parameter. Damping ν decreases with increasing distance h from the boundary with $\nu \sim h^{-\eta}$ [148]. The right-hand side of the equation corresponds to the fact that the regions where the spatial gradients of the nematic order parameter are high regions of effective polarity within the field, which then leads to an effective force. The sign of ξ determines the type of the stress. $\xi > 0$ leads to an extensile stress while $\xi < 0$ leads to a contractile stress. In the regime of the length scale l of the patterns, with the assumption damping dominates over viscosity as $\nu l^2/\mu \gg 1$, the equation simply becomes $\mathbf{u} = -\lambda_0\nabla \cdot Q$ where $\lambda_0 = \xi/\nu$.

Finally, the free energy can be written just like in eq. D.21,

$$G = \int \mathrm{d}^2x\Big(-\frac{\alpha}{2}\mathrm{tr}(Q^2) + \frac{\beta}{4}\mathrm{tr}(Q^4) + \frac{\gamma_0}{2}(\nabla Q)^2 + \frac{\gamma_2}{4}(\nabla\nabla Q)^2\Big) \tag{D.25}$$

where just like the polar case $\alpha, \beta > 0$ leads to an ordered phase (nematic ordering in this case), $\gamma_2 > 0$ is required for short-wavelength stability and the sign of γ_0 determines a transition from an homogeneous state at $\gamma_0 > 0$ to turbulent-pattern formation at $\gamma_0 < 0$ with characteristic lengths of $l \sim \sqrt{\gamma_2 / -\gamma_0}$. In passive liquid crystal ensembles, $\gamma_0 > 0$ penalizes the spatial inhomogeneities in the nematic order field Q. $\gamma_0 < 0$ state is special to active liquid crsyals. It corresponds to microtubule bundles that are buckling due to the motor-induced extensile shear stress caused by adjacent microtubule bundles. Within the ensemble, microtubule bundles grow against each other and spontaneously buckle upon extensile stress caused by the interactions during growth dynamics. Upon taking the derivative of the free energy, we end up with,

$$\partial_t Q - \lambda_0 \nabla \cdot [(\nabla \cdot Q) Q] - K[Q, \Omega] = \alpha Q - \beta Q^3 + \gamma_0 \nabla^2 Q - \gamma_2 (\nabla^2)^2 Q \tag{D.26}$$

which forms the most minimal model that captures pattern formation for active turbulence. Upon comparing eq. D.26 with eq. D.18, the three fields that were considered (namely, the filament concentration, hydrodynamic flow and nematic order parameter field) reduces to a single field in nematic order parameter field.

This minimalist approach is essentially based upon extension of Toner-Tu theory of flocking with Swift-Hohenberg theory of pattern formation. In Toner-Tu theory, a pseudo-scalar order parameter is Taylor expanded *a la* Landau, while in Swift-Hohenberg theory, an analogous expansion is carried out in Fourier space. The series expansion in Fourier space corresponds to higher-order spatial gradients in real space with transport coefficients (γ_0, γ_2) that describe interactions at intermediate length scales. In particular, γ_0 term can change sign due to the nonlinear interactions between active objects facilitated by high density, which then leads to pattern formation at negative values of γ_0, as it causes amplification of modes of a specific wavelength.

Eq. D.22 that describes the evolution of polarization field for polar active fluids can be extended to capture the hydrodynamic coupling of polarity to the flow. To achieve that, Dunkel, *et. al.* assumed a general strain-rate tensor E with components,

$$E_{ij} = \gamma_0 (\partial_i v_j + \partial_j v_i) - \gamma_2 \nabla^2 (\partial_i v_j + \partial_j v_i) + S q_{ij} \tag{D.27}$$

where $q_{ij} = v_i v_j - \delta_{ij} |\mathbf{v}|^2 / d$ and $S < 0$ describes pushers like *E. coli* or *B. subtilis* while $S > 0$ is for pullers like *Chlamydomonas algae* [50]. The spatial gradient of the strain-rate tensor will enter as a force on the right-hand side of Navier-Stokes equation for momentum conservation. Thus, keeping the quartic velocity potential, we get,

$$(\partial_t + \lambda_0 \mathbf{v} \cdot \nabla) \mathbf{v} = -\nabla p + \lambda_1 \nabla^2 \mathbf{v} - (A + C|\mathbf{v}|^2) \mathbf{v} + \gamma_0 \nabla^2 \mathbf{v} - \gamma_2 \nabla^4 \mathbf{v} \tag{D.28}$$

where $\lambda_0 = 1 - S$ and $\lambda_1 = -S/d$. Therefore, λ_1 term changes the onset of turbulent motion. The transition to active turbulence is thus easier for pushers, while it is made harder due to the positive sign of λ_1 for puller swimmers.

Fluid flow can be completely decoupled from active flow by considering $\mathbf{u} \sim \mathbf{v} + v_0\hat{p}$ where $\mathbf{u}$ is the bacterial veloctiy field and $\mathbf{v}$ is the solvent flow field. By using this decoupling, Slomka, *et. al.* considered the solvent flow field $\mathbf{v}$ at length scales larger than size of bacteria with,

$$\partial_t\mathbf{v} + (\mathbf{v}\cdot\nabla)\mathbf{v} = -\nabla p + \gamma_0\nabla^2\mathbf{v} - \gamma_2\nabla^2\mathbf{v} + \gamma_4\nabla^6\mathbf{v} \tag{D.29}$$

with higher-order spatial gradients [178]. Assuming a plane-wave solution at low Re numbers, in Fourier space, the equation $(\gamma_0 + \gamma_2 k^2 + \gamma_4 k^4)\mathrm{e}^{i\mathbf{k}\cdot\mathbf{x}} = 0$ has real positive roots only when $\gamma_2 < 0$, and thus, such solutions support patterns of length $\sqrt{\gamma_4/-\gamma_2}$.

The ordered phase of incompressible polar active fluids in two dimensions without momentum conservation is shown to be in the same universality class as growing one-dimensional interfaces (described by $1+1$ dimensional KPZ equation), $2D$ smectic liquid crystals without dislocations, and a divergence-free XY model in $2D$ [27]. As with these systems, formation of flocks are robust against fluctuations with long-ranged correlations of these fluctuations.

When the compressibility is taken into account in the minimal model as outlined in the nonlinear advection term in eq. D.26, then the model accounts for spontaneous microtubule buckling as mentioned. It also predicts a regime in which topological defects align in an antipolar state, which is somewhat similar to certain regimes in quantum gases [147]. Thus, by construction, fixed points of the minimal model describing a dense active liquid crystal ensemble coincide with the eigenstates of Gross-Pitaevski equation with wavelength selection, which renders dense active liquid crystals and strongly coupled quantum systems like Bose-Einstein condensates and Fermi gases somewhat analogous [147].

We have outlined two models that capture properties of active turbulence. Eq. D.18 describes an incompressible active liquid crystal ensemble at low Re numbers with three fields (filament concentration, hydrodynamic flow and nematic order field). A more minimal model based on Swift-Hohenberg extension of Toner-Tu theory of flocking captures similar behaviour with a single field (polarization field for dense polar active fluids like bacteria as outlined in eq. D.22) and nematic order field for dense active liquid crystal ensemble like kinesin-microtubule suspensions as outlined in eq. D.26). In modelling active turbulence, we neglected the role of density fluctutations thus far. In its most general form, we have to take into account four different fields in the concentration of active particles c, the total density ρ, the hydrodynamic flow velocity $\mathbf{u}$, and the nematic order tensor Q. Following Doostmohammadi, *et. al.* we write the following general set of hydrodynamic equations,

$$\begin{aligned}
&\partial_t c + \partial_i(u_i c) = \gamma_c^{-1}\nabla^2\mu \\
&(\partial_t + u_k\partial_k)Q_{ij} - S_{ij} = \gamma_Q^{-1}H_{ij} \\
&\partial_t\rho + \partial_i(\rho u_i) = 0 \\
&\rho(\partial_t + u_k\partial_k)u_i = \partial_j\pi_{ij} - \gamma u_i
\end{aligned} \tag{D.30}$$

where S_{ij} is a co-rotation term accounting for the response of the nematic order to the flow gradients as characterized by the strain-rate tensor and the vorticity tensor [45]. Note the difference between the advection of nematic order in eq. D.26 and the equation for nematic tensor in eq. D.30. The chemical potential $\mu = \delta F / \delta c$ encodes the relaxation of concentration to equilibrium. In a similar way, the molecular field $H_{ij} = -\delta F / \delta Q_{ij}$ determines the relaxation of the nematic order as before. The main difference between this model and the incompressible nematic flow described earlier in eq. D.18 is mainly related to the co-rotation term describing the coupling of the nematic field to the flow and the reactive elastic stress of the nematic field in response to activity. This model is more complicated and more general in including density fluctuations, frictional damping and more detailed couplings between hydrodynamic flow and nematic order. We refer the reader to ref. [45] for the full expressions of the terms in eq. D.30. In contrast to the earlier model, the free energy involves terms related to the concentration, and coupling of concentration field to the nematic order field.

We have already underlined certain properties of active turbulence in formation of vortices, topological defects, ordering of vortices and defects, and excitement of multiple length and time scales that result in power law regimes in energy and power spectrums. A velocity field marked with defects and vortices is indeed the quintessential feature of active turbulence. Defects acts as sources of vorticity. These features determine the dynamics of the system undergoing active turbulence. Now we will describe these active-turbulence features in somewhat more detail and match them to the three models that are outlined.

For the sake of brevity, we will refer to the first model that describes incompressible dense nematic suspensions in eq. D.18 as the active liquid crystal model, the second model incorporating Toner-Tu theory with higher-order spatial gradients in eq. D.22 and eq. D.26 as the minimal model, and the third model that includes the total density field in eq. D.30 as the active liquid crystal model with density variations.

As a function of increasing friction coefficient, the system dynamics change from wet hydrodynamics towards dry hydrodynamics where frictional damping dominates over viscous damping. Doostmohammadi, *et. al.* describes the dynamics generated by the active liquid crystal model with density variations by employing a phase diagram as a function of friction and temperature [45]. Temperature (or, equivalently noise) drives the isotropic-nematic transition. At low enough temperatures corresponding to the nematic phase, the limit of low friction (wet hydrodynamics limit with momentum conservation) corresponds to an active turbulence regime with vortical velocity fields. Keeping the temperature fixed while increasing the friction leads to the formation of a vortex lattice which forms as defects become ordered. This regime of low temperature and intermediate frictions is at the crossover region between wet and dry hydryodynamics. Increasing the friction further leads to the loss of collective motion at the dry hydrodynamics limit where momentum propagation is suppressed by high frictional damping [45]. This suggests that at a low enough density where concentration variations play a role, ordered collective motion is not expected to happen for dry hydrodynamics as long-range interactions are inhibited by friction. Therefore, active turbulence is a hydrodynamic feature. To put it more generally, the property of hydrodynamics that leads to active turbulence is the nonlinear long-range interactions. Elastic stresses in viscoelastic polymers play the same role which drives a turbulence transition at low *Re* numbers where role of hydrodynamics itself is diminished.

Active turbulence emerges as a result of an intrinsic hydrodynamic instability that destabilizes the nematically ordered regions. Small bend fluctuations in the ordered regions is propogated by local shear which results in the instability. These instable regions with lines of strong bend deformations are known as *walls* [189]. Once a wall is formed, it relaxes by tilting the local director until oppositely charged defects are created. In this way, walls relax by formation of oppositely charged defects. A +1/2 defect moving away from a −1/2 defect (which corresponds to a spontaneous defect pair creation) and a +1/2 defect moving towards a −1/2 defect (which corresponds to a defect pair annihilation) both result in the relaxation of a wall - a region of bend deformations. Correspondingly, defects are found in the regions with the strongest bend deformations [189].

Formation of walls depends on the interplay between extensile stress generated by active nematics which leads to distortions in the director field and the elasticity of the nematic field which prevents such distortions. As a result of this interplay between activity and elasticity, the dominant length scale of instability is determined with $\sqrt{K/\alpha}$ where K is the strength of elasticity and α is an activity parameter (proportional with the spatial gradient of the nematic order field in the case of active nematics, or the polarization field in the case of active polar fluids) [189, 78]. This length scale, determined by the balance of active and elastic stresses, dictate the defect dynamics regardless of the active stress being extensile or contractile. When elasticity is not strong (or equivalently when activity is strong), the instability length scale corresponding to the formation of walls is small, which allows formation of more walls, allowing then formation of more defects. Thus, number of defects increases with increasing activity, or decreasing elasticity [189]. Interestingly, the number of defects depend strongly on the elasticity, but only weakly on the activity. The scaling for the number of defects is found to be $\sim \sqrt{\alpha}/K$.

Increasing friction results in slower speeds accompanied by an increase in the number of walls and consequently the number of defects up to a friction value. When friction is further increased, topological defects start to disappear altogether and active turbulence regimes dies out leaving an overall jammed system. The velocity associated with flow decays slowly due to viscous damping in the limit of vanishing friction. However, as friction is increased, the decay of velocity increases. The ratio between viscosity and friction coefficient $l_{\text{diss}} = \sqrt{\mu/\gamma}$ defines a dissipation length scale. As friction is increased, or viscosity is decreased, the length scale over which a source flow decays decreases. Thus, with increasing friction, the spacing of walls first decreases as a consequence of rapid decays in velocity, generating more walls and more defects and then the system becomes jammed as the friction is increased further [188]. These observations holds when concentration variations are taken into account, *i.e.* in a model such as the active liquid crystal model with density variations. However, topological defects are still observed in vibrated rod experiments (which is in the dry limit). This could be alluded to the collision-induced nematic alignment and reorientations of the rods [45].

In the wet limit (for example, a free-standing fluid layer), concentration bands form perpendicular to the director field with anticorrelated concentration and nematic order. In the dry limit (for example, shaken rod experiments), the concentration bands occur parallel to the director field with correlated concentration and nematic order [45]. In fact, active curvature currents dominate the dynamics leading to concentration fluctations known as giant number fluctuations [135]. At the crossover regime between wet and dry limits, a vortex lattice forms. The vortex lattice is strongly coupled with a network of topological defects. $+1/2$ defects occur between pairs of counter-rotating vortices, while $-1/2$ defects are observed between pairs of co-rotating vortices [45].

Topological defects play an important role in determination of dynamics. Number of defects determine the spatial structure of the flow field [191]. Consequently, the vorticity correlations and order parameter correlations are controlled by the density of defects, or in other words, the distance between two defects [191]. Both spatial and time correlation functions of vorticity and order parameter correlations scale the same way, while in contrast, the velocity correlations is determined with a balance between activity and dissipation.

The correlation length of velocity is actually found to be independent of activity, while the characteristic velocity scale increases monotonically with increasing activity. As such, when the spatial velocity correlation functions are normalized with the characteristic velocity scale, all functions corresponding to different activity values collapse onto each other [190]. This also follows from the observation that velocity correlation length is set by the defect density, which depends only weakly on activity, while depending strongly on elasticity. The spatial structure of the flow changes only weakly with activity. However, activity still leads to formation of jets, which then increases the characteristic velocity scale (for example, the root mean square velocity).

Dunkel, *et. al.* observed a linear scaling between enstrophy and energy for $3D$ bacterial turbulence with $\Omega_z = E_{xy}/l^2$ where subscripts indicate dimensions and l indicates one half the typical vortex radius around $24\mu m$ by employing the minimal model (Note that characteristic vortex length scale is unique to active turbulence as vortex lengths are scale free in inertial turbulence.) [49]. The vortex radii do not depend strongly on the kinetic energy, consistent with previous observations. The same model shows that the in-plane velocity distribution is approximately Gaussian with slight broadened tails emanating from collective motion [49].

In eqilibrium, defect dynamics is determined with minimization of Landau-de Gennes free energy which results in same-signed defects to repel each other and opposite-signed defects to attract each other leaving a uniform ground state. However, in an active system defects are able to move. Opposite-signed defects can move away from each other. Defect dynamics depend on the level of activity and its contractile or extensile character. Contractile systems increase the annihilation dynamics while extensile systems tend to drive defects apart [67].

Stresses caused by activity alters the backflow (that is the flow caused by reorientation of the nematic order field due to elastic stress), which then alters the defect dynamics. When orientational relaxation is very large in comparison to the activity timescale, the relaxation of the nematic phase becomes overwhelmed with activity, leading to an increase of topological defects. Such dynamics is captured with three fields in active liquid crystal model [67]. If we ignore backflow, force balance between defect-pair interactions (with $F_{\mathrm{p}} = -\nabla E_{\mathrm{p}}$ where $E_{\mathrm{p}} \sim K \ln x/a$ with a the defect core radius) and effective fricition ($\mu\dot{x}$) leads to $\mu\dot{x} = K/x$. Thus, without backflow, the defect dynamics is entirely relaxational and opposite charged defects move in symmetric trajectories with the same velocity to annihilate each other.

Backflow affects the passive and active liquid crsytals different. For passive systems, it speeds up the $+1/2$ defects and slows down $-1/2$ defects, generating asymmetric trajectories [197]. For active systems, the effect depends on the extensile or contractile nature of the active stresses. Due to their polar configuration, in the case of contractile stress, $+1/2$ defects move in the direction of their tail. While in extensile systems, $+1/2$ defects move in the direction of their head. Due to their symmetric configuration, active backflow does not affect $-1/2$ defects [67].

The defect dynamics depend on the degree of activity. At small activity, the dynamics is similar to thermal systems. At large activity, $+1/2$ defects move independently along its symmetry axis (in the direction set by the contractile or extensile nature of the active stress). For large values of friction, on the other hand, the dynamics is determined by active flow at large separations. When distance between defects get smaller, the pair forces take over and defects behave as in the thermal case [67].

As seen earlier, defect motility can lead to some form of ordered behaviour alongside chaotic motion. In a pioneering experiment on microtubule-based active namatics, DeCamp, *et. al.* demonstrated a system-wide orientational ordering of topological defects by tracking thousands of defects over centimetre-scale distances [37]. Orientational distribution function of $+1/2$ defects exhibit peaks, and that of $-1/2$ defects show sixfold symmetry with smaller peaks. The order is nematic despite the fact that $+1/2$ defects are polar. The observed ordering is strictly orientational, as the radial distribution of defects does not result in any sort of positional order. The ordering behaviour is not strongly affected by sample boundaries, however increasing density results in less order [37].

The ordering mechanism is posited in topology and motility of defects. By construction, $+1/2$ defects occur perpendicular to the local nematic field in the front. It moves in a curved trajectory remaining always perpendicular to the local nematic field in front of it. The passage of a $+1/2$ defect rotates the nematic field it left behind perpendicularly, generating a region which can only relax by the passage of further defects. The orientational order emerges as further defects has to pass through the same area [37].

The orientational ordering of $+1/2$ defects in experiments is captured with Brownian dynamics simulations of extending rods that divide in half when a critical size is reached [37].

Thampi, *et. al.* demonstrates that an activity-induced effective free energy can lead to order in extensile active rods and in contractile active discs, as fluctuations that lead to order are enhanced by the flow active particles generate [192]. A simple force balance between active and viscous stresses yields $2\mu E_{ij} \sim \alpha c Q_{ij}$ where E_{ij} is the strain-rate tensor, c is the local active particle concentration, Q_{ij} is the nematic order tensor, μ is viscosity and α is an activity parameter. This relation is used to simplify the co-rotation term in eq. D.30 and the resulting new terms that are proportional with the alignment parameter and the strength of activity are interpreted as an effective free energy [192]. A rod has its stable position when it is aligned with the flow. Active particles generate dipolar flow fields favouring order for extensile stress and disorder for contractile stress. A fluctuation in the isotropic configuration of rods that induces a small orientational ordering will be enhanced if the stress is extensile. Thus, in extensile stress conditions, hydrodynamics facilitates an effective force which favours the alignment of rod-like active particles. Disc-like particles, on the other hand, are stable along their compressional axis. Therefore, for such particles, contractile stress favours ordering instead [192].

Ordered states of defects and defect motility opens the way for possible applications of active flows in microchannels. Confinement stabilizes the vortices of a highly concentrated *B. subtilis* suspension trapped in an oil emulsion into a steady single-vortex state [208]. The complex interplay between radial confinement, self-propulsion, steric interactions and hydrodynamics leads to the stabilization of chaotic motion. Lushi, *et. al.* studied the effect of confinement for such circularly confined bacterial suspensions in two dimensions. They incorporated cell-cell, cell-fluid interactions and swimmer-generated flows in a simulation model, and found that long-range hydrodynamic interactions are crucial in reproducing experimental results [127]. Despite the local alignment of bacteria by steric interactions, long-scale order emerges only when the bacteria motion is coupled to hydrodynamic flow. They observed that bacteria in the bulk actually swim against the flow, while bacteria at the surface swim with the flow [127].

Wensink, *et. al.* studied noiseless self-propelled rods that interact with Yukawa potential in $2D$ without hydrodynamics as a function of aspect ratio and density [205]. Starting from an incoherent phase, at small aspect ratios, increasing density leads to a transition towards jamming. At intermediate aspect ratios (which is the regime for *E. coli* with $a = 3$ and *B. subtilis* with $a = 6$), increasing density leads to formation of vortices and turbulence. Incidentally, the energy spectrum shows power laws with a slope of approximately $-5/3$ in the turbulent regime with a peak at high wavenumbers corresponding to the length of individual rods. At high aspect ratios, increasing density drives a transition towards laning and swarming [205].

Spherical self-propelled Brownian particles that interact with Yukawa potentials in three dimensions phase separate into a dilute and a dense phase [211]. Long-range correlations are observed in the dense part with scale-free spatial displacement correlations with an initial power law followed by stretched exponential decay, $C(r) = r^{-\alpha} e^{-(r/\eta)^{\beta}}$. The presence of a power law regime and long-range correlations is associated with an interface-induced sorting scheme. Fast-moving gaseous particles hit the initially flat interface between the dilute and the dense phases, and remain at the interface until rotational diffusion aligns them in a parallel orientation to the interface. At concave interfaces, reorientations take more time, leading to an effective trapping of particles at the interface. At convex regions (protrusions), particles easily escape towards neighbouring concave regions, leading to an accumulation of particles in the concave regions. Due to the escape mechanism, accumulated particles share a common polar direction at the concave regions. Since they point in a common direction, they push the orientationally disordered particles deep inside the dense phase. This is the origin of correlation occuring in particle displacements, instead of particle orientations [211].

Bacterial turbulence is used to actively transport a wedge-shaped bulldozer particle on experiments [98]. Bacterial suspension makes a transition from an initial dilute phase to a turbulent phase as the density is increased, with a further increase in density resulting in jamming. Experiments showed that the most optimal transport mechanism occurs in the turbulent phase, as bacteria trapped inside the wedge are shielded from the swirly motion around the bulldozer particle. As the wedge breaks swirly motion in the local environment, bacteria trapped inside the wedge, which are polar ordered, are able to propel the wedge [98].

Rod-like shapes of bacteria enhances orientational ordering through steric and hydrodynamic interactions. However, robust collective dynamics with vortical and jet-like motion is also observed for spherical bacteria (*Serrotia marcescens*) [163]. For larger bacteria, the mean speed and vorticity increase while correlation times and length scales remain the same [163]. Similar phases are observed for interacting self-propelled particles interacting self-propelled particles for which the center of mass of a single swimmer moves on a circle of radius R in $2D$ [96]. A radius of $R \to \infty$ represents a linear swimmer, an intermediate radius is like a rod, and a radius of $R = 0$ corresponds to a passive rotor. Phase diagram is a function of density and radius. Starting from a dilute regime at low density and low radius, when density is increased at low radius, individual particles move in single vortices forming a vortex array with strong ordering at large scales. At intermediate radius, increasing density couples the motion of two particles and they form double vortices. At high radius, an increase in density results in a slowed rotor fluid regime [96].

A self-propelled paricle model, inspired by the short-range activation and long-range inhibition of Turing mechanism of pattern formation in reaction-diffusion systems, exhibited periodic vortex patterns and active turbulence [75]. Making the self-propelled particles interact with short-range alignment and long-range antialignment are the minimal ingredients to induce active turbulence for active-particle models. Self-propelled nematic particles with Vicsek interactions (consisting of particles pointing in the same direction as their local neighbourhood) exhibit large-scale spatiotemporal chaos that consist of interacting bandlike structures in the dilute limit without hydrodynamics [138].

On an experimental system of dense suspension of asymmetrical Janus particles on a $2D$ surface, the application of an ac electrical voltage results in formation of vortices and abrupt changes of velocity resembling mesoscale turbulence [140]. Janus particles are dielectric colloids that are inherently asymmetrical with two hemispheres covered with different metals. Application of an ac electric field induces an asymmetrical flow around the Janus particle due to the dielectric constant different between the hemispheres. It drives the particles in a direction perpendicular to the applied electric field. Due to the induced rotational Brownian motion and collisions with other particles, their trajectory is curved, which then results in turbulent motion in the suspension [140].

Hemingway, *et. al.* studied the interplay between activity and polymer rheology by adding polymers to an active fluid of bacterial turbulence [77]. Just like in Navier-Stokes turbulence, adding polymers leads to drag reduction due to stretching of polymers. Polymers stabilize the short scales of active flow, decreases defect density and increases the correlation length of flow velocity towards the system size, which results in a more ordered flow [77].

Spindle-shaped cells (like smooth muscle cells and sarcomas) are observed to exhibit mesoscale turbulence at a regime when activity is damped by friction and the interaction between defects is controlled by elastic energy [48]. Duclos, *et. al.* used spindle-shaped NIH3T3 mouse embryo fibroblasts which interact with steric interactions when put on fibronectin-coated glass substrates. They got similar results with other spindle-shaped cells like retinal pigment epithelial cells (RPE1) and C2C12 mouse embryos [48]. Activity of the cells render motile defects that annihilate in pairwise fashion until cell displacements cease at very high densities. When cells are confined circularly, the system evolves towards a peculiar configuration in which two +1/2 defects go to particular places facing each other. These reduced positions of the defects are found to be independent of the size of the disk, activity of the cells, the cell type, but are only determined by equilibrium liquid crystal theory [48].

In epithelial tissues, unnecessary or pathological cells are removed from the tissue through a process known extrusion. Extrusion, which is linked to developmental and homeostatic processes as well as cancer metastasis, can be triggered by a variety of factors such as overcrowding of cells, oncogenic transformation, or apoptotic signalling. A recent experiment on Madin Darby canine kidney cells revealed that extrusion process is linked to the material properties of epithelia. In particular, apoptotic cell extrusion is found to coincide with the sites of +1/2 topological defects [171]. The mechanical stress associated with topological defects (instead of cell density) is found to be the precursor of extrusion process. Mechanical stress is higher for +1/2 defects in comparison to −1/2 defects. The correlation between cell extrusion sites and positions of +1/2 defects confirm the nematic nature of epithelia as well as demonstrating that defect-induced stresses are the primary precurors of further cell signalling for cell death and extrusion [171]. This also indicates that by controlling defects cell extrusion can be controlled with potential applications in tissue regeneration and suppression of cancer metastasis.

As the activity of cells is reduced by adding blebbistatin (which hinders actomyosin activity) to the epithelial tissue, number of defects decreased [171]. Knocking down α-catenin (α-catKD acts as a mechanosensor for force transmission across cell-cell junctions, thus knocking it down hinders intercellular junctions) results in smaller-sized defects with more focused stress patterns. The defect core size is expected to scale with $\sqrt{K}$ where K is nematic elasticity, thus knocking down α-catKD can be interpreted as a reduction in K, which favours collective cell bending. With lower nematic elasticity K and more collective bendings, number of defects increases. Thus, weakened cell-cell junctions facilitates collective cell bending that decreases nematic elasticity K, which then leads tan increase in number of defects and cell extrusion [171].

Cells of the central nervous system is generated from multipotent stem cells called as murine neural progenitor cells (NPCs). At low densitites, NPCs move like amoeba in a random manner, however, upon increasing density, they elongate and align their shapes with respect to one another and start to move much faster. The direction of motion reverses randomly along the alignment direction. In a recent experiment on dense NPCs (cultered from fetal mice), aligned cell patterns are observed in large length scales that resemble the migratory stream observed in the adult brain [101]. The alignment pattern is interspersed with nematic topological defects which results in cell accumulation at +1/2 defect sites, and cell escape from −1/2 defects.

Swarming ram semen sperm cells (with lengths of approximately $60\mu m$ and ellipsoidal heads) display enstrophy cascade at high concentrations of 50% filling ratios [33]. The energy spectrum saturates to an early white noise plateau at small wavenumbers corresponding to large length scales where fluctuations are uncorrelated in space. After the peak, the spectrum decays with a power law k^{-3} consistent with enstrophy cascade of Kolmogorov phenomenology of turbulence. At large wavenumbers, there is a second white noise plateau at around the size of individual sperms [33].

Defect topology is used to ensnare swimming bacteria by coupling bacterial motion to the topology of the nematic director at the defect cores of an underlying liquid crystal. To achieve that, a suspension of *B. subtilis* is put in a free-standing film of lyotropic liquid crystal disodium cromoglycate, and bacterial concentration is used to dictate the speed of defects [63]. Increasing bacterial concentration speeds up the defects. Thus, at lower concentrations, as the defect speed is slower, bacteria accumulate at +1/2 defects and pushed out of −1/2 defects. This directly emerges out of the coupling of motion of bacteria to the nematic director of the liquid crystal. When the nematic streamlines of the underlying fluid and bacterial trajectories converge at the core of a +1/2 defect, bacteria moving towards the defect accumulate, while bacteria swimming away from the defect are pushed away. In the meantime, bacteria are expelled from the −1/2 defects as the nematic streamlines help them go away from the defect core of the underlying liquid crystal [63].

Confinement of active turbulence can induce coherent flows. Wu, *et. al.* studies microtubules, bundled by depleting polymers, driven by kinesin clusters on different types of $3D$ channels and find such a transition that is determined entirely by the aspect ratio of the confining channel [210]. Coherent flows form robustly in square channels and disappear when the channel is too thin and wide or too tall and narrow. The result also holds for other types of geometries. For an annulus starting from $2D$ turbulent flow, increasing the height of the channel leads to coherent flow as aspect ratio becomes balanced by the increase in height. Coherent flows are found to take place when the cross section of the channel is rather symmetric with a height to width ratio of around 3 [210].

In a similar experiment of confinement of active turbulence in a channel, a dynamic vortex lattice is observed with defects moving in a dance-like pattern [177]. As defects move along the channel, they exchange partners just like in traditional Ceilidh dancing. $-1/2$ defects form near the boundaries and remain stationary, while $+1/2$ defects occur in the mid-parts of the channel and move in sinusoidal paths exchanging partrners continuously [177].

Upon confinement in a droplet, active turbulence can power cell-like motility with the interplay between moving defects, droplet size and surface tension resulting in different types of motility and rotation phases [61].

The confinement efffect is also used to compare inertial and active turbulence in somewhat more detail. Doostmohammadi, *et. al.* studied the onset of active turbulence from an initial ordered vortex-lattice in a microchannel [44]. At intermediate levels of activity, an ordered vortex lattice dominates the flow. Upon further increase of activity, the vortex lattice coexists with local active turbulence. Such regions are where vortex pairs split into smaller disordered vortices that are called puffs. The turbulence is started by these locally disordered patches of active puffs. They feed on the surrounding local flow in an absorbing state and drive the transition towards fully-developed turbulence by the short-ranged interactions between them. In inertial turbulence, puffs are created by external conditions like an induced pressure jump, while in active turbulence, they emerge from the intrinsic activity of individual objects. At low levels of activity, vortices take longer time to split up, so puffs are created at smaller rates, and the ones that are created decay. As activity is increased, number of puffs (or equivalently the turbulent fraction of the flow) increases with a power law. The critical exponents of this active turbulent transition is observed to be within the directed percolation universality class [44].

More detailed comparisons of active turbulence with inertial turbulence are gaining traction in the recent years. By employing the minimal model, Bratanov, *et. al.* argued that the interplay between nonlinearities of the cubic term in eq. D.22 and the quadratic term in Navier-Stokes equation leads to energy spectra with power laws at large length scales [18]. However, instead of being universal, the exponents are found to depend on finite-size effects and physical parameters. Similarly with inertial turbulence, energy is carried from intermediate to large length scales with an inverse cascade in $2D$ active turbulence. However, they argued that the nonlinear frequency of Navier-Stokes energy flux is not constant at large length scales. For inertial turbulence, this nonlinear frequency is the inverse of eddy turnover time at large scales and it depends on the wavenumber and energy. For active turbulence, the energy flux depends on both linear dissipation or injection (depending on the sign of the term in eq. D.22) and a cubic dissipation term. They computed scalings of k^2 to k^3 at small wavenumbers with a power depending on the energy injection parameter [18]. More injection makes the power law slope less steep with more energy at each scale and a peak shifted to smaller and smaller wavenumbers.

Such power-law spectra with nonuniversal exponents are generic features of systems with multiscale drive and/or damping like dense bacterial suspensions, space-filling fractal square grids, and laboratory plasmas [19]. These systems exhibit power-law spectra corresponding to turbulent regimes of their own, while not having an inertial range with a universal exponent that is extracted from dimensional analysis. A modified Kuramato-Sivashinsky equation is used to obtain nonuniversal power laws within a certain spectral range if the ratio between the nonlinear and linear time scales are scale indepedent in that range [19]. Kuramato-Sivashinsky equation captures chemical reaction-diffusion processes, turbulence in magnitized plasmas, flame front propagation,

$$\partial_t u = -u\partial_x u - \mu\partial_x^2 u - \nu\partial_x^4 u \tag{D.31}$$

in one dimesion with $\mu, \nu > 0$. In Fourier space,

$$\partial_t \hat{u}(k_n) = \frac{-ik_n}{2}\sum_m \hat{u}(k_n - k_m)\hat{u}(k_m) + (k_n^2 - \nu k_n^4)\hat{u}(k_n) \tag{D.32}$$

with $u(x,t) = \sum_n \hat{u}(k_n,t)\mathrm{e}^{ik_n x}$. When summed over all n, the nonlinear term vanishes, thus the nonlinearity of the equation does not lead to an energy injection or dissipation, but only redistributes the energy among the modes. Thus, in terms of energy, each mode is characterized by the drive or damp rate $\gamma = k_n^2 - \nu k_n^4$. This term is modified to $\gamma/(1 + bk_n^4)$ such that at the high wavenumber limit, the damp rate becomes constant at ν/b. With this contant high wavenumber damp rate, the energy spectrum becomes,

$$E(k) \approx E_0 k^{-2\nu/b} \tag{D.33}$$

which indicates that the exponent changes with the damp rate ν/b and is nonuniversal [19].

The effect of intermittency is observed to be smaller and less energetic in active flows in comparison to high Re numbers flows [200]. With increasing activity, departures from Gaussian statistics in velocity and vorticity become more frequent. A wavelet-based, scale-dependent flatness analysis reveals high intermittency in the small length scales, in particular in the $3D$ vorticity field [200]. For $2D$ bacterial turbulence, small scales are found to be more intermittent than large-scales, which might be due to the fact that activity emerges at the small scales [161]. The scaling exponents both for small and large length scales are convex, indicating multi-fractality [161].

Slomka, *et. al.* finds a generic inverse energy cascade for $3D$ active turbulence with flow-dependent spectral forcing by analysing the triad interactions analytically.

Giomi studied the geometry and topology of active turbulence to obtain scaling relations in energy spectrum [66]. By using the active liquid crystal model, he demonstrated that the vortex areas are exponentially distributed with a characteristic vortex size and vorticities remaining constant. The coherence length of the nematic phase $l_n = \sqrt{K/C}$ (parameters as they appear in eq. D.18) determine how quickly the nematic order drops in the vicinity of a topological defect and is a measure of the defect core size. The active length scale $l_a = \sqrt{K/|\alpha|}$ determines the balance between active and passive stresses, which can lead to elastic distortions and hydrodynamic flow. A uniformly oriented flow starts to become unstable once $l_a \sim L$ and as l_a gets lower than the system size L, the uniform flow turns turbulent. The number of unbound defects increases with decreasing l_a (*i.e.* increasing activity, or decreasing elasticity) until $l_a \sim l_n$. Around this point, active and passive stresses start to balance each other as the reduction in nematic order due to the high number of defects balances the increase in activity [66]. Thus, vortex areas follow an exponential distribution with a characteristic vortex size set by the balance of active and elastic stresses.

Activity does not change the spectral feature of the flow, but it merely changes its resolution [66]. Vortex areas becomes smaller with increasing activity. Thus, the mean kinetic energy scales linearly with activity as the vortices becomes smaller and smaller with the increase in activity [66]. This points to a picture of active turbulence in which kinetic energy can also be converted into elastic energy without the need for a cascade necessarily. The observed energy spectra follow k^{-4} and the corresponding enstrophy spectra follow k^{-2} [66].

E. Dynamics of a Single Cell

We model a single cell as a deformable ellipse-like object that performs active Brownian motion. It is a vesicle in terms of membrane configuration. As such, we distinguish the dynamics of the center of mass of the cell with active Brownian motion, while considering vesicle dynamics to tackle the motion of the beads of the cell. The goal is to establish connections of the single-cell dynamics to the analytical results derived earlier in Chapter 2. This serves both as an illustration and confirmation of our model.

The velocity of the center of mass of the cell is simply determined with $v_0 = f_m/\gamma$. A friction coefficient per bead of $\gamma = 1$ indicates that $v_0 = f_m$. At steady state, speed of the cell fluctuates around the value set by the magnitude of the motility force (see fig. E.1-a).

We next turn to the time autocorrelation of velocity. To obtain velocity, we consider the Langevin equation by adding an additional force term f_m for propulsion,

$$\frac{\mathrm{d}\boldsymbol{v}(t)}{\mathrm{d}t} = -\frac{\gamma}{m}\boldsymbol{v}(t) + \frac{f_m}{m}\hat{n} + \frac{1}{m}\boldsymbol{\eta}(t) \tag{E.1}$$

We employ a solution of the form $\boldsymbol{v}(t) = \exp(-\gamma t/m)u(t)$ to solve for the velocity, which yields

$$\boldsymbol{v}(t) = \frac{1}{m}\int_{-\infty}^{t} \mathrm{e}^{-\frac{\gamma}{m}(t-t')}\eta(t')\mathrm{d}t' + \frac{f_m}{m}\int_{-\infty}^{t} \mathrm{e}^{-\frac{\gamma}{m}(t-t')}\hat{n}(t')\mathrm{d}t' \tag{E.2}$$

For passive motion with $f_m = 0$ in the asymptotic limit, we found an exponential relaxation for the velocity autocorrelation with a relaxation time of $\tau_v = m/\gamma$ in eq. 2.8. As we sample data with time intervals of $\mathit{\Delta} t = 50\tau_v \approx 0.5\tau_D$, we see an immediate relaxation to zero for passive motion in fig. E.1-b. At increased motility, we observe identical exponential velocity relaxations with relaxation times larger than that of passive motion (~ 14 times larger). Ignoring the integral with the noise term in eq. E.2, we get,

$$\langle \boldsymbol{v}(t)\cdot\boldsymbol{v}(0)\rangle \approx \frac{f_m^2}{m^2}\langle \hat{n}(t)\cdot\hat{n}(0)\rangle \approx \frac{f_m^2}{m^2}\mathrm{e}^{-t/\tau_R} \tag{E.3}$$

where $\tau_R = 1/D_r$ is the relaxation time of orientation, which is $\tau_R = 1000\tau_v \approx 10\tau_D$. Therefore, velocity relaxation is determined by relaxation of orientation, which explains the identical relaxation as a function of motility.

Integrating eq. E.2 with time, we obtain the position,

$$\begin{aligned} x(t) &= \left(v_0 + \frac{f_m}{m}\right)\tau_v(1-\mathrm{e}^{-t/\tau_v}) + \frac{1}{m}\int_0^{t'}\int_0^{t} \mathrm{d}t''\mathrm{d}t'''\mathrm{e}^{-(t-t'')/\tau_v}(\eta(t'') + f_m\hat{n}(t'')) \\ &= \left(v_0 + \frac{f_m}{m}\right)\tau_v(1-\mathrm{e}^{-t/\tau_v}) + \frac{\tau_v}{m}\int_0^{t} \mathrm{d}t''(1-\mathrm{e}^{-(t-t'')/\tau_v})(\eta(t'') + f_m\hat{n}(t'')) \end{aligned} \tag{E.4}$$

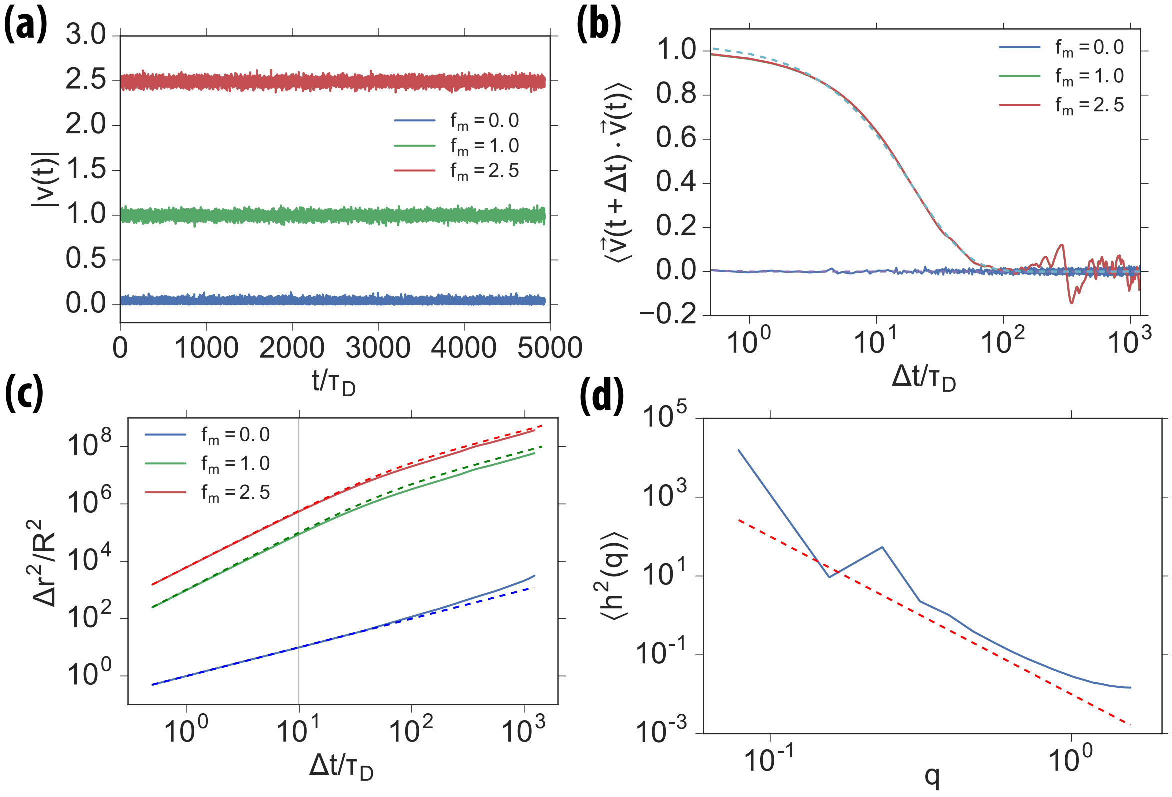

Figure E.1.: Single cell dynamics: (a) Speed of the center of mass of the cell as a function of time, (b) velocity autocorrelation function of the center of mass of the cell in time with dashed lines indicating exponential fits, (c) mean square displacement of the center of mass with dashed lines indicating the theoretical expectations, the gray line indicates the rotational diffusion relaxation time $\tau_r = 1/D_r$ and (d) fluctuation spectrum of the beads with the dashed line indicating the analytical result. Legends denote varying motility forces in all the plots.

which is essentially a superposition of an activity term to the position expression of the Ornstein-Uhlenbeck equation. We derived the mean square displacement for Ornstein-Uhlenbeck process in eq. 2.14, we can now follow the same procedure by changing friction term with the motility term, which gives the generic formula of,

$$\langle (x(t) - x(0))^2 \rangle = (2dD_t + v_0^2 \tau_R)t + \frac{v_0^2 \tau_R^2}{2}(\mathrm{e}^{-2t/\tau_R} - 1) \tag{E.5}$$

where d represents the dimensionality of the system [199]. Without activity, it scales linearly in time with the proportionality constant given by the translational diffusion coefficient as $4D_t$ for passive motion (fig. E.1-c). With activity, there is a cross-over from an initial ballistic scaling with t^2 to long-time diffusive regime with t. The cross-over occurs at the rotational relaxation time τ_r.

Transverse distance between consecutive beads of the cell remain constant due to the stiff bond potential. However, beads are free to fluctuate around a mean point in the normal direction to the bond vector. The spectrum of these fluctuations are calculated by the autocorrelation of Fourier transform of these position fluctuations around their average point. These fluctuations are expected to scale with q^{-4}, as derived in Appendix D, see eq. C.24. The fluctuation spectrum is observed to agree reasonably well with this scaling in fig. E.1-d.

Eigenhändigkeitserklärung

Ich versichere, dass ich die von mir vorgelegte Dissertation selbständig angefertigt, die benutzten Quellen und Hilfsmittel vollständig angegeben und die Stellen der Arbeit – einschließlich Tabellen, Karten und Abbildungen – , die anderen Werken im Wortlaut oder dem Sinn nach entnommen sind, in jedem Einzelfall als Entlehnung kenntlich gemacht habe; dass diese Dissertation noch keiner anderen Fakultät oder Universität zur Prüfung vorgelegen hat; dass sie – abgesehen von unten angegebenen Teilpublikationen – noch nicht veröffentlicht worden ist, sowie, dass ich eine solche Veröffentlichung vor Abschluss des Promotionsverfahrens nicht vornehmen werde. Die Bestimmungen der Promotionsordnung sind mir bekannt. Die von mir vorgelegte Dissertation ist von Prof. Dr. Gerhard Gompper betreut worden.

(Ort, Datum) (Unterschrift)

Teilpublikation

F. Curriculum Vitae

Özer Duman
Eschenweg 15, 52428, Jülich
01521 4577142
ozer.duman@gmail.com
05.02.1990
Bismil, Türkei

AUSBILDUNG

SEPT 2014 - JAN 2018	Doktorand, Physik, Forschungszentrum Jülich/ Universität zu Köln, Deutschland
SEPT 2012 - JULI 2014	Msc, Physik, Bilkent Universität, Türkei 3.63 / 4.0
SEPT 2008 - JULI 2012	Bsc, Physik, Bilkent Universität, Türkei 3.27 / 4.0
SEPT 2004 - JULI 2008	Milli Piyango Anadolu Hochschule, Türkei 4.9 / 5.0